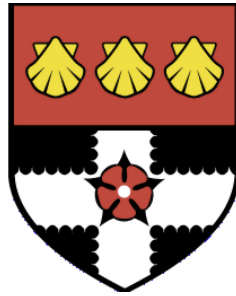


UNIVERSITY OF READING

Department of Meteorology



**Predicting the effect of the solar
wind on the ultra-low frequency
plasma waves driving Earth's
radiation belts**

Sarah N. Bentley

A thesis submitted for the degree of Doctor of Philosophy

October 2018

Abstract

Earth's radiation belts represent a hazardous environment for spacecraft. Ultra-low frequency (ULF, 1-20 mHz) plasma waves in Earth's magnetosphere are responsible for the bulk transport and energisation of energetic electrons via radial diffusion. These large-scale waves are strongly driven by the solar wind and need better characterisation in order to improve radial diffusion coefficients in radiation belt diffusion models; current parameterisations of radial diffusion coefficients vary by orders of magnitude. However, selecting solar wind properties on which to base an empirical model of ULF occurrence is difficult due to the complicated interparameter relationships between solar wind properties which mask their relationship to ULF wave power.

Using fifteen years of solar wind and ground-based magnetometer measurements, we identify three non-derived solar wind properties that are causally correlated to dayside ULF wave power at a single representative frequency and station. Solar wind speed v_{sw} , southward interplanetary magnetic field $Bz < 0$ and summed perturbations in proton number density δNp are all found to contribute significantly to ULF wave power. The corresponding driving mechanisms - magnetopause deformation processes - are discussed and it is concluded that they are highly interrelated.

With these three parameters, an empirical model for ground-based ULF wave power is developed and tested across a range of frequencies, magnetic latitudes and azimuthal angles throughout the magnetosphere. Model output is a probability distribution instead of a single deterministic value; this probabilistic approach will allow the uncertainty in radial diffusion coefficients to be quantified. This model can be used in two ways to reproduce wave power; by sampling from conditional probability distribution functions or by using the mean (expectation) values. A method is derived to test the quality of the parameterisation and the ability of the model to reproduce ULF wave power time series. Sampling is a better method for reproducing power over an extended time period as it retains the same overall distribution, while mean values predict the power in a time series better than the assumption that power persists from the preceding hour. Other sources of uncertainty in radial diffusion coefficients are reviewed.

Although this wave model is designed principally for the goal of improved radial diffusion coefficients to include in outer radiation belt diffusion based modelling, we give examples to illustrate how it may be used to investigate the occurrence of ULF waves throughout the magnetosphere and hence the physics of ULF wave generation and propagation.

DECLARATION

I confirm that this is my own work and the use of all material from other sources has been properly and fully acknowledged.

S. N. Bentley

Acknowledgements

Throughout this PhD, I have been grateful for the support of my supervisor Clare Watt who has encouraged me to follow up on any (often fruitful) topics that piqued my interest. Her enthusiasm kept the project alive when I couldn't see where it was going, and her insights brought out the significance of my work. I would also like to thank my second supervisor Mathew Owens for his advice on the solar wind, for helping me describe my work in a more accessible manner and for bringing me back to the big picture when I was too focused on the details. I would like to express my gratitude to both my supervisors for making time to read this thesis, and for their continual gentle reminders that I do not need to rederive everything from scratch.

I would like to thank various collaborators in the UK and US, and the members of SPATE at Reading, who put time and thought into my results and helped me see their wider context in space physics. Special thanks to Jonny Rae, who has given his time generously over the last few years and whose insight has improved my work.

Various resources have shaped my understanding of the different fields underlying this project, but few as much as two particular free online courses. I cannot adequately thank them in the thesis text, but I want to express my appreciation to the organisers of Plasma Physics and Applications on the edX platform, and to the organisers of Digital Signal Processing via Coursera. Thanks to the École Polytechnique Fédérale de Lausanne for encouraging their lecturers to make both these courses available.

Finally, I would like to thank my friends, officemates and family for their support and patience. Most especially, the patience of my partner Andrew Wallis through the more stressful parts of this project.

List of Figures	viii
List of Tables	xi
Nomenclature	xiv
1 Introduction	1
2 Plasma physics	6
2.1 Definition of a plasma	6
2.2 Single particle motions	8
2.3 Describing multiple particles: Distribution functions of plasma	10
2.4 Plasma as a fluid	13
2.5 General method for deriving plasma waves	16
2.6 MHD waves	17
2.6.1 Simplification of MHD equations	17
2.6.2 Method of deriving MHD waves	19
2.6.3 Alfvén Wave	21
2.6.4 Magnetosonic Waves	21
2.6.5 Other wave modes and radiation belt physics	22
2.7 Additional plasma physics	23
2.7.1 The frozen-in theorem	23
2.7.2 Magnetic reconnection	23
3 Background space physics	25
3.1 Overview of the Sun-Earth system	25
3.1.1 The Sun	26
3.1.2 The solar wind	26

3.1.3	Earth's magnetosphere	28
3.2	ULF waves in Earth's magnetosphere	32
3.2.1	Generation mechanisms	33
3.2.2	Propagation of ULF waves	34
3.2.3	Transformation of Alfvén modes through the ionosphere	35
3.2.4	Example of ULF wave observed at the ground	37
3.3	Earth's radiation belts	38
3.3.1	Particle motions and adiabatic invariants	39
3.3.2	Diffusion description of radiation belt dynamics: the Fokker-Planck equation	45
3.4	ULF waves driving radial diffusion	46
3.4.1	The role of ground and in-situ observations	48
3.5	Geomagnetic indices	49
3.5.1	Kp	49
3.5.2	Dst and SYM-H	50
3.5.3	Auroral indices	50
3.6	Co-ordinate systems	51
4	Data and processing	52
4.1	Power spectral density calculation methods	52
4.1.1	The Discrete Fourier Transform	53
4.1.2	Power Spectral Density	55
4.1.3	Reducing bias and variance in the spectral estimate	56
4.1.4	Alternatives: Wavelet methods	61
4.2	Data	63
4.2.1	Solar wind data	63
4.2.2	Ground-based magnetometer data	64
4.2.3	Data processing	65
5	Identification of model parameters	67
5.1	Introduction	68
5.2	Parameter reduction	70
5.3	Resolving solar wind interparameter relationships	71
5.3.1	Use of the median to characterise conditional probability distribution functions	73
5.3.2	Review of solar wind parameter interdependence	74
5.4	Method	78
5.5	Implicit assumptions	79

5.6	The effect of each solar wind parameter on ULF waves	81
5.7	Physically interpreting external ULF generation mechanisms	93
5.7.1	Kelvin-Helmholtz instability and v_{sw}	94
5.7.2	The Rayleigh-Taylor instability	94
5.7.3	Density perturbations and solar wind compressional waves	95
5.7.4	Perturbations arising at the bow shock or in the magnetosheath	96
5.7.5	Flux transfer events, reconnection and $B_z < 0$	97
5.7.6	Distinguishing potential driving mechanisms from the dominant solar wind parameters	98
5.7.7	Summary of contributing mechanisms	100
5.8	Discussion of causal parameter results	101
5.8.1	Summary	104
6	Prototype model	106
6.1	Model construction	107
6.1.1	Partitions of the magnetosphere	107
6.1.2	Parameterisation in each partition	109
6.2	Example: using this model	111
6.3	Testing the model	114
6.3.1	A “good” parameterisation	114
6.3.2	Ability to predict ULF wave power	118
6.3.3	Comment on other possible parameters	122
6.3.4	Comparison to Kp -based models	124
6.4	Other sources of uncertainty in radial diffusion coefficients	128
6.4.1	Background magnetic field	129
6.4.2	Other physics underlying the formalism	129
6.4.3	Summation over resonant frequencies	129
6.4.4	Accounting for azimuthal wave structure	130
6.4.5	Double-counting symmetric perturbations	130
6.4.6	Double-counting electric field perturbations	131
6.4.7	Methods of calculating power spectral density	132
6.4.8	Uncertainty from ground and space based observations	132
6.4.9	Statistical model construction	132
6.4.10	Summary	133
6.5	Conclusion	133

7 Towards physics from the model	135
7.1 Multiple regression model	136
7.1.1 Multiple regression overview	136
7.1.2 Assumptions used here	137
7.1.3 Where the model approximates the statistical model	138
7.1.4 Forecasting skill	140
7.1.5 Analysis possibilities	141
7.2 Separation proxy	142
7.2.1 Interpreting distributions of χ_S in each partition	143
7.2.2 Analysis of separation proxy χ_S across many partitions	146
7.3 Information loss during model construction	153
7.4 Testing ULF occurrence theories using the model	156
7.4.1 Power in the original data	156
7.4.2 Power in the statistical model	156
7.5 Summary	160
8 Conclusions	162
A Fast-mode compressional waves corresponding to observed density perturbations δN_p	167
Bibliography	171

LIST OF FIGURES

2-1	Collision frequencies in some typical space plasmas.	8
2-2	Ion motion in static magnetic field.	9
2-3	Ion and electron motion in crossed electric and magnetic fields.	10
2-4	Magnetic field topology change due to magnetic reconnection.	24
3-1	The Parker spiral of magnetic field embedded in the solar wind.	27
3-2	Solar wind compression and rarefaction regions around a stream interface.	28
3-3	Earth's magnetosphere.	29
3-4	The Dungey cycle.	30
3-5	Plasma populations in Earth's magnetosphere.	31
3-6	A deformation of the magnetopause driving ULF waves observed on the ground.	33
3-7	Poloidal and toroidal field line resonances.	35
3-8	Density and Alfvén velocity profile in magnetosphere.	36
3-9	Observations of field line resonances driven by magnetopause boundary oscillations.	37
3-10	The three periodic motions of magnetically trapped particles around Earth.	39
3-11	Magnetic mirror effect.	41
3-12	Timescales of drift, bounce and gyrofrequencies for trapped particles. . .	44
4-1	Butterworth filter used to remove high-frequency signals and prevent aliasing.	55
4-2	The <i>sinc</i> function is the Fourier transform of a rectangular window. . .	58
4-3	Spectral leakage due to using unmodified hour-long windows.	59

4-4	Fourier transform, windowed Fourier transform and multitaper spectral estimates of broadband and narrowband waves.	62
4-5	CARISMA magnetometer stations.	64
5-1	Analysis choices underlying the causal parameter study.	72
5-2	Lognormal conditional probability distributions of ULF PSD by Bz , δNp	75
5-3	Distribution of non-radial solar wind flow.	76
5-4	Distribution of number density Np by velocity in the solar wind.	76
5-5	Magnetic field component distributions observed in the solar wind.	77
5-6	Distribution of proton temperature T_p by velocity in the solar wind.	77
5-7	Diagram of the method used to identify causal solar wind parameters.	80
5-8	Two-parameter plots examining the relative contributions of v_x, v_y and v_x, v_z to ULF wave power.	83
5-9	Two-parameter plot examining the relative contributions of v_{sw} and δv_{sw} to ULF wave power.	84
5-10	Two-parameter plot examining the relative contributions of v_{sw}, Np and δNp to ULF wave power.	86
5-11	Two-parameter plot examining the relative contributions of v_{sw} and Bz to ULF wave power.	87
5-12	Two-parameter plot examining the relative contributions of v_{sw}, Bx and δBx to ULF wave power for $Bz > 0$	88
5-13	Two-parameter plot examining the relative contributions of v_{sw}, Bx and δBx to ULF wave power for $Bz > 0$, accounting for interdependence with δNp	89
5-14	Two-parameter plot examining the relative contributions of v_{sw}, T and δT to ULF wave power.	90
5-15	Ranking the three casual parameters $v_{sw}, Bz > 0$ and δNp	92
5-16	Cartoon of the three dominant processes driving ULF waves via magnetopause deformations.	102
6-1	Two-parameter plot examining the relative contributions of $v_{sw}, var(Np)$ and δNp to ULF wave power.	108
6-2	The normal approximation for probability distribution of logpower; best and worst examples.	110
6-3	Diagram of the nested bins in each magnetospheric partition of the ULF model.	111
6-4	Series of slices through ULF model.	112
6-5	Example time series of using the ULF statistical wave model.	113

6-6	Parameterisations with small vs. large variance between neighbouring distributions.	115
6-7	Mean and variance of the normals fitted to PSD distributions in all bins at 3.33 mHz, GILL.	117
6-8	Violin plots comparing the total fifteen-year ULF PSD distribution observed and reproduced by sampling and taking the mean.	120
6-9	Forecast skill for one station across 1-20mHz.	122
6-10	Violin plots comparing observations to predictions of ULF wave power for CARISMA non-training data.	123
6-11	A simpler Kp -based statistical model of ULF wave power.	126
6-12	Two-parameter plots examining the relative contributions of v_{sw} , $var(Np)$, Bz and Kp to ULF wave power.	127
7-1	Cost functions for the multiple regression approximation, by station, MLT sector and $Bz < 0$, $Bz > 0$	139
7-2	Cost functions for the multiple regression approximation, by frequency.	140
7-3	Forecast skill for one station across 1-20mHz, including multiple regression approximation.	141
7-4	Distributions of χ_S in each MLT sector for GILL, 3.33 mHz, $Bz < 0$	144
7-5	Distributions of χ_S in each MLT sector for GILL, 3.33 mHz, $Bz > 0$	145
7-6	Scatter plots of χ_S peak and width for all partitions.	147
7-7	Scatter plots of χ_S peak and width for all partitions, split by $Bz < 0$ and $Bz > 0$	147
7-8	Scatter plots of χ_S peak and width for all partitions, split by station.	149
7-9	Scatter plots of χ_S peak and width for all partitions, split by MLT sector.	151
7-10	Scatter plots of χ_S peak and width for all partitions, split by frequency.	152
7-11	Mean square error of statistical model when reproducing the original data. Median, upper and lower quartiles across all frequencies split by station, MLT sector and $Bz < 0$, $Bz > 0$	154
7-12	Mean square error of statistical model when reproducing the original data. Median, upper and lower quartiles across all station, MLT sector and $Bz < 0$, $Bz > 0$ split by frequency.	155
7-13	Mean logpower in partitions of the original data. Median, upper and lower quartiles across all frequencies split by station, MLT sector and $Bz < 0$, $Bz > 0$	157
7-14	Mean logpower in partitions of the original data. Median, upper and lower quartiles across all partitions, split by frequency.	157

LIST OF TABLES

2.1	Some typical space plasma properties.	7
3.1	Typical solar wind plasma values at Earth.	27
3.2	IAGA pulsation classification, [<i>Jacobs et al.</i> , 1964].	32
6.1	Parameters used to discretely partition statistical ULF wave model . . .	109
6.2	Forecasting skill at selected stations and frequencies	121
7.1	Median $\chi_s(v_{sw})$, $\chi_S(\text{var}(Np))$ and $\chi_S(Bz)$ for GILL, 3.33 mHz, noon. .	143
A.1	Table of median values used to calculate the resultant size of velocity perturbations we expect from fast mode compressional waves.	169

Symbols

A	magnetic vector potential
B	magnetic field
$B_{\hat{\eta}}$	bias of an estimate $\hat{\eta}$
c_f^2	square sum of Alfvén and sound speeds
c_S	sound speed
χ_S	separation proxy
Dst	disturbance storm time index
D_{LL}	radial diffusion coefficient
D_{LL}^E	electric field radial diffusion coefficient
D_{LL}^B	magnetic field radial diffusion coefficient
δX	summed amplitude in perturbations of a parameter X
E	electric field
ϵ_0	permittivity of free space
η	resistivity
η	a stochastic signal
$\hat{\eta}$	estimate of η
f_s	plasma distribution function of species s
f	frequency
Δf	frequency resolution
j	current density
J_2	second adiabatic invariant
J_C	cost function
k	wavenumber
Kp	planetary geomagnetic activity index
κ	discrete frequency index
L	McIlwain L-shell
L^*	Roederer L-parameter
λ_{De}	Debye length
m_s	mass of particles of species s
m	azimuthal wave number
μ	first adiabatic invariant (Chapter 3), mean (Chapter 6, Chapter 7)
μ_0	permeability of free space
n	plasma density
Np	proton number density
ω	frequency
ω_{pe}	electron plasma frequency
$\omega_{g,s}$	gyrofrequency of s
P	pressure
P_{dyn}	dynamic pressure
\mathcal{P}	power
Φ	magnetic flux
p	generalised momentum
\perp	perpendicular to magnetic field
\parallel	parallel to magnetic field
q	charge

(Symbols cont.)

$r_{g,s}$	gyroradius of s
ρ	charge density
R_E	radius of the Earth
\mathbf{R}_C	radius of curvature
$\sigma_{\hat{\eta}}^2$	variance of an estimate $\hat{\eta}$
σ	standard deviation
τ_p	characteristic timescale of process p
\mathbf{u}	average flow velocity
\mathbf{v}	velocity
v_A	Alfvén speed
v_{sw}	solar wind speed
w	width of χ_S distribution

Abbreviations

CANOPUS	Canadian Auroral Network for the OPEN Program Unified Study
CARISMA	Canadian Array for Realtime Investigations of Magnetic Activity
DFT	Discrete Fourier transform
FCHU	Fort Churchill magnetometer station
FTE	Flux transfer event
GILL	Gillam magnetometer station
ISLL	Island Lake magnetometer station
KHI	Kelvin-Helmholtz instability
MHD	Magnetohydrodynamics
MLT	Magnetic local time
MSE	Mean square error
NASA	National Aerospace and Space Administration
PINA	Pinawa magnetometer station
PSD	Power spectral density
RTI	Rayleigh-Taylor instability
ULF	Ultra-low frequency

CHAPTER 1

INTRODUCTION

The area of near-Earth space dominated by Earth's magnetic field - the magnetosphere - is home to numerous plasma processes. The region of high-energy, magnetically trapped charged particles (Earth's radiation belts) are capable of disrupting satellite services, one of the space weather risks listed on the UK National Risk Register [*Jursa*, 1985; *Horne et al.*, 2013; *Cabinet Office*, 2017]. The magnetosphere supports ultra-low frequency (ULF) plasma waves, oscillations in an ionised gas that can have compressional, magnetic and electric components. ULF waves in the 1-20 mHz range are implicated in the bulk transport, energisation and radial diffusion of electrons in the Earth's radiation belts [e.g., *Fälthammar*, 1965; *Elkington et al.*, 1999; *Elkington*, 2013; *Roederer and Zhang*, 2014]. The inward radial transport of electrons violates their third adiabatic invariant (a conserved quantity relating to azimuthal drift motion around the Earth) and results in an energy gain.

The key aim of this project is to improve statistical wave maps of ULF power underlying existing radiation belt modelling. Secondary aims include investigating the physics underlying ULF wave phenomena and considering appropriate ways to include ULF waves in radial diffusion coefficients. These goals are covered more fully at the end of this introduction.

The study of ULF waves is challenging due to the complexity of their generation mechanisms and their subsequent propagation, as established in multiple reviews of their role in magnetospheric dynamics [e.g., *McPherron*, 2005; *Menk*, 2011; *Mann et al.*, 2012; *Takahashi*, 2016]. Attempts to predict the power in these wave modes and hence the diffusion coefficients determining radial electron transport has long been an area of active research [*Fälthammar*, 1965; *Brautigam and Albert*, 2000; *Ozeke et al.*, 2014] in

order to better predict particle populations that pose a risk to space hardware [*Horne et al.*, 2013].

ULF waves are strongly driven by coupling of the magnetosphere to the solar wind, giving rise to disturbances of the magnetopause [e.g., *McPherron*, 2005]. Magnetospheric ULF waves can also be generated by internal sources such as the drift-bounce resonance and substorms [e.g., *Yeoman and Wright*, 2001; *Yeoman et al.*, 2016; *Murphy et al.*, 2011a; *Rae et al.*, 2011], but in this thesis we largely focus on how the solar wind controls magnetospheric ULF waves. External drivers can be categorised as either perturbations embedded in the solar wind, perturbations that originate near the bow shock or from magnetosheath instabilities, or perturbations arising at the magnetopause. All these mechanisms result in magnetopause perturbations that can launch fast mode compressional waves, which then penetrate into the magnetosphere and are then transformed and amplified by magnetospheric processes. Inwards-propagating fast mode waves can become trapped between the reflecting boundaries of the magnetopause and an inner turning point such as the plasmapause [*Kivelson et al.*, 1984; *Kivelson and Southwood*, 1986]. Any fast mode compressional ULF waves that reach a region where the length of the magnetic field line supports waves of a similar frequency can couple with the field line and drive standing Alfvén toroidal modes [e.g., *Obayashi and Jacobs*, 1958; *Radoski*, 1966]. Magnetic field perturbations observed at ground-based magnetometer stations are integrated over a large area of the ionosphere and will have mixed components of these standing Alfvén waves and of fast mode compressional waves. At higher latitudes, observations of magnetic field perturbations at ground level can be used with some success to estimate the equatorial electric field [*Ozeke et al.*, 2009; *Rae et al.*, 2012] and hence estimate electron radial diffusion coefficients [*Ozeke et al.*, 2012, 2014].

Modelling of the outer radiation belt can potentially enable satellite operators to protect their spacecraft from dangerous space weather such as spacecraft charging, deep dielectric charging and single upset events [*Baker et al.*, 1987; *Frederickson*, 1996; *Horne et al.*, 2013]. One of the areas identified as requiring better characterisation in order to improve forecasting and modelling of past events is the radial transport of electrons by ultra-low frequency plasma waves. This can be achieved by improving models of ULF occurrence, including understanding the azimuthal variation of ULF waves and the underlying coupling to the solar wind [*Horne et al.*, 2013]. In this thesis, ULF waves in the 1-10 mHz and 1 – 20 mHz ranges are studied, although frequencies at the lower end of this band are most effective at radial transport, as there is more power on average at lower frequencies [*Bentley et al.*, 2018, Figure 1(a)] and because lower frequencies can set up drift resonant diffusion [*Elkington et al.*, 1999, 2003]. Hence it

is important to examine the generation and propagation of the electromagnetic waves that drive this diffusion, and to construct a model of the resultant diffusion that will improve nowcasting and forecasting in the outer radiation belt. Current calculations of radial diffusion coefficients can be constructed from the electromagnetic field in MHD models [Fei *et al.*, 2006] or from observations, either solely using in situ measurements [Lejosne *et al.*, 2013; Liu *et al.*, 2016] or by incorporating ground-based magnetic field measurements mapped up to the equatorial electric field [Lanzerotti and Morgan, 1973; Brautigam and Albert, 2000; Ozeke *et al.*, 2009, 2012, 2014].

In situ spacecraft provide more reliable measurements of the electromagnetic waves driving radial diffusion, but spacecraft coverage is sparse and has limited temporal coverage. Ground-based magnetometer networks across the globe have produced many years of observations spanning multiple solar cycles [e.g. Rostoker *et al.*, 1995; Mann *et al.*, 2008; Tanskanen, 2009; Gjerloev, 2012]. By mapping these measurements of ULF waves up to the equatorial plane these networks can provide a long-term dataset with significantly better spatiotemporal coverage, allowing multiple simultaneous measurements at different locations and encompassing a large range of latitudes (and hence radial locations) and azimuthal (or magnetic local time, MLT) sectors. Therefore in this project, fifteen years of observations from a ground-based magnetometer chain in Canada [CANOPUS/CARISMA, Rostoker *et al.*, 1995; Mann *et al.*, 2008] are used in a long-term statistical study. By “ULF waves” we mean the mix of Alfvén and compressional waves detected by ground-based magnetometers in our frequency range. All these wave modes are implicated in wave-particle interactions in the magnetosphere [Elkington *et al.*, 1999, 2003; Zong *et al.*, 2007; Degeling *et al.*, 2008; Claudepierre *et al.*, 2013; Mann *et al.*, 2013; Ozeke *et al.*, 2014].

Existing models of radial diffusion coefficients are often parameterised by the geomagnetic activity index Kp [Brautigam and Albert, 2000; Lejosne *et al.*, 2013; Ozeke *et al.*, 2014; Ali *et al.*, 2016]. Individual radial diffusion models based on this parameterisation can differ by orders of magnitude [Liu *et al.*, 2016; Ali *et al.*, 2016]. This makes it difficult to accurately capture radial diffusion in radiation belt models as the uncertainty in models is unquantified but could easily extend across orders of magnitude. Whilst Kp is a proxy for geomagnetic activity, it is not directly related to processes driving ULF waves. Additionally, as a three-hour averaged index, only forecasted Kp rather than real time Kp can be used for nowcasting or forecasting. The choice of parameters is an important part of constructing any kind of empirical model as the parameters chosen should have a clear physical basis in order to represent (and ultimately, to interpret) the physical phenomena underlying the observations. We propose a model based initially on solar wind parameters measured by spacecraft

at the L1 Lagrange point, which has a lead time of around an hour [*Richardson and Paularena*, 1998; *Weimer et al.*, 2002; *King and Papitashvili*, 2005]. The solar wind parameters should be carefully chosen to ensure that they are truly related to changes in magnetospheric ULF wave power by accounting for nonlinear interdependent relationships between solar wind properties. Solar wind properties are highly dependent on the type of solar wind and therefore co-vary in multiple ways, some of which may result in spurious correlations with ULF wave power that must be considered.

To address the large difference between existing radial diffusion models, we also propose a probabilistic model. In meteorology and climate modelling, probabilistic approaches have met with considerable success in recent years as a method of improving models by accounting for uncertainty and variability in modelling, e.g. [*Berner et al.*, 2017]. Probabilistic models produce a probability distribution as output instead of the single values produced by deterministic models, and can be used to quantify the uncertainty introduced by each model component. Model components or steps with larger uncertainty will therefore indicate areas where the model can be improved to better approximate the underlying physics, regardless of the physical process being approximated. Component uncertainties that should be quantified include uncertainty due to initial conditions, boundary conditions, the underlying physics model and due to natural internal variability in the system. Probabilistic methods provide a way to quantify variability that either exists naturally, or exists due to a parameterisation that has yet to be optimised [*Watt et al.*, 2017].

The ultimate goal of this project is to improve the characterisation of ULF wave power for use in radiation belt modelling. There are three main components to this: the primary goal is a statistical model of ULF wave power to improve existing radiation belt diffusion models. Diffusion models are an effective and computationally cheap method of evolving radiation belt particles and ULF statistical wave maps have already been identified as an area requiring work to improve diffusion models [*Horne et al.*, 2013]. To satisfy the requirements of improved diffusion models, our statistical wave map will be parameterised by near-instantaneous physically significant solar wind properties, will be resolved in radial and azimuthal regions of the magnetosphere and will be probabilistic. Internal magnetospheric properties and time-lagged contributions may need to be considered in future. Two complementary secondary goals influence the approach taken to construct this model: firstly, to investigate the underlying physics. The long-term approach here can be used to identify which existing ULF generation and propagation processes occur often enough to be significant for ULF behaviour. Study of these processes could inform an improved statistical model, identify unexpected physical behaviour and ideally inform physics-based radiation belt modelling

(to complement the computationally cheaper diffusion approach). Secondly, one can also prioritise investigation into how ULF waves are used in radiation belt diffusion modelling, for example comparing existing formalisms to calculate ULF-driven diffusion. Clearly this will inform a sensible model of ULF wave occurrence but will also identify further steps necessary for an improved model of radial diffusion coefficients in future.

This thesis is structured as follows. In Chapter 2 the plasma physics underlying space-based processes is introduced, including the definition of a plasma, methods of describing a plasma and an outline of the derivation of ULF plasma waves. Background space physics for this project is covered in Chapter 3, beginning with processes in the Sun that give rise to the solar wind and the dynamics of Earth’s magnetosphere. This is followed by a review of magnetospheric ULF waves, including their generation, propagation and conversion to ground-based observations. Radiation belt particle motions and the diffusion equation used to describe their evolution in a conserved-quantity space (the Fokker-Planck equation) are given, along with the role of ULF waves in radial diffusion. This section also includes useful background physics such as descriptions of co-ordinate systems.

In Chapter 4 the solar wind and magnetometer datasets used throughout the analysis are presented and the pre-processing outlined. This chapter also contains a discussion of methods used to calculate the power in ULF waves and justifies the choice of the multitaper method. Analysis begins in Chapter 5, where the solar wind properties causally correlated to ULF wave power are identified after accounting for numerous solar wind interparameter relationships. The resulting ULF-effective parameters (solar wind speed v_{sw} , southward interplanetary magnetic field $Bz < 0$ and perturbations in proton number density δNp) are then compared to existing theories of solar wind-magnetosphere coupling processes capable of generating ULF waves. In Chapter 6 these solar wind properties are used to construct a statistical model of ULF wave power occurrence throughout the magnetosphere. This model is tested to establish whether it is a good parameterisation, whether it accurately predicts ULF wave occurrence and how it compares to a similar Kp -parameterised model. Other sources of uncertainty in diffusion coefficient calculations are also discussed. In Chapter 7 we outline how one may investigate the physics from this model. Finally, these results are discussed and future work is suggested in Chapter 8.

CHAPTER 2

PLASMA PHYSICS

Plasmas (ionised gases) are found throughout the solar system and hence an understanding of plasma physics is a necessary component of space physics. Indeed, the ultra-low frequency waves of this project are a plasma phenomenon and the main focus of this chapter is to review the theory behind their derivation. In Section 2.1 the definition and basic properties of a plasma are presented. To introduce some of the behaviour underlying a plasma, the motion of a single particle in electric and magnetic fields is reviewed in Section 2.2. This will underly the radiation belt phenomena described in Section 3.3. Then ULF waves will be briefly derived, beginning with a particle description of plasma (Section 2.3) and demonstrating how on larger scales, the plasma behaviour can be described as a magnetised fluid (Section 2.4). In Section 2.5 and Section 2.6 the plasma waves in the ultra-low frequency range are derived and the properties of these wave modes briefly demonstrated. Finally, in Section 2.7 other plasma processes and properties relevant to this project are reviewed. In this plasma review we use only non-relativistic plasma physics. This is sufficient to describe ULF waves, since the fluid motions that support the electromagnetic plasma oscillation is dominated by cold plasma inside Earth's magnetosphere.

2.1 Definition of a plasma

A plasma is a collection of positively and negatively charged particles that is quasineutral and displays collective behaviour [*Thorne and Blandford, 2017; Chen, 2016; Baumjohann and Treumann, 1996*]. More specifically, this means that the plasma appears electrically neutral, that effects of individual, local charges are shielded and that the plasma acts collectively in response to external forces. By examining the shielding effect

Table 2.1: Some typical space plasma properties.

Plasma	Density (m^{-3})	Temperature (eV)	Debye length (m)	N_D
Solar wind	10^7	10	10	10^{10}
Solar corona	10^{12}	10^2	10^{-1}	10^9
Magnetosphere	10^7	10^3	10^2	10^{13}
Ionosphere	10^{12}	10^{-1}	10^{-3}	10^4

Adapted from *Kivelson and Russell [1995]*.

of a cloud of charged particles around a charged test particle, one finds that the electric potential of a single charge in a plasma drops off exponentially over distances of the Debye length, [*Thorne and Blandford, 2017; Chen, 2016; Baumjohann and Treumann, 1996*],

$$\lambda_{De} = \sqrt{\frac{\epsilon_0 k_B T_e}{e^2 n_0}}, \quad (2.1)$$

where ϵ_0 is the permittivity of free space, k_B is the Boltzmann constant, T_e is the plasma temperature, e the charge of an electron and n_0 the plasma density. The derivation of this value assumes that there are many ($\gg 1$) particles in each Debye sphere, an assumption that holds in most space plasma. Example values of density, temperature, Debye length and number of particles N_D in a Debye sphere for some typical space plasmas are shown in Table 2.1. This distance λ_{De} is then a characteristic scale length of a plasma. Processes on much larger scales are only minimally affected by individual or local charges due to this shielding effect. Plasma behaviour occurs when electromagnetic plasma oscillations of the charged particles dominate over collisions between particles. In an electron-ion plasma, one can consider the resulting oscillation of electrons when displaced (assuming the ions remain fixed) to find the electron plasma frequency

$$\omega_{pe} = \sqrt{\frac{n_0 e^2}{\epsilon_0 m_e}}, \quad (2.2)$$

where m_e is the mass of an electron [*Chen, 2016*]. Hence electrons oscillate around their equilibrium positions at this frequency, which defines a characteristic timescale of a plasma. Collisions will not dominate the plasma if the collision frequency is far lower than ω_{pe} .

Together, these three conditions (length scales larger than the Debye length, a well-populated Debye sphere and small ratio of collision to plasma frequency) are the

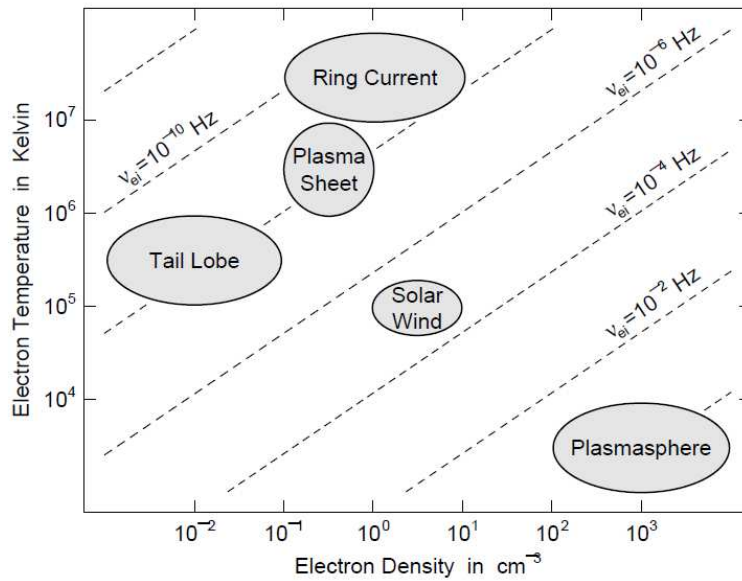


Figure 2-1: Coulomb collision frequencies between electrons and ions in some typical space plasmas. Taken from *Baumjohann and Treumann* [1996].

criteria necessary to observe plasma behaviour. In most space plasmas relevant to this project, the collision frequency is so low as to be negligible. For example, the collision time of electrons in the solar wind ($\sim 3 \times 10^5$ s) is comparable to the travel time of the solar wind to the Earth ($\sim 3.5 \times 10^5$ s) (and the proton collision time is even longer, $\sim 4 \times 10^6$ s) [*Kivelson and Russell*, 1995]. Collision frequencies for other plasma populations relevant to the magnetosphere are shown in Figure 2-1.

2.2 Single particle motions

It is often most intuitive to understand plasma behaviour by considering the motion of individual particles within that plasma. A particle with charge q moving with a velocity \mathbf{v} in a electromagnetic field is subject to the Lorentz force (gravity is neglected) [*Roederer and Zhang*, 2014; *Baumjohann and Treumann*, 1996]

$$\mathbf{F}_L = q(\mathbf{E} + \mathbf{v} \times \mathbf{B}). \quad (2.3)$$

In reality the electric and magnetic fields are in turn determined by the particle location and motion, which makes this description somewhat simplistic. However, it is useful for understanding radiation belt particles, which are relatively few in number compared to lower energy magnetospheric plasma and so contribute less to the electric and magnetic fields they are subject to. The single particle motions discussed here

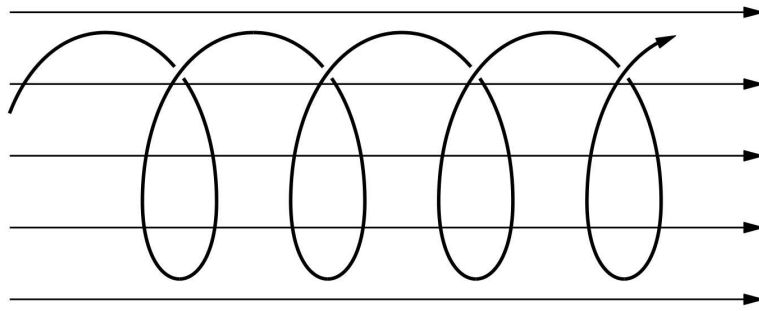


Figure 2-2: A helical path is traced out by an ion in a static magnetic field. Taken from *Baumjohann and Treumann [1996]*.

will be applied to the trapped magnetospheric particles comprising the radiation belts in Section 3.3. Examining single particle motions also provides temporal and spatial scales on which we can average plasma behaviour.

From equation (2.3) it can be inferred that in a region with no electric field and a static magnetic field a single charged particle moving in the direction of the magnetic field \mathbf{B} will be unaffected, while any motion perpendicular to the field will result in a circular motion. An example of the helical motion of a positively charged particle in a static magnetic field with both parallel and perpendicular velocity is shown in Figure 2-2. The gyroradius and gyrofrequency (or cyclotron frequency) of this motion are given by

$$r_{g,s} = \frac{m_s v_{\perp}}{|q_s| B}, \omega_{g,s} = \frac{|q_s| B}{m_s} \quad (2.4)$$

for a particle s of charge q_s and velocity v_{\perp} perpendicular to the magnetic field. When an electric field is also applied, the particle is accelerated when it is travelling in the direction of \mathbf{E} . Depending on the orientation of \mathbf{E} and \mathbf{B} , together this results in drifting loops as the particle is subject to different forces across its gyromotion. Figure 2-3 shows an example of this for perpendicular electric and magnetic fields; an initially stationary particle will be accelerated parallel to the electric field, with direction dependent on whether it is positively or negatively charged. As the particle velocity is no longer zero, the particle begins to trace out a circular motion due to the magnetic field. However, on the second half of this motion, the particle is decelerated by the electric field and the gyroradius returns to zero. This process is then repeated, constituting a continual $\mathbf{E} \times \mathbf{B}$ drift. In fact, the particle motion can be described by a superposition of guiding centre motion and the gyromotion. Drifts - guiding centre motion - occur due to different forces acting on particles across each gyration. By transforming to

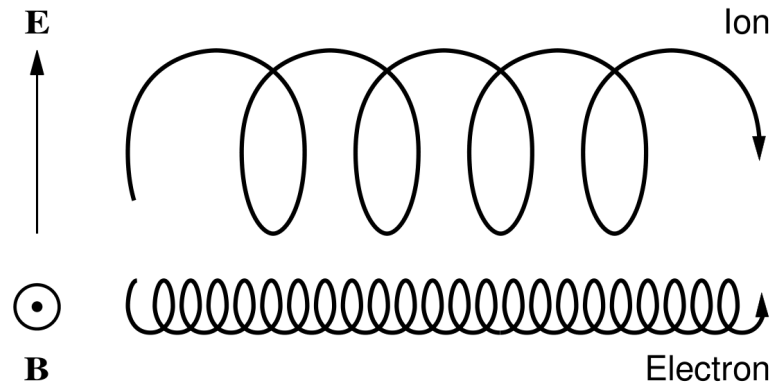


Figure 2-3: The combination of magnetic field induced gyromotion and electric field acceleration and deceleration drive a particle drift, where the drift direction is also dependent on the particle charge. Taken from *Baumjohann and Treumann* [1996].

a guiding centre frame of reference and calculating the resulting equations of motion one can systematically derive all the drifts that the guiding centre is subject to (up to the appropriate order with respect to scale size) [*Oberparleiter*, 2015; *Navarro*, 2012; *Cary and Brizard*, 2009; *Chan*, 1998; *Littlejohn*, 1983; *Northrop*, 1963]. Physically significant drifts in the radiation belts are the E cross B , gradient and curvature drifts, discussed in Section 3.3. Less rigorous but more physically intuitive descriptions of the drifts can be found in *Baumjohann and Treumann* [1996]; *Chen* [2016]; *Kivelson and Russell* [1995]. They are also derived in *Roederer and Zhang* [2014] for the radiation belts, although with a different definition of “order”. Once one considers a scale larger than the gyroradius, the guiding centre motion provides a useful description of single particle motion.

2.3 Describing multiple particles: Distribution functions of plasma

A plasma is fully determined by the collective motion of particles and the electromagnetic fields. These are coupled as the particles are subject to the forces applied by these fields but the fields are, in turn, determined by the location and motion of the particles. Hence to describe a plasma we need to describe the electric and magnetic fields (using Maxwell’s equations, equations (2.5) to (2.8)) and an equation of motion for the particles,

$$\nabla \times \mathbf{E} = -\frac{\partial \mathbf{B}}{\partial t} \quad (2.5)$$

$$\nabla \times \mathbf{B} = \mu_0 \left(\mathbf{j} + \epsilon_0 \frac{\partial \mathbf{E}}{\partial t} \right) \quad (2.6)$$

$$\nabla \cdot \mathbf{E} = \frac{\rho}{\epsilon_0} \quad (2.7)$$

$$\nabla \cdot \mathbf{B} = 0. \quad (2.8)$$

To describe the motion of large numbers of particles, one can use a distribution function for each species

$$f_s = f_s(\mathbf{x}, \mathbf{v}, t), \quad (2.9)$$

which determines the probability distribution function of a particle species s in a six-dimensional phase space; three spatial and three velocity dimensions, evolving in time. This determines the number of particles at a given time and location with a given velocity and therefore the distribution of particles in a plasma. Hence the total number of particles N_s in a plasma is determined by calculating $\int f_s d\mathbf{x}d\mathbf{v}$ [see e.g. *Baumjohann and Treumann, 1996; Thorne and Blandford, 2017; Chen, 2016*]. Similarly, fluid quantities of density and average fluid velocity are given as follows:

$$n_s(\mathbf{x}, t) = \int f_s d\mathbf{v} \quad (2.10)$$

$$\mathbf{u}_s(\mathbf{x}, t) = \frac{1}{n_s} \int \mathbf{v} f_s d\mathbf{v}. \quad (2.11)$$

The evolution of this distribution function f_s can be derived to determine the dynamical evolution of the plasma, by considering the conservation of particles,

$$\frac{\partial f_s}{\partial t} + \nabla_{6D} \cdot (\mathbf{u} f_s) = \sigma, \quad (2.12)$$

where $\nabla_{6D} = (\nabla_{\mathbf{x}}, \nabla_{\mathbf{v}}) = (\partial_x, \partial_y, \partial_z, \partial_{v_x}, \partial_{v_y}, \partial_{v_z})$ is the vector differential operator in our phase space, $\mathbf{u} = (\frac{\partial \mathbf{x}}{\partial t}, \frac{\partial \mathbf{v}}{\partial t})$ is the flow velocity and σ describes particles sinks or sources. Therefore this equation states that particles are moved in phase space (i.e. moved physically in \mathbf{x} or accelerated/decelerated in \mathbf{v}) or that they are lost or generated by processes included in σ (which can therefore include terms to couple

between different particle species). The continuity equation, equation (2.12), can be rearranged using vector identities and by noting that in this phase space description \mathbf{x} and \mathbf{v} are independent, i.e. $\nabla_{\mathbf{x}} \cdot \mathbf{v} = \nabla_{\mathbf{v}} \cdot \mathbf{x} = 0$. Then using $\mathbf{F} = m\mathbf{a}$ we can substitute $\dot{\mathbf{v}}$ with an expression for the force experienced by the particles in the plasma:

$$\frac{\partial f_s}{\partial t} + \dot{\mathbf{x}} \cdot \nabla_{\mathbf{x}} f_s + \nabla_{\mathbf{v}} \cdot \left(\frac{\mathbf{F}_{s.r.} + \mathbf{F}_{l.r.}}{m_s} f_s \right) = \sigma, \quad (2.13)$$

where we are considering “long range” forces as those fields acting on the entire plasma, and “short range” forces that describe interactions between plasma particles. If we neglect gravity (assuming electromagnetic fields are dominant) then the long range force is the Lorentz force $\mathbf{F}_{l.r.} = \mathbf{F}_L = q_s(\mathbf{E} + \mathbf{v} \times \mathbf{B})$. Since both electric and magnetic fields are dependent on \mathbf{x} and t (not \mathbf{v}) and $\mathbf{v} \times \mathbf{B}$ is perpendicular to \mathbf{v} , one can find the following equation by combining σ and the effects of short range forces:

$$\frac{\partial f_s}{\partial t} + \dot{\mathbf{x}} \cdot \nabla_{\mathbf{x}} f_s + \frac{\mathbf{F}_L}{m_s} \cdot (\nabla_{\mathbf{v}} f_s) + = \Sigma_C. \quad (2.14)$$

This is the Boltzmann equation, with collision operator Σ_C . Σ_C contains changes in the distribution function f_s due to collisions with particles of the same and different species. For a space plasma, we consider collisions to be negligible. Then $\Sigma_C = 0$ and we have the Vlasov equation

$$\frac{\partial f_s}{\partial t} + \dot{\mathbf{x}} \cdot \nabla_{\mathbf{x}} f_s + \frac{q_s}{m_s} (\mathbf{E} + \mathbf{v} \times \mathbf{B}) \cdot (\nabla_{\mathbf{v}} f_s) + = 0. \quad (2.15)$$

Together with the Maxwell equations (2.5) to (2.8)) this fully describes the plasma. These equations are coupled as the charge and current densities used to calculate the electric and magnetic fields are derived from f_s

$$\rho(\mathbf{x}, t) = \Sigma_s q_s \int f_s d\mathbf{v} \quad (2.16)$$

$$\mathbf{j}(\mathbf{x}, t) = \Sigma_s q_s \int \mathbf{v} f_s d\mathbf{v}. \quad (2.17)$$

However, actually using this system of equations is somewhat difficult. It is difficult to find analytical solutions whilst in simulations, it is expensive to examine the evolution of the Vlasov equation. A computationally cheaper option is to make a self-consistent plasma description evolving collections of superparticles (particle-in-cell, or PIC methods). However, for large-scale magnetospheric processes such as ULF waves it is unnecessary to focus on such small-scale processes, as the scale of ULF waves is far larger than single particle motions such the ion and electron gyroradii. For example,

electrons and protons with an energy of 1 keV at an orbit of ~ 6 Earth radii (R_E) have gyroradii of 0.76 km and 32 km respectively [Kivelson and Russell, 1995]. Instead the plasma can be approximated much more tractably as a fluid.

2.4 Plasma as a fluid

With a fluid description, macroscopic fluid quantities such as density, momentum and pressure are derived and their evolution in real space is considered using conservation equations. This reduces the phase space by integrating over (averaging) velocity space, for example the density, average bulk velocity and pressure are given as follows for a single charged particle species s :

$$n_s(\mathbf{x}, t) = \int f_s d\mathbf{v} \quad (2.18)$$

$$\mathbf{u}_s(\mathbf{x}, t) = \frac{1}{n_s} \int \mathbf{v} f_s d\mathbf{v} \quad (2.19)$$

$$\mathbf{P}(\mathbf{x}, t) = m_s \int (\mathbf{v} - \mathbf{u}_s)(\mathbf{v} - \mathbf{u}_s) f_s d\mathbf{v}. \quad (2.20)$$

These macroscopic quantities are known as velocity moments, where each one is an integral $\int \mathbf{G}^i f_s d\mathbf{v}$ of a rank i tensor \mathbf{G} and the distribution function f_s . Including higher order moments in our fluid approximation can be considered a method recovering the information lost when performing averages over velocity space. For example, the density is a zeroth order quantity (in \mathbf{v}), velocity is first order and pressure second order. When evaluated in real space these are then equivalent to polynomials of order i . If chosen correctly, polynomials of order up to n are orthogonal basis functions of an $n-1$ -dimensional space. This means that $\int \mathbf{G}^{n+1} f_s d\mathbf{v}$ contains information that cannot be fully described by $\int \mathbf{G}^n f_s d\mathbf{v}$, or any combination of lower order moments. Therefore by using an infinite number of moments a fluid approximation should converge towards a kinetic description, although typically only the first few are used. This can also be considered in terms of a multiple regression on an infinite number of points: a linear regression will contain much of the trend, but these points will be best described by a polynomial of order approaching infinity. Generally, only the density, bulk velocity and pressure are evaluated when considering space plasma. For this wave derivation, we consider the evolution of density and bulk velocity, which will require choosing a pressure constraint.

Evolution of the macroscopic fluid quantities can be found using conservation equations, derived in turn by taking moments of the Vlasov equation 2.15 with weight $g_i(\mathbf{v})$,

e.g.

$$\int g_i(\mathbf{v})[Vlasov]d\mathbf{v}. \quad (2.21)$$

We find the continuity equation for $g_1 = 1$ and conservation of momentum for $g_2 = m_s \mathbf{v}$, for each species s . The continuity equation is

$$\frac{\partial n_s}{\partial t} + \nabla \cdot (n_s \mathbf{u}_s) = 0 \quad (2.22)$$

and the conservation of momentum density can be found to be¹:

$$\frac{\partial(n_s \mathbf{u}_s)}{\partial t} + \nabla \cdot (n_s \mathbf{u}_s \mathbf{u}_s) + \frac{1}{m_s} \nabla \cdot \mathbf{P}_s - \frac{q_s}{m_s} n_s (\mathbf{E} + \mathbf{u}_s \times \mathbf{B}) = 0. \quad (2.23)$$

We now use $\nabla = \nabla_{\mathbf{x}}$ exclusively, as the velocity dependence of our plasma is averaged out. There are no viscosity or friction terms as we assume collisions are negligible. Note that the continuity equation describing evolution of n_s required the fluid quantity \mathbf{u}_s , the flow velocity, to be complete. Similarly, the momentum equation required the pressure tensor \mathbf{P}_s . This is a closure problem, where a higher order fluid quantity is always needed. At some point an approximation for the pressure tensor (or higher order moments such as heat flux) must be made to close this system of equations; an infinite hierarchy of fluid equations would converge to a full kinetic description [see e.g. *Chen, 2016*].

While separate fluids can be considered for each plasma species, here we assume that the length scales of interest are far larger than the kinetic scales of any of the individual species. When length scales are far larger than electron and ion gyroradii or inertial length (also called “skin depth”, i.e. how far into plasma radiation can penetrate) we can sum the species together to describe their effects as a single fluid. In that case we define new one-fluid quantities

¹In this notation, both $\mathbf{u}_s \mathbf{u}_s$ and \mathbf{P}_s are second rank (i.e. two-dimensional) tensors. $\mathbf{u}_s \mathbf{u}_s$ is an example of the tensor or dyadic product \mathbf{T} constructed from two vectors \mathbf{a}, \mathbf{b} as follows: $T_{ij} = a_i b_j$, or

$$\mathbf{T} = \begin{bmatrix} a_1 b_1 & a_1 b_2 & a_1 b_3 \\ a_2 b_1 & a_2 b_2 & a_2 b_3 \\ a_3 b_1 & a_3 b_2 & a_3 b_3 \end{bmatrix}.$$

Therefore it can be seen that all terms in equation (2.23) are vectors, since pressure \mathbf{P} can be written in terms of the tensor product in equation (2.20). Generally it is easiest to distinguish tensors and vectors using index notation. However, this is uncommon in space physics so here we use lowercase bold font to indicate vectors and uppercase bold font for higher rank tensors, with the exceptions that the electric (\mathbf{E}) and magnetic (\mathbf{B}) fields and force (\mathbf{F}) are vectors, but represented with uppercase characters for readability.

$$n(\mathbf{x}, t) = \sum_s n_s m_s = n_e m_e + n_i m_i \quad (2.24)$$

$$\mathbf{u}(\mathbf{x}, t) = \frac{\sum_s m_s n_s \mathbf{u}_s}{\sum_s m_s n_s} \quad (2.25)$$

$$\rho(\mathbf{x}, t) = \sum_s n_s q_s = e(n_i - n_e) \quad (2.26)$$

$$\mathbf{j} = \sum_s q_s n_s \mathbf{u}_s \quad (2.27)$$

$$\mathbf{P} = \sum_s \mathbf{P}_s = \sum_s n_s m_s \int (\mathbf{u}_s - \mathbf{u})(\mathbf{u}_s - \mathbf{u}) f_s d\mathbf{v}, \quad (2.28)$$

the mass density, centre-of-mass velocity, total electric charge, total electric current and centre-of-mass pressure respectively. Quasineutrality is given by $n_e = n_i$. The fluid equations for a single fluid are derived primarily by combining those for the single species derived above; for example by multiplying the single species continuity equations 2.22 by their relative masses, the single fluid continuity equation is given by

$$\frac{\partial n}{\partial t} + \nabla \cdot (n\mathbf{u}) = 0. \quad (2.29)$$

Similarly, by multiplying by each species charge, one can find the conservation of charge density

$$\frac{\partial \rho}{\partial t} + \nabla \cdot \mathbf{j} = 0. \quad (2.30)$$

Adding single species momentum equations 2.23 for ions and electrons, and using $m_e \ll m_i$ so that $m \sim m_i$, the momentum equation for a single fluid is

$$\frac{\partial(n\mathbf{u})}{\partial t} + \nabla \cdot (n\mathbf{u}\mathbf{u}) = -\nabla \cdot \mathbf{P} + \rho\mathbf{E} + \mathbf{j} \times \mathbf{B}. \quad (2.31)$$

By adding the momentum equations for the electrons and ions multiplied by $\frac{-1}{en_e}$ and $\frac{m_e}{em_i n_i}$ respectively, one can find the generalised Ohm's law determining the evolution of the current density, [Gurnett and Bhattacharjee, 2005]

$$\mathbf{E} + \mathbf{u} \times \mathbf{B} = \eta \mathbf{j} + \frac{1}{ne} \mathbf{j} \times \mathbf{B} - \frac{1}{ne} \nabla \cdot \mathbf{P}_e + \frac{m_e}{ne^2} \left[\frac{\partial \mathbf{j}}{\partial t} + \nabla \cdot (\mathbf{j}\mathbf{u} + \mathbf{u}\mathbf{j}) \right]. \quad (2.32)$$

where the terms on the right hand side are the resistive term, the Lorentz force (Hall) term, the electron pressure term and a term relating to electron inertia.

Therefore a plasma can be described as a single fluid using the following equations:

$$\nabla \times \mathbf{E} = -\frac{\partial \mathbf{B}}{\partial t} \quad (2.33)$$

$$\nabla \times \mathbf{B} = \mu_0 \left(\mathbf{j} + \epsilon_0 \frac{\partial \mathbf{E}}{\partial t} \right) \quad (2.34)$$

$$\nabla \cdot \mathbf{B} = 0 \quad (2.35)$$

$$\frac{\partial n}{\partial t} + \frac{\partial(n\mathbf{u})}{\partial \mathbf{x}} = 0 \quad (2.36)$$

$$\frac{\partial(n\mathbf{u})}{\partial t} + \nabla_{\mathbf{x}} \cdot (n\mathbf{u}\mathbf{u}) = -\nabla_{\mathbf{x}} \cdot \mathbf{P} + \rho\mathbf{E} + \mathbf{j} \times \mathbf{B} \quad (2.37)$$

$$\mathbf{E} + \mathbf{u} \times \mathbf{B} = \eta\mathbf{j} + \frac{1}{ne}\mathbf{j} \times \mathbf{B} - \frac{1}{ne}\nabla \cdot \mathbf{P}_e + \frac{m_e}{ne^2} \left[\frac{\partial \mathbf{j}}{\partial t} + \nabla \cdot (\mathbf{j}\mathbf{u} + \mathbf{u}\mathbf{j}) \right] \quad (2.38)$$

along with an equation of state, a closure equation defining the pressure (or a higher order moment). This fluid description is suitable for large enough time and length scales (compared to characteristic length and timescales of the plasma) although it also does well out of its strict area of validity [*Thorne and Blandford, 2017*].

2.5 General method for deriving plasma waves

Plasma waves describe the propagation of disturbances in a plasma. Due to the complex nature of interactions between particles and electric and magnetic fields, plasmas can support a large number of different wave modes. When these waves have relatively small amplitude with respect to the background plasma they are most easily described using a linear approximation, i.e. a small perturbation propagating against the background. These waves are described in terms of frequency ω and wavenumber \mathbf{k} instead of time t and spatial location \mathbf{x} . To describe the different wave modes, one can find a relationship between ω and \mathbf{k} , the dispersion relation, for each wave mode. This will include relevant plasma properties (e.g. density, electric and magnetic perturbations) and can be derived systematically from the governing plasma equations. To do so the plasma equations are linearised and a Fourier transformation is performed from \mathbf{x}, t to ω, \mathbf{k} co-ordinates. Then linear equations describing the perturbations can be derived in terms of a wave operator acting on electric field perturbations, where the wave operator contains the conductivity tensor and therefore information about the interaction of plasma components [*Baumjohann and Treumann, 1996; Treumann and Baumjohann, 1997; Thorne and Blandford, 2017*]. As an eigenvalue equation, the dispersion relation admits a finite number of solutions which correspond to plasma wave modes supported

by the plasma. A general dispersion relation for fluid quantities can be derived, which can then be extended to include kinetic processes if necessary (i.e. at higher frequencies close to electron and ion processes). In Section 2.6 we will derive the wave modes from single-fluid MHD equations, which are the modes relevant to ULF waves due to their very low frequency and large spatial scales. Although these waves could be derived from the general dispersion relation, in the case of MHD waves it is simpler to consider the linearised wave equations and the perturbations directly to find the wave modes.

2.6 MHD waves

2.6.1 Simplification of MHD equations

Using scale analysis, we can quantitatively identify terms which are negligible on the large temporal and spatial scale of ULF waves. This type of analysis can be used to simplify the MHD equations in equations (2.33) to (2.38), by reducing the number of terms as follows.

Equations 2.33 and 2.36 do not change. For momentum equation 2.37 we use quasineutrality, $n_e = n_i$ so that total charge $\rho = 0$ and the $\rho\mathbf{E}$ term disappears. In the curl of the magnetic field (equation (2.34)), the displacement current term $\epsilon_0 \frac{\partial \mathbf{E}}{\partial t}$ can be ignored using a low velocity approximation (i.e. the ratio of characteristic time to distance ratio is far smaller than the speed of light c [Gurnett and Bhattacharjee, 2005]). The generalised Ohm's Law is a bit more complex; terms must be compared against each other to identify the ones of significance [Baumjohann and Treumann, 1996]. The electron pressure term is negligible compared to the convection term ($\mathbf{u} \times \mathbf{j}$) for large spatial scales (specifically, when the ratio of the characteristic length scale to the electron gyroradius is much larger than the ratio of the electron thermal velocity to the fluid velocity). Similarly we can ignore the electron inertial term for timescales of longer than the electron gyroperiod. The Hall term is somewhat more complicated; when compared to the convection term it can only strictly be neglected when collision frequencies are far larger than magnetic gyrofrequencies, i.e. in dense plasma [Bittencourt, 2004; Baumjohann and Treumann, 1996]. However, this term is only important in thin regions of high current density [Priest, 2014] and so is commonly neglected. This reduces the generalised Ohms Law in equation (2.32) to

$$\mathbf{E} + \mathbf{u} \times \mathbf{B} = \eta \mathbf{j}. \quad (2.39)$$

The generalised Ohm's law can be further simplified by assuming our plasma is fully conductive, i.e. resistivity $\eta = 0$. This resistive term is negligible for small collision

frequencies which is appropriate to our plasma (although the existence of this term is important for reconnection in plasma simulations and acts like a diffusive term [*Birn et al.*, 2001]).

We also specify the fluid moment closure here; assuming the pressure tensor is scalar,

$$\frac{d}{dt}(Pn^{-\gamma}) = 0. \quad (2.40)$$

This is the adiabatic energy equation and assumes that changes in temperature are due to changes in density (e.g no thermal conductivity; no heat flux or viscous heating [*Gurnett and Bhattacharjee*, 2005; *Baumjohann and Treumann*, 1996]). γ can be chosen to represent situations such as constant pressure, constant temperature or the adiabatic index $\gamma = c_p/c_v = 5/3$ can be chosen. This value relates to the three degrees of freedom in our plasma and to the temperature as defined by a Maxwellian distribution. A better approximation is to split the parallel and perpendicular components of pressure and to explicitly include the effects of the magnetic field in pressure. However that is quite complex and the adiabatic equation used here is adequate for waves as we are assuming slow, reversible changes corresponding to low frequency phenomena.

Overall, the simplified MHD equations we use here are

$$\nabla \times \mathbf{E} = -\frac{\partial \mathbf{B}}{\partial t} \quad (2.41)$$

$$\nabla \times \mathbf{B} = \mu_0 \mathbf{j} \quad (2.42)$$

$$\frac{\partial n}{\partial t} + \frac{\partial(n\mathbf{u})}{\partial \mathbf{x}} = 0 \quad (2.43)$$

$$\frac{\partial(n\mathbf{u})}{\partial t} + \nabla_{\mathbf{x}} \cdot (n\mathbf{u}\mathbf{u}) = -\nabla \cdot \mathbf{P} + \mathbf{j} \times \mathbf{B} \quad (2.44)$$

$$\mathbf{E} + \mathbf{u} \times \mathbf{B} = 0 \quad (2.45)$$

$$\frac{d}{dt}(Pn^{-\gamma}) = 0 \quad (2.46)$$

$$\nabla \cdot \mathbf{B} = 0 \quad (2.47)$$

where \mathbf{E}, \mathbf{j} can be eliminated

$$\frac{\partial n}{\partial t} + \frac{\partial(n\mathbf{u})}{\partial \mathbf{x}} = 0 \quad (2.48)$$

$$\nabla \times (\mathbf{u} \times \mathbf{B}) = -\frac{\partial \mathbf{B}}{\partial t} \quad (2.49)$$

$$\frac{\partial(n\mathbf{u})}{\partial t} + \nabla_{\mathbf{x}} \cdot (n\mathbf{u}\mathbf{u}) = -\nabla \cdot \mathbf{P} + \frac{1}{\mu_0} (\nabla \times \mathbf{B}) \times \mathbf{B} \quad (2.50)$$

$$\frac{d}{dt} (Pn^{-\gamma}) = 0 \quad (2.51)$$

$$\nabla \cdot \mathbf{B} = 0. \quad (2.52)$$

$$(2.53)$$

This description is known as ideal MHD and will be used to derive wave modes relevant to ULF waves.

2.6.2 Method of deriving MHD waves

The derivation will only be outlined here, and can be summarised as follows:

- Linearise fluid quantities
- Examine the evolution of perturbation in linearised MHD equations
- Fourier mode analysis (transform to ω, \mathbf{k} space)
- Substitute a plane wave for the velocity perturbations
- Examine components of the resulting wave equation along and across the magnetic field by solving an eigenvalue problem

First, we reduce any physical quantity into an equilibrium, uniform, steady-state part plus small perturbations. Hence fluid quantities are linearised, for example $P = P_0 + P_1$ or $\mathbf{u} = \mathbf{0} + \mathbf{u}_1$. We will assume that the initial speed perturbation is a plane wave $\mathbf{u}_1 = \hat{\mathbf{u}}_1 \exp(i\mathbf{k} \cdot \mathbf{x} - i\omega t)$. These linearised quantities are substituted into the MHD equations describing our system, where terms that are too small are ignored (i.e. terms of order two or higher in perturbed quantities). The linearised Maxwell equations are then:

$$\begin{aligned}
\frac{\partial \mathbf{B}_1}{\partial t} &= \nabla \times (\mathbf{u}_1 \times \mathbf{B}_0) \\
\frac{\partial n_1}{\partial t} + n_0 \nabla \cdot \mathbf{u}_1 &= 0 \\
n_0 \frac{\partial \mathbf{u}_1}{\partial t} &= -\nabla P_1 + \frac{1}{\mu_0} (\nabla \times \mathbf{B}_1) \times \mathbf{B}_0 \\
P_1 &= \gamma \frac{P_0}{n_0} n_1 = c_s^2 n_1,
\end{aligned} \tag{2.54}$$

with sound speed $c_s = \frac{\gamma P_0}{n_0}$. To examine the resulting wave properties, we perform a Fourier mode analysis. Here, we transform to the Fourier domain of frequency ω and wavenumber \mathbf{k} . In this space the derivative operators are transformed as

$$\nabla_{\mathbf{x}} \rightarrow i\mathbf{k}, \quad \frac{\partial}{\partial t} \rightarrow -i\omega, \tag{2.55}$$

so that the evolution of perturbed quantities can be fully described in ω, \mathbf{k} space as follows:

$$\begin{aligned}
-\omega \mathbf{B}_1 &= \mathbf{k} \times (\mathbf{u}_1 \times \mathbf{B}_0) \\
-\omega n_1 + n_0 \mathbf{k} \cdot \mathbf{u}_1 &= 0 \\
-\omega n_0 \mathbf{u}_1 &= -\mathbf{k} c_s^2 n_1 + \frac{1}{\mu_0} (\mathbf{k} \times \mathbf{B}_1) \times \mathbf{B}_0 \\
P_1 &= \gamma \frac{P_0}{n_0} n_1 = c_s^2 n_1
\end{aligned} \tag{2.56}$$

where all quantities are now described in (ω, \mathbf{k}) space, e.g. $\mathbf{B}(\mathbf{x}, t) \rightarrow \mathbf{B}(\omega, \mathbf{k})$. We can then choose a co-ordinate system, without loss of generality. Choosing the magnetic field to be in the \hat{z} direction ($\mathbf{B}_0 = B_0 \hat{z}$), and then choosing $\mathbf{k} = k_{\perp} \hat{x} + k_{\parallel} \hat{z}$, the linearised, Fourier-transformed equations can be rearranged into an eigenvalue problem $\mathbf{W} \cdot \mathbf{u}_1 = 0$ where \mathbf{W} acts on the velocity perturbations

$$\mathbf{W} \cdot \mathbf{u}_1 = \begin{bmatrix} \omega^2 - c_s^2 k_{\perp}^2 - v_A^2 (k_{\perp}^2 + k_{\perp} k_{\parallel}) & 0 & -c_s^2 k_{\parallel} k_{\perp} \\ 0 & \omega^2 - v_A^2 k_{\parallel}^2 & 0 \\ -c_s^2 k_{\perp} k_{\parallel} & 0 & \omega^2 - c_s^2 k_{\parallel}^2 \end{bmatrix} \begin{bmatrix} u_{1x} \\ u_{1y} \\ u_{1z} \end{bmatrix} = 0 \tag{2.57}$$

where $v_A^2 = \frac{B_0^2}{\mu_0 n}$ is the Alfvén speed (μ_0 is the permeability of vacuum). As an eigen-

value problem², solutions to the system of equations are found when the determinant is equal to zero³, i.e.

$$\det[\mathbf{W}] = (\omega^2 - v_A^2 k_{\parallel}^2) \left[(\omega^2 - v_A^2 k_{\parallel}^2 - (c_s^2 + v_A^2) k_{\perp}^2) (\omega^2 - c_s^2 k_{\parallel}^2) - c_s^4 k_{\parallel}^2 k_{\perp}^2 \right] = 0. \quad (2.58)$$

2.6.3 Alfvén Wave

The first solution to equation (2.58) is the Alfvén wave,

$$\begin{aligned} \omega^2 = v_A^2 k_{\parallel}^2 &= \frac{k_{\parallel}^2 B_0^2}{\mu_0 n_0} \\ \Rightarrow \omega &= \frac{\pm \mathbf{k} \cdot \mathbf{B}_0}{\sqrt{\mu_0 n_0}}. \end{aligned} \quad (2.59)$$

Properties of this wave can be considered by comparing equation (2.59) to the directions of propagation and perturbation, and substituting these quantities into linearised MHD equation (2.56). Due to the dot product in the numerator, this wave only propagates along the direction of the magnetic field, at the Alfvén speed defined above. The only velocity perturbations possible in the original problem are u_{1y} , hence velocity perturbations are transverse to the direction of propagation. By substituting these properties into the linearised wave equations, it can be seen that magnetic field oscillations are also transverse to \mathbf{B}_0 and parallel to \mathbf{u}_1 , while electric field oscillations are along E_{1x} . Therefore this wave acts somewhat analogously to an oscillating string, travelling along the magnetic field and driving perpendicular magnetic field oscillations. Finally, as the velocity perturbations and direction of propagation are orthogonal, the wave is incompressible ($\nabla \cdot \mathbf{u}_1 = i\mathbf{k} \cdot \mathbf{u}_1 = 0$).

2.6.4 Magnetosonic Waves

The other two solutions to equation (2.58) can be rearranged to find

²Comparing to the eigenvalue form $(\mathbf{A} - \lambda\mathbf{I})\mathbf{x} = 0$, it can be seen that the eigenvalue $\lambda = \omega^2$ corresponds to eigenfrequencies supported by the plasma.

³For a matrix equation $\mathbf{A}\mathbf{x} = \mathbf{b}$, where $\mathbf{b} = \mathbf{0}$, $\det(\mathbf{A}) \neq 0$ indicates that the inverse of \mathbf{A} exists, and so $\mathbf{x} = \mathbf{A}^{-1}\mathbf{b} = \mathbf{0}$ (a trivial solution). When $\det(\mathbf{A}) = 0$, non-trivial solutions involving the components of \mathbf{A} and \mathbf{x} exist.

$$\omega^2 = \frac{k^2}{2} \left[v_A^2 + c_s^2 \pm \left[(v_A^2 + c_s^2)^2 - 4v_A^2 c_s^2 \cos^2 \theta \right]^{\frac{1}{2}} \right] = \frac{k^2}{2} \left[c_f^4 \pm \sqrt{c_f^2 - 4v_A^2 c_s^2 k_{\parallel}^2} \frac{1}{k^2} \right], \quad (2.60)$$

where $k^2 = k_{\parallel}^2 + k_{\perp}^2$ and $c_f^2 = c_s^2 + v_A^2$. The fast mode solution corresponds to taking the + root and the slow mode to the – root. Similarly to the analysis for the Alfvén wave above, the directions of propagation and perturbation can be established. Only the fast mode propagates perpendicular to the magnetic field, with a phase speed of c_f . The phase speed of the fast and slow modes parallel to the magnetic field depend on the relative magnitude of the Alfvén and sound speeds; the fast mode will roughly correspond to $\max(v_A, c_s)$ while the slow mode will correspond to $\min(v_A, c_s)$. Both these waves are compressible, involving density and pressure perturbations, hence their name “magnetosonic”. In the limit $v_A \ll c_s$, the fast mode corresponds to a sound wave and the slow mode travels at the Alfvén speed (a compressible Alfvén wave). Conversely, when $c_s \ll v_A$, the slow mode travels at the sound speed while the fast mode travels at the Alfvén speed. In total, perturbations can be seen in $B_x, B_{\parallel}, u_x, u_{\parallel}, P$ and n .

2.6.5 Other wave modes and radiation belt physics

In this section only the single-fluid plasma waves have been derived as they are the wave modes relevant to the ultra-low frequency range. However, there are many other wave modes in magnetospheric plasma whose wave-particle interactions underly radiation belt behaviour at other spatial and temporal scales [*Stix, 1997; Baumjohann and Treumann, 1996; Treumann and Baumjohann, 1997*]. They can be derived by treating electrons and ions as separate fluids, electrons as a fluid against an ion background, or by returning to kinetic theory [*Baumjohann and Treumann, 1996; Thorne and Blandford, 2017*]. Wave phenomena are complicated by resonances, where interactions with particles are particularly strong. Additionally, both linear and nonlinear instabilities in plasma can provide disturbances across a range of timescales [*Treumann and Baumjohann, 1997*]. Waves and instabilities act to reduce different plasma inequalities (e.g. gradients in distribution function temperature or density).

2.7 Additional plasma physics

2.7.1 The frozen-in theorem

One consequence of the ideal MHD approximation, equations (2.48) to (2.52) is the frozen-in theorem which states that under infinite electrical conductivity and large enough fluid velocities and length scales, the magnetic flux through a surface in the plasma remains constant. Typically this is characterised by the ratio of convective to diffusive terms in the inductive equation [see e.g. *Gurnett and Bhattacharjee, 2005; Baumjohann and Treumann, 1996*], but also follows as a consequence of the induction equation (2.49). The difference in magnetic flux Φ through a loop of surface area S at two different times reduces to

$$\delta\Phi = \delta t \int_S \left[\frac{\partial \mathbf{B}}{\partial t} - \nabla \times (\mathbf{u} \times \mathbf{B}) \right] \cdot d\mathbf{S} \quad (2.61)$$

which disappears when Equation (2.49) holds. Hence when using the ideal MHD approximation, the fluid and the magnetic field move together. As a result, the plasma moves with the magnetic field when the magnetic field dominates. Conversely, when the bulk flow of the plasma dominates over the magnetic field, the magnetic field moves with the bulk motion of plasma. This property is determined by the relative ratios of bulk flow, thermal motion and magnetic energy densities (i.e. dynamic pressure, thermal pressure and magnetic pressure respectively) [*Cowley, 1982; Priest, 2014*].

2.7.2 Magnetic reconnection

Where the magnetic field is suitably compressed, assumptions underlying ideal MHD break down. Then a process called magnetic reconnection can occur, where the magnetic field lines of opposing orientation can be reconfigured into a new magnetic topology and plasma can be heated and accelerated [*Kivelson and Russell, 1995; Treumann and Baumjohann, 1997; Baumjohann and Treumann, 1996; Jursa, 1985*]. A cartoon of this process is shown in Figure 2-4; in the first panel, magnetic field lines of opposing orientation are shown. As these are driven together in the second panel, eventually the spatial scale is so small that MHD breaks down. In the final panel it can be seen that the field lines at the boundary between the two fields have a new topology and are peeling off to the top and bottom of the diagram. Now the ends of the field lines are in both left and right plasma regions, so once out of the compressed reconnection region the particles travelling along the magnetic field can travel between regions. While the frozen-in theorem holds for most of space physics, this process is particularly important as it allows for the transfer of material across magnetic field lines and for

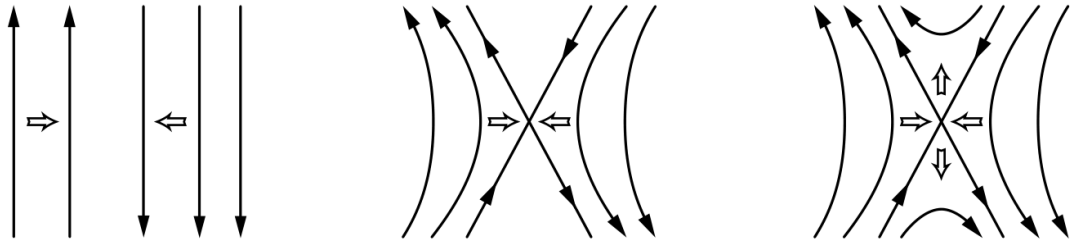


Figure 2-4: Magnetic field lines of opposing orientation can reconfigure into a new topology when plasma is compressed into non-MHD scales. Taken from *Baumjohann and Treumann* [1996].

a new magnetic field topology, which cannot happen under ideal MHD. Particles in the reconnection region are strongly accelerated to flow down the new field topology as magnetic field energy is converted into the heating and acceleration of the outflowing plasma [*Treumann and Baumjohann*, 1997; *Kivelson and Russell*, 1995; *Priest*, 2014]. In reality this highly dynamic process is somewhat more complicated in three dimensional configurations, compared to the flat ideal example here.

CHAPTER 3

BACKGROUND SPACE PHYSICS

This chapter provides an overview of the underlying space physics, beginning with plasma processes from the Sun to the Earth (Section 3.1) and a brief discussion of the complex phenomena in Earth's magnetosphere (Section 3.1.3). In Section 3.2 the generation and propagation of ULF waves in Earth's magnetosphere is reviewed. The behaviour of radiation belt particles and the resulting conserved physical quantities (i.e. adiabatic invariants) is presented in Section 3.3 along with an outline of the Fokker-Planck diffusion equation used to determine the evolution of the radiation belts. In Section 3.4 current methods of determining ULF-driven radial diffusion are shown. Some geomagnetic indices used to characterise magnetospheric behaviour are briefly reviewed in Section 3.5 and several common co-ordinate systems are introduced in Section 3.6.

3.1 Overview of the Sun-Earth system

The primary goal of this project is to characterise the behaviour of magnetospheric ULF waves in terms of upstream solar wind properties. Therefore, we review the origin of the solar wind and how propagation from the Sun to the Earth determines some of the characteristic interactions observed with our magnetosphere. In Section 3.1.3 the dominant, large-scale methods of coupling between the solar wind and the Earth are outlined, along with major internal processes of the magnetosphere.

3.1.1 The Sun

The Sun is the dominant source of energy and plasma in the solar system and drives many processes on Earth. As a massive collection of ionised gases (predominantly hydrogen and helium) held together under their own gravity, interior regions of the Sun are subject to huge pressures and temperatures. For this reason nuclear fusion, particle collisions and the force of electromagnetic fields generated by ionised gases all dominate in different regions of the Sun. The Sun's outermost layer (the corona) has relatively low density and high temperature [Kivelson and Russell, 1995]. An examination of the hydrodynamic equations for an equilibrium solar corona admits a constant flow of solar matter [Kivelson and Russell, 1995; Baumjohann and Treumann, 1996]. After a critical radius of between 5 and 10 solar radii this flow of plasma, known as the solar wind, is supersonic and superAlfvénic (i.e. travelling faster than Alfvén plasma waves). In addition to this relatively constant outflow, large amounts of solar mass can be expelled in episodic events such as coronal mass ejections [Bothmer and Daglis, 2007; Priest, 2014]. Outputs that affect the Earth include energetic particles and electromagnetic emissions such as x-rays, gamma rays and UV radiation [Bothmer and Daglis, 2007].

Coronal mass ejections are a result of magnetic reconnection between rising flux ropes near the solar surface, and are therefore typically highly accelerated and topologically distinct from the surrounding solar wind. Resulting properties typically include a high speed, a strong embedded magnetic field and signature density variations that make them particularly geoeffective and of interest to space physicists. These will be discussed in more detail in Chapter 5 when considering interdependence between solar wind parameters observed at the Earth.

The Sun is subject to cycles of behaviour, switching magnetic polarity every 11 years on average, so a full solar cycle takes around 22 years. As the solar output is moderated by the Sun's magnetic fields, the coupling of the Sun with the Earth varies over a solar cycle and over a solar rotation, which takes 27 days.

3.1.2 The solar wind

Solar wind speeds range from $\sim 200\text{km s}^{-1}$ to over 1000km s^{-1} . Typically the solar wind is classed into slow ($\sim < 450\text{km s}^{-1}$) and fast ($\sim > 450\text{km s}^{-1}$) wind. The slow solar wind is less hot, more dense and more variable than the fast solar wind [Bothmer and Daglis, 2007]. Fast and slow solar wind originates from different regions on the Sun, which vary strongly with heliospheric latitude and throughout the solar cycle. The solar wind observed at Earth is often a mix of fast and slow wind.

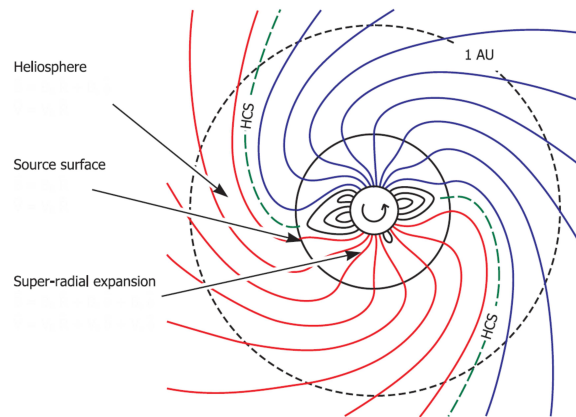


Figure 3-1: The spiral configuration due to the magnetic field lines embedded in the rotating, streaming solar wind. At the source surface (a few solar radii) solar wind flow and magnetic field are radial due to pressure driven expansion. Solar rotation results in the spiral configuration throughout the heliosphere. Adapted from *Owens and Forsyth* [2013].

Table 3.1: Typical solar wind plasma values at Earth.

Property	Value
Proton density	6.6 cm^{-3}
Electron density	7.1 cm^{-3}
He^{2+} density	0.25 cm^{-3}
Flow speed	450 km^{-s}
Proton temperature	$1.2 \times 10^5 \text{ K}$
Electron temperature	$1.4 \times 10^5 \text{ K}$

Adapted from *Kivelson and Russell* [1995] .

The spatial and temporal scale of the solar wind means that it is well approximated by ideal MHD and is therefore subject to the frozen-in theorem presented in Section 2.7.1 [*Baumjohann and Treumann, 1996*]. As a result the plasma and the magnetic field move together; in the solar wind the flow dominates this movement. As the Sun rotates, the radial flow is dragged into a spiral and the interplanetary magnetic field is bound with it, as shown in Figure 3-1. By the time the solar wind reaches Earth, the interplanetary magnetic field has an angle of around 45° to the Sun-Earth line. Typical solar wind values at the Earth are given in Table 3.1, from *Kivelson and Russell* [1995].

Variations in density, temperature and the magnetic field observed in the solar wind can originate from the Sun or can be due to solar wind interactions [*Pizzo, 1978; Owens and Forsyth, 2013*]. For example, as fast solar wind catches up to slow solar wind, regions of compression and rarefaction develop as shown in Figure 3-2.

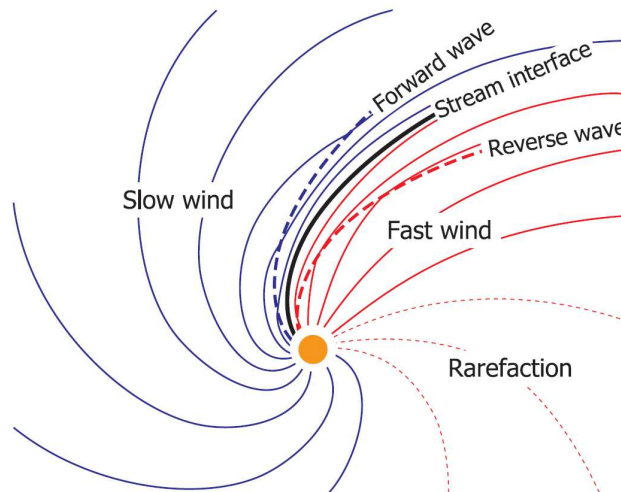


Figure 3-2: Regions of compression and rarefaction develop as high-speed solar wind streams catch up to slower solar wind. Adapted from *Owens and Forsyth* [2013].

3.1.3 Earth’s magnetosphere

The Earth’s magnetosphere presents an obstacle to the solar wind flow. As the solar wind is supersonic and superAlfvénic, a bow shock forms upstream of the nose of the magnetosphere. The shocked plasma (the magnetosheath) is diverted around the magnetosphere, creating a turbulent region that mediates solar wind-magnetosphere coupling. The magnetopause forms the boundary between magnetospheric and solar wind plasma. These regions are shown in Figure 3-3. The location of the nose is set by the pressure balance between the solar wind and the magnetospheric plasma, and generally sits at around $10R_E$ [*Baumjohann and Treumann, 1996; Kivelson and Russell, 1995*].

The depiction of the magnetosphere in Figure 3-3 shows topologically distinct regions of plasma, again due to the frozen-in approximation. When this holds, the solar wind and magnetospheric plasma populations cannot mix across field lines. As a consequence, the Earth’s magnetosphere is a cavity with the configuration of a compressed dipole and a tail stretching out behind the Earth.

However, the compression of the plasma at the nose of the magnetosphere allows the magnetic field to vary on short length scales. This constitutes a breakdown of MHD, allowing reconnection to occur (see Section 2.7.2). Reconnection enables solar wind plasma to enter into Earth’s magnetosphere via a dynamic process called the Dungey cycle [*Baumjohann and Treumann, 1996; Kivelson and Russell, 1995; Dungey, 1961*], shown in Figure 3-4. When the magnetic fields in the solar wind and magnetosphere

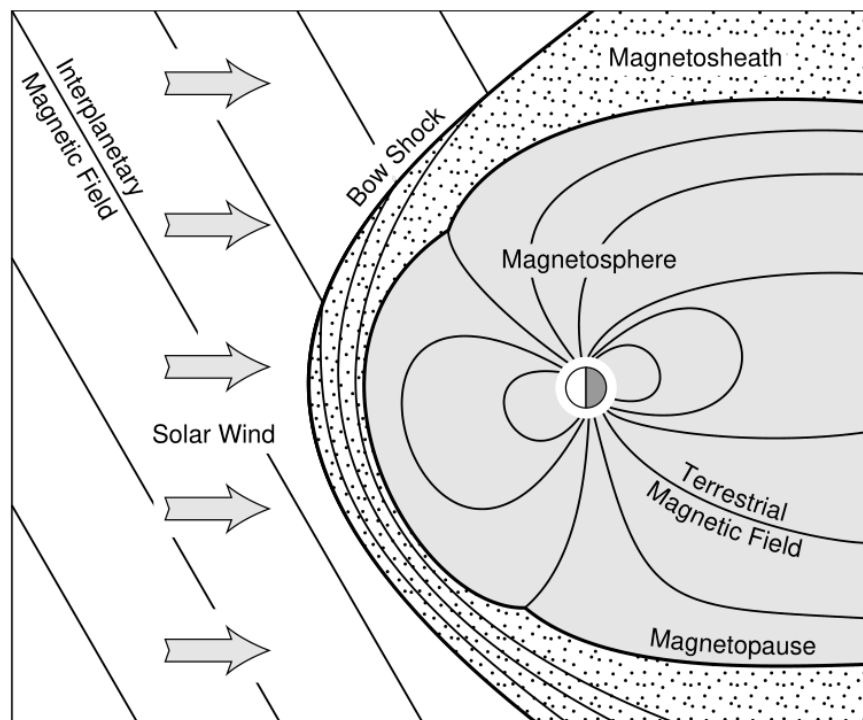


Figure 3-3: A diagram showing the impact of the solar wind on the Earth's magnetosphere; shocked solar wind plasma forms the magnetosheath and is diverted past the Earth, while draped magnetic field lines build up on the nose. Taken from *Baumjohann and Treumann [1996]*

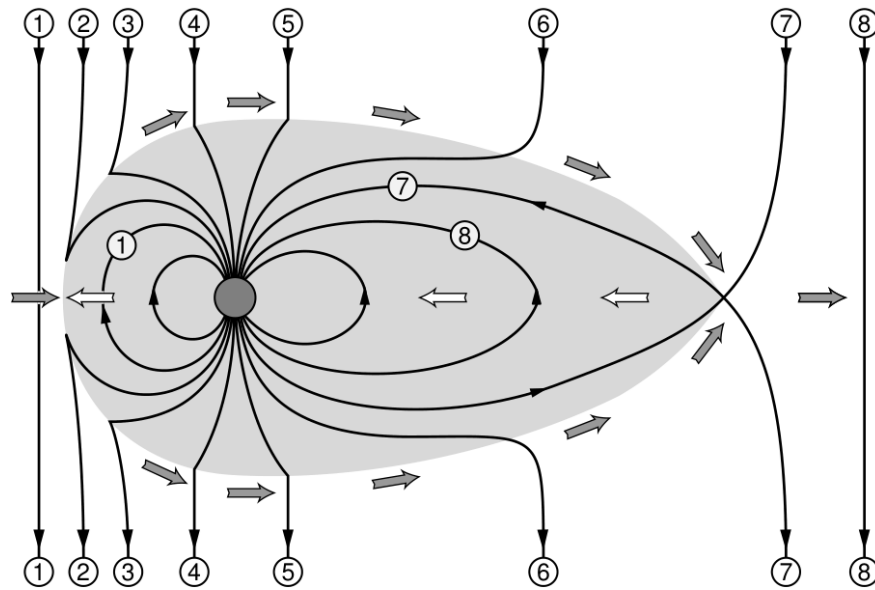


Figure 3-4: The Dungey cycle, taken from *Baumjohann and Treumann [1996]*. Reconnection on the nose alters the magnetic field topology, and newly opened magnetic field lines are dragged back across the magnetosphere as the solar wind flows by. The resulting build-up in the tail region is also susceptible to reconnection, closing the field lines which can then convect back to the dayside.

have opposing orientations reconnection can occur on the magnetopause. Magnetic field lines that were solely in the solar wind or connected to the Earth (“closed”) are now connected to both regions (“open” field lines), and particles may travel into previously inaccessible regions. As the solar wind continues to flow past the Earth, these open magnetic field lines are dragged along with it, to build up in turn in the magnetotail. Since this is also a compression of oppositely oriented magnetic field lines, reconnection again occurs, so that field lines to the Earth close once more. Once closed, the magnetic field lines convect back to the dayside to return to the beginning of this cycle.

Two important aspects of this reconnection process are the topology changes and the acceleration of particles. Bursts of reconnection form distinct flux tubes, which are once more subject to the frozen-in approximation as they traverse tailward along the magnetopause or away from the tail towards the dayside. The particle accelerations and plasma instabilities caused by reconnection events in the tail (substorms) travel along newly-reconnected field lines towards the Earth to drive aurora and other perturbations. The Dungey cycle is one of the largest sources of particles in the magnetosphere, although other sources are particles from Earth’s ionosphere and from the open field lines at the poles (i.e. the cusps).

As particles are tied to magnetic field lines (Section 2.2), particle populations are

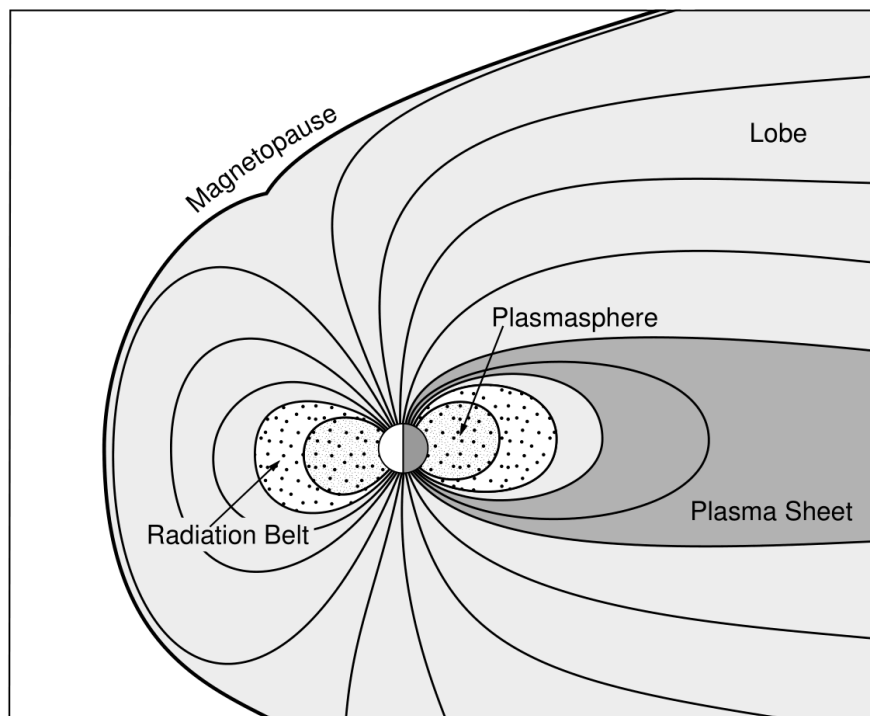


Figure 3-5: Particles trapped in Earth's magnetosphere are concentrated in the cold dense plasmasphere, the energetic radiation belts and the plasma sheet. Taken from *Baumjohann and Treumann [1996]*.

Table 3.2: IAGA pulsation classification, [*Jacobs et al.*, 1964].

	Label	Period range (s)	Frequency range
Continuous pulsation	Pc1	0.2 - 5	0.2 - 5 Hz
	Pc2	5-10	0.1-0.2 Hz
	Pc3	10 - 45	22-100 mHz
	Pc4	45-150	7-22 mHz
	Pc5	150 - 600	2-7 mHz
Impulsive pulsation	Pi1	1-40	0.025 - 1 Hz
	Pi2	40-150	7 - 25 mHz

strongly determined by the magnetic field topology. While plasma can be found throughout the magnetosphere, there exist several distinct populations as shown in Figure 3-5. The radiation belts contain electrons and protons trapped in oscillatory motion by the the Earth’s magnetic field, as will be discussed in Section 3.3. This overlaps spatially with the less energetic but more dense cold plasmasphere, which rotates with the Earth. The plasma sheet separating the two lobes of the magnetotail is hotter than the plasmasphere but less energetic than particles in the radiation belts [*Baumjohann and Treumann*, 1996].

3.2 ULF waves in Earth’s magnetosphere

Originally, the low frequency waves studied here were called “micropulsations”. Following an IAGA (International Association of Geomagnetism and Aeronomy) committee meeting, *Jacobs et al.* [1964] suggested a new nomenclature for these waves based on their continuous and impulsive nature, and their physical properties within the magnetosphere. This notation is shown in Table 3.2.

This description is often used today, where the classifications are still appropriate to the physics. Waves in our range of interest were also called “ultra-low” frequency following definitions at the time. Today, the International Telecommunications Union (ITU) define ULF waves to be between 300 Hz - 3 kHz. However, the space physics community continues to use the definition of ULF found in the NRL Plasma Formulary [*Huba*, 2016]; < 30 Hz. We are interested in the very lowest frequencies of 1-20 mHz, which are relevant to radial diffusion. Therefore in this project, by “ULF” we refer only the 1-20 mHz range. This section discusses of the generation mechanisms for these particular wave frequencies, how they are transmitted through to the inner magnetosphere and finally how they interact with the ionosphere to produce signals detected by ground-based magnetometers.

In Section 2.6 the wave modes in an ideal plasma were derived. Magnetospheric ULF

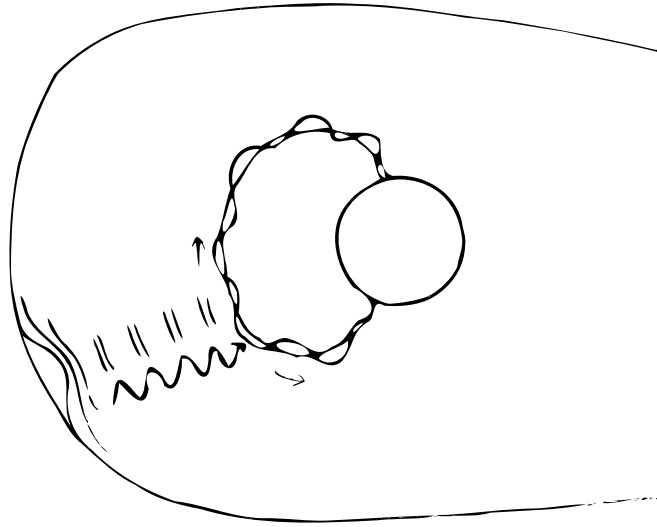


Figure 3-6: A perturbation of the magnetopause compresses the magnetospheric plasma, driving waves that propagate towards the Earth. These modes can couple with dipole magnetic field to drive resonances observable on the ground.

waves can be Alfvén modes (propagating along the magnetic field) or compressional fast mode waves (propagating along or across the magnetic field). While the two wave modes can be coupled, they often occur in different parts of the magnetosphere. The simplest description of ultra-low frequency wave generation reduces to solar wind-driven magnetopause perturbations, which in turn drive fast mode waves that propagate towards the Earth. As shown in Figure 3-6 these fast mode ULF waves can couple with dipole field lines to drive Alfvén wave modes measurable from the ground. The following sections outline these processes in more detail, while an example of ULF waves observed at the ground is presented in Section 3.2.4.

3.2.1 Generation mechanisms

Magnetospheric ULF waves can be driven by internal processes or by solar wind interactions. In this project we are focused on solar wind driven waves; typically, these are the main drivers of the lowest frequency waves [McPherron, 2005]. The external generation mechanisms outlined here will be returned to in more detail in Section 5.7 when their relationship to various solar wind parameters is examined.

Magnetopause perturbations on a timescale corresponding to ULF frequencies will compress the magnetospheric magnetic field, driving waves that propagate inwards. Such perturbations have many possible sources which are most easily classified into global and local drivers. Whole-magnetosphere expansions and contractions are a result

of solar wind compression and rarefaction regions or changes in the average embedded magnetic field. These, along with macroscale fluid instabilities such as the Kelvin-Helmholtz or Rayleigh-Taylor instabilities, can drive ULF waves across a large region of Earth's magnetopause [McPherron, 2005; Treumann and Baumjohann, 1997; Walker, 2005; Keiling *et al.*, 2016]. On a local scale, variations embedded in the solar wind are mediated by the magnetosheath to drive ULF waves along with positive and negative pressure pulses from smaller bow shock and magnetosheath instabilities [McPherron, 2005; Keiling *et al.*, 2016]. Finally, smaller perturbations such as density pulses and flux islands are convected along the magnetopause, driving a rippling effect along the flanks that can drive ULF waves on the interior [McPherron, 2005; Keiling *et al.*, 2016].

The main internal sources of 1-20 mHz waves include the drift-bounce resonance (the resonance of drifting, bouncing particles with magnetohydrodynamic waves to drive wave growth [Yeoman *et al.*, 2016]) and reconnection driving field-aligned currents which are also capable of generating magnetohydrodynamic waves in this frequency range [McPherron, 2005; Alperovich and Fedorov, 2007; Keiling *et al.*, 2016].

3.2.2 Propagation of ULF waves

Externally driven waves generated at the magnetopause are strongly transformed by magnetospheric processes [Wright and Mann, 2013; Walker, 2005; Alperovich and Fedorov, 2007]. In the relatively static depiction shown in Figure 3-6, fast mode waves generated by magnetopause disturbances propagate inwards and couple to the dipole field line. This in turn drives Alfvén waves that travel along the magnetic field. These can become standing waves if the length of the field line corresponds to the frequency of the driving wave (field line resonances, [Samson *et al.*, 1971; Chen and Hasegawa, 1974b,a; Southwood, 1974; Walker, 2005; Alperovich and Fedorov, 2007]). In this simple description, field line resonances can be either poloidal (i.e. radial oscillations of a magnetic field line) or toroidal (azimuthal oscillations). An example of each type of resonance is shown in Figure 3-7 for a single antinode at the equator. In practice most field line oscillations have both poloidal and toroidal components and the fast mode wave does not fully couple with to the field line.

Other types of standing waves are also possible in the magnetosphere, for example fast mode standing waves between the magnetopause and the reflective plasmasphere. These are known as cavity mode resonances, [Kivelson *et al.*, 1984; Wright, 1994; Walker, 2005; Wright and Mann, 2013; Alperovich and Fedorov, 2007]. However, as the magnetosphere is not a true dipole, the cavity resonance effect acts as a waveguide, ducting any resonances into the tail, while the reflectivity of the magnetopause varies between nose and flanks [Mann *et al.*, 1999].

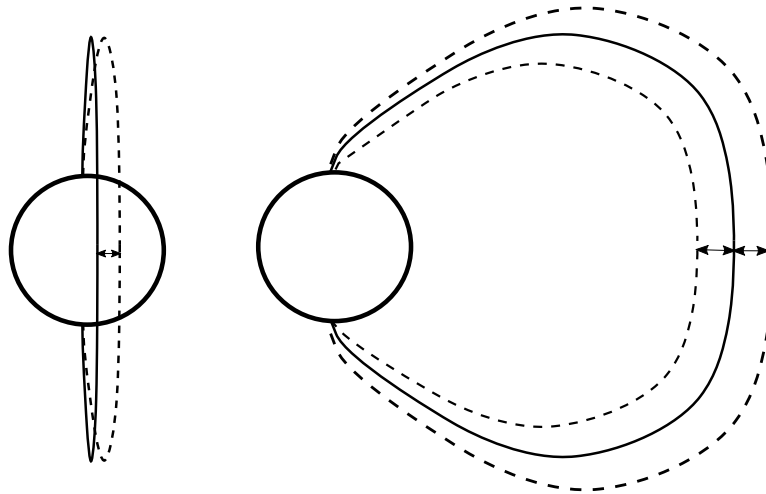


Figure 3-7: Field line resonances with a single antinode, at the equator. On the left is a toroidal resonance (i.e. azimuthal oscillations) and on the right a poloidal resonance (i.e. radial oscillations).

Waves generated at the boundary are attenuated as they propagate inwards. As the density profile varies considerably between the magnetopause and the ionosphere, the Alfvén speed profile varies also. When there is a step change in density at the edge of the plasmapause, the radial profile of the Alfvén velocity (and therefore the turning frequency - the wave frequency at which waves are reflected) decreases sharply, allowing the existence of standing waves between the ionosphere and plasmasphere. This change in Alfvén velocity with radial distance due to an inhomogeneous cold plasma is shown in Figure 3-8, along with the fundamental frequency of field line resonances at that location. The variable nature of the plasmasphere population [Sheeley *et al.*, 2001] and of the plasmapause location [Moldwin, 2002] means that the density profile is constantly changing and so is the ability of the magnetosphere to support travelling and standing waves.

3.2.3 Transformation of Alfvén modes through the ionosphere

The existence of ULF standing wave modes in the above section is strongly dependent on the assumption of a dense (and hence reflective) ionosphere, binding the footpoint of each field line [Kivelson *et al.*, 1984; Wright and Mann, 2013; Alperovich and Fedorov, 2007]. Ground-based magnetic field observations, therefore, do not directly measure the wave observed in the magnetosphere. Indeed, if the ionosphere were perfectly reflective we could not use ground based observations at all.

The transmission of ULF waves through the ionosphere is often simplified by as-

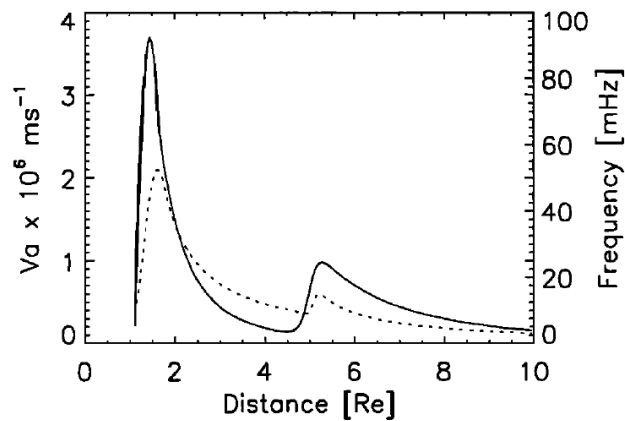


Figure 3-8: The change in Alfvén velocity (and hence fundamental frequency of field line resonances) due to an inhomogeneous cold plasma. Taken from *Waters et al.* [2000].

suming that Alfvén waves travelling along the field line are attenuated and rotated by ninety degrees between the magnetosphere and the ground, as they pass through the anisotropically conducting ionosphere and the insulating atmosphere [Hughes, 1974; Hughes and Southwood, 1976; Hughes, 1983]. Other wave modes not directly perpendicular to the ionosphere are assumed to be reflected rather than transmitted. Therefore ground-based measurements are assumed to be rotated; north-south components correspond to magnetospheric toroidal modes and east-west ground perturbations to poloidal modes in the magnetosphere. However, in reality this is much more complicated. Of course both Alfvén and fast mode waves are incident upon the ionosphere, and are subsequently coupled. The ionosphere is not uniform, and the ambient magnetic field is not always perpendicular to the ionosphere [Alperovich and Fedorov, 2007; Sciffer, 2002; Walker, 2005; Keiling et al., 2016; Hughes, 1974].

In the mapping derived by *Ozeke et al.* [2009] to convert ground-based observations to the power spectral density in the equatorial electric field it is assumed that the ground-based PSD is due to an Alfvén wave incident on the ionosphere. The magnetic field measured at the ground can be mapped to the magnetic field at the top of the ionosphere. This corresponds to the electric field at the top of the ionosphere, whose relationship with the equatorial electric field can be estimated. This chain means that ground-based observations can be used to approximate the equatorial electric field and hence the electric radial diffusion coefficient D_{LL}^E .

The transformation discussed in this section is specific to ULF waves due to their low frequency and large spatial scale; other waves are affected differently.

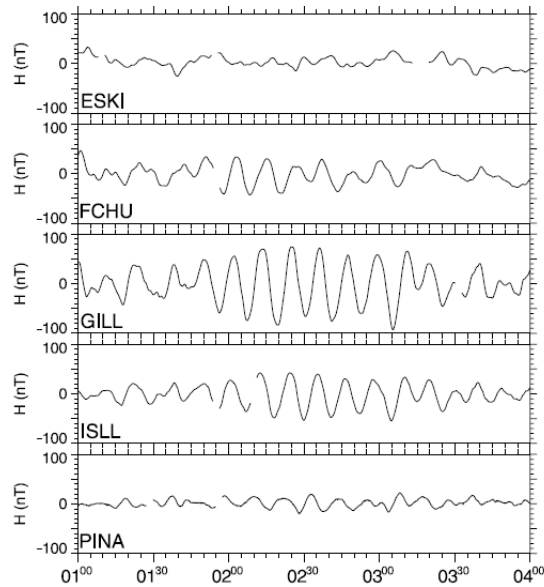


Figure 3-9: Example observations of ULF waves of the unfiltered north-south (“H”) component of Earth’s magnetic field, measured from a chain of ground-based magnetometers from low to high latitude ($60.56 - 71.20^\circ$ latitude, adjusted to magnetic north). Taken from *Rae et al.* [2005].

3.2.4 Example of ULF wave observed at the ground

ULF waves are highly modified during their passage from solar wind drivers, to the inner magnetosphere and via coupling with the ionosphere to reach ground-based stations. However, a clear example of a narrowband (monochromatic) ULF wave observed at the ground can be found in *Rae et al.* [2005], from which Figure 3-9 has been adapted. In this figure the unfiltered north-south component of the ground magnetic field is shown for several stations at different latitudes (but the same longitude) of a single magnetometer chain on 25th November 2001. There is a clear wave of a single frequency lasting for several hours, which was suggested to be a field line resonance driven by Kelvin-Helmholtz waves. This monochromatic oscillation observed from the ground corresponds to observations in the magnetosphere. Fortuitously, the Polar spacecraft was positioned near the point of mode conversion (i.e. the field line resonance) in the magnetosphere while the Cluster spacecraft observed boundary oscillations on the dusk side magnetopause. As there were no monochromatic pressure variations in the solar wind (which was steady and fast), these results indicated that the Kelvin-Helmholtz instability was driving the resonance. Hence the example in *Rae et al.* [2005] demonstrates how a magnetopause deformation drives a fast mode wave which converts to a field line resonance in the magnetosphere, and is subsequently observable at the ground.

3.3 Earth's radiation belts

Earth's radiation belts are regions of near-Earth space where energetic charged particles are trapped by the magnetic field. The energy of the trapped particles define whether we call them ring current or radiation belt particles; particles of higher energy are considered to be in the radiation belts although the energy boundary between the two processes is often defined by the processes under study. There is considerable overlap of the two populations and the split is chosen by considering whether particles contribute more to the current density of the ring current or to penetrating radiation [Kivelson and Russell, 1995]. One definition is to use electrons with energy < 0.5 MeV (the electron rest mass) as radiation belt particles as then they can be considered relativistic. Alternatively, one can examine the dependence of the distribution function on energy and set the energy boundary where the distribution function changes [Cayton *et al.*, 1989]. Using more physical considerations, electron acceleration by waves dominates for energies < 500 keV but losses dominate at tens to hundreds of keV [Glauert *et al.*, 2014]. For this reason Glauert *et al.* [2014] use this lower boundary in radiation belt modelling to include the source population for subsequent acceleration. The upper limit used by Glauert *et al.* [2014] is 10 MeV as there are negligible electrons with this energy or higher - they are lost very quickly.

The radiation belts at Earth (also known as the Van Allen belts, after the person credited with their discovery) are split into two belts: a highly variable outer belt ranging from $L \sim 2.5 - 7+ R_E$ [Bothmer and Daglis, 2007; Glauert *et al.*, 2014], comprising mostly energetic electrons ($> \text{MeV}$) and an inner belt at very low L-shell which consists mostly of protons. This split is not well understood. The outer radiation belt is particularly of interest for understanding the environment of geostationary orbits and is subject to radial diffusion by ULF waves (Section 3.4).

Attempts to describe the radiation belts focus on the evolution of the particle population, hence phenomena of interest include particle sinks and sources, particle transport, and acceleration and loss. Particle motions are most easily considered in terms of adiabatic invariants, which are physical quantities conserved with three periodic motions of particles in Earth's magnetic field; gyromotion around a guiding centre, bounce motion between magnetic poles and drift around the Earth [Roederer and Zhang, 2014; Jursa, 1985; Schulz and Lanzerotti, 1974; Northrop, 1963]. These motions are depicted in Figure 3-10 and their corresponding conserved quantities are introduced in Section 3.3.1. Most radiation belt phenomena of interest are related to violation of these invariants. Whilst there are no collisions (Figure 2-1) radiation belt processes are instead moderated by a plethora of wave modes at a variety of spatial and

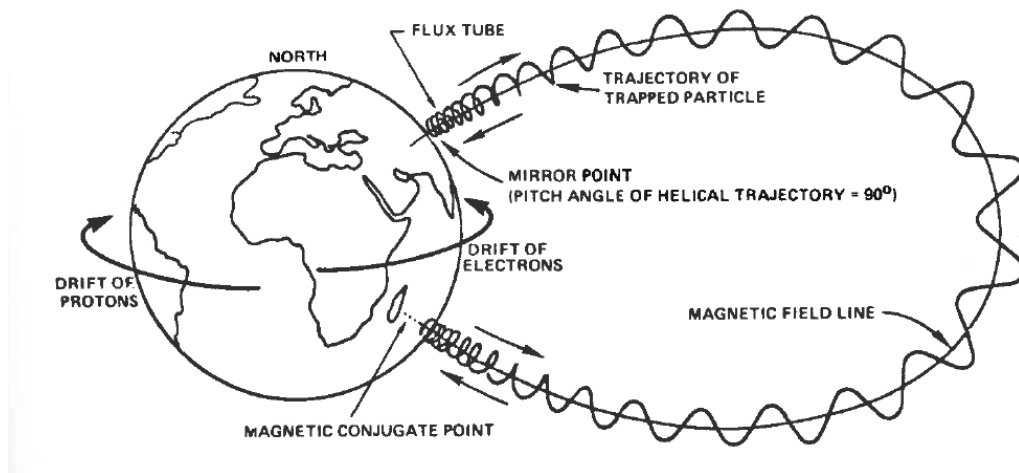


Figure 3-10: The three periodic motions traced out by magnetically trapped particles, from [Jursa, 1985]

temporal scales [Stix, 1997; Schulz and Lanzerotti, 1974]. Usually, each set of waves is associated with one of the periodic motions as they will be related to violating the adiabatic invariant associated with that timescale [Schulz and Lanzerotti, 1974]. ULF waves are related to violation of the third adiabatic invariant, magnetic flux through a drift contour.

Radiation belt modelling is done today using convection and diffusion models. Diffusion models solve the Fokker-Planck equation, which determines the evolution of a distribution function f due to diffusion by wave-particle interactions. Examples are the BAS model, [Glauert et al., 2014], VERB [Subbotin et al., 2010] and STEERB [Su et al., 2010]. Diffusion models are particularly suited to long timescales and forecasting as diffusion models are relatively quick to run. The effect of ULF waves on the third adiabatic invariant is included by calculating the radial diffusion coefficient, which will be covered in Section 3.4. Convection models instead include convective transport due to electric and magnetic fields, which is especially important for the ring current. An example is the Rice Convection Model [Toffoletto et al., 2003]. Combined models exist but do not contain all processes, for example VERB-4D [Shprits et al., 2015] or CIMI [Fok et al., 2014], which does not include radial diffusion due to ULF waves.

3.3.1 Particle motions and adiabatic invariants

The small number of particles in the radiation belts (relative to the cooler, denser plasmasphere) is best described using single particle motion (Section 2.2). The three periodic motions of radiation belt particles each correspond to a quantity conserved

under adiabatic changes on a characteristic timescale. Invariant co-ordinates based on these quantities are particularly suitable for tracking the energy in the radiation belts.

In classical mechanics, for a conservative system Hamilton-Jacobi methods can be adapted to easily find conserved quantities (“action-angle variables”) J from periodic motions [Goldstein *et al.*, 2002]. For the single particle motion in Section 2.2 this conserved quantity is then

$$J_i = \oint_i \left[\mathbf{p} + \frac{q}{c} \mathbf{A} \right] \cdot d\ell, \quad (3.1)$$

where \mathbf{p} is then the particle momentum, \mathbf{A} the vector potential of the magnetic field ($\mathbf{B} = \nabla \times \mathbf{A}$) and $i = 1, 2, 3$ indicates the three quasiperiodic particle motions in the radiation belts [Jursa, 1985; Schulz and Lanzerotti, 1974].

Strictly, this applies to a conservative system, where work done is reversible (i.e. no dissipation) and is independent of the path taken. For the electric and magnetic fields here this is approximately true when the system changes on a slow enough timescale; under gradually changing (adiabatic) conditions the energy exchange between particles and fields is reversible. The three periodic motions described below each have a characteristic timescale where changes can be considered adiabatic (and hence the system conservative), so that the quantities $J_{i=1,2,3}$ are conserved. When phenomena on faster timescales occur, these quantities are no longer conserved over the periodic motions and the adiabatic invariants are violated.

First adiabatic invariant: the magnetic moment

The first periodic motion is gyromotion around a guiding centre. The associated conserved quantity is the (nonrelativistic) magnetic moment

$$\mu = \frac{mv_{\perp}^2}{2B} = \frac{1}{2}|q|r_g v_{\perp}, \quad (3.2)$$

where m is the particle mass and v_{\perp} the velocity perpendicular to the guiding centre [Roederer and Zhang, 2014; Jursa, 1985; Schulz and Lanzerotti, 1974]. This is essentially the ratio of the particle kinetic energy to the magnetic field. Note that increases in the magnetic field will result in corresponding increases in v_{\perp} , and decreases in the gyroradius r_g . This quantity is conserved for timescales much longer than the gyroperiod, so the characteristic timeperiod for μ is τ_{gyro} .

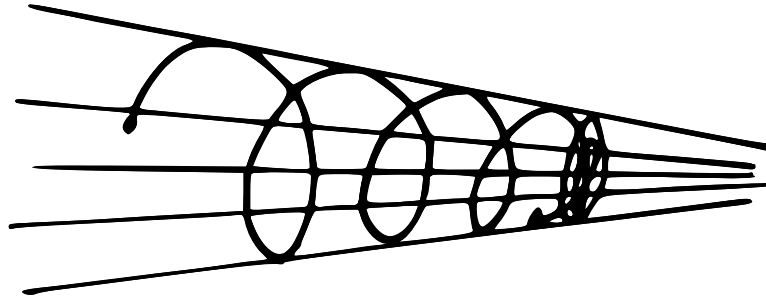


Figure 3-11: The magnetic mirror effect, where a particle with conserved μ is reflected by a strong enough magnetic field.

Second adiabatic invariant: total parallel momentum

The second adiabatic invariant corresponds to a periodic motion that arises as a consequence of conserving μ ; the magnetic bottle effect shown in Figure 3-11. When a particle with conserved μ enters a region of stronger magnetic field, v_{\perp} increases and gyroradius decreases so that the particle is moving in a tighter and tighter spiral. When total kinetic energy of the particle is conserved, while v_{\perp} increases, v_{\parallel} decreases, so that eventually there is some magnetic field amplitude at which the velocity along the field line is zero (the mirror point). This is unstable and the particle will then bounce back along the field line.

The loss of energetic particles to atmospheric collisions can be described using pitch angle $\alpha = \tan^{-1}\left(\frac{v_{\perp}}{v_{\parallel}}\right)$ [Jursa, 1985; Baumjohann and Treumann, 1996]. The pitch angle of a particle will increase as it travels from the equator towards Earth's poles until it reaches the bounce point at $\alpha = 90^{\circ}$, i.e. when $v_{\parallel} = 0$. To describe the particles lost to the atmosphere, we define the equatorial loss cone of width α_L such that if $\alpha_{eq} < \alpha_L$ (or $|\pi - \alpha_{eq}| < \alpha_L$) then the bounce point of that particle will be low enough for that particle to be lost to atmospheric collisions. As the bounce point is a function of pitch angle and the Earth's magnetic field (i.e. independent of the particle's charge, mass or energy) it varies with the radius of the field line. At geostationary orbit ($6.6R_E$) the loss cone is less than 3° wide. While atmospheric loss due to bounce motion is not energy dependent, it should be noted that highly energetic particles with a large enough gyroradius may still be lost to either the atmospheric collisions or through the magnetopause.

This bounce motion between mirror points is associated with a conserved quantity as per equation (3.1),

$$J_2 = \oint mv_{\parallel} dl, \quad (3.3)$$

total parallel momentum over the bounce path. The characteristic timescale of this is $\tau_{bounce} \gg \tau_{gyro}$, which has timescales of minutes (see the characteristic timescales section below).

Third adiabatic invariant: L^* and magnetic flux through a drift contour

In Section 2.2 the guiding centre approximation was considered as a method of simplifying particle motion. When the gyromotion is neglected, and only the guiding centre effects considered, there are multiple drifts that affect the motion of the guiding centre. As well as being derived from the guiding-centre frame Lagrangian, they can be considered individually [Baumjohann and Treumann, 1996; Kivelson and Russell, 1995]. Physically significant drifts are the $\mathbf{E} \times \mathbf{B}$, gradient and curvature drifts:

$$\mathbf{v}_{E \times B} = \frac{\mathbf{E} \times \mathbf{B}}{B^2}, \quad \mathbf{v}_{gradient} = \frac{mv_{\perp}^2}{2qB^3}(\mathbf{B} \times \nabla B), \quad \mathbf{v}_{curv} = \frac{mv_{\parallel}^2}{q} \frac{\mathbf{R}_C \times \mathbf{B}}{R_C^2 B^2} \quad (3.4)$$

where \mathbf{R}_C is the radius of curvature [Baumjohann and Treumann, 1996]. These result respectively from an applied electric field ($\mathbf{v}_{E \times B}$), and from inhomogeneities in the magnetic field across a gyroperiod, due to increased magnetic field strengths closer to the Earth ($\mathbf{v}_{gradient}$), and due to curvature of the magnetic field line (\mathbf{v}_{curv}). The \mathbf{E} cross \mathbf{B} drift results in all particles drifting in the same direction, but the gradient and curvature drifts are dependent on the particle charge, so positive particles in the magnetosphere drift westward and negative particles eastward (this is the source of the ring current) [Kivelson and Russell, 1995]. Gravity-induced drifts can be included as an external force [Kivelson and Russell, 1995; Baumjohann and Treumann, 1996] but are generally neglected in radiation belt physics.

The third adiabatic invariant can be found by applying equation (3.1) to periodic drift motion, averaged across gyro and bounce motion. One finds that the magnetic flux Φ enclosed by the azimuthal drift path is conserved, [Jursa, 1985]

$$\Phi = \oint \mathbf{A} \cdot d\boldsymbol{\ell} = \int_S \mathbf{B} \cdot d\mathbf{S}. \quad (3.5)$$

This is more often used in the form of the L^* parameter [Roederer and Zhang, 2014]

$$L^* = \frac{2\pi B_E R_E}{\Phi}, \quad (3.6)$$

which can be understood as the equatorial radius r_0 of the drift contour in a magnetic dipole, in Earth radii ($L^* = r_0/R_E$). Under adiabatic changes (i.e. changes no faster than characteristic timescale τ_{drift} on the orders of minutes or hours, where $\tau_{drift} \gg$

$\tau_{bounce} \gg \tau_{gyro}$) this drift contour may be distorted such that L^* no longer corresponds to the drift orbit radius in units of Earth radii but is nonetheless conserved.

The Roederer L^* should not be confused with the McIlwain L-shell parameter L [McIlwain, 1961, 1966], even though they are very similar close to the Earth. The McIlwain L-shell describes the relaxation of a realistic magnetic field to a dipole. It is measured in R_E , i.e. $L = 2$ corresponds to a magnetic field that would cross through the equatorial plane at $2 R_E$ if the magnetic field were an uncompressed dipole.

In this work L^* is used to indicate the Roederer value, an adiabatic invariant relating to a particle (or a collection of particles) whilst L is a mapping from magnetic shells to their corresponding magnetic shells in a dipole field.

Characteristic timescales and violations of the adiabatic invariants

Particles of different kinetic energy each have their own set of characteristic timescales for each periodic motion. Example values are shown in Figure 3-12 for particles that are equatorially mirroring (i.e. the bounce point is at the equator). For each particle, timescales follow $\tau_{drift} \gg \tau_{bounce} \gg \tau_{gyro}$. This leads to a hierarchy where breaking the first invariant (i.e. processes with timescale $\tau \sim \tau_{gyro}$) will result in violating the second and third invariants. However, violating the second invariant will break the third but not necessarily the first invariant. Hence processes that occur on timescales of seconds will typically violate both J_2 and Φ , but not μ , as $\tau_{gyro} \sim$ milliseconds. Finally, the third invariant Φ may be violated by processes on longer timescales without breaking either μ or J_2 . In fact this is often the case, as an electron with energy ~ 0.1 MeV will have a drift period of around an hour, while many magnetospheric processes occur on timescales less than this (Section 3.1.3). In Figure 3-12 it can be seen that the timescales required for adiabatic motion increase at large L-shells; the drift and bounce motions are far longer and the weaker magnetic field results in a larger drift radius. However, there is an energy limit for particles supported by the radiation belt. Particles of high enough energy can have a gyroradius that takes them out of the Earth's magnetic field. Alternatively, particles with fast enough parallel motion can have a bounce point low enough that they enter the atmosphere.

Violations on any of these timescales ($\tau_{gyro}, \tau_{bounce}, \tau_{drift}$) can therefore result in particle loss, transport and acceleration in the radiation belts. For this reason, waves modes supported by the plasma on a variety of timescales (and the subsequent wave-particle interactions) are studied to determine radiation belt physics.

The timescale of particular relevance to the third adiabatic invariant and hence to this project is τ_{drift} , i.e. minutes or hours. This corresponds to the periods of ULF waves and impulses such as changes in magnetopause location [Southwood and Kivelson,

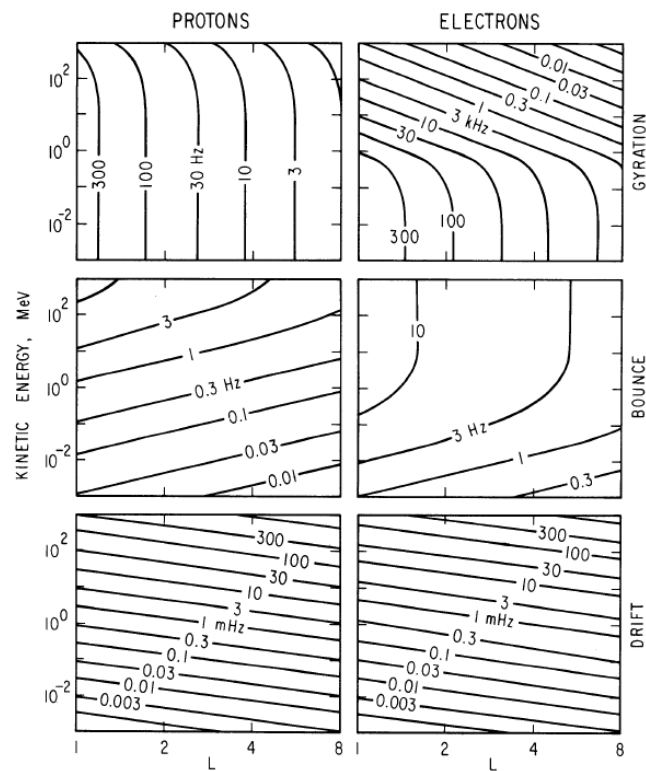


Figure 3-12: Drift, bounce and gyrofrequencies for protons and electrons across a range of energies at different L -shells. Taken from *Schulz and Lanzerotti* [1974].

1990; *Kepko et al.*, 2002; *McPherron*, 2005; *Keiling et al.*, 2016]. A disturbance on such a timescale is particularly of interest when coupled to particle sinks or sources; if there is a source of particles at high L -shell, radial transport can represent energy transport inwards, particularly particle populations accelerated by substorms. Radial diffusion also accelerates particles due to the electric field responsible for the inwards drift of the guiding centre; this energy increase would cancel with the energy increase due to a distorted drift path if magnetic flux Φ through the drift contour were conserved, but in the case of radial diffusion it is not [*Roederer and Zhang*, 2014; *Elkington*, 2013]. This energy change is most easily understood by considering the ideal case of a drift resonant interaction, where a particle whose drift is in phase with a ULF wave will be accelerated [*Elkington et al.*, 1999, 2003; *Elkington*, 2013; *Roederer and Zhang*, 2014].

The characteristic timescale of drift periods is such that L^* is more often broken than conserved, not only because there is always some underlying ULF wave power but also because many magnetospheric processes occur on timescales of an hour or less. For this reason radial diffusion plays an important role in radiation belt energisation and transport.

3.3.2 Diffusion description of radiation belt dynamics: the Fokker-Planck equation

As radiation belt particles are high energy and low density, collisions between them can be ignored. Therefore behaviour can be modelled as a diffusion equation in invariant space, using the three invariants defined above. The phase space distribution function $f(\mu, J, \Phi)$ then evolves with diffusion due to wave-particle interactions. However, sources and sinks such as collisions with ionospheric particles cannot be ignored and so non-diffuse terms must also be included in the simplified Fokker-Planck equation

$$\frac{\partial f}{\partial t} = \sum_{i,j=1,2,3}^3 \frac{\partial}{\partial X_i} \left(D_{X_i X_j} \frac{\partial f}{\partial X_j} \right) + Q - S, \quad (3.7)$$

where Q and S are sources and sinks respectively and $X_{i=1,2,3}$ are the invariants μ, J, Φ . The diffusion coefficients are

$$D_{X_i X_j} = \frac{\langle \Delta X_i \Delta X_j \rangle}{2\Delta t} \quad (3.8)$$

as derived in *Roederer and Zhang* [2014]. In this formulation the diffusion coefficients are half the value of the original Fokker-Planck coefficients, a result of assuming these are small perturbations to a uniform distribution function.

To use a different set of invariant co-ordinates one can find and apply the appropri-

ate Jacobian, $G_{XY} = \det(\mathbf{G}_{ij}) = \det(\partial X_i / \partial Y_j)$. To transform the diffusion due solely to violations of the third adiabatic invariant for a distribution function $f = f(\mu, J, \Phi, t)$,

$$\frac{\partial f}{\partial t} = \frac{\partial}{\partial \Phi} \left[D_{\Phi\Phi} \frac{\partial f}{\partial \Phi} \right] \quad (3.9)$$

into diffusion in terms of L^* and a new distribution function $g = g(\mu, J, L^*, t)$, one can use $G_{L^*\Phi} \sim L^{*2}$, $G_{\Phi L^*} \sim 1/L^{*2}$ and $f(\mu, J, \Phi, t)d\Phi = g(\mu, J, L^*, t)dL^*$ to find

$$\frac{\partial g}{\partial t} = \frac{\partial}{\partial L^*} \left[\frac{1}{L^{*2}} D_{LL} \frac{\partial}{\partial L^*} (L^{*2}g) \right] \quad (3.10)$$

(note that $D_{\Phi\Phi} = G_{\Phi L} D_{L^* L^*} G_{\Phi L}$, [Roederer and Zhang, 2014])¹. Here, the stars have been dropped on the diffusion coefficient for simplicity, so that the diffusion coefficient is

$$D_{LL} = \frac{\langle (\Delta L^*)^2 \rangle}{2\tau_{drift}}, \quad (3.11)$$

i.e. the average square changes in L^* across the relevant timescale - here, a drift period.

Finding expressions for D_{LL} (and other diffusion coefficients) is a current problem in radiation belt physics [Horne et al., 2013] and is one of the eventual purposes of the ULF model developed in this project. Values for all diffusion coefficients may be based in theory but are generally developed empirically; Roederer and Zhang [2014] sum this up on page 121:

Fokker-Planck diffusion theory is “the art of creating pleasing diffusion coefficients” (where “pleasing” means yielding solutions of the diffusion equation are in agreement with the data).

3.4 ULF waves driving radial diffusion

Calculating the power at each frequency (power spectral density) for ULF waves is a vital step in calculating D_{LL} , as it falls naturally out of Equation (3.11) and allows us to focus on the effect of resonances when necessary to simplify. Calculating the mean square displacement in L^* , $(\Delta L^*)^2$, reduces to an integral whose non-negligible terms use the autocorrelation of electromagnetic field amplitudes [Fälthammar, 1965;

¹If one wants to retain a distribution $f(\mu, J, \Phi, t)$ dependent on Φ but to use a diffusion coefficient D_{LL} , this equation can be transformed to find

$$\frac{\partial f}{\partial L^*} = L^{*2} \frac{\partial}{\partial L^*} \left[D_{LL} \frac{1}{L^{*2}} \frac{\partial f}{\partial L^*} \right]$$

[Schulz and Lanzerotti, 1974; Haerendel, 1968]

[*Falthammar*, 1968; *Fei et al.*, 2006; *Lejosne et al.*, 2012]. The Fourier transform of the autocorrelation function and power spectral density (PSD) are related via the Wiener-Khinchin theorem (assuming a weakly stationary and stochastic signal). Hence PSD at each frequency is an important component of D_{LL} [*Fälthammar*, 1965; *Schulz and Lanzerotti*, 1974; *Fei et al.*, 2006]. Typically, for radiation belt modeling $(\Delta L^*)^2$ is estimated using electric and magnetic ultra-low frequency wave PSDs [*Brautigam and Albert*, 2000; *Brautigam et al.*, 2005; *Fei et al.*, 2006; *Ozeke et al.*, 2012, 2014; *Liu et al.*, 2016; *Ali et al.*, 2016]. As the period of ULF waves ranges from minutes to hours, they are of the necessary timescale to provide perturbations of the magnetic field on the order of a drift period.

The most-used formulation today is that introduced by *Fei et al.* [2006],

$$D_{LL} = \sum_m \left(D_{LL}^{Asym,m-1} + D_{LL}^{Sym,m} + D_{LL}^{Asym,m+1} \right), \quad (3.12)$$

for relativistic electrons in a magnetic dipole with a day/night asymmetry. The symmetric and asymmetric components are

$$\begin{aligned} D_{LL}^{E,Sym} &= \frac{1}{8B_E^2 R_E^2} L^{*6} \sum_m \mathcal{P}_m^E(m\omega_d) \\ D_{LL}^{B,Sym} &= \frac{\mu^2}{8q^2 \gamma^2 B_E^2 R_E^4} L^{*4} \sum_m m^2 \mathcal{P}_m^B(m\omega_d) \\ D_{LL}^{E,Asym} &= \frac{2}{9B_E^2 R_E^2} \left(\frac{\Delta B}{B} \right)^2 L^{*12} \sum_m m^2 \cdot [\mathcal{P}_m^E((m+1)\omega_d) + \mathcal{P}_m^E((m-1)\omega_d)] \\ D_{LL}^{B,Asym} &= \frac{2\mu^2}{9q^2 \gamma^2 B_E^2 R_E^4} \left(\frac{\Delta B}{B} \right)^2 L^{*10} \sum_m m^2 \cdot [\mathcal{P}_m^B((m+1)\omega_d) + \mathcal{P}_m^B((m-1)\omega_d)], \end{aligned} \quad (3.13)$$

where γ is the Lorentz factor, $(\frac{\Delta B}{B})$ the asymmetry factor and \mathcal{P}_m^B , \mathcal{P}_m^E the power spectral densities of the compressional magnetic wave and azimuthal electric field at resonant frequency $m\omega_d$. Underlying assumptions for this derivation (and other similar ones) are reviewed in Chapter 6. For example, the formulation in equations 3.12 and 3.13 does not include the phase relations between the electric and magnetic fields, and the variability due to the choice of background magnetic field has not been quantified.

This definition of diffusion coefficient has been used by *Ozeke et al.* [2009, 2012, 2014] (plus a ground-to-magnetosphere mapping) to express D_{LL} in terms of McIlwain L-shell and geomagnetic index Kp . This builds on previous work ([*Brautigam et al.*, 2005; *Brautigam and Albert*, 2000]) which made a similar parameterisation with less data from the CRRES mission. *Fei's* formulation is also used by *Liu et al.* [2016]

to compare diffusion coefficients calculated using THEMIS observations to both the approaches above, while *Ali et al.* [2016] adds Van Allen probe observations to this list. *Lejosne et al.* [2012, 2013] takes a different approach, based instead on calculating radial diffusion coefficients by quantifying the asymmetric part of the background magnetic field instead of focusing on summed electric and magnetic power spectral density contributions at resonant frequencies. All of these approaches produce radial diffusion coefficients that vary across orders of magnitude [*Liu et al.*, 2016; *Ali et al.*, 2016].

This variation in existing models suggests a new approach is necessary. Power spectral density is the largest component in any D_{LL} formulation and as such is the first whose uncertainty should be identified. For this reason we choose to make a probabilistic model of ULF wave power. Other sources of uncertainty in the radial diffusion coefficient calculation will need to be quantified; known problems with existing formulations are covered in Section 6.4. These problems include restrictions imposed by observation methods and by our choice of statistical model, in addition to difficulties expressing the underlying formalism in a useful manner.

3.4.1 The role of ground and in-situ observations

Both ground and space-based measurements are required to estimate radial diffusion. Neither type of observation can fully characterise the wave activity driving radial diffusion and so typically both are used to estimate the diffusion coefficient.

In situ observations of the magnetic field are generally reliable but the electric field is more difficult to measure as three long booms are required to avoid sheath electrostatic fields [*Lai*, 2011]. This is difficult to construct; more typically, spacecraft have one short and two long booms, reducing the quality of electric field measurements. Additionally, spacecraft provide only point measurements which are not ideal for processes that can vary in both space and time. If the spacecraft is located near a node of a standing wave the power in that wave will be poorly estimated. Therefore sparsely populated spacecraft cannot fully estimate the waves driving radial diffusion, but in situ magnetic field measurements can be used to estimate contribution to diffusion from compressional waves (D_{LL}^B) which are not fully transmitted through the ionosphere and cannot be estimated using ground magnetometers.

In contrast to single-point spacecraft measurements, ground-based magnetic field data is easily available with good spatial and temporal coverage. These measurements can be mapped to the equatorial azimuthal electric field, containing the average effects over the entire field line. However, using ground observations effectively is dependent on the quality of our mapping through the ionosphere. Higher frequencies are not transmitted through the ionosphere and the wave attenuation at all frequencies must

be estimated. The mapping from the ground includes perturbations from Alfvén modes and from a varying proportion of coupled fast mode waves. The radial diffusion coefficient component calculated by mapping the ground magnetic field observations to the equatorial electric field (D_{LL}^E) therefore represents perturbations across a larger area along the whole field line, but does not fully represent contributions from compressional modes.

Both components are necessary but separating the radial diffusion this way will result in some unavoidable double-counting as perturbations are included in both D_{LL}^E and D_{LL}^B . Their relative contribution to D_{LL} depends on the efficiency of fast mode-Alfvén coupling and the relative number of Alfvén compared to fast mode waves, properties which vary throughout the magnetosphere. Unfortunately both spacecraft and ground stations are difficult to map to L^* .

Clearly both ground based magnetometers and spacecraft have a role to play in the calculation of radial diffusion coefficients. Ground-based radar observations of ULF waves can complement these, but are not as widely available as the coverage of either spacecraft or ground magnetometer data. In this project the ground-based components have been considered as their availability and coverage make them particularly suited for large statistical studies. Methods that prove appropriate on this large dataset will inform future work that can be applied to other observations of ULF waves in the radial diffusion coefficient framework.

3.5 Geomagnetic indices

Geomagnetic indices are used as a data reduction measure to simplify complex magnetospheric processes to tractable, physically representative numbers.

3.5.1 Kp

The Kp index is a measure of geomagnetic activity, introduced to standardise and combine observations from multiple stations to make a single planetary index. It has integer values ranging from 0-9 and is calculated from the horizontal magnetic field disturbance at a selection of subauroral stations. Currently, 13 stations are used. Calculations of the “disturbance” (a range value) at each station includes subtracting estimated daily, seasonal and annual variations, and normalising the remaining values. Each station has a unique normalisation - a conversion table - intended to make results comparable between stations. These values are then averaged over all stations in a three hour window to give the global Kp index. Kp values are difficult to average due to their nonlinear processing. Low values of Kp indicate a “quiet” magnetosphere

while a value of 5 or above is considered a geomagnetic storm. Despite the lack of clear physical interpretation, Kp works well as a simple measure of geomagnetic activity. It is a common output to space weather modelling customers and is often used in studies to distinguish quiet times. It is calculated by the GFZ Helmholtz Centre Potsdam (<http://gfz-potsdam.de>) and a detailed description of the derivation can also be found in *Kivelson and Russell* [1995].

3.5.2 Dst and SYM-H

Another global index is the disturbance storm time index. This hourly value is a measure of the change in the north-south component (in the plane parallel to the surface at Earth) of the Earth's magnetic field at the equator. After eliminating the quiet-day average and the effect of quiet solar variations, Dst is found by averaging over all stations. Variations are measured in nT and a strongly negative Dst is considered to be indicative of a storm. Dst is strongly related to changes in the ring current; the ring current magnetic field directly opposes Earth's magnetic field and therefore a negative Dst indicates a weaker equatorial magnetic field and a stronger ring current. Dst is calculated by the World Data Center for Geomagnetism, Kyoto (<http://wdc.kugi.kyoto-u.ac.jp>). The calculation of Dst can also be found in *Kivelson and Russell* [1995]. The coverage of Dst stations is not equally distributed around the globe; a similar measure involving more stations is SYM-H.

3.5.3 Auroral indices

Auroral indices are not used in this project but will be important for future work. AU and AL describe the upper and lower limit of magnetic field variations in a set of magnetometer stations across the auroral oval. AE defines the maximum deflection ($AU - AL$) and $A0$ the displacement of the midpoint of AU and AL , $((AU + AL)/2)$ [*Davis and Sugiura*, 1966]. These are measures of the current system across the auroral oval, and are often used as indicators of substorm activity [e.g. *Meredith et al.*, 2001]. These are also calculated by the World Data Center for Geomagnetism, Kyoto.

Similar indices are the SMU , SML and SME values, calculated using the much larger SuperMAG magnetometer chain which has far better spatial coverage [*Newell and Gjerloev*, 2011].

3.6 Co-ordinate systems

Two common co-ordinate systems are the geocentric solar ecliptic (GSE) and geocentric solar magnetospheric (GSM) frames. In both of these systems the origin is at the Earth and the \hat{x} basis vector points towards the Sun along the Earth-Sun line. In the GSE frame, \hat{z}_{GSE} is oriented upwards (“north”) perpendicular to the ecliptic plane, and \hat{y}_{GSE} completes the set. This frame is particularly useful for solar wind quantities. The GSM frame is designed for magnetospheric process; the \hat{z}_{GSM} vector is the projection of Earth’s magnetic north onto the $\hat{y}_{GSE}\hat{z}_{GSE}$ plane, and \hat{y}_{GSM} completes the set [Jursa, 1985; Hapgood, 1992]. In this way the GSM frame is rotated with respect to the GSE frame and quantities such as the interplanetary magnetic field southward/northward component (Bz) are directly related to magnetospheric and ionospheric phenomena. This frame is used almost exclusively in our analysis.

Two other quantities often used as co-ordinates in magnetospheric physics are magnetic local time (MLT) and McIlwain L-shell, L [McIlwain, 1961, 1966]. The L value was discussed in Section 3.3.1 and often used as a radial co-ordinate. Magnetic local time is oriented to the nose of the magnetosphere, so that “noon” is the nose and “midnight” the tail.

Finally, we note that when using magnetic co-ordinates any ground-based observations at a given latitude must be rotated to point to magnetic rather than geographic north. This rotation varies slightly each year.

CHAPTER 4

DATA AND PROCESSING

The bulk of this thesis is devoted to determining a model of (and the uncertainty in) ULF wave power spectral density in order to find radial diffusion coefficients. Therefore in Section 4.1 a definition of power spectral density (PSD) is given, along with an overview of the challenges in determining this for discrete signals. The multitaper method is chosen to address these difficulties. This processing technique is then applied to the solar wind and magnetic field data introduced in Section 4.2.

4.1 Power spectral density calculation methods

Fourier analysis is a set of methods used to analyse signals using frequency attributes. At its simplest, this involves decomposing a signal into sinusoidal oscillations, which can be used to analyse that signal in frequency space instead of its initial domain (i.e. space or time). “Power spectral density” then describes of how much power from the original signal can be found at each frequency. In Section 3.4 the role of power spectral density in calculating radial diffusion coefficients was introduced. The PSD of electric and magnetic fields describe changes in the fields that result in radial diffusion. This frequency-space description is therefore commonly used to isolate radial diffusion due to specific resonant frequencies but is also of use for broadband signals and their effects as we can sum over all nearby, physically effective frequencies.

Whilst we are mainly interested in the data analysis and spectral estimation properties of the Fourier transform in this work, generally the strength of the transform lies in the fact that convolutions in the time domain transform to simple multiplications in the frequency domain (and vice versa). As many operations can be described as convolutions (such as combining two distributions, many image processing techniques

or multiplying polynomials) this provides a tractable way of completing otherwise expensive computations. This is because the fast Fourier transform algorithm (FFT) provides a computationally efficient transform to frequency space, where a multiplication rather than a convolution can be performed. However, we will see that one consequence of this is that simple operations in one domain have complicated effects in the other domain. As a result we cannot simply use the unmodified Fourier transform to estimate PSD.

The Fourier transform is also used in data analysis due to the relationship between frequency and time-lag information; a time lag corresponds to a phase shift in the frequency domain. However, we are solely interested in the spectral estimation properties of the Fourier transform. Much of the terminology comes from electrical engineering purposes but Fourier analysis is also heavily relied on in image processing, data analysis in many fields and in signal processing as an efficient description of a signal. These other fields are all good sources for understanding the transform and for finding new applications.

4.1.1 The Discrete Fourier Transform

The Fourier transform from the time to the frequency domain and the inverse transform can be written as

$$\begin{aligned} X(\omega) &= \int_{-\infty}^{\infty} x(t)e^{-2\pi i\omega t} dt \\ x(t) &= \int_{-\infty}^{\infty} X(\omega)e^{2\pi i\omega t} d\omega, \end{aligned} \tag{4.1}$$

where $x(t)$ is the original signal in the time domain and $X(\omega)$ the frequency-domain signal.

However, this is a transform between infinite continuous domains, whereas we are interested in finite signals discretely sampled in time. Instead we should consider the discrete Fourier transform, the DFT:

$$\begin{aligned}
X(\kappa) &= \sum_{t=0}^{N-1} x(t) e^{-\frac{i2\pi t\kappa}{N}} \\
x(t) &= \frac{1}{N} \sum_{\kappa=0}^{N-1} X(\kappa) e^{\frac{2\pi t\kappa}{N}},
\end{aligned} \tag{4.2}$$

where κ is the frequency index, so that the frequency is κ multiplied by the frequency resolution. Similarly t here is the time index $t = 0, \dots, N - 1$ rather than continuous time.

The DFT is a sampled version of the continuous transform [Prandoni and Vetterli, 2008]. Hence we can decompose a length- N signal in the temporal domain into sine and cosine waves. ($e^{i\omega}$ can be understood as a frequency description via Euler's identity $e^{i\omega} = \cos \omega + i \sin \omega$).

This transform is a valid transform between basis functions as the new basis vectors span the original space (a length- N complex vector, \mathbb{C}^N) and are orthogonal. This is because the basis vectors $e^{-2\pi i\kappa t/N}$, $\kappa = 0, \dots, N - 1$ are the N complex roots of unity ($(e^{-2\pi i\kappa t/N})^N = 1$) which are orthogonal,

$$\sum_{t=0}^{N-1} e^{-2\pi i\kappa t/N} \cdot e^{-2\pi i\kappa' t/N} = \begin{cases} 0 & \text{if } \kappa \neq \kappa' \\ N & \text{if } \kappa = \kappa'. \end{cases} \tag{4.3}$$

Note that these exponential functions are orthogonal but not orthonormal, hence a normalisation factor of is required. By convention, this is often placed on the inverse transform back to the time domain, such as in Equation (4.2).

Due to the DFT being evaluated on a finite number of points we no longer have infinite time or frequency resolution, as we did with equation (4.1). The resulting time and frequency resolution are related by a time-frequency uncertainty principle, $\Delta f = 1/T = 1/(N\Delta t)$. One impact of having a finite frequency support is the existence of a frequency limit determining how high a frequency we can distinguish. This limit, known as the Nyquist frequency, is half the sampling frequency $f_{Nyq} = \frac{1}{2\Delta t}$. Higher frequency components will simply appear as aliasing; the signal is not sampled with high enough time resolution to identify them and instead they appear to be additional lower frequency contributions instead. Therefore a signal cannot be uniquely reconstructed when these higher frequencies exist. This effect can be removed by filtering out any high frequency components, which is particularly suitable in our case as

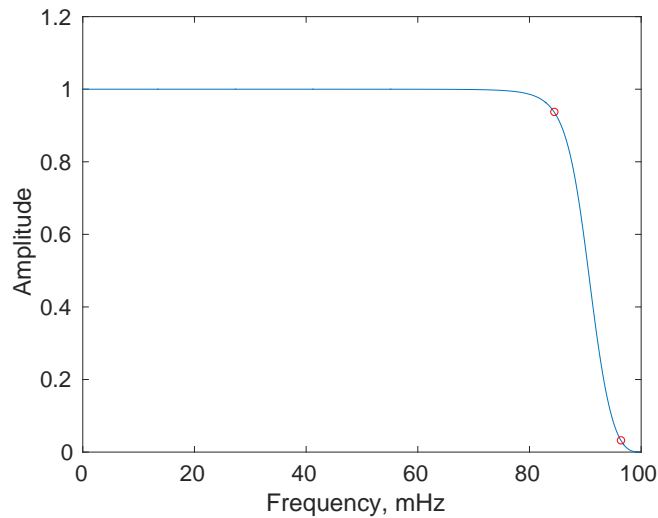


Figure 4-1: The Butterworth filter used to prevent aliasing by removing higher frequency contributions to our signal. The edges of the passband (84 mHz) and stopband (96 mHz) are indicated with red circles.

we are only interested in the lower frequencies. We can use a window in the frequency domain which is roughly uniform across the frequencies we want to retain (i.e. low frequencies) and that drops to zero at higher frequencies. We use a Butterworth filter, which has a smooth transition between passband and stopband. In this thesis we almost exclusively use hourly windows at 5s resolution (Section 4.2). Hence the Nyquist frequency is $f_{Nyq} = 100$ mHz and we choose the Butterworth filter with a passband of 0 – 84 mHz and a stopband from 96 mHz. A small maximum passband ripple (3dB) is specified (ensuring that lower frequencies are not smeared, even near the edge of the transition region) and the stopband has a minimum attenuation of 30 dB to ensure higher frequencies are filtered out. This filter is shown in Figure 4-1.

4.1.2 Power Spectral Density

As the DFT is a change of basis, we expect the norm to be conserved, i.e.

$$\sum_{\kappa=0}^{N-1} \|X(\kappa)\|^2 = \sum_{t=0}^{N-1} \|x(t)\|^2, \quad (4.4)$$

and we can also define a quantity “power” in the time domain for finite signals:

$$\mathcal{P}_x = \frac{1}{N} \sum_{t=0}^{N-1} |x(t)|^2, \quad (4.5)$$

which can be considered as the “energy per unit time” [Prandoni and Vetterli, 2008]. The terminology of “energy” and “power” here stem from electrical engineering. There are multiple ways of defining power spectral density, so comparing the conserved total power between domains is a convenient method of validating each transform and comparing results with alternative methods. Given the DFT definition above, a first description of power spectral density, i.e. the power per frequency, is

$$PSD(\omega) = \begin{cases} \frac{\Delta t}{N} |X(\kappa)|^2, & \text{if } \kappa = 0, \frac{N}{2} \\ \frac{2\Delta t}{N} |X(\kappa)|^2, & \text{if } \kappa \in [1, \frac{N}{2} - 1], \end{cases} \quad (4.6)$$

where Δt is the time resolution of the real-time signal. With these constants, the summed square signal between domains is conserved as follows:

$$\sum_{\kappa=0}^{\frac{N}{2}} PSD(\kappa) = \Delta t \sum_{t=0}^{N-1} |x(t)|^2 \quad (4.7)$$

An estimate of PSD such as this, based entirely on the DFT, is known as the periodogram. In Equation (4.6) we only need to calculate the sum for half of the frequencies. This is a result of solely using real-valued signals; the positive and negative frequencies have the same amplitude so we only need to calculate one half of the frequency domain to determine the entire power.

Note that we actually use the detrended signal $x(t) = x_0(t) - \text{mean}(x_0(t))$ because of spectral leakage from the zeroth frequency; the zeroth component (the mean value of the signal) is usually very large compared to any other frequency components so if there is any bleed-over across frequencies due to our estimation method, the mean will dominate low-frequency estimations of PSD. It is generally advisable to ignore the first few frequency values. Spectral leakage will be discussed in more detail in the following section.

4.1.3 Reducing bias and variance in the spectral estimate

So far only the simple periodogram has been discussed as a method of calculating power spectral density. An assumption implicit in most treatments of spectral analysis (and indeed ULF waves) is that the signal is wide-sense (or “weakly”) stationary, i.e. the mean and autocovariance do not vary with time. Here, this assumption allows us to examine certain statistical properties of any kind of spectral estimate. However, this assumption is also necessary for the Wiener-Khinchin theorem, which states that for such a signal, the spectral density estimate is the Fourier transform of the autocorrelation function. As previously mentioned, this is the basis for PSD in radiation

belt diffusion coefficients. In any case, the ability to study these statistical properties informs our choice of PSD calculation.

We define the bias and variance of a spectral estimator as follows [*National Semiconductor Corporation*, 1980]:

$$B_{\hat{\eta}} = \eta - E[\hat{\eta}] \quad (4.8)$$

$$\sigma_{\hat{\eta}}^2 = [(\hat{\eta} - E[\hat{\eta}])^2], \quad (4.9)$$

hence bias is the difference between the true value of η and the expectation (i.e. mean) $E[\hat{\eta}]$ of an estimate $\hat{\eta}$, while the variance is the width of an estimate around the expectation. When the bias and variance of an estimator tend to zero as the number of observations tend to infinity, that estimator is called consistent. It can be shown that the discrete (i.e. sampled) autocorrelation of a signal is consistent [*National Semiconductor Corporation*, 1980]. However, somewhat counter-intuitively, the periodogram is not consistent even though it is the Fourier transform of the autocorrelation function. Whilst the periodogram can be shown to be asymptotically unbiased (a long enough signal sample should have a mean equal to the true value) the variance does not converge. Using different - even very long - signal lengths will produce different spectral estimates, and the expected value is not significantly larger than the uncertainty [*National Semiconductor Corporation*, 1980]. Therefore the unmodified periodogram should not be used.

One method to reduce this variance is to take multiple smaller periodograms of the same signal and average over them. In this case the variance is reduced at a cost of spectral resolution, as multiple smaller windows will have a smaller resolution frequency $\Delta f = 1/T$, and also an increase in bias via spectral leakage. Unfortunately, as a multiplication in one domain is equivalent to convolution in the other domain, using something as simple as a rectangular window will introduce many ripples into the other domain as the cost of this transformation. The Fourier transform of the rectangular window is the *sinc* function, so the equivalent of multiplying the time signal by the rectangular window is a convolution of the frequency representation with the *sinc* function. As can be seen in Figure 4-2, there will be spectral leakage due to the side lobes of the *sinc* function (Figure 4-2(a)); for infinitely long windows this function converges to a delta function but for shorter finite windows the side lobes grow. As the zeroes of the *sinc* function only occur at multiples of the frequency resolution, any frequency contributions between bins will be smeared. Hence using a rectangular window in either the frequency or time domain will affect the corresponding signal in the other domain. Other windows are often chosen that have a much smaller magnitude

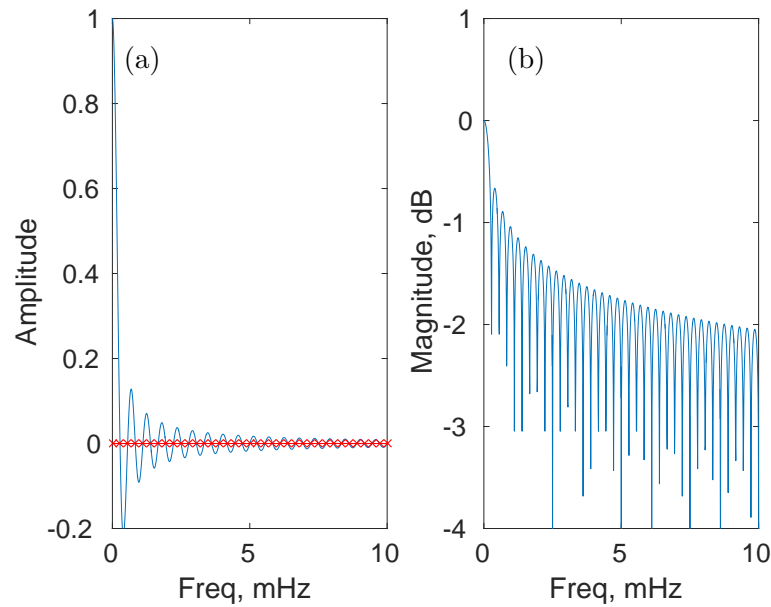


Figure 4-2: The Fourier transform of a rectangular window is a *sinc* function, shown on a linear scale in (a) and in decibels in (b). The *sinc* function is only zero at multiples of the frequency resolution (the red crosses in (a)) and has significant non-zero values at other frequencies.

away from the zero frequency. Splitting one single periodogram up into multiple shorter periods is equivalent to windowing by the rectangular function, as shown in Figure 4-3. In panel (a) a three-hour signal can be seen with eight oscillations (0.74 mHz). When a periodogram is performed on this signal, it can perfectly find the frequency (Figure 4-3(b)) as the frequency is an integer multiple of the frequency resolution. However, for an hour window of the same signal (Figure 4-3(c)), the frequency is now between two frequency vectors in the Fourier basis and the frequency domain description (Figure 4-3(d)) spreads across multiple nearby frequencies.

Therefore as well as averaging over multiple smaller periodograms to improve variance, we must also use a non-rectangular windowing function to reduce the bias (the spectral leakage). Ideally we would have something approaching a delta function in the frequency domain and a rectangular window in the time domain. Instead we must compromise by choosing a window tapered at the edges whose Fourier transform is a function in the frequency domain with very small amplitude side lobes, to reduce spectral leakage. There are multiple window choices that can be chosen that satisfy each of these properties to varying degrees. Obviously a tapered rectangular window leads to information losses at the edges of each window so it is often recommended that overlapping windows are used, known as Welch's method. This averaged, windowed

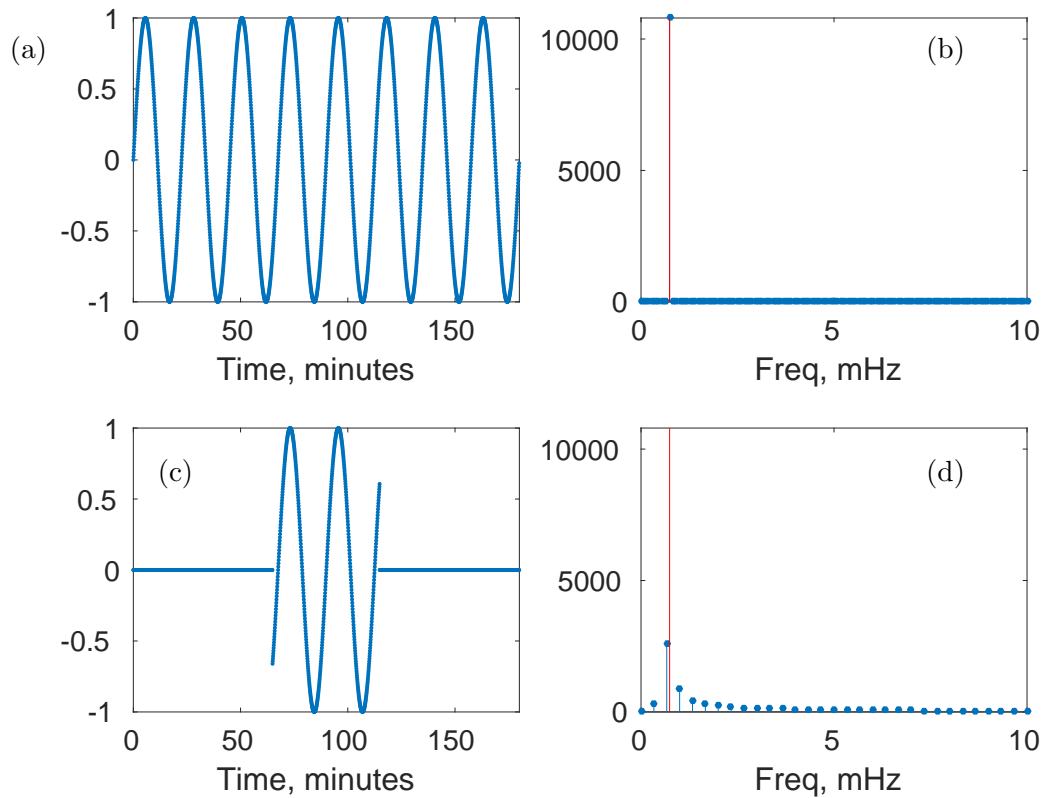


Figure 4-3: (a) A three-hour signal with frequency 0.74 mHz, which has eight full oscillations. (b) the periodogram of the three hour signal, transforming it to the frequency domain. All power is at a single (correct) frequency. (c) An hour window of the signal. (d) The periodogram of the hour window. The power is smeared across several frequencies. The red line shows the true frequency of the signal.

periodogram can then be used to reduce the bias and variance in an estimate of a signal by reducing the spectral resolution.

However, the purpose of this piece of work is to examine the change of frequency properties across time. The modified periodogram described above will not be suitable; when the time period of interest is an hour and the frequencies of interest very low, we cannot split each window up further. Therefore we must use a more sophisticated technique: average over multiple windows which cover each entire hourly signal, and are orthogonal. This will reduce the variance (by averaging over multiple windows) without reducing the spectral resolution further due to taking shorter windows.

This method is called the multitaper method [*Thomson, 1982; Percival and Walden, 1993*]. Of course, there is still a compromise; to improve the variance we trade-off in bias instead, this time by introducing spectral leakage dependent on our choice of orthogonal windows. However, we will show that by using the multitaper method the amount of bias is not as dependent on whether the frequency content of the signal is an integer multiple of our frequency resolution (and hence dependent on window length and time resolution). The windows (“tapers”) chosen to satisfy orthogonality with minimal leakage are known as Slepian tapers, or discrete prolate spheroidal sequences [*Thomson, 1982*]. When applying this method one must choose between the number of tapers and their width, which corresponds to spectral leakage. Generally, a few options are tested to examine the best representation of the spectrum but this is not suitable for fifteen years’ of observations; instead we choose a single value in advance based on properties of our data and ULF waves. When choosing these settings, the user specifies the resolution bandwidth of the multitaper estimate $[-W, W]$, where W should be some integer number of the frequency resolution. Hence W specifies the width of any expected spectral smoothing, as $2W$ defines the bandwidth outside which we want sidelobes of the Fourier transformed tapers to be zero, or very small. W is then used with length N of the window to specify the time half-bandwidth product NW , which is commonly the value used to decide the number of tapers in a decomposition. It turns out that the maximum number of tapers suitable for this can be found using the formula $2NW - 1$ ($2NW$ is the Shannon number describing the point at which the eigenvalues of the tapers drop sharply from one to zero, and hence should not be used)[*Percival and Walden, 1993*]. In general, using more tapers reduces the variance but to be able to use more, a higher NW and hence more spectral smoothing is the trade-off.

Recommended uses of the multitaper method include a half-bandwidth a few integer values of Δf wide and a common starting time half-bandwidth product is $NW = 4$; however, as we have only 720 data points in a single hour this would mean that

$W = 20\Delta f$, which would be an unacceptable amount of smoothing. Instead we choose $NW = 1.4$ which allows us to use two tapers and $W = 7\Delta f$. Using more tapers would have meant a more reduced variance, but this is unattainable with such short windows as the resolution bandwidth W is already quite large. Despite only using two tapers, this method is still the most appropriate for our problem; this is shown in Figure 4-4. In Figure 4-4(a) a signal with six full oscillations ($f = 1.667\text{mHz}$) is shown. Spectral estimates for this signal are shown in Figure 4-4(b) using rectangular and tapered windowed periodograms (specifically, a Hann window), and two multitaper estimates using the default and our time-halfbandwidth products ($NW = 4$ and 1.4 respectively). As expected, the windowed Fourier transform and the multitaper estimates are both smeared across nearby frequencies whilst the rectangular-windowed (unmodified) Fourier estimate finds the correct frequency. Clearly, the default setting $NW = 4$ of the multitaper method is not suitable. However, for a very similar signal of frequency $f = 1.651\text{ mHz}$ (Figure 4-4(c)), a frequency exactly between two frequency bins, the spectral estimate is quite different (Figure 4-4(d)). Here the unmodified fast Fourier transform poorly characterises the spectral properties of the signal whereas the windowed Fourier transform and the multitaper methods are smeared as they were previously. Finally, we consider a broadband signal in Figure 4-4(e) with equal contributions from $f = 1.667, 1.651$ and 1.357 mHz . The spectral estimate of this signal, shown in Figure 4-4(f) is calculated most accurately by the multitaper method with $NW = 1.4$.

Figure 4-4 shows that the leakage from periodograms with rectangular or tapered windows is highly dependent on the frequency content of the signal, while the multitaper method is smoothed more consistently. The multitaper method also captures broadband contributions more accurately. Therefore, the multitaper method is the most suited for our purposes. The remaining bias and variance is an unavoidable consequence of studying low-frequency signals in relatively short windows.

4.1.4 Alternatives: Wavelet methods

An alternative method of calculating spectral estimates is to use wavelet analysis. Similarly to the Fourier transform, this type of analysis decomposes a real-world signal on to a different set of basis vectors. Then, the same operation is performed on smaller or larger windows of the real-world signal, where the basis vectors have been scaled to this new window. This allows both a time and “frequency” representation of a signal, although the precise meaning of “frequency” in this context will depend on the choice of basis function. It can be seen that the spectrogram (a series of periodograms calculated on successively smaller windows) is then a specific example of a wavelet

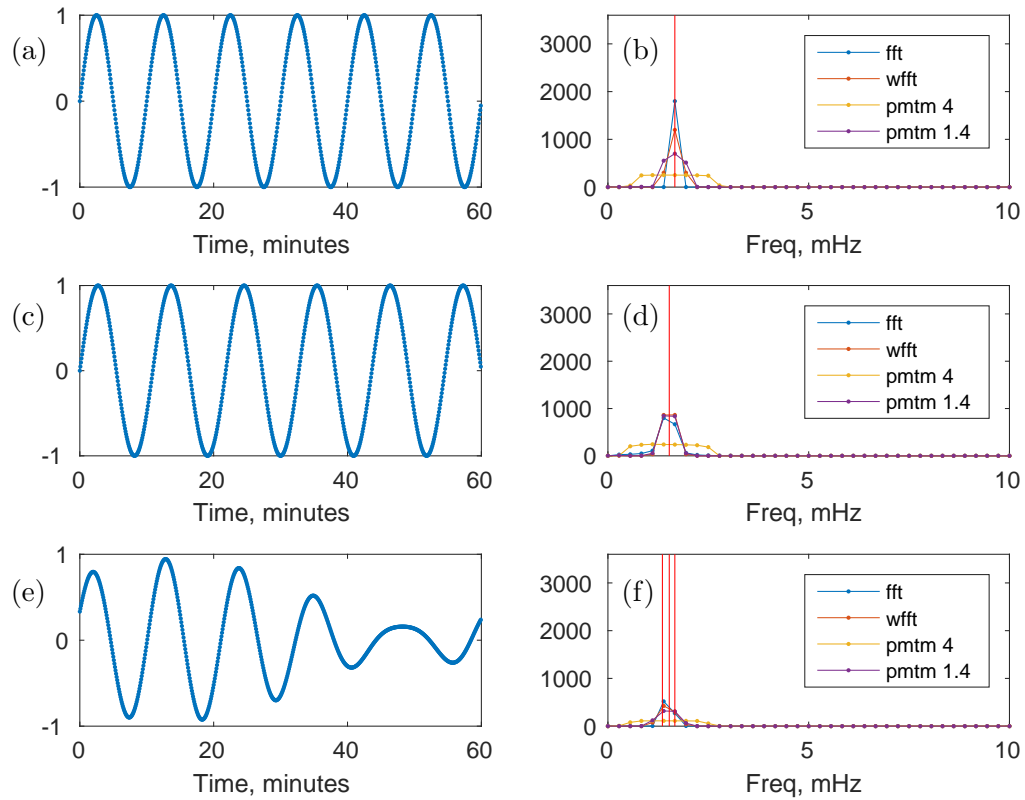


Figure 4-4: Three signals and four spectral estimates of each: the unwindowed fast Fourier transform, the Hann-windowed fast Fourier transform and the multitaper method with time-halfbandwidth products of $NW = 4$ and $NW = 1.4$. (a) a signal with six full oscillations, i.e. $f = 1.667$ mHz. The spectral estimate of this signal can be seen in (b). (c) a signal of frequency $f = 1.651$ mHz (i.e. between integer values of the frequency resolution) (d) the corresponding spectral estimates. A broadband signal is shown in (e), with equal contributions from $f = 1.667, 1.651, 1.357$ mHz, and the corresponding spectral estimates are shown in (f). The multitaper estimate is smeared equally regardless of spectral content of the signal, unlike the Fourier transform methods.

transform onto sinusoidal oscillations. Wavelet transforms are very powerful and are used in a multitude of ways. Different choices of basis vectors are suitable for different purposes, for example compression in communications or images (JPEGs) or for data analysis. For data analysis they are particularly suited to bursty, pulsy non-stationary signals, particularly in fields such as neuroscience. For example, the Morlet wavelet is a complex exponential windowed by a Gaussian function and hence represents a brief sinusoidal “pulse”. Whilst this would allow a very detailed analysis of sinusoidal pulses at different time and frequency scales, it is not clear how this corresponds to spectral estimation and hence the calculation of diffusion coefficients. Most existing statistical analyses of ULF wave behaviour assume that ULF waves are mostly stationary; the extent to which these waves are stationary remains to be seen but it is clear that the magnetosphere is capable of supporting them for periods of several hours [Rae *et al.*, 2005]. For the purposes of this project we have not used wavelets as they would introduce more complexity without resolving the time-frequency uncertainties that make spectral estimation difficult. However, a future analysis of ULF waves using wavelet methods may allow us to investigate the validity of the stationarity assumption and also to examine the spatial and temporal scale of ULF occurrence.

4.2 Data

4.2.1 Solar wind data

Solar wind observations are extracted from NASA/GSFC’s OMNI data set through OMNIWeb at <http://omniweb.gsfc.nasa.gov/>. These measurements are made from multiple spacecraft at the L1 Lagrange point, $\sim 225R_E$ away from the Earth between the Sun and the Earth. Observations are time-shifted to the edge of Earth’s magnetosphere; on average this is around ~ 45 minutes [King and Papitashvili, 2005].

We exclusively use the geocentric solar magnetospheric (GSM) co-ordinate system [Hapgood, 1992]. From the low resolution (hourly) OMNI data, we use proton number density N_p , speed v_{sw} , proton temperature T and magnetic field B with components B_z, B_x, B_y , along with the variability of each of these parameters as processed in Section 4.2.3. In addition to hourly solar wind conditions we use variability δX and/or variance $var(X)$ of each solar wind parameter X , which is calculated in one hour intervals from the high-resolution 1-minute OMNI data as described in Section 4.2.3. Due to the availability of spacecraft, there are some large data gaps before 1995.

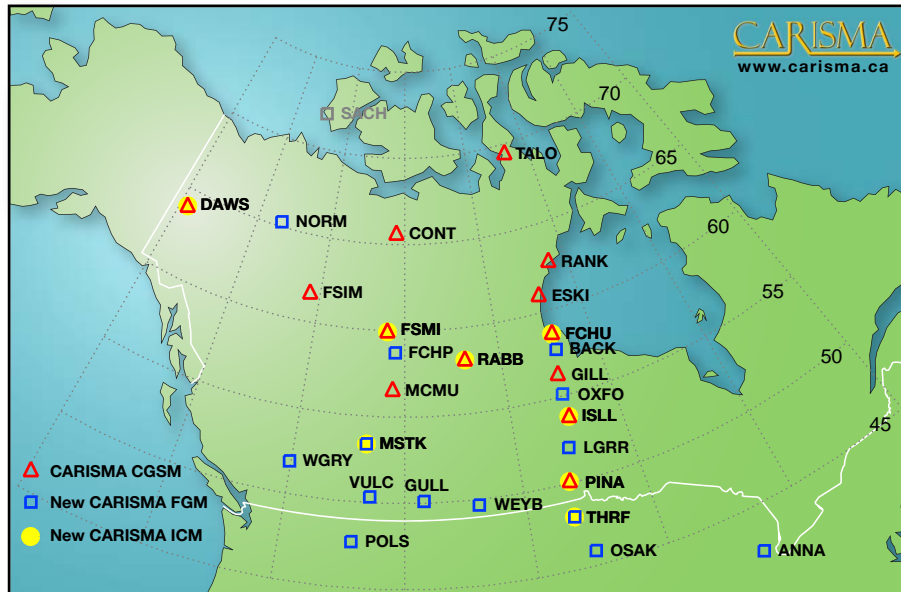


Figure 4-5: CARISMA magnetometer stations, taken from www.carisma.ca. Four stations FCHU, GILL, ISLL and PINA from a single longitudinal chain are used in this work.

4.2.2 Ground-based magnetometer data

To characterise magnetospheric ULF wave power we use measurements from a ground-based magnetometer array across Canada (CANOPUS, [Rostoker *et al.*, 1995], now known as CARISMA [Mann *et al.*, 2008]) from Jan 1990 to Dec 2004. These magnetometers are ringcore fluxgate magnetometers, composed of two coils wrapped around a single core. An alternating current is passed through one coil to induce a magnetic field in the core and hence an electric current in the second coil. The input and output currents are compared to find the background magnetic field.

In this work we use observations from four stations in the Churchill Line, a chain of magnetometers at a single longitude. We use stations FCHU (Fort Churchill), GILL (Gillam), ISLL (Island Lake) and PINA (Pinawa). These correspond to L-shells of $\sim 7.9, 6.5, 5.4$ and $4.21R_E$ respectively in the middle year of the study. More details about these stations over this time period, including L-shell ranges, can be found in

Rae et al. [2012]. Each magnetometer sensor has a range of $\pm 80,000$ nT, a sensitivity of $\frac{1}{40}$ nT and a sample rate of 8 Hz [*Rostoker et al.*, 1995]. Output is processed to provide magnetic field data at 5s resolution which we used to calculate the amount of energy contained in oscillations at each frequency (power spectral density, or PSD) at ground level. Note that this initial processing does include a 0.1 Hz lowpass digital filter. In conjunction with the Butterworth filter shown in Figure 4-1 this means that anti-aliasing is performed twice, which should not affect power in the passband frequencies. CANOPUS data was stored on-site on small buffers for regular satellite uplinks, and timestamps were provided by a complex GOES interface. Mistakes in the clock system meant that sometimes multiple output is measured for the same time and as a result some data at each station must be discarded [*Andy Kale, personal communication*]. This is not a problem for the new or upgraded CARISMA stations, which have 1s resolution and can be used for testing of our initial results, for adding stations later and for further study of results arising from this project.

For the investigation into causal parameters, results from a single stations are presented. We chose GILL (Gillam) station, whose location over this period corresponds on average to geostationary orbit at L-shell $L \sim 6.5R_E$. GILL also contains the largest power out of a series of stations located along the same meridian [*Rae et al.*, 2012]. The full four stations are used in the final statistical model and we anticipate more stations will be added in future.

4.2.3 Data processing

Variance and perturbation of solar wind properties is calculated in hourly windows from the higher resolution OMNI data. If there are eight minutes or fewer missing per hour, data gaps are interpolated. If there are more than eight minutes of missing data per hour, the interval is discarded. Power in each hour is found by detrending and using the multitaper method [*Thomson*, 1982]. We define the variability δX in the solar wind to be the sum of power across 1.7-6.7 mHz, which represents the the power in perturbations of parameter X , a broadband solar wind source.

The ground-based magnetometer data is transformed to geomagnetic H,D,Z coordinates (north-south, east-west and orthogonal to the surface of the Earth) using IGRF/DGRF (International/Definitive Magnetic Reference Field) values for that year and station, from http://omniweb.gsfc.nasa.gov/vitmo/cgm_vitmo.html. Magnetic local times (MLT) are calculated from the same source. Data timestamps are inspected to prevent double-counting, any instances of which are removed. We require that absolute values of the ground magnetic field lie between $5.8 - 6.4 \times 10^4$ nT, regarding anything outside this range as unphysical. We interpolate up to five minutes

of every hour from the time series; if any more data is missing the hour is omitted from our dataset. This is more stringent than for the OMNI data because we require better frequency resolution; we use summed power for each δX but want to consider individual frequencies in the magnetosphere. At this point corresponding solar wind properties from the same hour are assigned to the magnetometer data and we consider only hourly data that is complete in both sets. Power spectral density is calculated as detailed in Section 4.1: first, each hourly time series is detrended and a lowpass Butterworth filter is applied to prevent aliasing. The power spectral density (PSD) is then estimated using the multitaper method, where several spectral estimates are constructed and averaged using orthogonal windowing functions. This provides a spectral estimate with frequency resolution 0.278 mHz. The multitaper method was chosen as it provides a more statistically consistent estimate than a simple fast Fourier transform and it also mitigates some of the effects of cutting up our data into arbitrary hours using rectangular windows [Stoica and Moses, 2005; National Semiconductor Corporation, 1980]. Our definition of PSD conserves the square of the signal in the time (t) and frequency (f) domain as follows:

$$\sum_f PSD(f) = \Delta t \sum_t |x(t)|^2 = \int_{t=0}^T |x(t)|^2, \quad (4.10)$$

where $x(t)$ is the detrended signal in the time domain and Δt the time resolution.

CHAPTER 5

IDENTIFICATION OF MODEL PARAMETERS

For a model of magnetospheric ULF waves we are faced with a compromise between predictive capabilities and containing the appropriate underlying physics. In this project, the compromise is resolved by choosing physically motivated parameters to create a statistical model of ULF wave power. This chapter contains the justification for the solar wind parameters used in Chapter 6. The work presented in this chapter has been adapted from *Bentley et al.* [2018], the goal of which was to find solar wind properties that drive magnetospheric ULF waves in the 1-10 mHz range and to identify the ULF driving mechanisms that those properties represent. Using fifteen years of ground magnetometer and solar wind observations at a single frequency and station, three solar wind properties were identified that contribute significantly to ULF wave power. These were solar wind speed v_{sw} , southward interplanetary magnetic field B_z and perturbations δN_p in proton number density.

We introduce the problem in Section 5.1, reviewing existing work relating ULF wave power to solar wind parameters and outlining our goals. In Section 5.2 the difficulty in identifying ULF drivers throughout the magnetosphere is reduced to a smaller problem with fewer parameters. In Section 5.3 the complicated relationships between solar wind properties are reviewed and the use of the median to characterise ULF wave power on each parameter is justified. In Section 5.4 the method is outlined; a naïve but systematic approach is chosen to account for solar wind interparameter relationships that may be nonlinear and contain thresholds of behaviour change. This approach considers all solar wind parameters as possible driving parameters, and distinguishes those which are causally correlated to ULF wave power. Before using this method, all implicit assumptions in this reduced problem are discussed in Section 5.5. In Section 5.6 we

iteratively compare solar wind parameters to find the dominant parameters contributing to ULF wave power and, by accounting for their interdependencies, any secondary drivers which are masked by their relationship with the dominant parameters. v_{sw} , Bz and δNp are identified as the dominant drivers of magnetospheric ULF wave power and it is shown that for a moderately high solar wind speed, Bz and δNp contribute an extra order of magnitude compared to binning by v_{sw} alone. In Section 5.7 we review current theories of external ULF generation mechanisms and hypothesise which ones are represented by our results from Section 5.6. It is concluded that three parameters most likely represent driving by a combination of the Kelvin-Helmholtz instability, flux tubes travelling along the magnetopause and density perturbations frozen in to the solar wind sweeping past. Finally, the applicability of our conclusions is discussed in Section 5.8 and our main results are summarised in Section 5.8.1.

5.1 Introduction

In this work we aim to identify the solar wind properties that characterise external driving of magnetospheric ULF waves. Internal sources of magnetospheric ULF waves exist but the focus of this study is driving mechanisms dominated by the solar wind. For example, narrowband oscillations have been observed in both the incident solar wind pressure and the magnetospheric magnetic field [Kim *et al.*, 2002; Kepko and Spence, 2003]. Foreshock disturbances such as hot flow anomalies can create dynamic pressure perturbations and magnetosheath pressure anisotropies can give rise to instabilities [see e.g. Hwang and Sibeck, 2016, and references therein]. The Kelvin-Helmholtz instability has long been considered a potential driver of magnetospheric ULF waves [Chen and Hasegawa, 1974b,a], as have magnetopause perturbations such as flux transfer events [Russell and Elphic, 1979] or simply more idealised “running pulses” along the magnetopause [Wright and Rickard, 1995]. Distinguishing how these mechanisms contribute to ULF wave occurrence in different regions of the magnetosphere or by different solar wind driving conditions is commonly attempted by studying the solar wind properties.

Solar wind velocity has been strongly implicated in the generation of ULF waves; Mathie and Mann [2001] showed that to first order, ULF power can be estimated from solar wind velocity v_{sw} using an L-shell dependent power law and Pahud *et al.* [2009] showed that the magnetic local time (MLT) dependence of ULF wave power on v_{sw} varied with radial distance, or L-shell [McIlwain, 1961]. Other studies have attempted to include other solar wind properties, as advocated by Engebretson *et al.* [1998]. These investigations, examining the contribution of individual solar wind parameters, have been performed using both satellite and ground-based measurements

of ULF waves. Satellite-based studies typically find that a combination of solar wind dynamic pressure, pressure fluctuations and velocity dominates observed power. Using in situ magnetic fields at geosynchronous orbit *Takahashi and Ukhorskiy* [2007, 2008] found a predominant dependence on pressure and pressure variation while *Berube et al.* [2014] found that ULF wave power correlates primarily with v_{sw} outside of $L \sim 6$ and variations of solar wind dynamic pressure P_{dyn} inside. Similarly *Liu et al.* [2010] found an overall dependence on pressure and pressure variations using magnetic field data but a v_{sw} dependence using electric field data, suggesting we may expect different results based on our methods of measuring ULF waves. Ground-based ULF studies generally find that power depends on v_{sw} across a range of L-shells [*Mathie and Mann*, 2001; *Pahud et al.*, 2009; *Simms et al.*, 2010] and *Takahashi et al.* [2012] found that control switches from v_{sw} to pressure variation at $L \sim 5$. The diversity of results indicate that we need to consider a systematic approach.

The importance of considering solar wind parameter interdependencies is well known; different solar wind parameters co-vary and thus non-causal correlations with ULF wave power exist. However, these interdependencies are difficult to account for. *Wolfe* [1980] identified solar wind velocity v_{sw} as the dominant driving parameter using a stepwise multiple regression but recognised that the identification of secondary parameters was restricted by the difficulty in deconvolving the effect of nonlinear interdependencies on their relatively small dataset. More recently, *Simms et al.* [2010] found that v_{sw} , B_z contribute to a ULF wave index directly, and that Dst and variations in number density and IMF contribute indirectly. They used path analysis to account for linear, exponential and power law relationships between likely contributing parameters. Indeed, most statistical tools for disentangling such relationships assume that they are linear or require a predetermined model. Instead, in this chapter we begin with a “naïve” approach, where we assume nothing about the solar wind parameter interdependencies. We systematically consider all parameters as possible ULF wave drivers to exclude those that do not contribute to magnetospheric ULF wave power and therefore identify those parameters that do. This straightforward but comprehensive approach allows us to control our assumptions carefully and determine which parameters are related to increased ULF wave power without the need to assume linear interdependencies between parameters.

While we also aim to identify physical driving mechanisms, one of the goals of this study is to set a foundation for future models and analysis of ULF wave power parameterised by solar wind properties. For such a model we would ideally have a minimal set of input parameters that are (a) ULF-effective, (b) have a clear physical interpretation and (c) are orthogonal. We do not expect to satisfy all these requirements but begin

by examining the relationship between ULF power and all non-derived parameters as a compromise between inputs that are maximally physically representative and minimally interdependent. “Non-derived” quantities are defined as not explicitly dependent on other observed quantities, e.g. in the OMNI data solar wind dynamic pressure P_{dyn} is calculated using velocity v_{sw} and proton number density N_p and hence is highly correlated with them. In this work we parameterise ULF wave power using the incoming solar wind properties and use the results to study ULF wave drivers. We account for solar wind interdependencies and attempt to rank the parameters and mechanisms by their effect on ULF waves. Solar wind and ground-based magnetometer data are processed as discussed in Section 4.2. In this study we use only information from 3-21 MLT, excluding the midnight sector to remove effects such as substorm-related ULF wave power to focus on external drivers.

5.2 Parameter reduction

Ideally, a statistical ULF wave model will be dependent on all physical drivers, will vary spatially with azimuth and radial location (latitude is currently unnecessary for bounce-averaged radiation belt models), will include various timescales to account for different generation and propagation processes and will cover a range of frequencies to enable study of both broadband and narrowband ULF waves. However, to identify the solar wind related drivers, this parameter space is too large. We must therefore examine a reduced problem with a manageable number of parameters in order to identify solar wind properties most effective at driving ULF waves *on average*. In the next chapter we will construct a statistical model of ULF waves using these solar wind properties which can be used to study the importance of the parameters neglected here. In this section we justify the simplifications used in the reduced problem; a timescale corresponding to our frequency range, a representative frequency for that range, a single station over all MLT sectors and a single magnetic field component.

Since ULF waves of frequency 1-10 mHz have periods of order minutes, hour-long windows are a compromise between adequate resolution of the required frequency band and adequate temporal resolution of solar wind drivers. An hour window includes time for wave generation and propagation, as the estimated propagation time of compressional waves to the radiation belts is on the order of minutes [Chi *et al.*, 2006]. We assume that the magnetosphere is close to stationary on timescales of an hour. The stationarity assumption is necessary for use of the multitaper method and is a reasonable approximation given the timescale of ULF wave processes which may last from minutes to hours [Rae *et al.*, 2005]. More dynamic drivers exist, such as transient ion foreshock

phenomena, [see e.g. *Hartinger et al.*, 2013; *Hwang and Sibeck*, 2016]. However, these cannot be easily studied using data at L1 and their transiency would require a shorter window which would have reduced frequency resolution.

The lower bound of our frequency range is chosen to exclude spectral leakage from 0 mHz during the PSD calculation. Figure 5-1 provides justification for various analysis choices in this investigation into causal parameters. In Figure 5-1 (a) the median PSD value is shown for sextiles of solar wind velocity across our frequency range. (b) shows the occurrence statistics of all PSD at 2.5 mHz binned by solar wind speed, which is used to create probability distribution functions for each speed bin in (c). Several examples of these distributions are extracted and shown in (d). These probability distributions are explained fully below.

From Figure 5-1 (a) we see that power decreases smoothly with frequency and hence there is no clear upper limit and no preferred frequency within this range to study. We have chosen 10 mHz as an arbitrary cut-off point since this includes most of the power in the system. Thus the processed data consists of a set of solar wind conditions associated with magnetospheric power spectral densities across frequencies 1-10 mHz from four geomagnetic stations across fifteen years. We choose a single representative station, GILLAM, whose latitude maps out to roughly geostationary $L \sim 6.6R_E$ over our fifteen years [*Rae et al.*, 2012]. To reduce the problem further, we consider only a single frequency and will study the full frequency range later. We choose a single frequency, 2.5 mHz, which is at the high-powered end (i.e. the low frequency end).

Previous work [e.g., *Cao et al.*, 1994; *Baker et al.*, 2003; *Pahud et al.*, 2009; *Takahashi et al.*, 2012] has identified an MLT dependence of ULF wave power which will need to be addressed in the full statistical model. However, in this chapter we use all data from 3-21 MLT to find the solar wind properties that are important on average. We also only present the results for the geomagnetic north-south ground co-ordinate (H) corresponding to azimuthal fluctuations in the radiation belts. Individual MLT sectors are examined briefly to confirm qualitatively similar results (i.e. the same parameters) in the supplementary materials of *Bentley et al.* [2018]. In Chapter 6 we will build a statistical model based on the solar wind parameters resulting from this analysis, with the intention of examining the dependence of ULF wave power on these parameters across frequencies, MLT sectors, stations and co-ordinates quantitatively.

5.3 Resolving solar wind interparameter relationships

In order to characterise the relation between the solar wind parameters and the observed ULF wave power it is necessary to first account for the fact that some solar wind

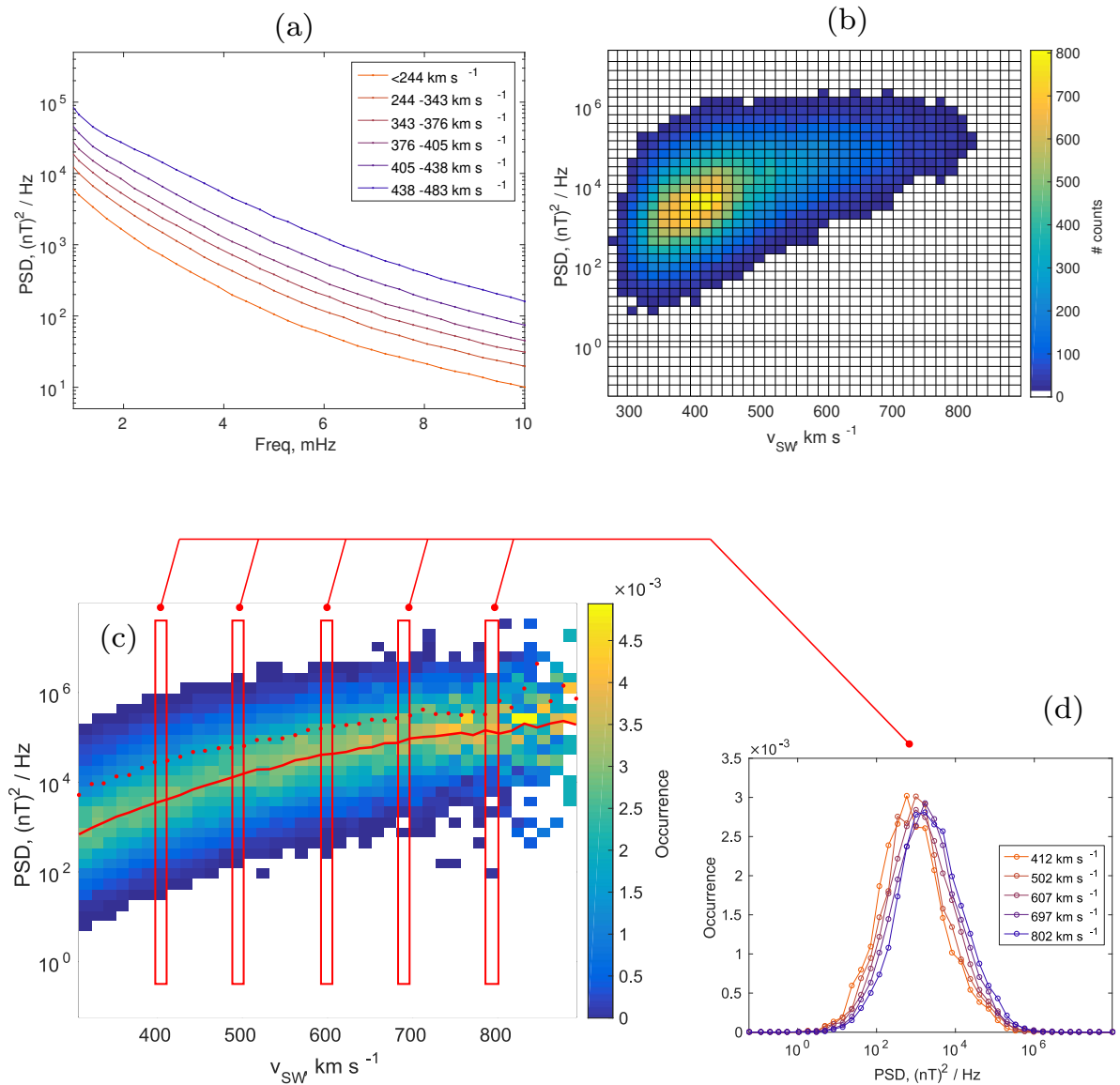


Figure 5-1: (a) Example median ULF wave power spectral density (PSD) for each solar wind speed sextile at GILL station across 1-10 mHz. (b) Occurrence statistics of PSD at 2.5 mHz at each solar wind speed at GILL. (c) Probability distribution functions from the occurrence statistics in (b), normalised such that the probability adds up to one in each solar wind speed bin. The red solid line indicates the median ULF wave power in each speed bin which here follows the “peak” of the distribution, while the red dotted line is the mean which is skewed to the high-powered tail. For each solar wind speed bin the distribution of power is roughly lognormal, as shown by the example distributions in (d), which displays some of the sample probability distribution functions in specific speed bins from (c).

conditions occur more often than others. Otherwise any resultant distributions or relationships we extract will be skewed. This is illustrated in the intensity maps found in Figure 5-1 panel (b), where we bin the occurrence of ULF wave power at a given frequency ($f = 2.5$ mHz) at a single station (GILL) by solar wind speeds. The triangle shape in (b) demonstrates that our data is not evenly distributed over all solar wind speeds, for example we have more data for a solar wind speed of $300 - 400 \text{ km s}^{-1}$ than for $500 - 600 \text{ km s}^{-1}$.

5.3.1 Use of the median to characterise conditional probability distribution functions

It is interesting to note that the triangle distribution in Figure 5-1 (b) is very similar to the occurrence of electron flux and v_{sw} in both *Reeves et al.* [2011] and Figure 1 of *Kellerman and Shprits* [2012], especially as ULF waves are related to distributions of electron flux [*Mathie and Mann*, 2000]. We follow the approach in *Kellerman and Shprits* [2012] to calculate the probability distribution function of the y-axis parameter (here, power spectral density) in each bin along the x-axis (i.e. solar wind speed bins). The observed counts of power spectral density in each (x, y) bin is normalised by the sum of counts in the whole x bin. Then the total number of counts in each vertical slice is the same. Applying this to the PSD - v_{sw} intensity map of Figure 5-1 (b) produces the conditional probability of observing each power value for a given solar wind speed bin centred at v_{sw} . This normalised intensity map is shown in Figure 5-1 (c) and some selected conditional probability distributions (i.e. the vertical slices) are shown in Figure 5-1 (d). In Figure 5-1 panel (c) it can be observed that the resultant distributions for PSD increase smoothly with solar wind speed and that for each vertical slice (each v_{sw} bin) the probability distribution of power is apparently roughly lognormal (Figure 5-1 (d)).

In fact this appears to hold true for other solar wind parameters. The normalised intensity maps for Bz and δNp are shown in Figure 5-2, as are some of the vertical slices. The distribution of ULF wave power for values of each solar wind parameter - the vertical slices - also appear to be lognormal, although more noisy. Given these distributions, we consider the median PSD of each parameter bin to be the concise and representative reduction of the data set we need. Furthermore, the median is conserved (and indeed converges) with additional observations. Although the arithmetic mean is often used to describe statistical wave amplitude characteristics [e.g., *Spasojevic et al.*, 2015], in lognormal distributions the mean is highly skewed towards the high-powered tail whereas the median is directly related to the mean of the corresponding normal distribution [*Johnson et al.*, 1995]. The median will therefore be used exclusively in our

analysis of causal driving parameters of ULF power. A descriptor of the spread of each distribution (such as the variance, or the interquartile range) would be of additional value and will be explored in later chapters.

5.3.2 Review of solar wind parameter interdependence

Relationships between solar wind parameters are determined by the type of the solar wind (and hence their origin on the Sun) and by interactions as the solar wind travels towards Earth. For example, the faster solar wind is less dense and the slow solar wind is often more variable [Geiss *et al.*, 1995], but the faster solar wind may catch up with slower solar wind, creating areas of compression and rarefaction that make up stream interaction regions (SIRs) [e.g., Jian *et al.*, 2006; Pizzo, 1978]. In this section the relationships expected in our subset of the solar wind data are discussed. Corresponding figures are produced using the fifteen years of solar wind data from OMNI (Section 4.2). In Figure 5-3 the occurrence of non-radial solar wind velocities across our fifteen year dataset is shown. The solar wind flow has small non-radial components. Large deviations from radial flow which result in large values of v_y and/or v_z are often the result of CMEs (coronal mass ejections) [Owens and Cargill, 2004] but these are too rare to show up in our analysis. In Figure 5-4 the normalised distribution of proton number density Np for each solar wind speed bin is shown. The normalisation here accounts for the disproportionate amount of data at certain values of v_{sw} and reveals an anticorrelation between Np and v_{sw} as expected from Hundhausen *et al.* [1970]; at lower speeds the solar wind is more dense. There is a change of behaviour at $\sim 500 \text{ km s}^{-1}$, indicating that the Np - v_{sw} relationship is neither linear nor a power-law. This nonlinearity with v_{sw} means that deconvolving the individual effects of Np and v_{sw} on any magnetospheric processes will be difficult.

The interplanetary magnetic field components are shown in Figure 5-5. Evidence of the Parker spiral can be seen in Figure 5-5 (a), as the x and y magnetic field components indicate a striking angle of $\sim 45^\circ$ [Wilcox, 1968]. In Figure 5-5 (b) the normalised distribution of Bz across varying solar wind speeds is shown. For all v_{sw} , the Bz distribution is symmetric around zero; the magnetic field is on average in the ecliptic plane [Lockwood *et al.*, 2016].

In Figure 5-6 we show the normalised distribution of proton temperature T_p in each solar wind speed bin. Faster solar wind includes hotter protons, as expected from previous solar wind observations [Hundhausen *et al.*, 1970].

These known interdependencies will need to be accounted for. In our method we will also consider relationships with perturbations δX of each parameter X . If all perturbations observed near L1 are due to some combinations of random processes,

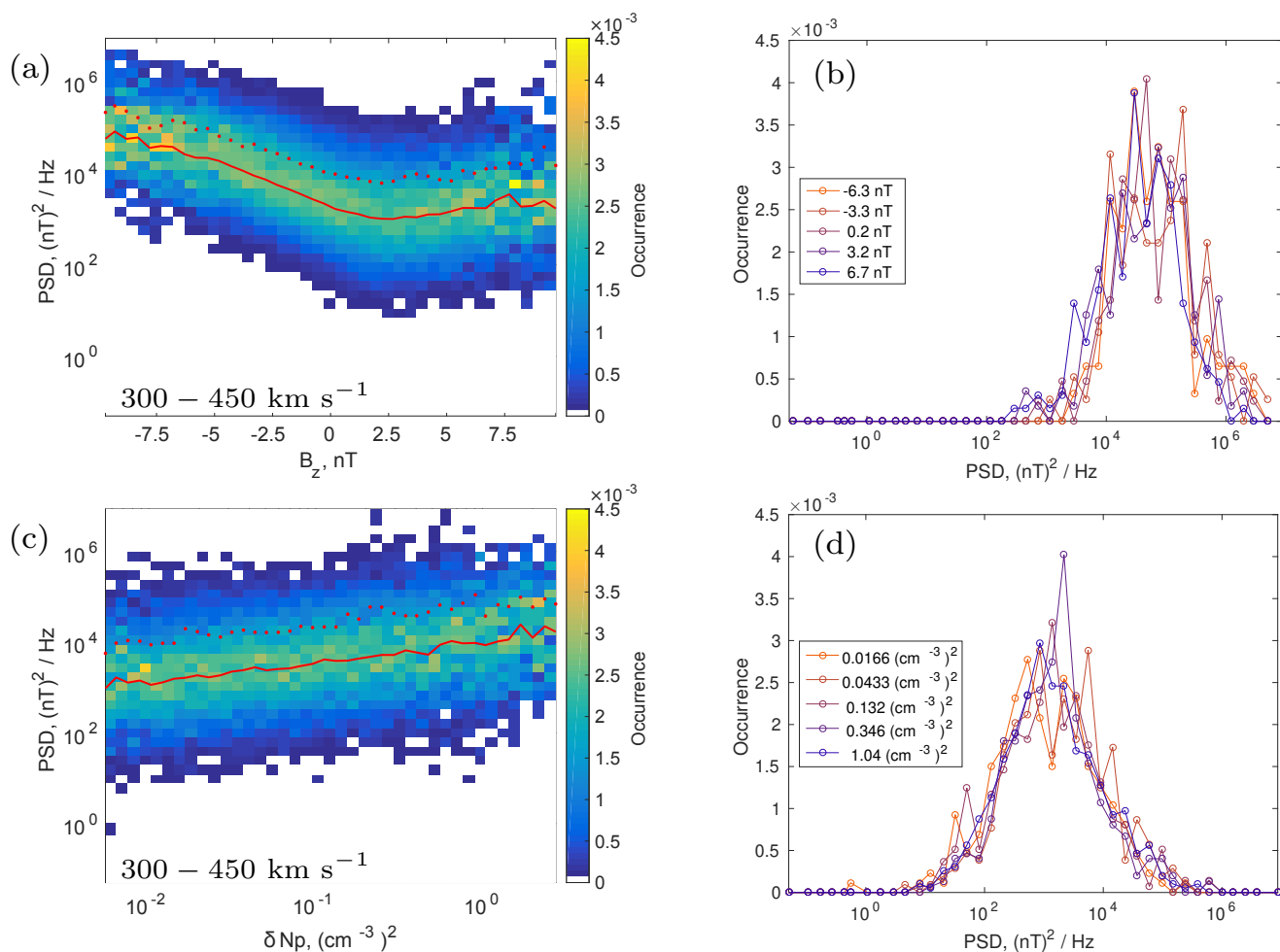


Figure 5-2: Normalised intensity maps as in Figure 5-1 (c) and (d). The power distribution is normalised by the amount of data in each parameter bin. We show this for (a) B_z and (b) δN_p , for a single solar wind speed bin. Median power is indicated by the red solid line and the mean is shown by the red dotted line. Panels (b) and (d) show the power distributions at constant values of B_z and δN_p , as in Figure 5-1.

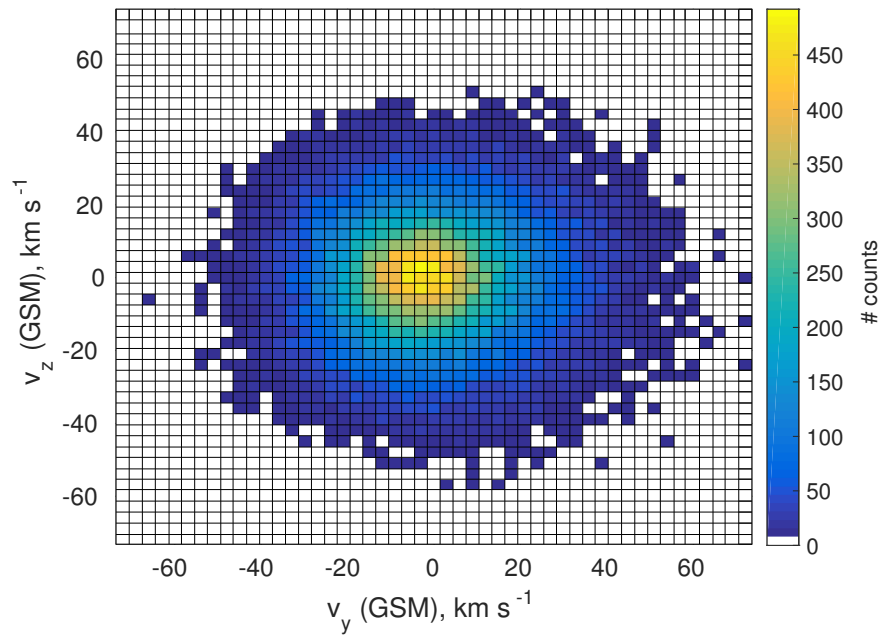


Figure 5-3: The distribution of OMNI data from Jan 1990 - Dec 2004 by solar wind velocity components v_y and v_z . Both components are close to zero, indicating that radial flow dominates.

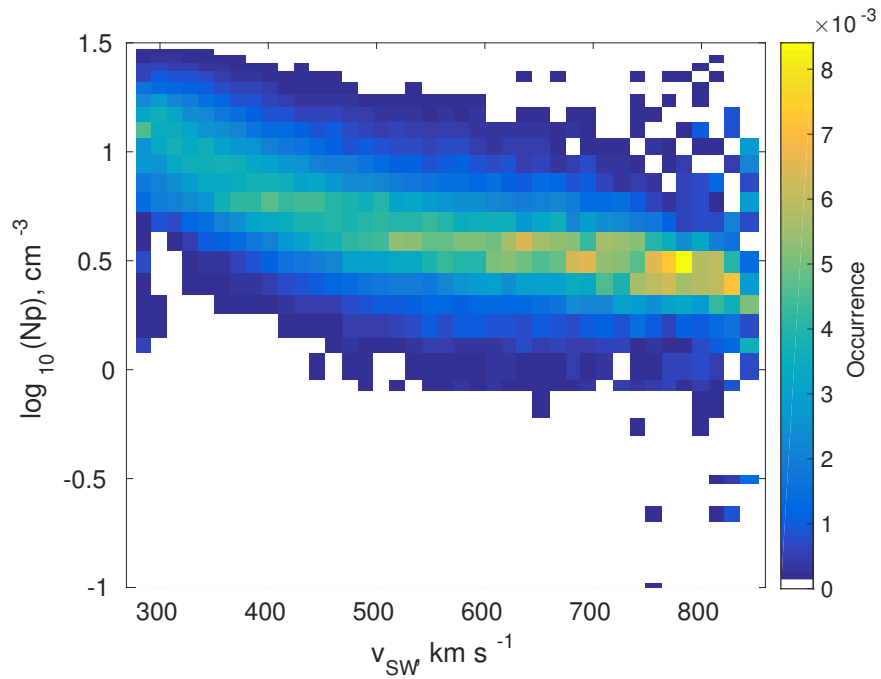


Figure 5-4: The distribution of OMNI data from Jan 1990 - Dec 2004 by solar wind velocity and proton number density. Normalised to account for uneven velocity distribution in the solar wind.

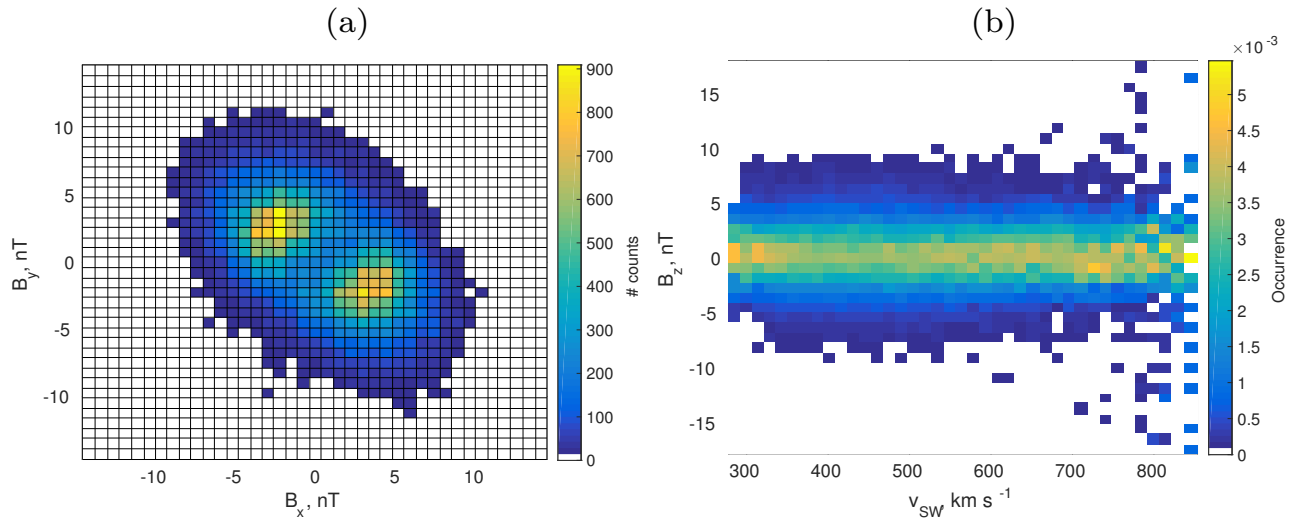


Figure 5-5: The distribution of OMNI data from Jan 1990 - Dec 2004 by magnetic field components. (a) shows the distribution of B_x and B_y . (b) shows the distribution of B_z by solar wind velocity, normalised in each solar wind bin.

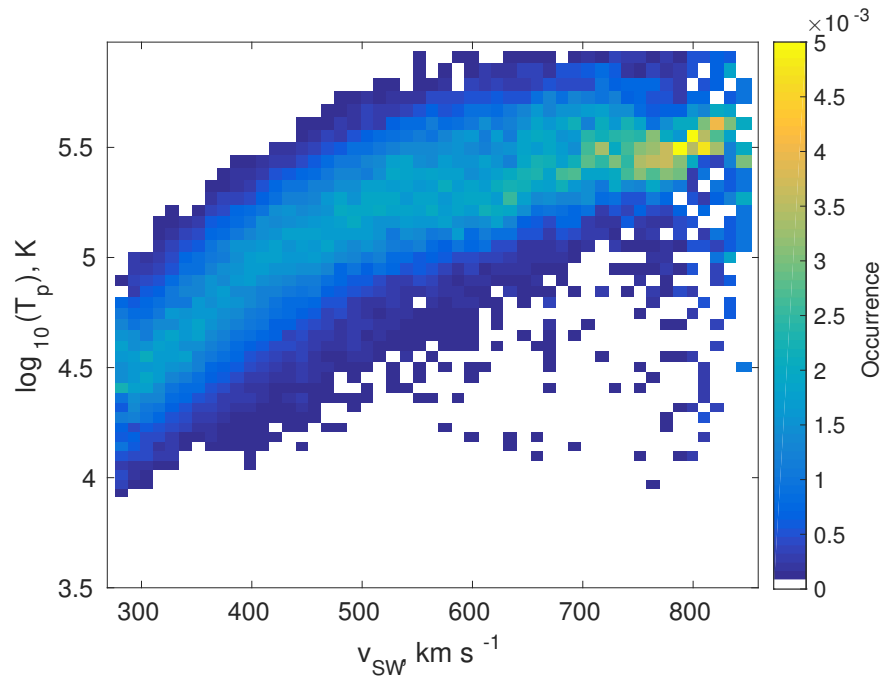


Figure 5-6: The distribution of OMNI data from Jan 1990 - Dec 2004 by solar wind velocity and proton temperature. Normalised to account for uneven velocity distribution in the solar wind.

wave processes and structures from interactions between solar wind regions we may expect that δX contain contributions both independent from and related to the original parameter X . Therefore we assume that δX inherits interdependencies from X , in addition to the relations between perturbations of velocity, number density and the magnetic field from magnetohydrodynamic waves. $\delta B_{x,y,z}$ and δN_p are found in the same types of solar wind and will therefore appear to correlate with one another; in the coronal mass ejection (CME) sheath region there is lots of variability as the faster solar wind causes the preceding solar wind to bunch up, often forming planes of different magnetic field orientation. This bunching up is the region in which the largest δN_p are found [Nakagawa *et al.*, 1989]. The interior region of CMEs exhibit other interdependencies; there is often a low proton temperature, high B_z and low number density N_p [Owens *et al.*, 2005]. While events such as CMEs are relatively rare and so are not obvious in large statistical distributions, they are also particularly geoeffective [e.g., Plunkett and Wu, 2000] and so it is possible that they might weight parameter contributions to ULF wave power. Therefore we must be able to account for all such interdependencies.

As electron density and temperature are not included in the OMNIWeb dataset, they cannot be analysed despite our aim to investigate all non-derived parameters. However, we are not concerned as the electron number density follows the proton number density fairly well over hour-long timescales (otherwise charge neutrality would not be valid in the solar wind) and electron temperature has been found to be roughly 141,000 K independently of any other solar wind characteristics [Newbury *et al.*, 1998], and hence does not have parameter interdependencies to resolve.

5.4 Method

To find the solar wind properties responsible for driving magnetospheric ULF waves, we will identify properties which are causally correlated to changes in ULF wave power. In this context, “causal” parameters are those parameters which correlate with magnetospheric ULF wave power and whose correlation cannot be attributed to their covariance with other solar wind parameters in our analysis. In particular, the solar wind velocity correlates strongly with ULF wave power and with most other solar wind parameters. The numerous interdependencies between solar wind parameters outlined in Section 5.3.2 suggest that resolving these relationships is necessary to identify secondary drivers from dominant ones such as the solar wind velocity.

However, the difficulty in identifying driving parameters in multiple long term studies (Section 5.1) suggests that the assumption of linear interparameter relationships

may be an unsuitable solution. Other alternatives include using quantities from information theory, such as mutual information and transfer entropy [Wing *et al.*, 2016]. However, it is still difficult to properly account for interparameter relationships using such quantities. Furthermore, although information theoretical approaches are well suited to predictive models it is more difficult to study the underlying physics as the physical meaning of quantities such as mutual information is unclear.

Instead, we assume that all parameters may be interdependent, and that the relationship between any two parameters can be nonlinear and even nonsmooth, i.e. there may be one or more thresholds at which behaviour changes drastically. It is assumed that all parameters are likely to have a strong correlation with solar wind speed v_{sw} , as it is a good proxy for different types of solar wind. Thereafter all parameters are systematically considered as possible ULF wave drivers.

The method used is outlined in Figure 5-7. Beginning with a list of all non-derived solar wind parameters, we determine which ones are possible causal parameters. This is done by comparing the relative contribution of two solar wind parameters to ULF wave power via two-parameter plots. Examples of these are given in Section 5.6. For each pair of parameters, we can identify whether ULF wave power varies with the first parameter, the second parameter, or both at a single station and frequency. As v_{sw} is the dominant parameter, we first compare the contribution of all parameters X and δX to that of v_{sw} to identify whether each X or δX could have an independent contribution. Any parameters that appear to contribute to changes in ULF wave power could be causal and must be considered further. This is done by taking a single speed bin such as $v_{sw} = 300 - 450 \text{ km s}^{-1}$ to remove the effect of solar wind speed correlations, and comparing the relative contribution of remaining pairs of parameters to determine which are truly causal. By systematically comparing all pairs of parameters we therefore identify which ones correlate causally to changes in ULF wave power. This iteration is particularly necessary for N_p and $B_{x,y,z}$, as will be shown in Section 5.6. In Section 5.6 the progression through all the major two-parameter plots used to identify our model parameters v_{sw} , Bz and δNp are shown.

5.5 Implicit assumptions

Before proceeding further, we note the additional implicit assumptions in this approach and examine their corresponding physical limitations. To begin with, taking multiple hour-long snapshots assumes that it makes sense to compare them - that the behaviour of the magnetosphere will be similar under similar solar wind conditions, and that the behaviour we see is due solely to those conditions. We do not account for internal

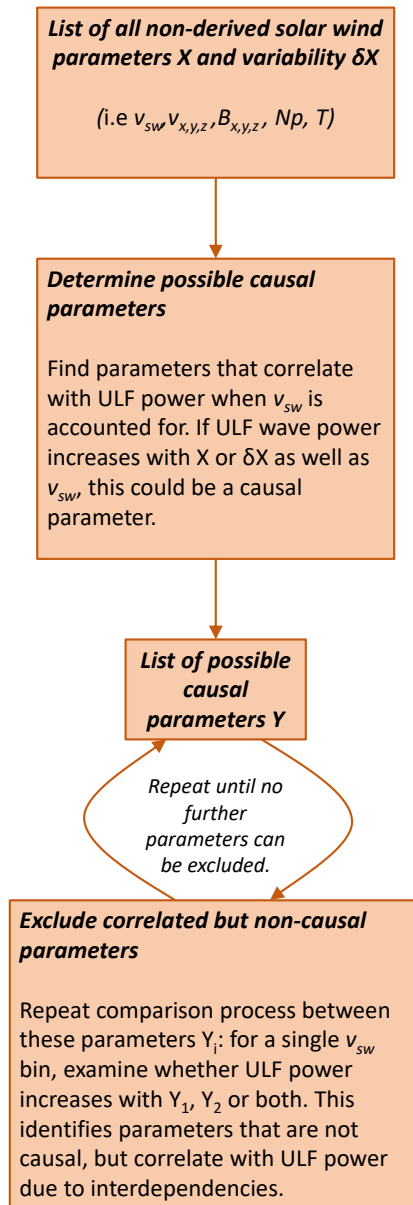


Figure 5-7: An overview of the method followed in this paper to systematically identify causal parameters. By systematically comparing the relative contribution of pairs of solar wind parameters to ULF wave power at a single station and frequency, solar wind properties causally correlated to ULF waves are identified. The iterative process enables us to account for the co-variance between multiple solar wind properties.

processes or for the initial state of the magnetosphere, i.e. the magnetosphere has no history longer than an hour. Obviously this is not always a good approximation but we assume that over the long time period of our analysis it adds noise rather than any systematic bias. Furthermore, by using the median we assume that the system can be described statistically and that essentially each hour-long observation is a separate run of the same “experiment” under different conditions. This assumption is supported by the existence of lognormal power distributions for each parameter. Finally, as the driving variables we are considering are interdependent we need to find a way to isolate the contribution of each and to identify the causal parameters. We consider “causal” parameters to be those parameters which correlate with magnetospheric ULF power and whose contribution cannot be attributed to their co-variance with other solar wind parameters in our analysis. In particular we need to compare relative contributions between parameters since the correlation of power with solar wind speed is dominant and may be masking other secondary mechanisms. The clear dependence of ULF wave power on increasing solar wind speed is shown in Figure 5-1 (a).

Ideally we would bin by all solar wind parameters to examine the contribution of a single parameter to ULF wave power when all others are held constant. However, this would result in a high-dimensional parameter space that would be difficult to analyse and would have poor data resolution. Instead we have simplified by studying only two parameters at once, comparing their relative contributions with adequate data resolution.

5.6 The effect of each solar wind parameter on ULF waves

In this section we work through all non-derived solar wind parameters using the method outlined in Section 5.4. Parameters are presented individually to identify which are causally correlated. We have used observables in the solar wind that are not derived from one another; hence, we do not study electric field E or dynamic pressure P_{dyn} which are derived from $v_{sw}B$ and $N_p v_{sw}^2$ respectively. To compare the relative contribution of any two parameters to magnetospheric power we use two-parameter plots; we bin all data using those two parameters and then calculate the median observed PSD of all hours in each bin containing at least ten points. Then it can be observed whether median ULF wave power increases with one or both of the solar wind parameters. In particular, if one of these binning parameters is solar wind speed we will have controlled for any speed-dependent relationship. This type of by-eye analysis is not ideal but serves to identify model parameters which can be compared quantitatively using other methods.

A summary of the resulting ULF-effective parameters can be found in Section 5.6, while a discussion of the physical mechanisms they represent is presented in Section 5.7.

Solar wind velocity components

While the solar wind velocity is expected to dominate contributions to ULF power, for our systematic approach it should be confirmed whether this contribution is contained within the bulk flow v_{sw} or within the velocity components (in GSM co-ordinates) v_x , v_y or v_z . Since v_{sw} is almost entirely composed of radial flow v_x , this question becomes whether the $v_{y,z}$ contributions to magnetospheric ULF power are significant compared to that from v_x . Figure 5-8 contains the first two-parameter plots in our systematic series. In Figure 5-8 (a) and (b) hours are binned by the solar wind v_x and v_y and v_x and v_z respectively, where the median PSD at 2.5 mHz of those hours is shown in each bin. In Figure 5-8 (c)-(f) cut-throughs of the median PSD at individual bins is shown. For these cut-throughs, we hold one parameter constant and show whether, for that constant value, an increase in the second parameter (along the x-axis) is associated with an increase in PSD. Therefore any horizontal results would indicate that there is no dependence of power on that second parameter, whereas a steep gradient would indicate that PSD increases strongly with increases in that parameter. Hence Figure 5-8 panels (a) and (b) show that the majority of observed ULF wave power can be attributed to v_x . While there are small possible effects due to higher absolute v_y, v_z velocities, particularly at lower v_x , ULF power is largely controlled by the v_x component. This is particularly clear from the cut-throughs shown in the side panels (c)-(d) and (e)-(f), where the PSD is highly ordered by v_x but shows little or no relationship with v_y or v_z .

One effect of increased v_y, v_z would be to change the geometry of the magnetosphere, e.g. shifting the nose location relative to the Earth. Since this analysis is performed over observations where our ground station lies in 3-21 MLT, it is possible significant increases and decreases of power could exist due to a shift towards dawn or dusk, but still not appear in our statistics as they are averaged out over multiple MLT sectors. However, this nose shift is relatively small; given extreme non-radial flows in 1-hour data (e.g. $v_{NR} = 50 \text{ km s}^{-1}$) primarily occur within the sheath region of fast ICMEs [Owens and Cargill, 2004], they are typically accompanied by high radial velocity, e.g. $v_x > 600 \text{ km s}^{-1}$. Thus the solar wind striking angle $\theta = \arctan \frac{v_{NR}}{v_x}$ is constrained below $\sim 5^\circ$ off the radial Sun-Earth line. In terms of magnetic local time co-ordinates, this shift of the nose corresponds to a relatively small change of ~ 24 minutes. Hence we would expect this effect to be negligible. Given this and the two-parameter plot results in Figure 5-8, we therefore choose speed $v_{sw} \sim v_x$ to characterise the solar wind

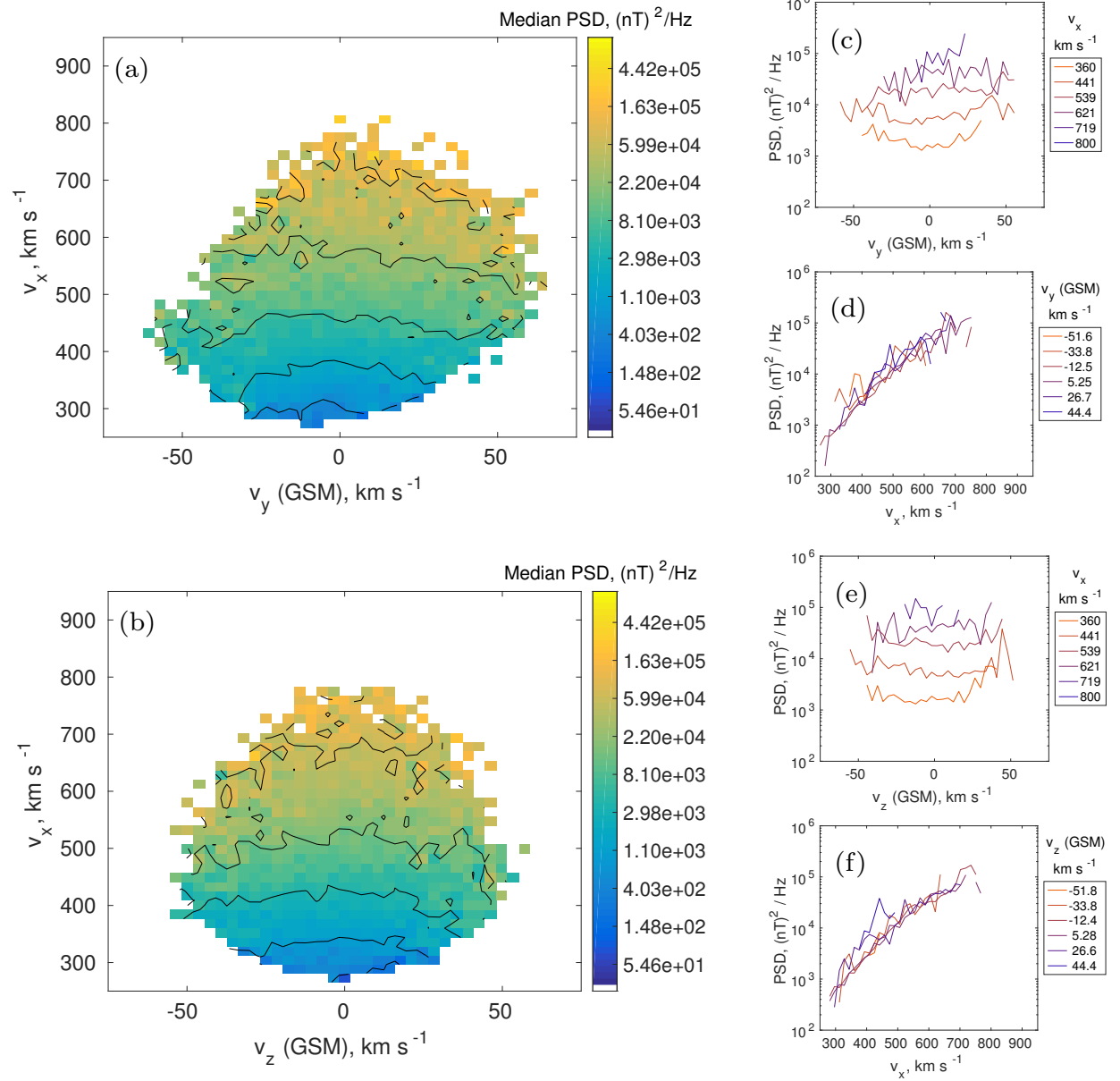


Figure 5-8: Hourly data is binned using by the solar wind velocity in (a) GSM x and y and (b) GSM x and z directions. In each bin, the median PSD found at 2.5mHz at GILL is displayed. Five contours across the median PSD values are shown. On the right, vertical and horizontal slices are taken at constant, equally spaced values to show the relationship between PSD and the individual variables.

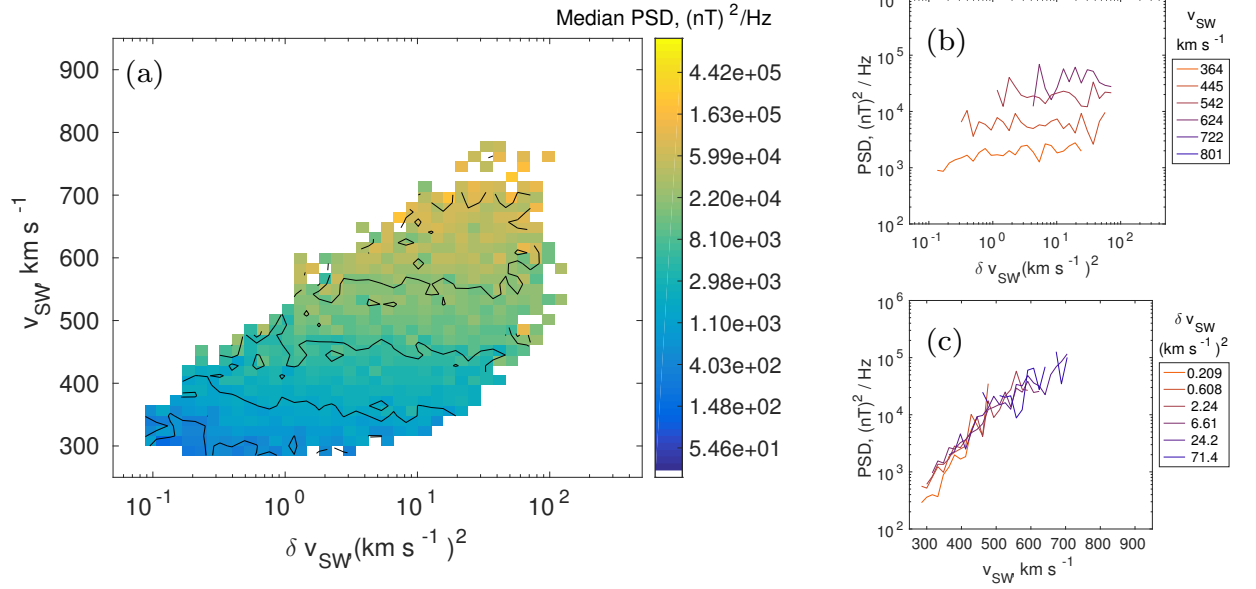


Figure 5-9: Two-parameter plot exploring the dependence of magnetospheric ULF power on the mean solar wind speed and the power δv_{sw} in its perturbations. We bin by v_{sw} and δv_{sw} and display the median power observed in each bin at 2.5 mHz. Cut-throughs at constant v_{sw} and δv_{sw} are shown in (b) and (c) respectively.

velocity control of magnetospheric power for ease of comparison with other studies.

Speed perturbations δv_{sw}

Previous studies have indicated a ULF wave power dependence on speed perturbations or variability [Pokhotelov *et al.*, 2015], but the interdependence of δv_{sw} with v_{sw} has not been fully explored. It is possible that the summed power δv_{sw} (or indeed the variance) will increase in magnitude with the speed v_{sw} , so there is an interdependence to account for. In Figure 5-9 panel (a) we bin the observations by v_{sw} and δv_{sw} values for that hour and take the median observed ULF power in each bin. The coverage in $(v_{sw}, \delta v_{sw})$ -space indicates that δv_{sw} does increase with v_{sw} . However, magnetospheric ULF power increases only with v_{sw} , not with power δv_{sw} in the perturbations. In particular, both the horizontal and vertical cut-throughs at constant v_{sw} (Figure 5-9 (b)) and constant δv_{sw} (Figure 5-9 (c)) indicate a power dependence only on v_{sw} , because the cut-throughs in Figure 5-9 (b) are roughly horizontal. Hence it is likely that the relationship shown in [Pokhotelov *et al.*, 2015] is due to the interdependence between v_{sw} and δv .

Proton number density N_p and perturbations δN_p

The relationship between v_{sw} and N_p or δN_p depends strongly on the type of solar wind. Generally, due to differences in the fast and slow solar wind, we can expect to observe high N_p with low v_{sw} and vice versa. In addition to any relationship between N_p and δN_p we will expect to see higher δN_p in compression regions and in sheath regions [Owens *et al.*, 2005] where we would also see high v_{sw} and magnetic field perturbations.

In Figure 5-10 we examine whether N_p makes a contribution to ULF wave power independently from v_{sw} . In Figure 5-10 panel (a) we see that power increases with v_{sw} as expected, but that it also increases with N_p . However, this also appears to be true for δN_p as shown in panel (c). We can suppose that there may be some relationship between δN_p and N_p and so we must see which contributes to the observed power. To exclude the dependence of N_p and δN_p on v_{sw} Figure 5-10 (b) shows median ULF wave power calculated only using hours where the solar wind speed is between 300 and 450 km s⁻¹. Here we see that increases in ULF median PSD correspond to increasing δN_p and not increasing N_p . For completeness, the corresponding plot for all speeds is included in the supplementary materials of Bentley *et al.* [2018] as it illustrates the necessity of controlling the N_p - v_{sw} interdependency in the solar wind. Therefore we conclude that δN_p , not N_p , is the more immediate contributor to power observed in magnetospheric ULF waves measured using ground-based magnetometers.

The cut-throughs in Figure 5-10 panels (d)-(e) reinforce this v_{sw} - δN_p dependence; in (d), purely horizontal slices would indicate a dependence solely on v_{sw} whereas a vertical result would show that power depended only on δN_p . The angle of the constant speed slices confirm that v_{sw} is the dominant parameter. We also note that in (d) the additional δN_p contribution is observed at all speeds.

Interplanetary magnetic field components and their perturbations

As interplanetary magnetic field (IMF) \mathbf{B} is a vector with highly interdependent components we must first examine all components $B_{x,y,z}$ and their perturbations $\delta B_{x,y,z}$ for a correlation with PSD, and then compare against each other to recognise whether each possible correlation is causal or due to inter-component relationships. Components $B_{x,y}$ are interdependent due to the Parker spiral while B_z is highly dependent on the type of solar wind, for example it is often far larger in sheath regions of CMEs [Owens and Forsyth, 2013]. The total field magnitude $|B|$ is higher in compressed regions of the solar wind and each δB_i inherit these dependencies plus contributions from wave activity and random processes. Therefore we must first compare individual components $B_{x,y,z}$ to v_{sw} and, subsequently, components $\delta B_{x,y,z}$ to v_{sw} . By splitting the analysis

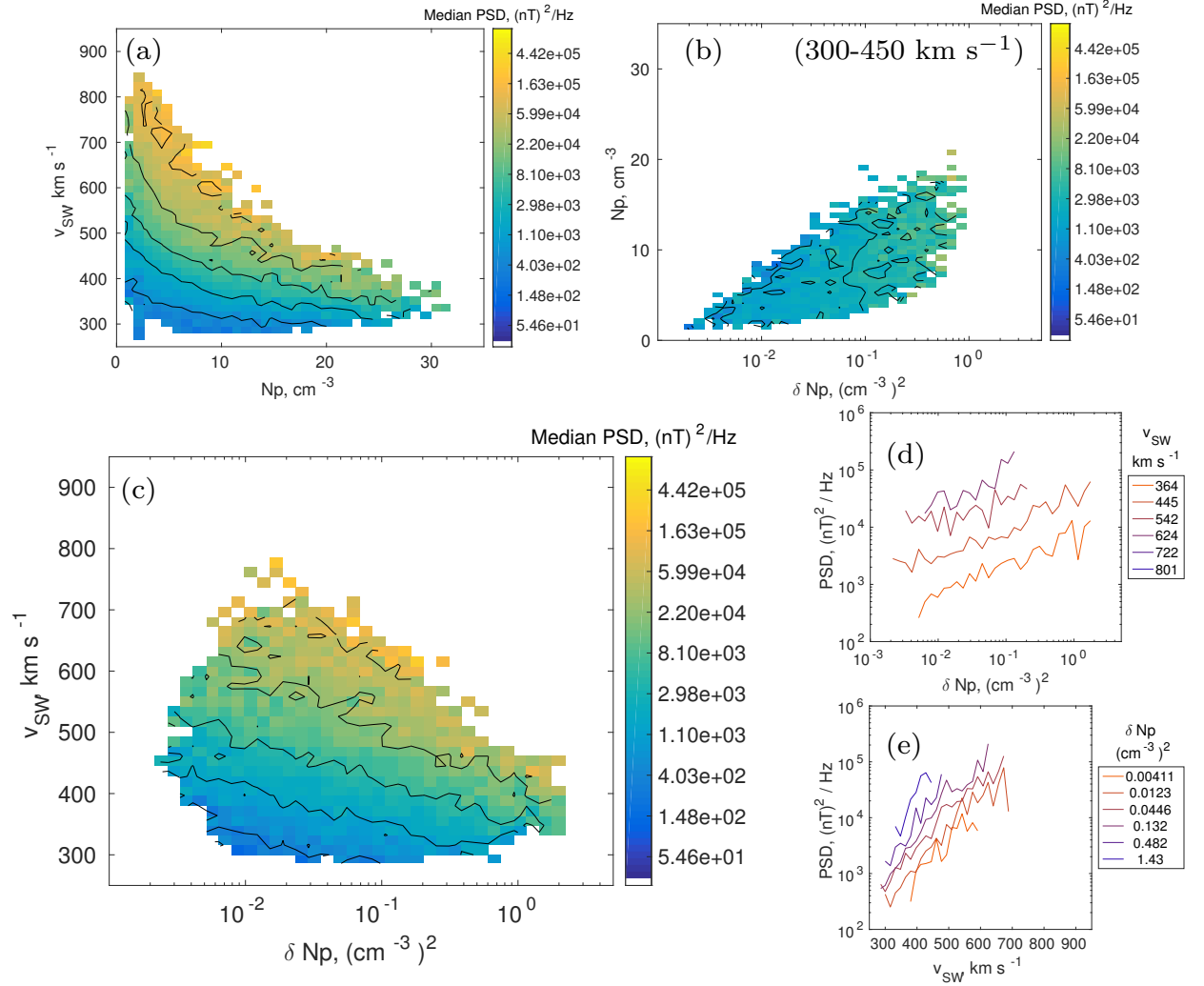


Figure 5-10: Data is binned by two solar wind parameters as in previous figures, and the median magnetospheric ULF power is shown. In (a) we extract the relationship of N_p and v_{sw} to magnetospheric ULF power and in (c) we do the same for δN_p . To disentangle which of N_p , δN_p is the causal parameter for this contribution we compare the two in (b), for a single speed bin of $300 - 450 \text{ km s}^{-1}$. Slices of constant v_{sw} and δN_p are taken from (c) and displayed in (d) and (e).

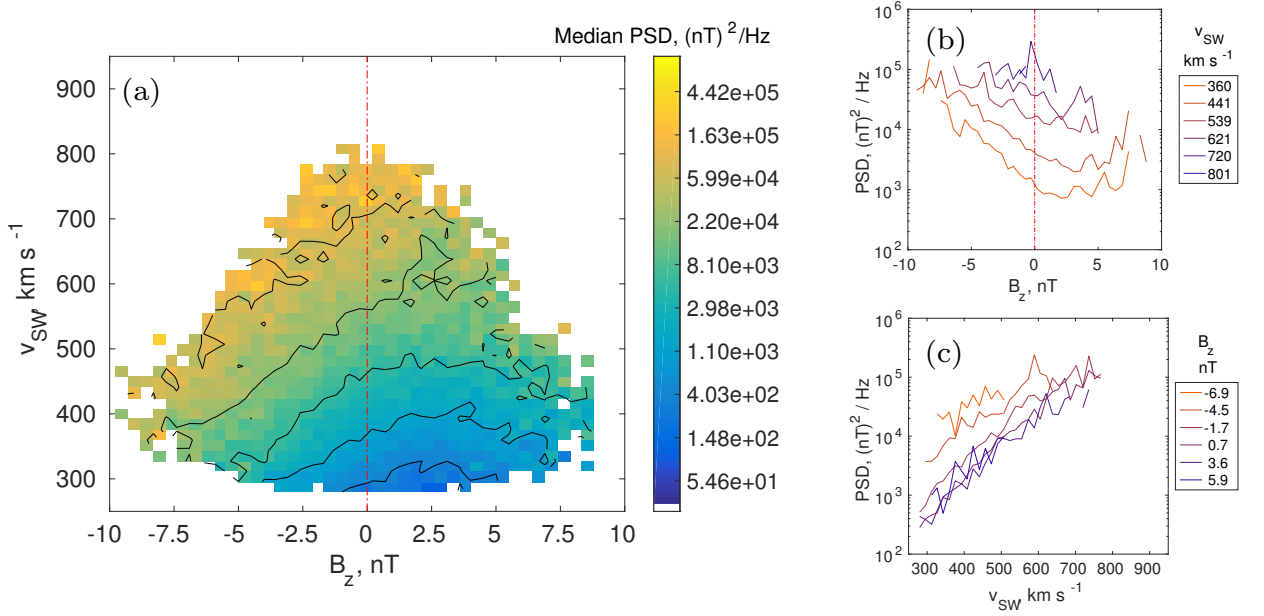


Figure 5-11: (a) Power spectral density (PSD) observed at 2.5 mHz at GILL is binned using the solar wind parameters speed v_{sw} and the B_z component of the interplanetary magnetic field of the preceding hour. The median PSD in each bin is shown. A red line at $B_z=0$ is included to show the change of behaviour across positive and negative B_z . Cut-throughs at constant v_{sw} and B_z are shown in (b) and (c).

in this way we will identify any possible causal parameters whose interdependencies we can resolve by then comparing to each other, for example comparing each B_i and δB_i contribution, ideally while holding v_{sw} constant.

We present B_z first as it is important for studying solar wind coupling to the magnetosphere [e.g., *Dungey, 1961*]. Figure 5-11 (a) shows ULF power as a function of v_{sw} and B_z . We see that for $B_z > 0$ there is very little contribution to observed ULF power due to the magnetic field component B_z . However, there is a clear increase in power for more strongly negative B_z at any given solar wind speed. B_z clearly contributes to observed power but only below the threshold $B_z = 0$. For example, at $v_{sw} \sim 600 \text{ km s}^{-1}$ for $B_z > 0$ the median power is $2.9 \times 10^4 (\text{nT})^2/\text{Hz}$. For $B_z = -7.5 \text{ nT}$, to get a comparable amount of power (that is, $3.0 \times 10^4 (\text{nT})^2/\text{Hz}$) we only require $v_{sw} = 400 \text{ km s}^{-1}$. Therefore B_z clearly represents a significant contribution to ULF wave power and we will examine other magnetic field effects only for observations where $B_z > 0$ to remove this relationship.

As for each component B_i and their perturbations δB_i , the comparison of each component to v_{sw} and to each other is quite involved and can be found in the supplementary materials of *Bentley et al. [2018]*. We present only the component B_x here for

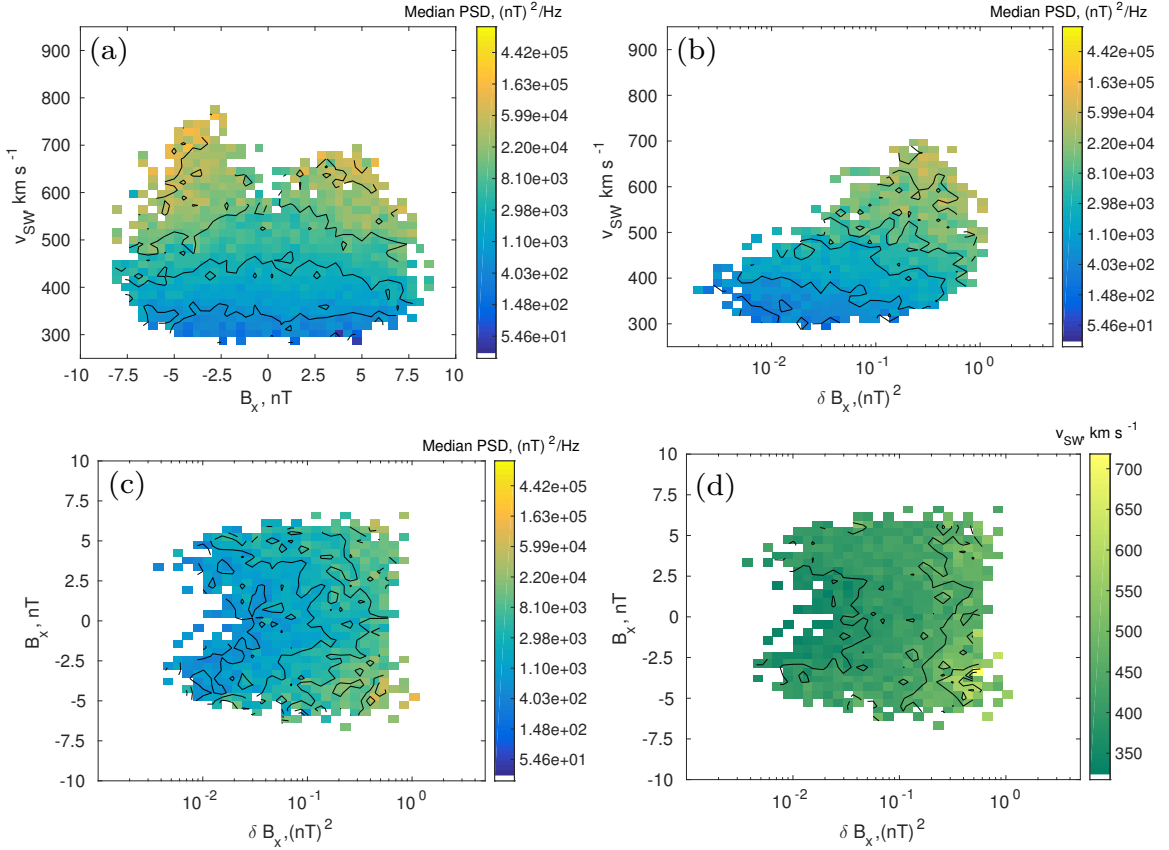


Figure 5-12: Observations (for $B_z > 0$ only) are binned by (a) v_{sw} and B_x , (b) v_{sw} and δB_x , (c) B_x and δB_x and the median power spectral density at GILL, 2.5 mHz is shown. In (d) we show the corresponding median solar wind speed v_{sw} for each bin in (c).

brevity. In Figure 5-12 we compare the contributions from v_{sw} , B_x and δB_x . In panels (a) and (b) there appears to be a change in power associated with both $|B_x|$ and δB_x . Just as for N_p and δN_p , we need to establish whether this is due to the average field B_x or to the perturbations δB_x . In panel (c) we bin by $|B_x|$ and δB_x , showing the median ULF wave power. While at first examination the power appears to be due to δB_x , this power increase follows the corresponding median solar wind speed in panel (d) which we know is dominant. Unfortunately this ambiguity is not resolved by taking a single speed bin as we did for N_p in Figure 5-10. We find the same results for B_y , δB_y , $B_z > 0$ and δB_z (included in the supplementary materials of *Bentley et al.* [2018] as they are very similar to the results for B_x). From this initial analysis we can identify that both the mean field and the perturbations are possible contributors to ULF wave power but cannot confirm whether one or both are causal.

We must therefore examine whether any apparent contribution from components B_i

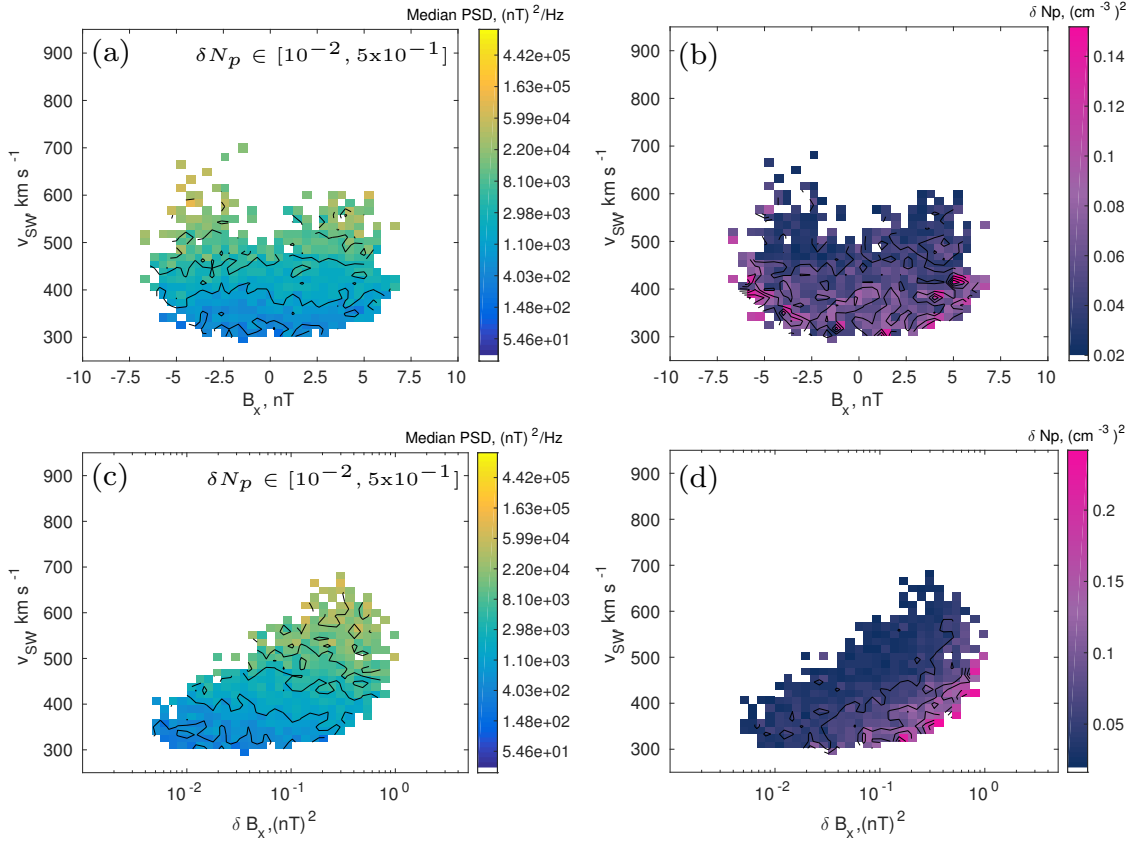


Figure 5-13: For $B_z > 0$ and $\delta N_p \in [10^{-2}, 5 \times 10^{-1}]$, (a) and (c) are the same as (a),(b) in Figure 5-12 where we bin by solar wind speed and $B_x, \delta B_x$ respectively and display the median power spectral density at GILL station, 2.5 mHz. (b) and (d) show the corresponding median perturbation δN_p in each bin.

or δB_i is due to a correlation between B_i and δB_i or between existing causal solar wind parameters. We have already controlled for $B_z < 0$ contributions (by only considering hours where $B_z > 0$) and for v_{sw} contributions (by choosing speed to be one of our binning parameters). However, δN_p has not been controlled, which also makes an independent contribution. This is necessary as we know that δB_i and δN_p are not independent and often occur in similar types of solar wind, in particular the sheath region before CMEs. They also inherit relationships from wave processes and from B_i and N_p , as discussed in Section 5.3.2. To resolve this we take only data where $B_z > 0$ and $\delta N_p \in [10^{-2}, 5 \times 10^{-1}] \text{ cm}^{-3}$ to remove these effects. Then it remains to deconvolve the parameter pairs v_{sw} and δB_i , and v_{sw} and B_i , which we present for the x component in Figure 5-13. (Again, similar results for y and z components can be found in the supplementary materials of Bentley *et al.* [2018]). Here we can see that once δN_p has been controlled, there is no contribution to ULF wave power from B_x or δB_x when

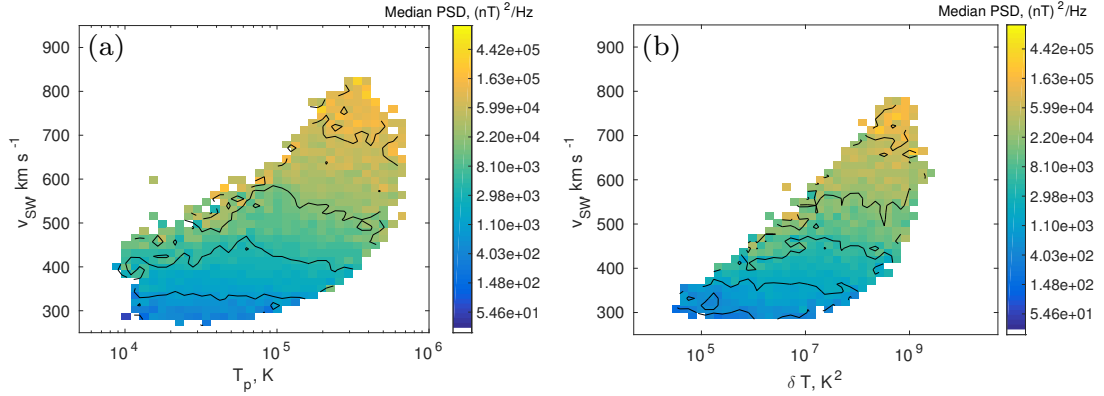


Figure 5-14: Data binned by (a) v_{sw} and T , (b) v_{sw} and δT . The median power spectral density at GILL at 2.5 mHz is shown, as in Figure 5-9.

compared to v_{sw} . Hence we conclude that components $B_{x,y}$ and perturbations $\delta B_{x,y,z}$ are unlikely to constitute “causal” parameters and do not indicate a separate physical mechanism, instead reflecting the results for δN_p because large values of $\delta B_{x,y,z}$, $B_{x,y,z}$ and δN_p often appear in similar types of solar wind.

To summarise, we can see a clear contribution to power from B_z when $B_z < 0$ independently of the contribution from the dominant driving parameter v_{sw} . Apparent contributions from $B_{x,y}$ and/or $\delta B_{x,y,z}$ are in fact due to correlations with δN_p . It is unclear whether there is increased ULF power correlated with increasing $|B_i|$ or δB_i because the effect is small and cannot be deconvolved from v_{sw} and δN_p whilst retaining enough data. Therefore of all the magnetic field parameters we only consider $B_z < 0$ as an additional causal driving parameter.

Temperature

In general, proton temperature T increases with v_{sw} although the low temperature inside CMEs may create other relationships. In Figure 5-14 we examine median PSD as a function of v_{sw} and T , and v_{sw} and δT . We see that ULF power increases with v_{sw} but that T appears to contribute little in comparison. Examining δT_p we see that this also does not appear to contribute to magnetospheric power.

Angles of solar wind bulk flow and IMF orientation

These do not contribute any further information and simply confirm conclusions from earlier in this section using components v_i and B_i . They are included in the supplementary materials of *Bentley et al.* [2018] for completeness.

Dynamic pressure P_{dyn} and perturbations δP_{dyn}

Using our definitions above, P_{dyn} is a “derived” parameter (it is calculated using $N_p v_{sw}^2$ in the OMNI data set). Physically it is often implicated in ULF driving [see e.g. references above in Section 5.1]. However, while there is some correlation between v_{sw} and N_p (or δN_p) due to solar wind structure, this correlation is inherently easier to deconvolve than v_{sw} and P_{dyn} , making N_p a better choice to construct an orthogonal basis of solar wind input parameters. We therefore consider N_p in this paper instead of P_{dyn} . For completeness and comparison with previous work, two-parameter plots for P_{dyn} and δP_{dyn} are shown in the supplementary materials of *Bentley et al.* [2018].

Summary of contributing parameters

We have considered all available non-derived solar wind parameters and their perturbations: v_{sw} , $v_{x,y,z}$, δv , N_p , δN_p , $B_{x,y,z}$, $\delta B_{x,y,z}$, T_p , δT_p , and bulk flow and IMF angles. These have been analysed in a systematic manner to account for interdependencies and identify causal properties.

We have identified the following parameters as characterising increased ULF power in the radiation belts and hence indicators of physical mechanisms coupling solar wind activity to magnetospheric ULF wave power:

1. v_x (or v_{sw})
2. $B_z < 0$
3. δN_p

While other parameters than those above may still contribute to ULF wave power, that contribution is too small to be observed. With a larger dataset we could explore other parameters in more detail but v_{sw} , $B_z < 0$ and δN_p will remain dominant. We note that the clear threshold at $B_z = 0$ indicates that in general we should consider treating $B_z < 0$, $B_z > 0$ separately as they represent two different regimes for ULF wave generation.

The goal of this work was to identify driving parameters in the solar wind (particularly those secondary to v_{sw}) and to discuss the mechanisms they represent, which we will do in the next section. First, we can compare δN_p and B_z to establish the order of dominance, which we show in Figure 5-15. We see that as expected, when controlling for v_{sw} , for $B_z > 0$ any change in power is due to δN_p , although there is some leakage near the threshold $B_z = 0$. We can also see that for $B_z < 0$, it is B_z that dominates over any δN_p contribution. Since the increases in power here do not follow

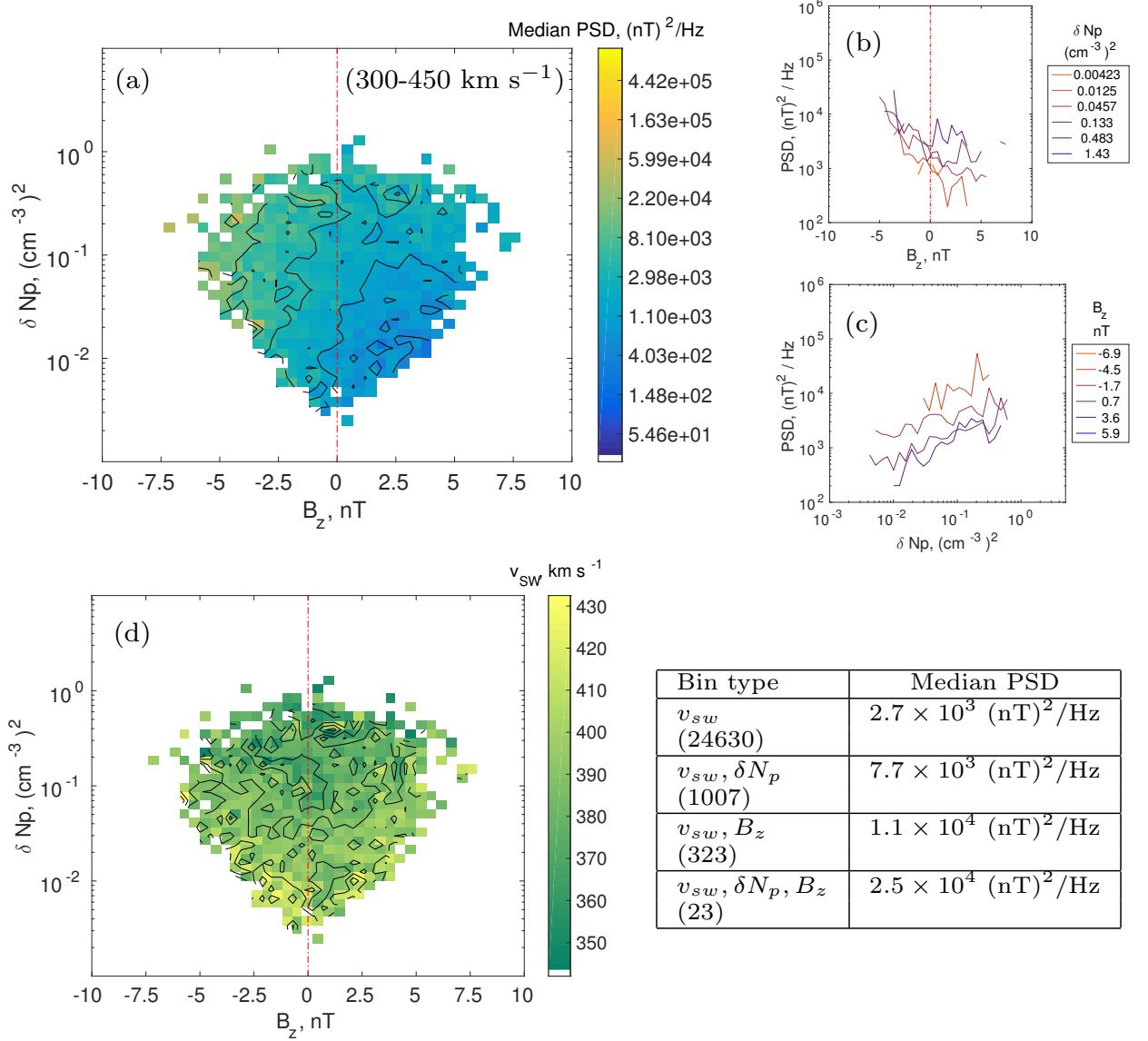


Figure 5-15: The contributions of the ULF-effective parameters are ranked. In (a) we control for speed by using only observations between 300-450 km s $^{-1}$. In this interval we bin by δN_p and by B_z and take the median observed PSD at 2.5 mHz at a single station. Corresponding cut-throughs at constant B_z and δN_p are shown in (b) and (c) on the right, and the median speed in each bin of (a) can be found in the (d) to identify remaining velocity correlations. In the table (lower right) we take this single speed bin (300 to 450 km s $^{-1}$) and find the median PSD at this speed normally compared to with a single moderately high δN_p (5×10^{-1} to $1 (\text{cm}^{-3})^2$) and/or moderately negative B_z (-5.25 to -4.75 nT) occur. The values in brackets in the first column indicate the number of data points in that bin. More power is observed at this speed for higher-amplitude δN_p perturbations and more negative B_z .

the increases in median v_{sw} (bottom panel) and in fact the contours for median power and median speed are perpendicular to one another, we can be sure that the apparent dominance of $B_z < 0$ over δN_p is not due to any remaining correlation with v_{sw} . Hence the parameter contributions in order of dominance is v_{sw} then δN_p for northward IMF, and v_{sw}, B_z and δN_p for southward IMF.

We also briefly consider the additional effect of introducing compression regions (i.e. higher δN_p) and/or negative B_z on the median observed PSD for the same speed bin in the table of Figure 5-15. Individually, both δN_p and B_z contribute noticeably to the overall power. Note that we have not chosen particularly high δN_p or strongly negative B_z due to data constraints, yet for this particular speed bin, their joint contribution results in ULF wave power an order of magnitude higher. Initial results for bins at higher speed indicate that δN_p and B_z can individually account for up to an extra order of magnitude of PSD each, and slightly more than an order of magnitude when combined. This effect will need to be quantified more thoroughly in future work in order to more accurately predict magnetospheric ULF wave power.

5.7 Physically interpreting external ULF generation mechanisms

Having isolated the solar wind parameters which drive ULF power entering the radiation belts, we can begin to identify the physical mechanisms that they characterise. In Chapter 6 these parameters are used to make a statistical model of ULF wave power. Here, the causal parameters v_{sw} , δN_p and $B_z < 0$ are used to distinguish possible physical mechanisms and hence the plasma processes implicated in the creation of ULF waves. While we are considering each mechanism separately here, in reality they are often difficult to distinguish. Indeed, they may be actively driving ULF waves concurrently and even interacting with each other.

Since solar wind dynamic pressure variations are implicated in several magnetospheric ULF wave generation mechanisms, we are obliged to begin with a discussion of the interdependence of dynamic pressure $P_{dyn} = m_p N_p v_{sw}^2$ with our causal parameters v_{sw} and δN_p , where m_p is the proton mass. In particular, we consider the magnitude of possible perturbations of P_{dyn} . A pressure perturbation δP_{dyn} could be composed of perturbations $\delta N_p, \delta v_{sw}$ or both. However, the comparative size of median mass density perturbation amplitude $n_1 = m_p N_{p1}$ to the median background mass density $n_0 = m_p N_{p0}$ is far larger than the same ratio for speed perturbations. We calculate these to be $\frac{n_1}{n_0} \sim 0.69$ and $\frac{v_1}{v_0} \sim 0.09$ respectively from our dataset. This suggests that we would not necessarily expect δv_{sw} to contribute meaningfully to dynamic pressure

perturbations in the solar wind.

5.7.1 Kelvin-Helmholtz instability and v_{sw}

The Kelvin-Helmholtz instability (KHI) is an instability that arises from a velocity shear between two contiguous fluids. The same instability can be found in plasma. At the magnetopause Kelvin-Helmholtz waves have been demonstrated to be potential drivers of Pc3-5 ULF waves in the radiation belt region, as theoretical drivers of field line resonances [Chen and Hasegawa, 1974b,a], by modelling throughout the magnetosphere [Walker, 1981] and by observations of ULF waves whose energy appeared to derive from surface Kelvin-Helmholtz instabilities [Rae *et al.*, 2005; Agapitov *et al.*, 2009].

The incidence of Kelvin-Helmholtz waves at the magnetopause has been established by Kavosi and Raeder [2015], who showed that there appears to be no lower v_{sw} threshold to observe Kelvin-Helmholtz waves and that their occurrence increases with increasing non-shocked solar wind speed. They also confirm that Kelvin-Helmholtz waves occur at all IMF values, although they are less common for a southward IMF. As Kelvin-Helmholtz waves occur more often with increasing solar wind speed we can assume that the causal parameter v_{sw} represents this mechanism, although the relationship may be quite complex. For example, Mann *et al.* [1999]; Mann and Wright [1999] demonstrate that at high enough speed ($v_{sw} \sim 500\text{km s}^{-1}$), the boundary along the flanks of the magnetosphere becomes “overreflecting”, i.e. incident fast mode compressional waves from the magnetosphere are reflected with increased amplitude. This would increase the ULF-effectiveness of Kelvin-Helmholtz waves at higher solar wind speeds.

While v_{sw} counted for the largest contribution to power in Section 5.6, we must examine the v_{sw} dependence of other possible mechanisms before we can assert that v_{sw} represents the KHI and that Kelvin-Helmholtz boundary waves are the dominant driver external driver of magnetospheric ULF waves.

5.7.2 The Rayleigh-Taylor instability

The Rayleigh-Taylor instability (RTI) occurs between two fluids of different densities where the lighter fluid is accelerated into the heavier one. Mishin [1993] demonstrated that growth rates of instabilities are increased while the magnetopause is under an accelerated motion, adding to the Kelvin-Helmholtz instabilities predicted for plasma under a velocity shear. When the magnetosphere is experiencing an expansion, the less dense magnetospheric plasma pressing on the denser plasma in the magnetosheath can then become Rayleigh-Taylor unstable. Further studies by Gratton *et al.* [1996]

and *Farrugia et al.* [1998] showed that the growth of these instabilities is dependent on local time, latitude, IMF conditions and the thickness of the boundary layer. In particular we can expect a dependence on v_{sw} , N_p and their perturbations, although as the KHI also depends on these it is unlikely we would be able to distinguish a RTI contribution using these parameters. We may expect δP_{dyn} (and hence δN_p and δv_{sw}) to represent an additional Rayleigh-Taylor contribution to the instability because they contribute to pressure perturbations and hence the resultant expansions and contractions of the magnetosphere. We would not necessarily see this for δv_{sw} , as discussed in the beginning of this section.

While the difficulty in distinguishing the contribution of individual mechanisms to ULF wave power is discussed in Section 5.7.6 we note here that the Rayleigh-Taylor instability is particularly challenging to isolate. Firstly, pressure perturbations themselves constitute a distinct driving mechanism (see Section 5.7.3). Secondly, the RTI requires an acceleration of the magnetopause and the resulting effect will simply add to Kelvin-Helmholtz instability growth rates, making it difficult to distinguish the contribution of RTI to magnetospheric ULF wave power. Future theoretical work is required in this area to determine the additional ULF wave power from a joint Rayleigh-Taylor-Kelvin-Helmholtz instability and to determine how well δN_p represents the Rayleigh-Taylor contribution.

5.7.3 Density perturbations and solar wind compressional waves

Observations of magnetospheric ULF waves corresponding to solar wind density oscillations [*Kepko and Spence, 2003*] indicate that the movement of the magnetopause in response to solar wind dynamic pressure P_{dyn} changes can enable generation of fast-mode compressional waves; a sudden decrease in solar wind dynamic pressure allows the magnetosphere to expand, resulting in a decrease in the magnetospheric magnetic field. Conversely, a sudden increase in P_{dyn} compresses the magnetosphere resulting in an increase in the magnetic field. These magnetic field perturbations then propagate inwards. This mechanism does not need to be global; variations in the shocked magnetosheath could constitute local generation of fast-mode compressional waves.

However, the source of these ULF-effective pressure perturbations in the solar wind is unclear. The proposed origins can be considered in two ways; (1) solar wind “structures” that change slowly, are fixed with respect to the plasma and are swept past the Earth, and (2) plasma processes which (mainly through processing in the foreshock) can interact with the Earth’s magnetosphere as they evolve rather than being swept past. Examples of the first are entropy waves (density structures bound to the moving plasma) and sheath regions and examples of the second include propagating MHD

waves and magnetosheath instabilities. Of course, using OMNI data we can only examine the response to MHD waves observed near L1. In particular *Walker* [2002] studied the possibility of coherent solar wind MHD waves carrying density perturbations and driving magnetospheric ULF waves via transmission through the bow shock and subsequent incidence upon the magnetopause. We can consider the ULF-effectiveness of solar wind compressional waves carried through the magnetosheath.

Specifically, we can investigate whether solar wind compressional waves are ULF-effective by looking at the causal parameters found previously. If the power increase is only due to structures sweeping past, both δN_p and δv_{sw} would affect magnetospheric power as they indicate pressure perturbations and hence perturbations of the location of the magnetopause - although at the beginning of Section 5.7 we have already discussed that δN_p will give rise to larger pressure perturbations δP_{dyn} , so we may not resolve any such direct δv_{sw} contribution. If the cause of the pressure perturbations is instead predominantly from compressional waves in the solar wind, we would expect relationships between δN_p , δv_{sw} and $\delta B_{x,y,z}$ following plasma wave theory. That is, for a given mass density perturbation amplitude n_1 at a single frequency, we can estimate the magnitude of corresponding speed perturbation amplitude $|\mathbf{v}_1|$ for a compressional wave in the solar wind. If these perturbations are within our resolution, we would expect to also see a relationship between increased magnetospheric ULF wave power and $|\mathbf{v}_1|$ (and hence δv_{sw}) when compressional waves are active.

As described in the appendix, we use the median amplitude of number density perturbations $N_{p0} \sim 3.7 \text{ cm}^{-3}$ at 2.5 mHz to find a range $44 - 106 \text{ km s}^{-1}$ for the corresponding speed perturbation amplitude of an “average” wave. Velocity perturbations of this size are clearly within our resolution. Therefore we can rule out coherent compressional waves as ULF drivers as follows: To identify whether compressional waves are the mechanism, we first assume that the majority of ULF-effective δN_p are due to compressional waves. If this assumption is true, then every time we see increased δN_p we would expect to see increased δv within our visible range and hence a corresponding correlation between δv and ULF power. However, we do not see this δv correlation. Therefore there can be no particular relationship between δv and δN_p at the times when δN_p is ULF-effective, which is only possible if the predominant origin of ULF-effective δN_p (and hence δP_{dyn}) is not compressional waves. This suggests that the ULF-effective δN_p are instead due to structures sweeping past the magnetosphere.

5.7.4 Perturbations arising at the bow shock or in the magnetosheath

While we have considered ULF waves observable in the solar wind near L1, perturbations can also arise between L1 and the magnetosphere. Near the bow shock, tran-

sient ion foreshock phenomena (such as hot flow anomalies, among other phenomena) have been shown to drive magnetospheric ULF waves in our range of interest [e.g. *Hartinger et al.*, 2013; *Archer et al.*, 2013; *Wang et al.*, 2017] both directly and via waves modes arising from the resulting magnetosheath instabilities; these foreshock-origin ULF waves are then convected downstream to “ring” against the magnetopause [e.g. *Hwang and Sibeck*, 2016]. Although these mechanisms are all external drivers they occur downstream of L1 and it is unclear how our solar wind parameters relate to these, particularly in an hour-long window when these are relatively rare events and so may not show up in our analysis. For example, *Schwartz et al.* [2000] found that hot flow anomalies occur ~ 3 times a day and only last a few minutes. We note that *Hartinger et al.* [2013] found that ULF waves around our frequency range driven by ion foreshock phenomena correlate with dynamic pressure pulses in the ion foreshock. Indeed, the dependence of ULF waves on δN_p may be indicative of this effect but we cannot distinguish the effect of density perturbations observed at L1 and the amplification of this in the magnetosheath. Therefore we consider these mechanisms to be “post-L1 processing” and cannot extract their role explicitly in the generation of magnetospheric ULF waves.

5.7.5 Flux transfer events, reconnection and $B_z < 0$

In Section 5.6 we identified that B_z was a causal parameter during southward IMF, i.e. when below the threshold $B_z = 0$. Since we know that strongly negative values of B_z correlate with higher reconnection rates at the dayside magnetopause [*Komar and Cassak*, 2016] we look at how this could relate to the generation of magnetospheric ULF waves.

Bursty reconnection has been associated with the formation of magnetic flux tubes called “flux transfer events” (FTEs) which contain the reconnected field lines and constitute a plasma entry mechanism to the magnetosphere. They have long been considered a potential source of magnetospheric ULF waves [*Russell and Elphic*, 1978], and simultaneous observations of FTEs and 2-7 mHz waves in the magnetosphere were first made by *Glassmeier et al.* [1984]. The details of this mechanism were described in more detail by *Gillis et al.* [1987], who also estimated that the resultant waves would be in the 2-22 mHz range. The draping of the magnetospheric magnetic field around a flux tube results in a local increase in the magnetic field outside the event [*Paschmann et al.*, 1982; *Farrugia et al.*, 1987] as confirmed by observations of FTEs perturbing the magnetosphere as they propagate [*Liu et al.*, 2008]. If we consider the plasma to be compressible then we would also expect to see accompanied local increases or decreases in the density outside the flux tube as it propagates along the magnetopause. This

movement has a rippling effect on the magnetospheric boundary and as the flux tube is pulled along tailward, driving fast mode waves in the magnetospheric plasma which propagate inwards and can couple with the field line to drive standing waves.

While we are studying external drivers here, we also note that the IMF B_z may additionally characterise ULF waves driven by substorms such as those generated directly by bursty bulk flows, by velocity shears in these flows or from instabilities arising from the new particle distributions [e.g., *McPherron*, 2005, and references within]. However, they would be associated with a time lag rather than our instantaneous interval [*Cowley and Lockwood*, 1992] and are also from a short-lived source compared to external driving sources. As we are averaging over hour timescales and using dayside data, we therefore consider the ULF power increase with B_z to predominantly represent flux transfer events rather than substorm activity.

5.7.6 Distinguishing potential driving mechanisms from the dominant solar wind parameters

It remains to establish which mechanisms the parameters v_{sw} , $B_z < 0$ and δN_p represent as we have only considered them individually, not as a whole, and we have not discussed their interdependence.

The dependence of ULF wave power on δN_p could provide evidence for either a Rayleigh-Taylor instability or a pressure (i.e. density) perturbation contribution. For the RTI we would expect to see additional growth rates of boundary instabilities which are already dominated by v_{sw} . Instead we believe δN_p represents the pressure perturbation theory as there is clear evidence of this acting as an individual mechanism; there have been observations of the same discrete frequencies in both solar wind pressure oscillations and magnetospheric ULF waves [*Kepko and Spence*, 2003]. If there is an extra contribution from the Rayleigh-Taylor mechanism it is subordinate to the others discussed in this paper; it is also possible that RTI contributions do not show up due to our hour timescale. Future work could investigate the necessary timescale.

It has been theorised that the number density affects the Kelvin-Helmholtz instability condition [*Engebretson et al.*, 1998], but we saw no increased ULF wave power for N_p once we accounted for δN_p . We believe that similar to the Rayleigh-Taylor effect, the additional instability growth does not contribute as much to ULF wave power as other mechanisms and so cannot be resolved.

In Section 5.7.4 we discussed the difficulty in characterising ULF drivers that arise downstream of L1, for example near the bow shock and from waves generated by magnetosheath instabilities. This processing has been shown to affect ULF waves but as events such as hot flow anomalies are relatively rare, occurring ~ 3 times a day

and lasting a few minutes [*Schwartz et al.*, 2000], they are unlikely to show up in our statistical analysis over fifteen years. We consider it possible that such processing is a factor in the δN_p contribution observed here, but exploring the role of bow shock and magnetosheath processes in this context is beyond the scope of this study.

It has previously been noted that FTEs propagating along the magnetopause share several properties with Kelvin-Helmholtz waves [*Kavosi and Raeder*, 2015] and appear very much like the ripples resulting from solar wind pressure oscillations [*Sibeck*, 1990]. These have already been established as distinct phenomena [e.g., *Lockwood*, 1991; *Song, P. Le, G. Russell*, 1994; *Otto et al.*, 1995] and now, with our study of the causal parameters, it appears that they individually contribute to ULF wave power near $L \sim 6.6 R_E$. However, it is difficult to compare the relative contributions of each mechanism using just the three parameters v_{sw} , $B_z < 0$ and δN_p as they share solar wind parameter dependencies. In addition to this, these mechanisms can interfere with each other. For example, while the strongest controlling factor for FTE formation is B_z [*Kuo et al.*, 1995; *Russell et al.*, 1996] and while the separation time of FTEs appears to be independent of our causal parameters [*Wang et al.*, 2006], the magnetic amplitude of FTEs is weakly dependent on solar wind dynamic pressure and the rate of propagation of FTEs will depend on both the magnetic curvature force on reconnected field lines and the solar wind speed. Furthermore, it has been indicated that flux transfer events and Kelvin-Helmholtz boundary waves can interact; FTEs can provide the seed for Kelvin-Helmholtz waves and propagating FTEs can interfere with the growth of Kelvin-Helmholtz boundary waves [*Hwang and Sibeck*, 2016, and references therein]. In fact, *Kavosi and Raeder* [2015] found fewer and shorter Kelvin-Helmholtz boundary waves for southward IMF. For this reason, while it is clear that for $B_z > 0$ it is Kelvin-Helmholtz waves that represent the dominant contributing mechanism, the prevalence of v_{sw} for $B_z < 0$ could indicate the dominance of either (or both) Kelvin-Helmholtz boundary waves and FTE formation and propagation as magnetospheric ULF drivers.

Note that while the magnetopause flanks are expected to be more Kelvin-Helmholtz unstable, we observed no additional contribution to power from increased non-radial flow compared to the parameters v_{sw} , $B_z < 0$ and δN_p .

We have not discussed physical properties of the magnetosphere that may affect ULF power observed at a fixed point on the ground. Particularly of relevance to this study is magnetopause location. A compressed magnetosphere will affect ground-observed power as the spatial location in the equatorial plane corresponding to any magnetometer station moves closer to the Earth, and as the distance from this point to the magnetopause decreases. For example, waves generated by a Kelvin-Helmholtz instability at the magnetopause decay with distance from the source [*Southwood*, 1974],

hence a closer source could cause increased ULF PSD measurements on the ground. *Takahashi and Ukhorskiy* [2007] discuss this as a possible cause of P_{dyn} control of ULF wave power. [*Murphy et al.*, 2015] showed that during storm times there is a clear dependence of ground-based ULF wave power on magnetopause location and also suggested that ULF wave power may become more concentrated when the volume of the magnetosphere reduces. Since the model they used ([*Shue et al.*, 1998]) depends on B_z and P_{dyn} it is clearly difficult to distinguish between the mechanisms discussed here and a simple change in the magnetopause location. We note that these dependent parameters are slightly different; N_p would be expected to correlate with P_{dyn} control of magnetopause location yet we see increased ULF wave power with perturbations δN_p rather than with N_p . Since there is evidence for ULF driving by both flux tube propagation and solar wind density perturbations as discussed above, it is likely that the action of these drivers as observed at GILL is modulated by magnetopause location. As magnetopause location is dependent on B_z and P_{dyn} (as calculated in *Shue et al.* [1998] and used in *Murphy et al.* [2015]) this makes it very difficult to determine just how much each physical process contributes to ULF wave power.

One result of interest is the clear dominance of $B_z < 0$ over δN_p , even though they represent physically very similar mechanisms; a direct deformation of the magnetopause causing perturbations of density and the magnetic field. Because we cannot know how well the parameters B_z and δN_p represent their respective mechanisms, and how much these parameters also represent modulation by magnetopause location, we cannot be certain that FTEs are truly more ULF-effective than solar wind density perturbations. It is possible that not all perturbations δN_p are ULF-effective and so their apparent parameter contribution is diminished, or it may be that broadband power δN_p is not the most relevant method of considering density perturbations. We suggest that further work is necessary to more precisely quantify the contributions of all of these mechanisms, which are highly interdependent.

5.7.7 Summary of contributing mechanisms

We conclude that the three dominant external generation mechanisms for magnetospheric ULF waves are the (1) Kelvin-Helmholtz instability, (2) the formation and/or propagation of flux tubes and (3) direct driving by solar wind density perturbations, which result from solar wind structures rather than coherent compressional plasma waves in the solar wind, and may also include processing downstream of L1. For $B_z > 0$ it is likely that Kelvin-Helmholtz waves are the dominant ULF drivers, while it is unclear whether this holds for $B_z < 0$ as FTEs share many driving parameters with (and interact with) Kelvin-Helmholtz waves.

Idealistic cartoon of the main driving processes

All these proposed mechanisms directly involve deformations of the magnetopause. They are all depicted idealistically in Figure 5-16. In (a)-(d) the Kelvin-Helmholtz instability grows from an initial perturbation. The velocity shear between the magnetosphere and the faster solar wind means that this mode is unstable; troughs deepen whilst peaks grow. Compressional waves are launched in the magnetosphere which propagate inwards, while eventually the instability develops into vortices. Panel (e) depicts the direct driving of compressional waves by a proton number density perturbation (note that while the arrow points “downstream” along the magnetopause, there must be a velocity component normal to the magnetopause for any deformations to occur). A region of more dense plasma perturbs the magnetospheric boundary and the resulting compression of the magnetospheric magnetic field is propagated inwards. Similarly in (f), a flux tube is shown as a rigid cylinder propagating along the magnetopause. The draping of the magnetic field around this tube as it travels launches Earth-bound compressional plasma waves. In reality these mechanisms may well co-occur and interact, and their effectiveness will be moderated by magnetosphere configuration such as the location of the magnetopause.

5.8 Discussion of causal parameter results

Previous studies using ground-based magnetometers have concentrated on the dependence of ULF wave power as a function of L-shell and MLT [e.g., *Mathie and Mann*, 2001; *Pahud et al.*, 2009]. In this chapter, we have adopted a different approach in order to first identify the dominant driving mechanisms. We have accounted for solar wind parameter interdependencies; controlling for v_{sw} clearly reveals the ULF wave power dependence on δN_p and B_z . *Wolfe* [1980] is an early example of a similar approach, using stepwise multiple regressions to identify that v_{sw} is the dominant parameter and that N_p is a likely second. However, they could not deconvolve the nonlinear relationship between v_{sw} and N_p with their limited amount of data, in contrast to the large dataset available here. A regression approach also assumes a continuous relationship between two parameters, whereas here we found a distinct threshold at $B_z = 0$. More recently, *Baker et al.* [2003] compared FLR and non-FLR characteristics and found that v_{sw} , N_p and B_z affected near-monochromatic ULF wave activity in the form of field line resonances (FLRs). However, they discounted N_p as to first order, any N_p contribution was due to an anti-correlation with v_{sw} . *Baker et al.* [2003] also found that $B_z > 0$ had a slightly stronger effect than $B_z < 0$, unlike in our analysis. The reason for this discrepancy is unclear, although it is possibly due to the fact that they focused

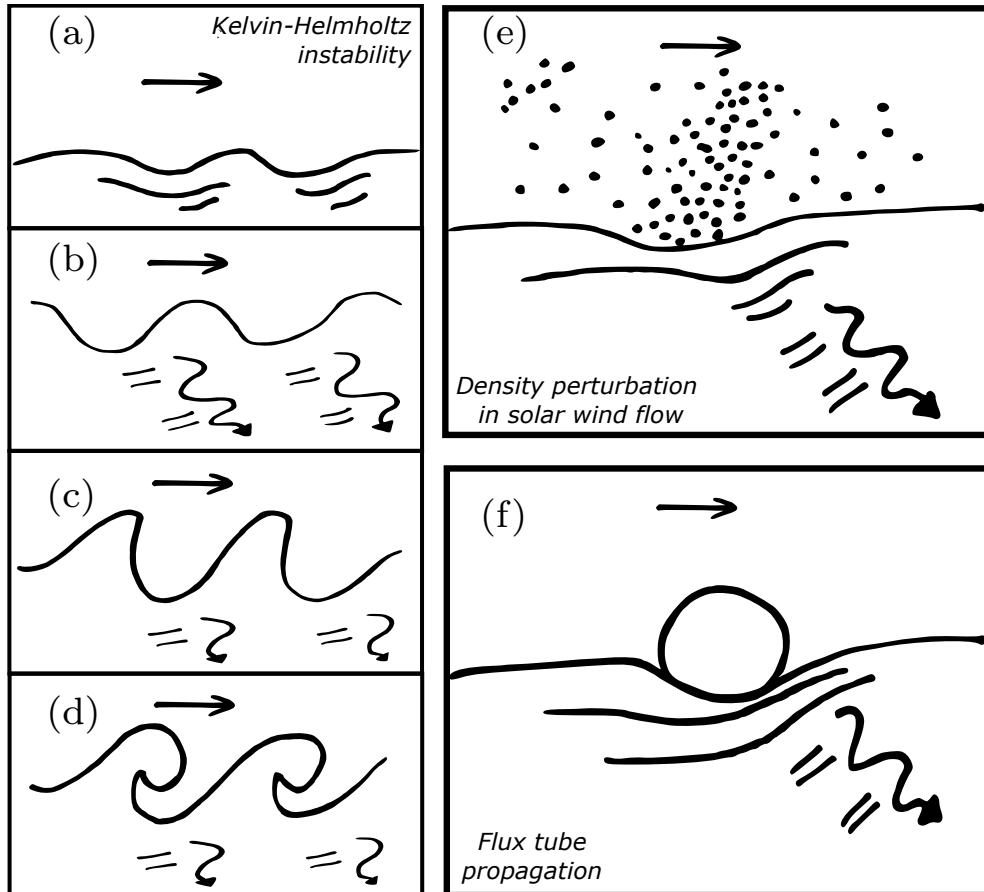


Figure 5-16: The three main driving mechanisms by which the solar wind directly gives rise to magnetospheric ULF waves, depicted idealistically. In (a)-(d) the Kelvin-Helmholtz instability grows from an initial perturbation. Panel (e) depicts the direct driving of compressional waves by a proton number density perturbation in magnetosheath flow, where there is a velocity component normal to the magnetopause. In (f), a flux tube is shown as a rigid cylinder propagating along the magnetopause. These are idealistic descriptions of processes which probably interact in a complicated manner.

on field line resonances and near-monochromatic activity where we have considered all ULF activity at 2.5 mHz. Indeed, the differences noted in *Baker et al.* [2003] for FLR versus non-FLR ULF wave activity indicates future work is needed on their respective generation mechanisms and subsequent propagation. *Simms et al.* [2010] used path analysis to control the interdependencies between nonderived solar wind parameters affecting a ULF wave index and found v_{sw}, B_z to be the main parameters with an additional contribution from Dst and variations in number density and IMF. In contrast, we too found $v_{sw}, B_z < 0$ and δN_p to dominate ULF power but could not resolve any additional δB contribution. We also found that the B_z contribution has an onset threshold at $B_z = 0$. Our comprehensive and systematic analysis of all non-derived parameters has shown that nonlinear solar wind interdependencies do indeed impact the resultant parameters correlating with power. In general our results match those of other ground-based studies, with v_{sw} the dominant driver around geosynchronous orbit. While *Takahashi et al.* [2012] found that the dominant driver switched to variations of P_{dym} at lower L-shells, we do not extend to these L-shells in this study.

Baker et al. [2003]; *Pahud et al.* [2009]; *Takahashi et al.* [2012] found that ULF wave dependence on solar wind parameters varied with MLT. Throughout this work we have focused on 3-21 MLT, but have confirmed these results for individual MLT sectors, which can be found in the supplementary materials of *Bentley et al.* [2018]. To summarise, we find some minor differences between non-midnight sectors (dawn, noon and dusk) but the same parameter dominances $v_{sw}, B_z < 0$ and δN_p . We find the same parameters v_{sw}, B_z and δN_p for the midnight sector but the threshold $B_z = 0$ does not hold. These figures are not shown here as we intend to confirm these results quantitatively using the statistical model developed in Chapter 6.

In this study we chose to examine only instantaneous power. Using time lags would allow us to account for substorm contributions, which we expect to correlate roughly with time-lagged B_z [*Cowley and Lockwood, 1992*], as substorm onset can be described using a probability distribution [*Freeman and Morley, 2004*]. However, it would be difficult to properly account for time-lagged interdependencies, particularly as solar wind properties change with the solar cycle. For example, solar wind speed persists for several hours while B_z does not [*Lockwood et al., 2016; Owens et al., 2017*]. Similarly, to include the initial state of the magnetosphere we would need to know more about the persistence of existing ULF waves. Therefore using instantaneous magnetospheric ULF wave power eliminates these questions by “averaging” over any previous history. Furthermore, we expect an hour timescale to be sufficient time for the generation of ULF waves by the external sources discussed in Section 5.7. Future work could involve the development of a more sophisticated approach to determine optimal

time lags while controlling solar wind parameter interdependencies. Additionally, the interactions between these proposed drivers and the role of magnetosheath processes could be explored.

We have produced manageable results by using only a single frequency at a single station (and therefore at a narrow range of L-shells) over dayside magnetic local times. A brief look at the results for other stations, other frequencies and the geomagnetic east-west co-ordinate provides the same qualitative results (i.e. the same causal parameters in the same order of dominance). The development of a quantitative approach to compare these meaningfully will be greatly simplified by the use of the three parameters established here. It is clear that the inclusion of these subordinate parameters is important; for example, the observed ULF wave power spectral density for $v_{sw} = 600$ km s⁻¹ and $B_z > 0$ nT is comparable to a speed of only 400 km s⁻¹ if $B_z = -7.5$ nT.

5.8.1 Summary

We have performed a systematic and comprehensive series of straightforward two-parameter comparisons to identify the dominant solar wind parameters (measured near L1) contributing to magnetospheric ULF wave power. Since speed v_{sw} dominates, we begin by examining power spectral density as a function of v_{sw} and each parameter X to determine whether each X is a potential contributing parameter, then examine all remaining parameter relationships iteratively, as explained in Figure 5-1. This method accounts for interdependencies between parameters, revealing subordinate contributions which we have used to consider physical processes by which ULF waves can be generated. Our main results are as follows:

1. ULF wave power increases for increasing v_{sw} , strongly negative $B_z < 0$ and increasing perturbations δN_p . All three parameters contribute significantly to the total power.
2. Considering interdependencies is important: in particular we find that δN_p contributes to ULF wave power rather than N_p . Interdependence is difficult to sort out as the relationships between parameters are not simply linear. Furthermore, the ULF driving mechanisms themselves are also highly interdependent.
3. We find we must consider hours with $B_z < 0, B_z > 0$ separately and this may be necessary elsewhere. There are no such onset thresholds for v_{sw} and δN_p contributions to ULF wave power.
4. We conclude that the three dominant external generation mechanisms are the Kelvin-Helmholtz instability, flux tube events during bursty reconnection and

solar wind density perturbations deforming the magnetopause. For northward IMF ($B_z > 0$) the KHI is the dominant mechanism. For southward IMF it is unclear whether the KHI or FTEs are dominant, although both are more ULF-effective than solar wind density perturbations. It is unknown how magnetopause location modulates the effectiveness of these processes.

5. ULF-effective solar wind density perturbations can be attributed to solar wind structures (spatial variations in the solar wind sweeping past) rather than compressional waves originating in the solar wind. We have not considered the processing of these variations between L1 and the magnetopause.

Our straightforward but systematic approach has focused on controlling the assumptions and examining which driving parameters can be ruled out. This reduction to three main parameters and three main external driving mechanisms can be used to discover more about the physical processes involving magnetospheric ULF waves and to predict power in the radiation belts.

We have observed that simple parameterisations dependent only on v_{sw} cannot fully describe the magnetospheric ULF wave power because δN_p and B_z both represent significant contributions. Therefore to be able to characterise ULF wave power fully we will need to consider the effects of multiple physical mechanisms acting simultaneously; a flip to B_z southward or a sudden compression region striking the magnetosphere will result in higher ULF power observed in the radiation belt region. While v_{sw} predominantly determines the magnetospheric ULF wave power, the additional contribution of masked subordinate mechanisms is significant and needs to be considered if we are to be able to predict ULF wave power and hence properties of the electron population near geostationary orbit.

CHAPTER 6

PROTOTYPE MODEL

With the driving solar wind properties identified, it remains to construct a model of ULF wave power suitable for the goals outlined in Chapter 1. To satisfy the requirements of improved radiation belt diffusion modelling, the azimuthal and radial variation of ULF wave occurrence throughout the magnetosphere need to be addressed. We choose to construct a probabilistic model in order to characterise uncertainty in radial diffusion coefficients. This will allow us to identify model requirements most requiring improvement, address the large differences between radial diffusion coefficients currently in use [*Liu et al.*, 2016; *Ali et al.*, 2016] and also describe the natural variability inherent to complex systems. The work presented in this chapter is drawn from work accepted in Space Weather [*Bentley et al.*, 2019], and data published in the Reading Research Data Archive [*Bentley*, 2019].

In this chapter we discuss the method of construction of a statistical map of ground-based ULF wave power, parameterised by physical properties that have been demonstrated to causally correlate with power ([*Bentley et al.*, 2018], Chapter 5). Here, “causally correlated properties” are properties whose correlation to ULF power cannot be attributed to covariance with other solar wind parameters. The probabilistic model we outline can be used to estimate the uncertainty in predictions of ULF wave PSDs. We will show that the conditional probability distributions resulting from this parameterisation can be approximated by a family of normal distributions whose mean and variance values make a “good” parameterisation. We discuss possible uses and testing of such a probabilistic model and in future we also intend to use this to investigate the underlying physics of ULF generation and propagation, which will be discussed in Chapter 7. In this chapter is also included a review of other difficulties in the calcu-

lation of radial diffusion coefficients, in addition to the uncertainty in the underlying model of ULF wave power occurrence.

6.1 Model construction

To construct this statistical wave map we continue to use the solar wind and ground-based magnetometer data as detailed in Section 4.2. Here, we use all stations and MLT sectors.

In the previous chapter we identified three near-instantaneous solar wind properties that are causally correlated with ULF PSD: solar wind speed v_{sw} , interplanetary magnetic field $B_z < 0$ and summed perturbations in number density across 1.69 – 6.79 mHz, δN_p [Bentley *et al.*, 2018]. The method used to identify these properties accounts for skewed data distributions and solar wind interparameter relationships by deconvolving the contribution of each individual solar wind parameter to ground ULF wave power from the relationship with other correlated solar wind parameters. Hence these solar wind properties are each directly related to the occurrence of ULF wave power. In this chapter we demonstrate the construction of a parameterisation using the three solar wind parameters above, with the expectation that further parameters such as geomagnetic activity, magnetospheric plasma density distribution, substorms, time lags and history of the magnetosphere will be added as necessary in future. In this work we choose to use $var(N_p)$ in place of δN_p as it is equivalent in the analysis method of Chapter 5 but is simpler to use. To demonstrate this equivalence, the two-parameter plot for $var(N_p)$ and speed v_{sw} is shown in Figure 6-1(a). The change in ULF wave power is very similar to for v_{sw} and δN_p in Figure 5-10. The relative contribution of $var(N_p)$ and δN_p to ULF wave power in a single solar wind speed bin is shown in Figure 6-1(b). ULF wave power increases with both $var(N_p)$ and δN_p ; they are equivalent descriptions of the driving property.

6.1.1 Partitions of the magnetosphere

To capture the changing behaviour of ULF waves in different regions of the magnetosphere, we define a set of nested bins. We call the magnetospheric bins “partitions”, which depend on frequency, azimuthal angle (i.e. magnetic local time) and radial location (i.e. L-shell, determined by station latitude). These are reviewed in Table 6.1. The parameterisation using three solar wind properties is performed separately in each partition, so that our final empirical model is dependent on the solar wind, the region of the magnetosphere, and wave frequency. For the remainder of this chapter, “bins” will solely refer to the nested solar wind parameter bins nested in each partition.

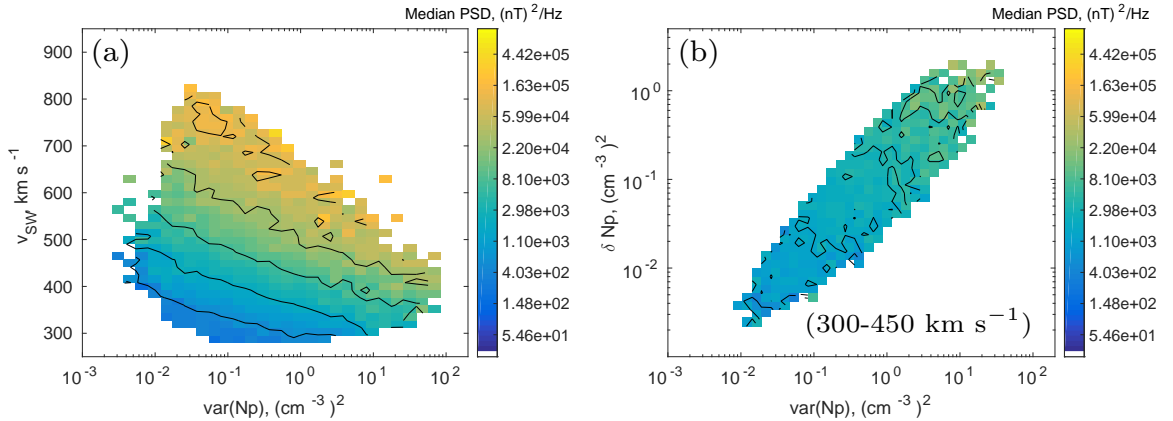


Figure 6-1: A pair of two-parameter plots following those in Chapter 5. Power at GILL station, 2.5 mHz, from 1990-2004 is binned by (a) solar wind speed v_{sw} and variance of proton number density $var(Np)$, and (b) by summed power in number density δNp and variance in number density $var(Np)$ for a single solar wind speed bin 300 – 450 $km\ s^{-1}$. In each bin in the two-parameter plots, the median ULF wave power is shown.

We choose to cover frequencies from 0.8 to 20 mHz. This extension to higher frequencies than those covered in Chapter 5 is intended include more frequencies that may still be of interest to radial diffusion. Once in the statistical model, they can be removed later. Lower frequencies contain the most power but as the power tends to drop off gradually with frequency (Figure 5-1 (a)), we can choose an arbitrary upper limit that contains most of the power. Therefore we also include higher frequencies in order to examine their contribution. The dataset is already discretised by radial location and frequency (due to the use of different ground magnetometer stations and our PSD calculation) and we subdivide the data further into four MLT sectors centred at dawn, noon, dusk and midnight. Use of four sectors allows us to resolve azimuthal variations while retaining enough data to construct a parameterisation. In addition, we split the data at $B_z = 0$ as Section 5.6 indicates that the physical processes either driving or propagating ULF waves differs for $B_z > 0$ and $B_z < 0$. This will aid future analysis of the physics. The full L-shell ranges corresponding to the four magnetometer stations FCHU, GILL, ISLL and PINA over this time period can be found in Table 1 of *Rae et al.* [2012].

Therefore in total we have $4 \times 69 \times 4 \times 2 = 2208$ partitions. In each of these, we parameterise ULF wave power using $v_{sw}, B_z < 0$ and $var(Np)$ bins. In this chapter we present and test the results of the ground based geomagnetic north-south component in order to validate our approach. The east-west component is also included in the dataset. Together, these comprise the magnetospheric toroidal and poloidal modes

Table 6.1: Parameters used to discretely partition statistical ULF wave model

Parameter	Values	num. values
Radial L-shell (Station latitude)	Four stations FCHU, GILL, ISLL and PINA ($L \sim 7.94, 6.51, 5.40, 4.21$)	4
Frequency	0.83 – 20 mHz	69
Azimuthal angle (MLT)	Dawn, noon dusk and midnight (3-9, 9-15, 15-21 and 21-3 MLT)	4
$B_z = 0$ threshold	$B_z > 0$ and $B_z < 0$	2

These parameters define the separate partitions. Solar wind properties v_{sw} , $B_z < 0$, $var(Np)$ are used in each partition to parameterise the power observed.

[Elkington, 2013] plus some mixing. The final, perpendicular component represents the compressional mode and is not included.

6.1.2 Parameterisation in each partition

The model in each partition is constructed by binning ground-based ULF wave power by the corresponding solar wind properties. We remove the 0.1% most extreme solar wind values to improve data resolution, (i.e. the lowest and highest 0.05% values). This results in a parameter space where the ends bins are not unnecessarily large and empty. The relevant ranges are velocity: 282 to 783 km s⁻¹, variance of proton number density: 0.0038 to 42.814 cm⁻³ and B_z : -12.3 to 11.5 nT. From this point onwards we use $\log_{10}(var(N_p))$ instead of $var(Np)$ in order to work with linear scales in our parameterisation. Bins are equally spaced on this linear scale and are the same in each partition.

In any one partition (i.e. for one station, MLT sector, frequency and for $B_z < 0$ or > 0) we determine conditional probability distributions of ULF wave power given observations of solar wind properties v_{sw} , $\log_{10}(var(Np))$ and B_z . We bin observed power into a 10x10x5 grid, and examine the distribution of $\log_{10}(PSD)$ in each bin. Since we split at $B_z = 0$, the B_z dimension only has 5 bins instead of 10. For each partition, this creates a 3d look-up table of probability distributions that are parameterised by the solar wind observations. These are therefore conditional probability distributions as they express the probability distribution given a particular set of solar wind properties. The distribution of $\log_{10}(PSD)$ in each bin is approximated with a normal distribution, by fitting a normal to the log-power observed in each bin containing at least 10 points. While the majority of bins contain distributions of log-power that are

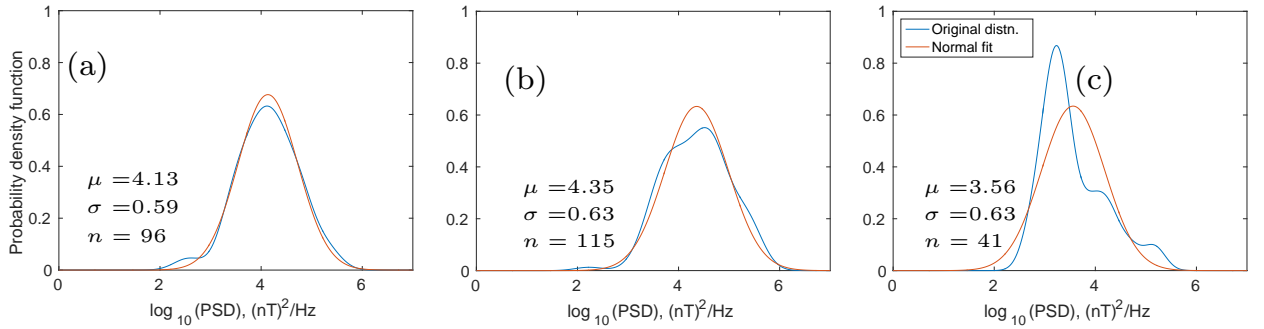


Figure 6-2: The original and normal (fitted) distributions of logpower in three example bins from the GILL station at $L \sim 6.6R_E$, 3.33 mHz, with $B_z < 0$ in the noon sector; the three distributions most likely (a), highly unlikely (b) and least likely (c) to be drawn from a normal distribution, with chi-square p-values of $p = 0.95, 0.13, 0.01$ respectively. Bin (a) is centred at $v_{sw} = 558 \text{ km s}^{-1}$, $\log_{10}(\text{var}(Np)) = -0.059 \text{ cm}^{-3}$, $B_z = -1.23 \text{ nT}$. (b) is centred at 608 km s^{-1} , -0.999 cm^{-3} , -1.23 nT and (c) is centred at 407 km s^{-1} , 0.620 cm^{-3} and -1.23 nT . For each bin, the mean μ and standard deviation σ of the distribution of the n points in that bin are shown.

technically statistically distinct from normal distributions, they are nonetheless reasonable approximations. In Figure 6-2 we show example distributions from three bins in a single partition; a probability distribution that is highly likely to be drawn from a normal distribution as measured using a chi-square goodness of fit test (panel (a)) and two others that are far less likely (b) and highly unlikely (c). While all three may not be exactly normally distributed, this makes a reasonable approximation, with the arguable exception of (c). However, even for this poor fit, a normal approximation is preferable to having nothing in this bin. The poor fit of Figure 6-2 (c) indicates how uncertainty can enter PSD prediction when underlying approximations (here, the log-normal assumption) are less valid. Examining where these fits are good approximations is an example of the future analysis that can be done to investigate the physics, as the type of distribution may provide insight into the underlying physical processes.

Constructing a distribution for each bin in a given partition provides multiple benefits compared to simply taking the mean or median; firstly, if we choose to use the mean or median in future we retain information about the range and variance. Secondly, we are able to then use these distributions for probabilistic forecasting. We note that as the distribution in each bin describes the occurrence of ULF wave PSD depending on the solar wind conditions, this is a set of conditional probability distribution functions, which allows us to explore the physics of ULF occurrence in new ways. By approximating these probability distributions as lognormals we can use this information relatively cheaply, as for every single bin in a given partition we need only store the mean and

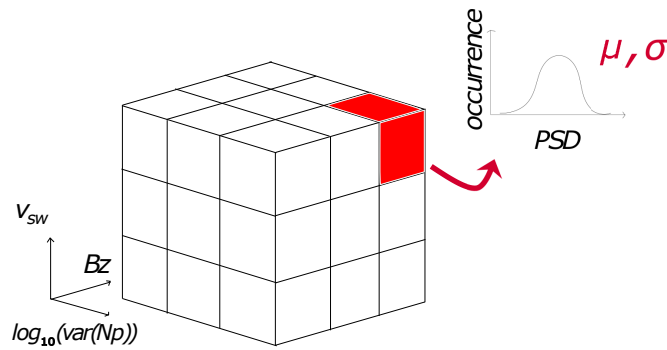


Figure 6-3: A visualisation of our parameterisation for each station, magnetic local time sector and frequency partition. Using a 3-d grid with solar wind speed, variance of proton number density and interplanetary magnetic field axes, ground-measured ULF wave log-power is binned and the corresponding probability distributions (a family of normal distributions) are used to model the power. We use 10, 10 and 5 bins for each solar wind parameter respectively in the model.

variance of each normal distribution of log-power rather than the entire distribution.

6.2 Example: using this model

We have produced a series of look-up tables which, for each partition (station/freq/MLT/ $B_z < \text{or} > 0$), contain a family of normal distributions parameterised by the near-instantaneous solar wind properties. Figure 6-3 illustrates this; we can use the bins nested in each partition to look up the distribution function of ULF PSD values for a given solar wind speed, variance of proton number density and B_z observed in the solar wind (i.e. conditional probability distribution functions). Hence at each point in time this model can be used in two ways; given the solar wind observations, we can look up the corresponding conditional probability distribution and either use the expectation value (i.e. the mean) of the distribution, or sample the entire distribution. Sampling will randomly obtain PSD values drawn from the probability distribution in a given bin. With many such samples, the distribution of our predicted values will converge towards the original distribution in that bin. In this way, time series of reproduced power can then be built up an hour at a time, either deterministically (i.e. using the mean) or stochastically (by sampling).

To help visualise our model, the mean value in each magnetospheric partition is shown in Figure 6-4 for a selection of frequencies, in a single solar wind bin centred at $[v_{sw}, \log_{10}(\text{var}(N_p)), B_z] = [507 \text{ km s}^{-1}, -0.998 \text{ cm}^{-3}, -3.69 \text{ nT}]$. There are clear variations with MLT sector and station, which will be investigated once we have tested the ability of the model to reproduce ULF wave power, both overall and for time series.

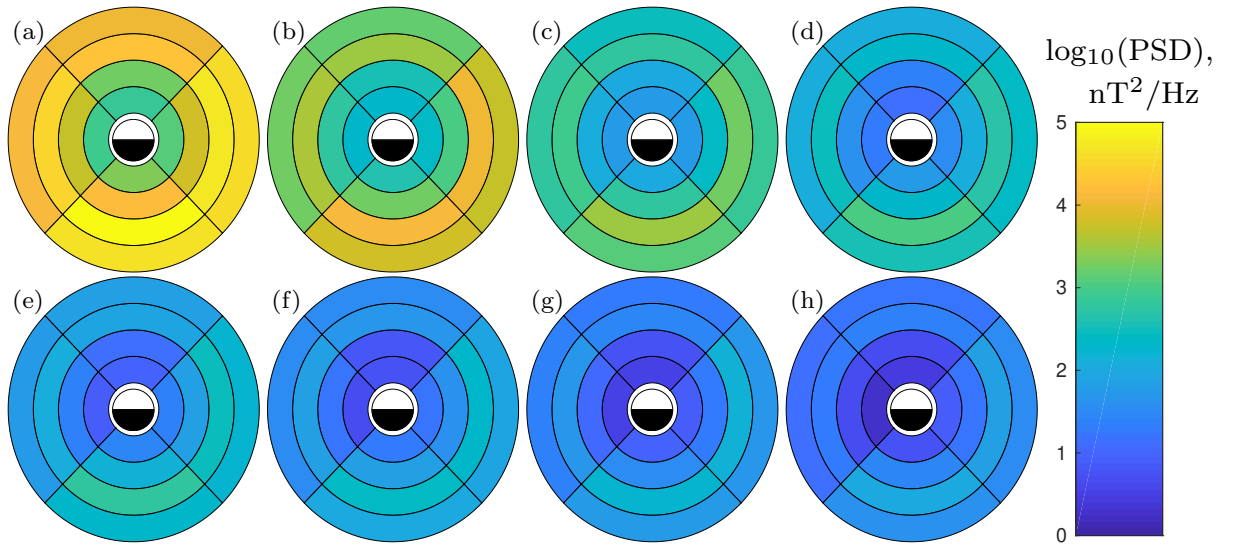


Figure 6-4: The mean value of \log_{10} -power in our statistical model throughout the magnetosphere for increasing frequency in a single solar wind bin centred at $[v_{sw}, \log_{10}(\text{var}(Np)), Bz] = [507 \text{ km s}^{-1}, -0.998 \text{ cm}^{-3}, -3.69 \text{ nT}]$. In each image, four MLT sectors are shown (noon (north), dusk (west), midnight (south) and dawn (east)) and four radial locations corresponding to PINA, ISLL, GILL and FCHU (from centre to edge). Mean PSD values are shown for frequencies (a) 2.5 mHz, (b) 5 mHz, (c) 7.5 mHz, (d) 10 mHz, (e) 12.5 mHz, (f) 15 mHz, (g) 17.5 mHz and (h) 20 mHz.

An example reproduced hourly times series can be found in Figure 6-5 where we show the solar wind speed v_{sw} , variance in number density $\log_{10}(\text{var}(Np))$, B_z and the original and reproduced log-power measured at GILL station, 3.33 mHz, for two weeks in May 2001. We also show the number density Np for reference. The reproduced power shown in (e) can be found by using the mean values in each look-up table (orange) or by sampling. For the sampling method, 2000 time series were constructed and for each hour in Figure 6-5 the blue sleeve indicates the the interquartile range of samples taken. This time period was chosen for the variety of solar wind speed conditions; however, the few gaps in our reproduction also highlight some areas of our model that can be improved. These gaps are primarily due to data gaps in the solar wind observations in variance of number density (absent $\sim 15\%$ of the time from 1990-2005 when OMNI data is supplied for v_{sw}, Bz) and also due to too few observations in the more extreme bins, preventing us from determining the underlying probability distribution. We anticipate that these will be addressed using additional solar wind observations and/or Np correlations for the former, and additional years of data and/or extrapolations for the latter. More simply, approximations could be made using only v_{sw} and Bz . In Figure 6-5(e) it can be seen that the observed and reproduced log-power

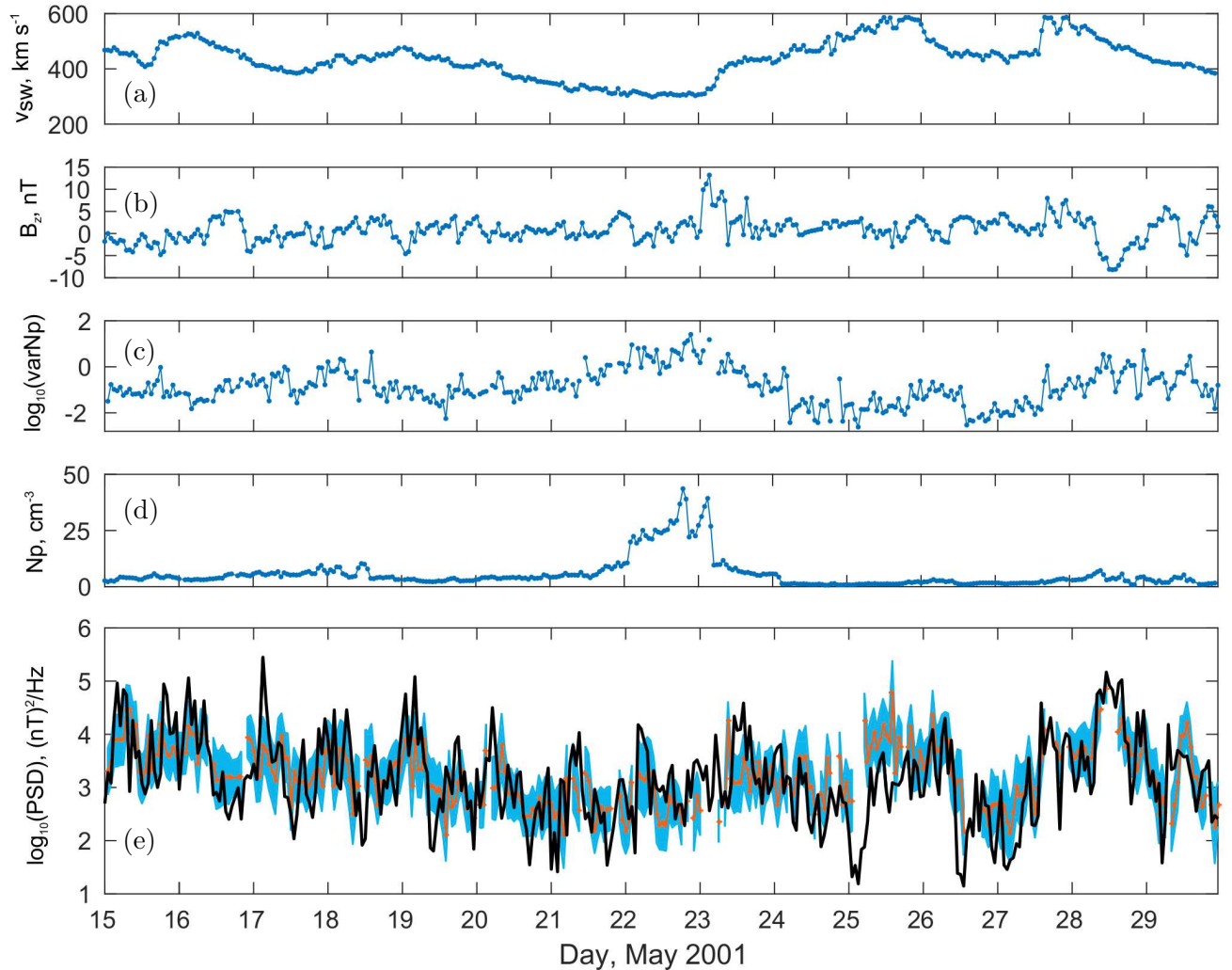


Figure 6-5: Using instantaneous solar wind speed v_{sw} (a), southward interplanetary magnetic B_z (b) and variance in proton number density $\log_{10}(\text{var}(Np))$ (c), the power spectral density observed across all MLT sectors at a single station and frequency (GILL, 3.33 mHz) can be reproduced using a family of normal probability distributions parameterised by solar wind properties. Panel (e) shows the original power time series (black) and power reproduced using our model, either by taking the mean of the probability distribution given the observed solar wind values (orange) or by sampling from that distribution multiple times (the interquartile range of 2000 samples is shown in blue). Panel (d) shows the proton number density in the solar wind for reference.

roughly follow each other. Overall the model appears to have performed exceedingly well given that it depends primarily on the instantaneous contribution of three solar wind properties, and includes no time lags or properties internal to the magnetosphere. There appears to be a diurnal variation which is captured reasonably well by the four MLT sectors used here; the relative contribution of the solar wind parameters and MLT sectors to the PSD observed throughout the magnetosphere will be considered in future work. However, first we must verify that our model is a good approximation to the original PSD observations. We discuss different metrics for testing this model below.

6.3 Testing the model

While the ability to reproduce observed phenomena is an important test of a model, other model qualities determine whether it is fit for purpose and whether it produces statistically significant results. We discuss all these qualities first, before building metrics in Section 6.3.2 to measure the ability of our model to reproduce ULF wave power observations and comparing to a similar Kp -based model in Section 4.3.

6.3.1 A “good” parameterisation

We use the following criteria to define a good parameterisation, in no particular order:

1. The parameterisation reproduces behaviour well, as measured by a relevant metric.
2. Parameters chosen are significantly related to changes in power spectral density, i.e the probability distribution of power values in neighbouring bins are distinct. Variance is minimised while the mean values are much larger and vary more.
3. Parameters are physically motivated and we can interpret their impact
4. The parameterisation can be used for nowcasting and forecasting
5. Excess parameters are excluded to avoid overfitting, as models with larger degrees of freedom are less statistically significant.

The ability of our model to reproduce observed PSD values is examined in Section 6.3.2. The importance of the second criterion is illustrated in Figure 6-6(a) and (b); the larger the variance in each bin, the more likely that neighbouring probability distributions overlap. This is a consequence of our finite amount of data, which in turn can only be binned by a finite number of parameters. With infinite data, considerable

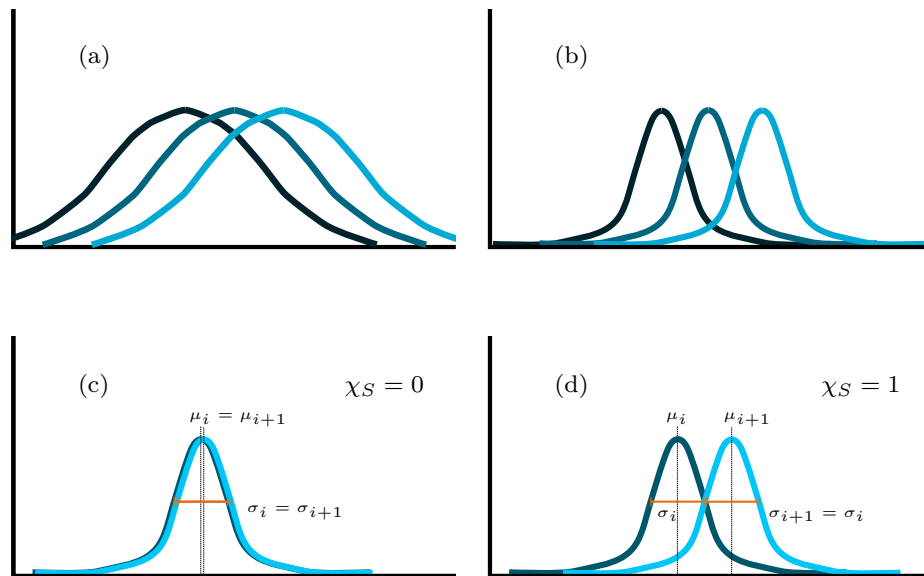


Figure 6-6: (a)-(b) An illustration of two sets of three normal distributions, which have the same three mean values but a larger (a) and smaller (b) variance. We would consider (b) a better parameterisation as there is considerably more overlap between neighbouring probability distributions in (a). (c) and (d) show the distribution overlap corresponding to separation proxy values of zero and one respectively, when the standard deviations of each distribution are roughly the same.

overlap would be fine and we could bin by all physically motivated parameters. Instead, when we can only use a finite number of parameters a clear evolution of PSD distribution across neighbouring bins suggests that the parameters chosen are significantly related to changes in PSD. Numerous overlap coefficients exist to examine the relationship between two normal distributions, but we can define a simple metric here specifically to quantify how this overlap affects the quality of our parameterisation. This metric is particularly suitable as the standard deviation of all our bins are so similar (discussed below). We use the ratio of the standard deviation in each bin to the difference in mean values; for two neighbouring bins b_i, b_{i+1} this quantity is then the separation proxy

$$\chi_S = \frac{\|\mu_i - \mu_{i+1}\|}{\langle \sigma_{i,i+1} \rangle} \quad (6.1)$$

which (as illustrated in Figure 6-6 (c) and (d)) will be zero for two completely overlapping distributions but will be equal to 1 for two distributions with equal standard deviations, where the point of overlap is exactly one standard deviation of either mean. The median values of this separation proxy between all neighbouring bins for GILL, 3.33 mHz, noon, $Bz < 0$ is 0.5 for probability distributions along the speed axis, 0.28 along $\log_{10}(\text{var}(Np))$ and 0.37 along Bz . For GILL, 3.33 mHz, noon, $Bz > 0$ these values are 0.6, 0.29 and 0.25 respectively. The magnitude of these values corresponds to the order of dominant contributing parameters $v_{sw}, Bz < 0$ and $\text{var}(Np)$ as expected and indicate that in future such a measure can be used to investigate where the solar wind parameters contribute meaningfully to changes in ULF power.

This separation proxy χ_S is very similar to the well established effect size measure Cohen's d [Cohen, 1988]. Instead of standardising the two mean values by the average standard deviation $\langle \sigma_{i,i+1} \rangle$, Cohen's d standardises by the "pooled" standard deviation which weights by the number of points in each distribution. This is unnecessary here as the normal distributions are already known to be approximations, and the uncertainty arising from that approximation should be decoupled from our separation proxy and investigated separately. However, we note that in the case where $\sigma_i = \sigma_{i+1}$, much of the existing literature on interpreting Cohen's d can still be applied here.

Indeed, the separation proxy χ_S is most meaningful where the standard deviations of all distributions are roughly the same, hence a more detailed comparison of mean and standard deviation (μ, σ) values is made for all bins at GILL, 3.33 mHz in Figure 6-7. Figure 6-7(a) shows the distribution of all σ values, which is clustered around ~ 0.7 . This can be compared to Figure 6-7(b), which shows the σ of normal distributions fitted to the same number of power values which were randomly selected from the

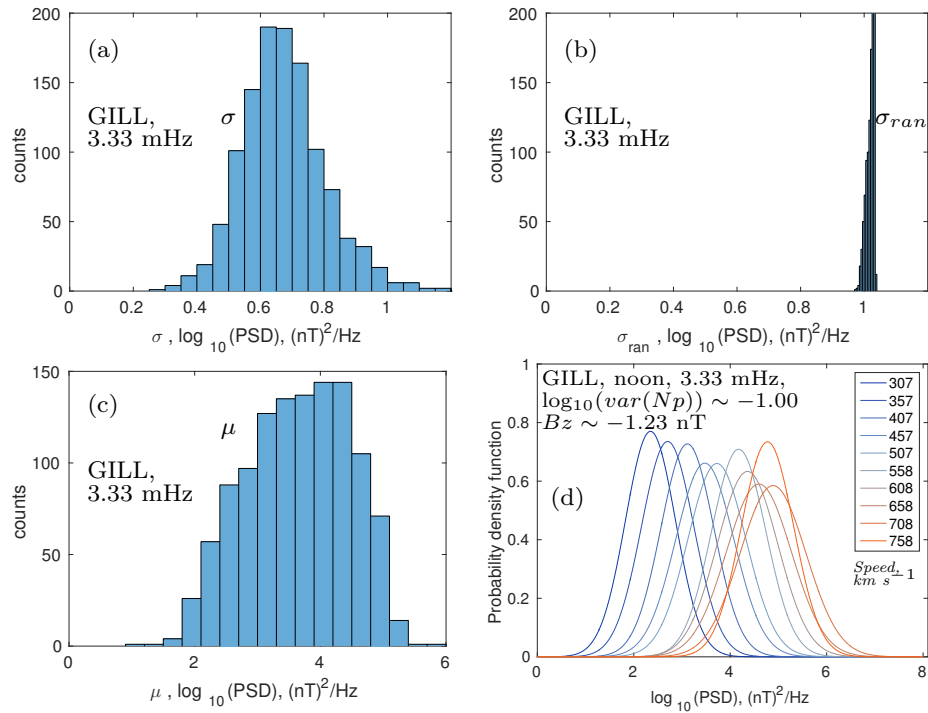


Figure 6-7: (a) the standard deviation (σ) values of the normal fitted probability distributions for all bins at GILL, 3.33 mHz. (b) the σ values of normal distributions fitted to bins of equal size as those in (a), but randomly sampled from the original distribution. (c) the mean (μ) values of the normal probability distributions, corresponding to those in (a). There is less variance in each probability distribution when binning by three solar wind parameters than in equivalent randomly sampled distributions, and this variance is small and consistent relative to the range of mean values. (d) An example of the variation of probability distributions with speed in a constant $Bz, \text{var}(Np)$ bin in a single partition.

original distribution rather than using our binning technique. (This was run 1000 times). As the variance is smaller for our parameterisation, our model is outperforming randomly selected distributions. Figure 6-7(c) shows the μ values for GILL, 3.33 mHz, corresponding to the σ shown in (a). This range of mean values indicates that the mean power (i.e. PSD, not $\log_{10}(PSD)$) varies over several orders of magnitude while the variance of each distribution is about an order of magnitude for each bin. Hence the family of probability distributions we use is better than randomly selected distributions as the variance is smaller, and the variance/mean ratio is such that changes in the solar wind parameters correspond to the probability distribution shifting up and down the power axis without changing shape. An example of this can be seen in Figure 6-7(d); the probability distributions associated with different solar wind speed values for constant $Bz, var(Np)$ bin is shown for GILL, 3.33 mHz in the noon sector, $Bz < 0$. For lower solar wind speeds the distributions are distinct, while at higher speeds they overlap. Future improvements of this parameterisation could involve identifying where such distributions should be merged using χ_S , while identifying what this corresponds to physically is one example of the future work that can be done to understand the underlying physics using this probabilistic model.

Criteria 3 and 4 reflect the intention that our model be capable of investigating existing physics and, eventually, to be capable of forecasting. For a model parameterising radial diffusion coefficients, the chosen parameters should also be clearly and significantly related to changes in the diffusion coefficients. The solar wind parameters used in this model were selected as they have been shown to be causally correlated to ground ULF wave power; a review of their physical interpretation can be found in Chapter 5. As they are drawn from solar wind observations they can be used for now-casting and forecasting. We have attempted to reduce the degrees of freedom by only using causally correlated solar wind parameters, and by using a long time period, which makes overfitting on the five parameters here (L,MLT, v_{sw} , Bz , $var(Np)$) unlikely.

6.3.2 Ability to predict ULF wave power

We anticipate that our model will be put to two main uses: calculating the total power distribution over an extended event or predicting the power for each hour in a time series. For example, the total distribution method will be useful for long timescale reconstructions where it is important to reproduce signal properties that include the overall distribution, while the time series will be useful for forecasting. Both outputs may be useful to case studies of individual events. Therefore we examine the efficacy of this model using two tests. The first (a series of violin plots) compares the total distribution of log-power from the original observed log-power to the distribution of

log-power reproduced from our model. The second test (forecasting skill) examines the ability to predict power in the oncoming hour compared to a reference model. Both these tests are completed first on sample partitions of the entire 15 years of original data and on a small set of CARISMA data from Jan-Mar 2015, i.e. we test our model on both the training data and on data outside the training window. Customarily such testing is not done on training data, however the size of the dataset compared to the few parameters we have used suggests that this is a reasonable test.

We use vertically plotted probability distribution functions (violin plots) in Figure 6-8 to compare original and reproduced probability distributions of PSD over an extended time. Here we have chosen four representative combinations of station and frequency; the frequency for each station is the average eigenfrequency over all MLT as calculated by the cross-phase technique [Waters *et al.*, 1991; Sandhu *et al.*, 2018] over several years. Hence this is a stricter test than choosing consistently “quiet” frequencies for each station. For each combination the total original power distribution (black) is compared to reproduced power using the mean of each probability distribution (right, blue) and to sampling from the probability distributions (left, blue). As the original distribution falls roughly between the interquartile range when using the sampling method, but is clearly very far off for the means method, this suggests that a sampling method is suitable for obtaining the power distribution over an extended event while the mean is not. PINA and FCHU appear to have the worst fits, which may be due to the changing plasmopause and magnetopause locations crossing these respective stations. This is an example of the latitude and MLT dependent physics we intend to explore in future. Unfortunately it is very difficult to statistically quantify the ability to reproduce these distributions without overly favouring either the centre of the distribution or the tails; we have been unable to find a suitable metric. Existing measures designed to measure the similarity of two distributions found our sampled reproductions to be either all very good or all very poor. Therefore future study is necessary to identify a metric that accurately reflects our ability to reproduce the physical distributions and that can be used as a tool to improve our model by distinguishing where fits are good or bad.

Forecasting skill is a simple measure that can be used to compare the ability of two methods to predict a time series. In space physics, it has previously been used to test solar wind predictions, e.g. Owens *et al.* [2013]. It is calculated as follows:

$$Skill = 100 \left(1 - \frac{MSE_{model}}{MSE_{ref}} \right) \quad (6.2)$$

using the mean square error (MSE) between each model and the observed values. Forecast skill scores can range from $-\infty$ to 100 and positive values indicate that the

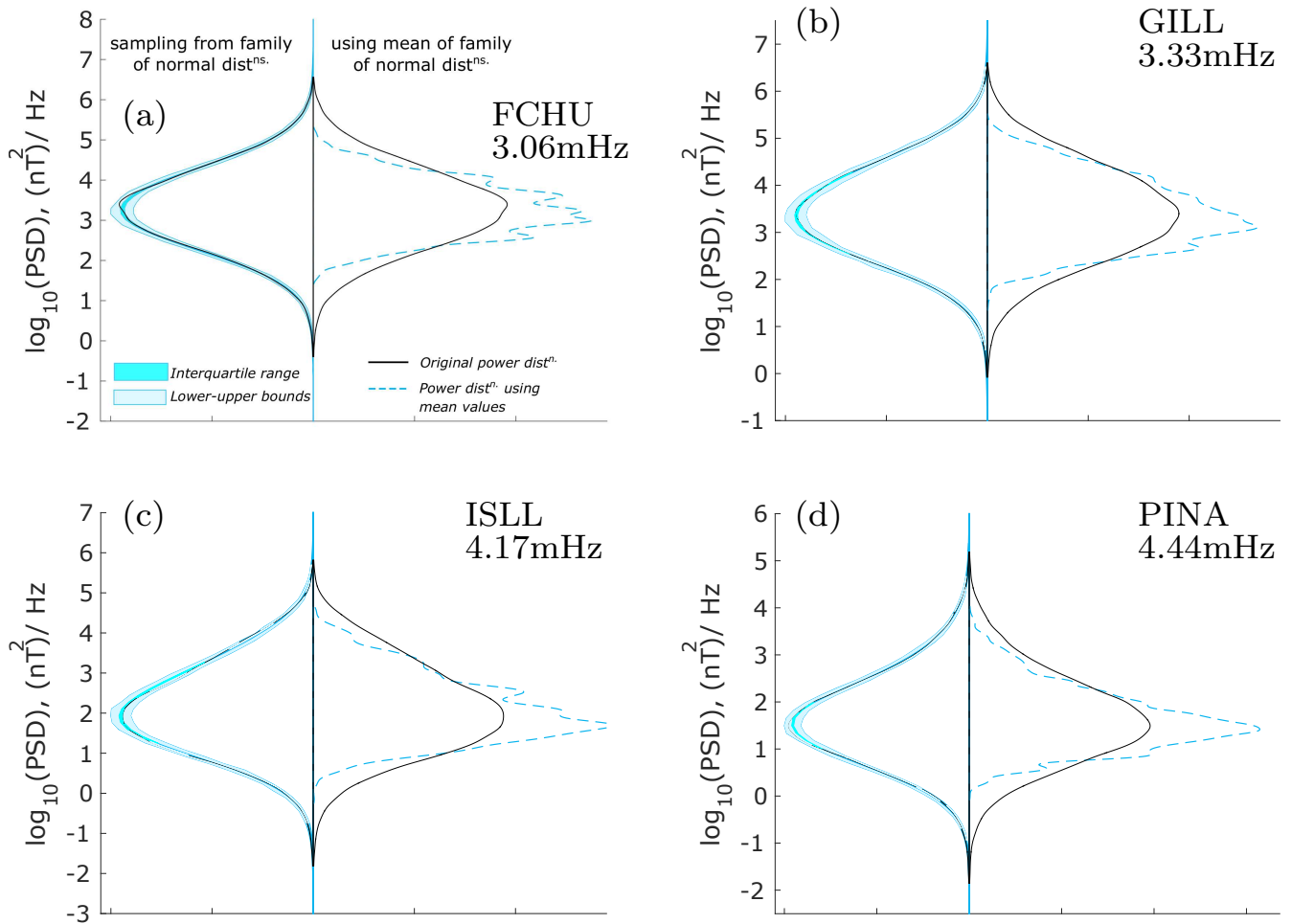


Figure 6-8: Violin plots showing the probability distribution of power over the original fifteen years of data, compared to reproduced distributions of power using the two methods possible with our model. For each hour the model defines a probability distribution of power which is dependent on solar wind conditions; this is used to reproduce the original fifteen-year distribution. The left hand side of each violin compares the original total power distribution to the reproduced distribution found by sampling from the conditional probability distribution of power for each hour, while the right hand side compares to taking the mean value of the conditional probability distribution for each hour. Black lines indicate the original distribution while the reproduced values are indicated by a dashed blue line (mean values), a blue region (interquartile range of 2000 samples) and light blue region (upper and lower bounds from sampling). This is shown for four combinations of station and frequency. Violins are all scaled so that the area under the original and reproduced distributions are equal to 1.

Table 6.2: Forecasting skill at selected stations and frequencies

Partition Tested	Model skill score vs random reference model			
	24h persistence	1h persistence	Model (sampled)	Model (means only)
FCHU, 3.06 mHz	34.9	69.1	48.7	74.6
GILL, 3.33 mHz	38.0	74.1	55.6	78.0
ISLL, 4.17 mHz	37.6	76.2	56.5	78.4
PINA, 4.44 mHz	35.3	72.7	54.8	77.6

Forecasting skill scores for four stations and frequencies, testing the ability of the solar wind parameterised model to reproduce the original fifteen years of data. The baseline reference model used is a “random” model, where power is sampled from the original total distribution of the given partition. Simple 24-hour and 1-hour “persistence” models are tested against this baseline (i.e assuming power in the oncoming hour is the same as the previous day or hour) in addition to the solar wind-parameterised model. The probability distributions predicted for each hour by the solar wind model were either sampled or the mean value was taken to construct each fifteen year time series. Where sampling methods were used, 2000 time series were made and the forecast skill calculated for each one; the median is shown here.

tested model is better than the reference model. We compare both mean and sampling methods of applying our model and two “persistence” models to a random model sampling from the entire original distribution of power, as per *Owens et al.* [2013]. The two persistence models assume that the power we see in the next hour will be the same as that observed 24 hours ago and 1 hour ago respectively. Calculating forecasting skill is relatively simple using the means or persistence method as the reproduced time series is always the same. To calculate forecasting skill for random and sampling methods, 2000 time series were constructed by sampling from either the random or appropriate normal distributions. The forecasting skill was calculated for each of these time series and the median forecasting skill of these 2000 runs taken. Results of this are shown in Table 6.2.

For all four examples, both means and sampling methods of using our model were better than randomly sampling, as expected. However, both methods were also superior to assuming 24 hour persistence and using the expected (mean) value from our look-up tables is a better predictor of power than assuming that power continues from the previous hour. For example, at FCHU 3.06 mHz, all four models tested are better than the baseline “random” model as they all have positive values. With the highest forecasting skill score of 74.6, using the mean values of each parameterised probability distribution outperforms all other models, followed by 1h persistence with a score of 69.1. Sampling from the probability distributions lags behind this with a skill score of 48.7 and 24h persistence performs least well with a score of 34.9. To confirm that this ranking is not frequency dependent, we have also calculated forecasting skill across 1990-2005 for every frequency at a single station (GILL) using a smaller number of runs, shown in Figure 6-9. Across all frequencies, the ranking of models compared to

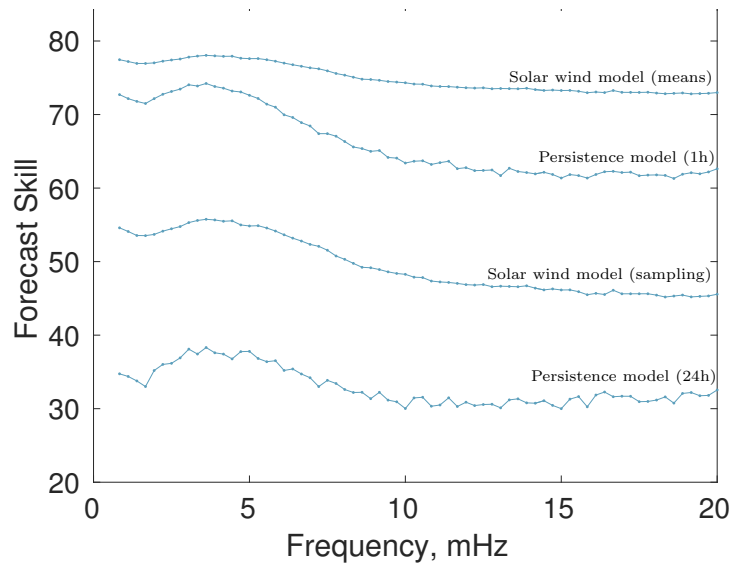


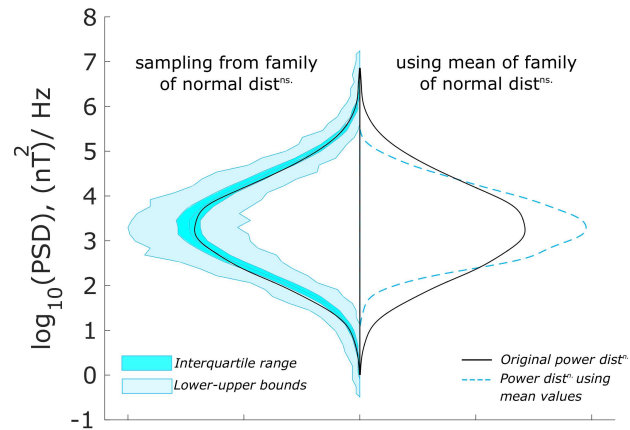
Figure 6-9: Forecasting skill at all frequencies for GILL, 1990-2005, where models are compared to a random reference model. Where any kind of sampling was used (i.e. random and solar wind model sampling), 500 runs were taken. The ranking of model types is consistent across all frequencies.

a random reference model remains the same. Hence using the mean value is the best method for reproducing a time series whereas the sampling method is outperformed by 1h persistence. However, it should be recalled that the sampling method outperformed the mean method for reproducing the total distribution (as tested using violin plots in Figure 6-8). Therefore different construction methods should be used depending on the desired output.

Similarly, we test these methods for 3.33 mHz at GILL using CARISMA data for Jan-Mar 2015 in Figure 6-10. Again, the sampling method is best for reproducing the total power distribution over these two months and the mean method is superior at predicting the power in individual hours. Note that while the sleeve between the upper and lower bound in the violin plot of Figure 6-10 is wider than in Figure 6-8, this is a slightly misleading visualisation artefact due to plotting less populated distributions, as the CARISMA data is considerably shorter. It is more important to note that the original power distribution shown in black still lies within the interquartile range of our samples. This emphasises the need for a metric that quantifies the ability of the model to reproduce total power distributions, rather than relying on visualisations.

6.3.3 Comment on other possible parameters

The parameters used so far correspond to three near-instantaneous solar wind proper-



Model skill score vs random reference model			
24h persistence	1h persistence	Model (sampled)	Model (means only)
37.3	73.8	53.9	76.7

Figure 6-10: Testing the ability of a solar wind-parameterised model to predict ground-based power not in our training set, across January-March 2015, GILL, 3.33mHz. The violin plot compares both the sampled and mean-value methods against the original total power distribution over an extended time period (as in Figure 6-8) and the forecasting skill tests the ability of models to reproduce a time series. Here we compare the performance of two persistence models and our solar wind-parameterised model (using both sampling and the mean methods) to a baseline “random” model, as described in Table 6.2. Results are very similar to the tests carried out on the training data; the sampling method reproduces the power distribution well (as the original power lies within the interquartile range of reproductions) while the mean value predicts the oncoming hour best.

ties and the radial and azimuthal location in the magnetosphere. Therefore there is no history of the solar wind or the magnetosphere, including the persistence of existing ULF waves. The method presented in this paper does not represent internal properties such as substorm activity or magnetospheric plasma density; therefore our current distributions average over all internal configurations. This is likely to contribute to the variance in each distribution and requires further study. While no internal parameters or geomagnetic indices are included, we compare our results to a Kp based model below. Finally, our selection of parameters includes no long-term dependencies, such as seasonal or solar cycle variations. It has long been understood that ULF wave activity varies with solar activity phase [Saito, 1969; Murphy *et al.*, 2011b]. An underlying assumption of this work is that such effects can be characterised by the changing solar wind parameters v_{sw} , Bz , $var(Np)$, rather than representing this changed solar output indirectly using a parameter such as F10.7. As the magnetospheric mass density also varies over a solar cycle, once internal properties have been included the ability of our chosen parameters to represent ULF wave power changes across a solar cycle could be compared to F10.7. More sophisticated methods will be necessary to add further parameters as we cannot further reduce the number of data points in each bin.

6.3.4 Comparison to Kp -based models

Existing models of radial diffusion coefficients and ULF wave PSD use Kp . We cannot compare directly to the values predicted by the Kp -parameterised ground-based empirical model of Ozeke *et al.* [2014] as our prototype model describes ground-based power instead of total power in the equatorial azimuthal field. Instead we can briefly examine the properties of a Kp -based model of ground PSD, constructed similarly to the solar wind model already presented. Ground-based PSD at 3.33 mHz, GILL is binned by the corresponding Kp value and the probability distribution function is calculated in each bin. These distributions are shown in Figure 6-11(a). By merging overlapping high Kp bins, a parameterisation could be constructed where the distributions are distinct with relatively small variance. Hence a Kp -based model based on sampling empirical probability distribution functions could be constructed that satisfies point 2 of the necessary conditions for a “good” parameterisation in Section 4.2. However, it would not fully satisfy the requirement for forecasting or nowcasting capability (due to the 3-hr averaged nature of Kp) or the requirement for physically motivated parameters (it is difficult to ascribe a direct physical property to Kp due to the processing involved in constructing it, as discussed below). The variance of the Kp bins are similar to those in our solar wind-parameterised model (Figure 6-7); there may be a lower limit to the variance, either dependent on our hourly timescale or due to underlying physical

processes that require better characterisation.

The variance of each Kp bin in this model (explicitly shown in Figure 6-11(b)) is clearly smaller than those from the storm-time data set used by *Murphy et al.* [2016], even while the mean values are similar. The storm list used by *Murphy et al.* [2016] is based on times where the magnetosphere is driven by corotating interaction regions and coronal mass ejections, although part of the list was also constructed with a Dst threshold. The greater uncertainty in the storm-time values (i.e. the larger variance) is therefore likely to be caused by more extreme solar wind conditions, while the similarity in the mean values is most likely due to either a correlation between Dst and Kp , to the fact that a portion of the storm list does not use a Dst threshold and so the internal conditions of the magnetosphere may not be significantly different to the average, or most probably a combination of the two. Regardless of the similar mean values, the increase in uncertainty indicates that Kp does not capture ground ULF wave power behaviour as well under extreme solar wind conditions. It is likely that our model will perform better, being solar wind based, but future work should quantify this.

To compare the Kp -based model directly to our solar wind based model, we have used the Kp probability distribution functions to reproduce PSD values for the same time series as Figure 6-5, shown in Figure 6-11(d). The time series is reasonably well followed by both models, but forecasting skill scores indicate that the Kp model does not perform quite as well as our solar wind based model. At GILL over the fifteen years, for 3.33 mHz the solar wind based model has a positive skill value of 10.6 when compared to Kp as a reference model. Nevertheless, Kp is a surprisingly good proxy for ground-based PSD. Examining the relationship between Kp and the solar wind parameters suggests that Kp represents an independent contribution to power; the two-parameter plot in Figure 6-12 shows that median PSD increases with Kp independently of v_{sw} , Bz or $\log_{10}(\text{var}(Np))$. (This analysis is in line with that followed in Chapter 5 to identify causally correlated parameters). As Kp is a mid-latitude index it is related to the magnetospheric convection electric field [*Thomsen, 2004*], while as a range index it is particularly related to explosive changes such as substorms. Since it is a three-hour index and substorm cycles generally last within three hours [*Borovsky and Yakymenko, 2017*], Kp is therefore related to substorm activity [*Lockwood, 2013*]. However, very large amplitude ULF waves may also contribute to Kp , as they may cause significant magnetic field deviations on the dayside stations used to construct Kp , particularly during times of low substorm activity. Hence the independent contribution indicated by Kp may represent substorm activity or ULF wave persistence. This suggests that ULF wave persistence should be studied, and that one of the first improvements to this prototype model should account for internal magnetospheric processes such as

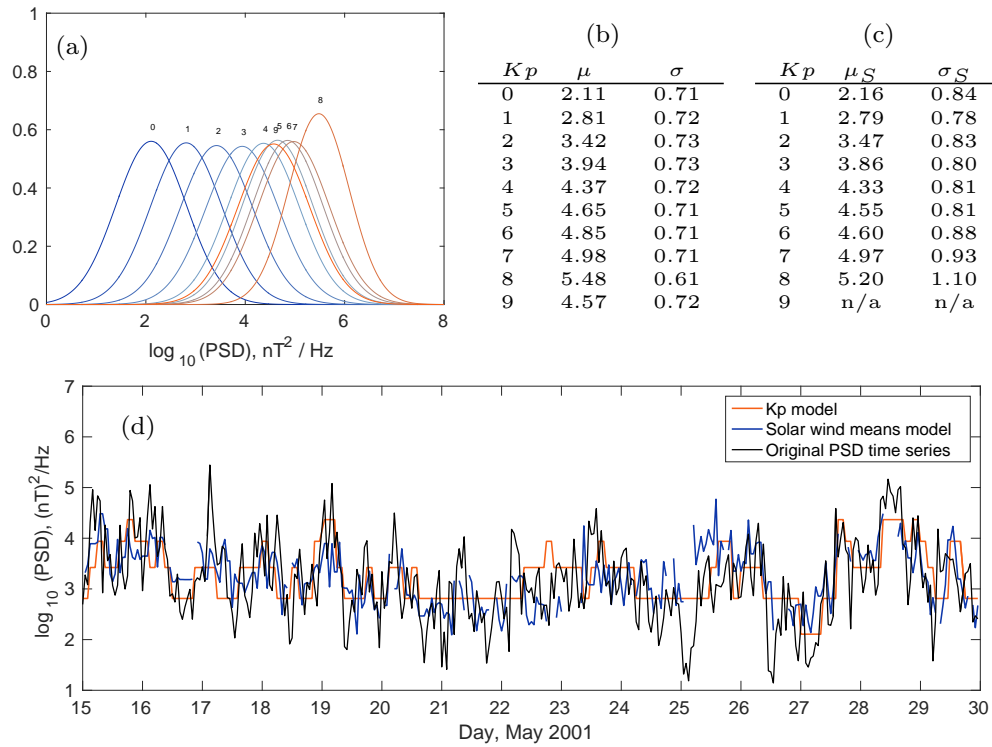


Figure 6-11: A Kp -based model using probability distributions to predict ULF wave power at GILL, $L \sim 6.6$, 3.33 mHz. (a) the fitted normal distributions of power for each Kp values, (b) the mean and standard deviation of both these fits and (c) similar storm-time only fits. In (d) we use both the Kp and solar wind parameter models to reproduce power over a short period of time (two weeks in May 2001, the same as Figure 6-5).

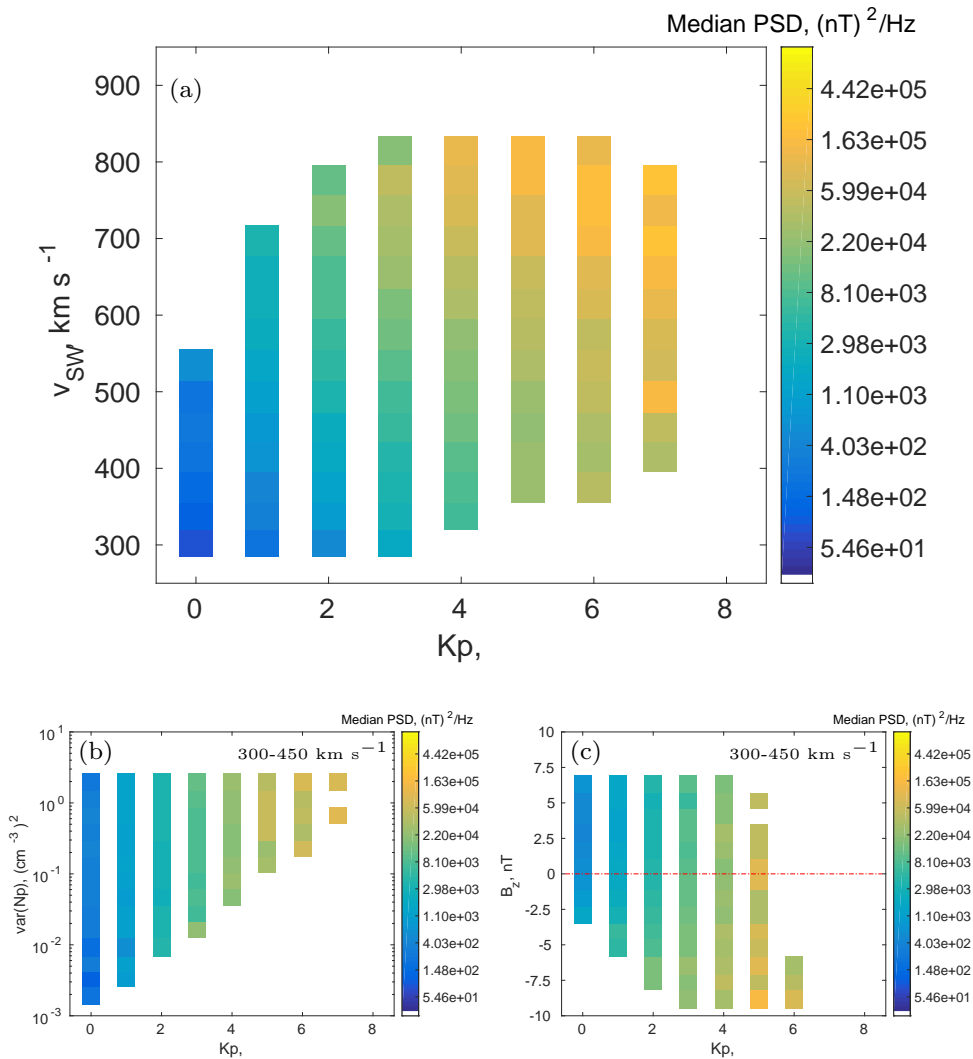


Figure 6-12: A series of two-parameter plots, where observations are binned by a solar wind parameter and Kp , and the median power in each bin at GILL, 3.33 mHz is shown. (a) Power is binned by both speed and Kp . Median ULF wave power is shown, which increases with both parameters. (b) Power is binned by variance in proton number density N_p and Kp for a single speed bin. Median ULF wave power increases with Kp but not with variance in number density. (c) Power is binned by B_z and Kp for a single solar wind speed. Median ULF wave power increases with both $B_z < 0$ and Kp . Hence Kp represents a contribution to median ULF wave power independent of any correlations with solar wind speed, B_z or variance in proton number density.

substorm activity. However, as Kp is highly averaged and processed, suitable options would be either a more physically based internal parameter, a solar wind time lag or the recent history of the magnetosphere. These different approaches will need to be considered for both their physical interpretability and their suitability for nowcasting and forecasting.

6.4 Other sources of uncertainty in radial diffusion coefficients

In this chapter we have focused on a model of ULF wave PSD that will allow us to quantify the uncertainty introduced to calculation of radial diffusion coefficients. However, to construct a probabilistic description of diffusion coefficients we will need to include all sources of uncertainty; in this section additional sources of uncertainty are reviewed. Physical assumptions used in our theoretical formalism, constraints due to observational capabilities and different statistical methods all contribute to this uncertainty. Indeed, some sources of uncertainty have multiple knock-on effects such as the underlying magnetic field model, which can give rise to uncertainty in the formalism and again when calculating L^* , i.e. in processing observational data and when constructing averages for statistical wave maps.

The following review is ordered from purely physical assumptions, through approximations of theory that make up our formalism, to observational restrictions and finally uncertainty from our statistical model construction.

1. Background magnetic field model
2. Other physics underlying the formalism
3. Summation over resonant frequencies
4. Accounting for azimuthal wave structure
5. Double-counting symmetric perturbations
6. Double-counting electric field perturbations
7. Methods of calculating power spectral density
8. Uncertainty from ground and space based observations
9. Statistical method construction

These known sources of uncertainty are all briefly reviewed below.

6.4.1 Background magnetic field

As discussed in Section 3.4, the diffusion coefficient D_{LL} can be derived from perturbations of electromagnetic fields. *Fälthammar* [1965] considered the radial diffusion of equatorially mirroring particles due to small symmetric and asymmetric perturbations of the dipole field, while others have extended this to other magnetic field models [*Schulz and Eviatar*, 1969; *Elkington et al.*, 2003]. Clearly, the choice of magnetic field model will contribute some uncertainty to the resulting diffusion coefficients, particularly at higher radial distances and during geomagnetically extreme periods when magnetic field models are often less accurate. This choice also gives rise to uncertainty in using observations, as we map in situ observations from real space to L^* , or ground-based observations up to the equatorial plane.

6.4.2 Other physics underlying the formalism

Diffusion coefficients are bounce-averaged and hence calculated in the equatorial plane, using equatorially mirroring particles. This assumes that there is no latitude dependent field variation such as the South Atlantic Anomaly. Additionally, the radial diffusion coefficient used in radiation belt modelling is generally drift-averaged. However, there is no conventional method of constructing a drift-averaged diffusion coefficient as it is unclear whether it is more physically representative to calculate D_{LL} in each azimuthal sector and average, or to calculate $(\Delta L^*)^2$ in each sector, average these and then calculate D_{LL} . Instead, the lack of simultaneous measurements across a wide range of MLT sectors often dictates our choice. Finally, we also note for completeness that an underlying physical assumption used in these derivations is that the frozen-in theorem is valid, i.e. that there is no parallel electric field [*Fälthammar*, 1968].

6.4.3 Summation over resonant frequencies

Radial diffusion coefficients for a particle of a given energy are found in many existing formulations by evaluating the power at frequencies corresponding to the resonant and harmonic drift frequencies of a particle [*Brautigam et al.*, 2005; *Fei et al.*, 2006; *Ozeke et al.*, 2014; *Ali et al.*, 2016]. An example of this mechanism can be found by *Elkington et al.* [1999]. They showed that global toroidal mode ULF oscillations can accelerate electrons, particularly with the addition of a dawn-dusk electric field. However, integrating over a broader frequency range than just resonant frequencies results in larger final diffusion coefficients via a sum of smaller scatterings, where this frequency range is determined by the drift frequency and the sampling frequency (up to the bounce frequency limit) [*Lejosne et al.*, 2013]. Hence clarifying the role of resonant

and non-resonant diffusion will be necessary to understand the energy dependence of diffusion coefficients.

When using the resonant frequency method, a common assumption used is that radial diffusion is caused by a magnetic impulse similar to a step function, so that power decays very slowly and is proportional to inverse square frequency, $\mathcal{P} \propto f^{-2}$, [Schulz and Lanzerotti, 1974; Ozeke et al., 2014]. This assumption is particularly useful as it causes the energy dependence of D_{LL} to cancel out and hence makes the diffusion coefficient easier to calculate. This approximation appears to be valid for average power spectra, but may not hold for the spectrum in an individual hour.

6.4.4 Accounting for azimuthal wave structure

Using observations to calculate D_{LL} via a sum over drift resonances involves yet more uncertainty in using and determining wave structures from in situ observations. Where the formalism sums only over resonant frequency contributions we must estimate the power at harmonics of that frequency. In their radial diffusion coefficient derivation, Fei et al. [2006] use a sum over azimuthal mode numbers m to describe this effect. However, in practice this is often simplified by assuming $m = 1$. Sarris and Li [2017] found that the amplitude of power is indeed concentrated in low m -numbers for the dayside and for less geomagnetically active time periods, but less so for the nightside and geomagnetically active periods. Murphy et al. [2018] found that the m -number during a moderate storm is typically low but the distribution of positive or negative values depends on radial location; this initial study gives some idea how the direction of propagation (i.e. $m < vs > 0$) is distributed among ULF waves but due to challenges in measuring m much more work is required. It is also unclear how direction of propagation should be included in existing radial diffusion coefficient calculations, yet the orientation of these oscillations will clearly affect the resultant diffusion.

6.4.5 Double-counting symmetric perturbations

Another source of uncertainty that comes into both the theoretical framework and when using observations is double-counting from background magnetic field perturbations. This arises from the inclusion of both symmetric and asymmetric magnetic field perturbations, when only asymmetric (i.e. azimuthally dependent, or varying in magnetic local time) variations contribute to radial diffusion [Fälthammar, 1965; Lejosne et al., 2012, 2013]. While axisymmetric variations in the magnetic field may distort the entire drift contour (hence moving particles in real space) particles will not be moved to a new drift contour (i.e. changing the value of enclosed flux, or L^*) without asymmetric

perturbations. Observationally, it is difficult to identify asymmetric components from in situ data as it is generally a set of sparsely located point measurements, yet the asymmetric component is of smaller amplitude at the ground where there is better coverage of observations. This difficulty was resolved by *Lejosne et al.* [2012, 2013], who avoid the issue of confusing symmetric with asymmetric perturbations by using an analytical model of disturbances added to a dipole field. By sampling multiple in situ locations, the value of these additional terms can be determined. *Lejosne et al.* [2013] also describes a method to approximate this type of analysis using only single point measurements, which reduces the number of spacecraft coverage necessary to cover the L^* -shells and sectors of interest. While this approach removes symmetric double-counting, uncertainty remains from the use of a dipole field model. This emphasises the necessity of calculating uncertainty to allow us to choose between physical assumptions in diffusion coefficient estimation methods.

6.4.6 Double-counting electric field perturbations

The second type of double counting arises from our treatment of electric fields. Theoretically, if the inductive electric field term is neglected from the magnetic component of diffusion D_{LL}^B , adiabatic changes in the magnetic field may appear to result in spurious changes in L^* and hence in our radial diffusion coefficients [*Fälthammar*, 1965]. However, it is difficult to quantify this term as in situ observations simply provide the localised value of the electric field, and it is difficult to distinguish how much of that is due to induction (i.e. $\frac{dB}{dt}$). Hence any diffusion coefficient calculation is at risk of double-counting electromagnetic field contributions. Using the method briefly mentioned in the previous section, *Lejosne et al.* [2012, 2013] also address this inductive electric field double-counting. More commonly, simplifying assumptions are made to make this problem more tractable. *Fei et al.* [2006] simply sum the electric and magnetic components $D_{LL} = D_{LL}^E + D_{LL}^B$. This approach is approximately valid where either the two electric components can be distinguished, (for example by making assumptions on the background magnetic field model and the types of wave present, which determines the relationship between the electric and magnetic field perturbations, [*Ozeke et al.*, 2012]) or when either $D_{LL}^E \ll D_{LL}^B$ or $D_{LL}^B \ll D_{LL}^E$. However, these coefficients may be of comparable magnitude [*Pokhotelov et al.*, 2016] so it is unclear how often this approximation can be used.

6.4.7 Methods of calculating power spectral density

While power spectral density is vital to our diffusion coefficient derivations, there are multiple valid transforms between the time and frequency domain. Different transform methods are better suited for either broadband or narrowband signals and so may over or underestimate the power at a single frequency, hence the choice of transform should reflect either the drift-resonant sum or frequency-range integral method of coefficient derivation. For example, if D_{LL} is calculated at specific resonant frequencies, then different methods of calculating power spectral density could result in different amounts of diffusion. Additionally, the underlying assumptions of a transformation to the frequency domain via the Wiener-Khinchin theorem have not been fully explored, such as stationarity on a range of timescales. It is not clear whether this would contribute uncertainty to the final diffusion coefficients but is included here for completeness.

6.4.8 Uncertainty from ground and space based observations

Some types of uncertainty are unique to the observation method. While the real-space location of in situ data may be known, it is difficult to be certain of the L^* -value. Spacecraft are often located at the equator and therefore may be at the node of any resonant field line oscillations, which they will therefore underestimate. As point measurements, it is difficult to make assumptions about the spatial and temporal scale of oscillations from single spacecraft measurements. However, ground-based data has its own set of uncertainties; each ground station corresponds to some field-line centred volume of variable width, and the mapping of ground power to the equatorial plane relies on assumptions of ionospheric conductivity and number density variations along the field, in addition to the magnetic field model and $E_{\parallel} = 0$ approximations discussed previously [Ozeke *et al.*, 2009].

6.4.9 Statistical model construction

When constructing statistical models of diffusion coefficients, additional uncertainty enters due to our methods of averaging and parameterisation. For example, while azimuthal resolution is important for statistical wave maps as it is the asymmetric (azimuthally dependent) contributions that account for radial diffusion, it is unclear what size azimuthal sector to average over to account for spatial variability in ULF waves. Similarly, the plasma density distribution affects the occurrence and penetration of ULF waves and hence radial diffusion. Averaging over periods with both high and low density will introduce more variability in statistical models.

Finally, the method of constructing a statistical model can also introduce uncertainty by our choice of parameters. Several recent studies calculating diffusion coefficients across the magnetosphere parameterise by Kp and L [Ozeke *et al.*, 2014; Lejosne *et al.*, 2013; Brautigam and Albert, 2000; Brautigam *et al.*, 2005; Ali *et al.*, 2016; Liu *et al.*, 2016]. Using L as a parameter is fraught with difficulty due to the difficulty mapping L to L^* . The quality of such a parameterisation can be quantified by examining the fits and the choice of parameters, as discussed in Section 6.3.1.

6.4.10 Summary

There are many sources of uncertainty in our existing methods of calculating diffusion coefficients. Quantifying the uncertainty introduced by different theoretical formalisms and by different physical assumptions will aid in selecting the most appropriate model approach with minimal uncertainty. Uncertainty due to observational restrictions, underlying natural variation and due to statistical methods may not be as easily avoided but still needs to be quantified in order to accurately describe the ability of radial diffusion coefficients to reproduce radiation belt phenomena in modelling. In this chapter we have focused on producing a statistical model of ULF power spectral density that is suitable for nowcasting and forecasting yet can capture the uncertainty due to underlying natural variation. This is only one component of a final, fully probabilistic radial diffusion coefficient model. Until then it can be used to improve existing models and to better understand the physics underlying the generation and propagation of ULF waves.

6.5 Conclusion

A description of ULF wave power is an important component of any radial diffusion coefficient calculation. We have outlined a method to construct a model of ground-based ULF wave power that is dependent on solar wind parameters, azimuthal angle (i.e. magnetic local time), station latitude and frequency. This model outputs probability distributions, which will allow us to produce probabilistic forecasts and to identify areas of uncertainty in future statistical models of radial diffusion coefficients.

The probability distribution in each bin is approximated by a normal distribution of log-power, which allows us to use two methods of predicting ULF wave power. By looking up the appropriate normal distribution corresponding to solar wind observations in a given hour, that distribution can either be sampled or the mean can be taken. Sampling each distribution is suitable for reproducing the total distribution of power over an extended event while using the mean value is the best method of reproducing

a time series. Comparing this to a similarly constructed model based on Kp , we find that our prototype model based only on three solar wind parameters slightly outperforms the Kp model and that Kp represents an independent contribution to power that should later be included in our model. We also find that the uncertainty in a Kp parameterisation increases during storm times. Hence future improvements could include a dependence on internal magnetospheric properties that satisfy the characteristics of a “good” parameterisation, which we have defined in Section 6.3.1.

To apply this prototype model to the production of radial diffusion coefficients involves extending to more stations and mapping ground based power to the equatorial electric field [Ozeke *et al.*, 2009, 2012], then examining whether this is an effective model and where the largest uncertainty stems from. Identifying the source of this uncertainty will allow for targeted improvement of a statistical radial diffusion coefficient model. In Chapter 5 we reviewed other ways that uncertainty can enter the radial diffusion coefficient calculation in addition to the underlying wave model. We anticipate that the methods and tests outlined throughout this paper can be used to inform construction of other components of a fully probabilistic radial diffusion coefficient model.

Future improvements to reduce any uncertainty from the solar wind based model outlined here could be made by including time-lagged solar wind contributions, substorms, magnetospheric plasma density, magnetospheric conditions and also the time history of the magnetosphere. Additionally, the underlying normal distribution approximation could be further examined to identify where this approximation holds; as well as quantifying the resulting uncertainty this will indicate magnetospheric regions or solar wind conditions of physical interest for the generation and propagation of ULF waves.

To summarise, our simple parameterisation based on magnetospheric regions and just three solar wind properties predicts ULF wave power time series better than assuming that power carries on from the previous hour. We submit that this is a surprisingly effective result for such a simple model and therefore constitutes a step towards a probabilistic model of radial diffusion coefficients. This prototype model can also be used to investigate questions about the occurrence of ULF waves; immediate future work includes examining the parameterisation results across a variety of stations and MLT sectors.

CHAPTER 7

TOWARDS PHYSICS FROM THE MODEL

Following construction of a statistical model, this chapter consists of several pilot studies investigating how to analyse and use this model further. In particular, how this model can be used to investigate the effectiveness of each driving parameter used, to test existing theories of ULF wave generation and propagation and whether our current model can be simplified further using a multiple regression. It was initially hoped that a multilinear regression would allow us to construct coefficients for each solar wind property that we could then examine; unfortunately, analysis throughout the chapter suggests that both the solar wind parameters and the driving processes themselves are so interdependent that this would not be meaningful. However, the multiple regression performs surprisingly well and represents a simplified model that is more likely to be adopted by the space physics community. Instead of using these coefficients, we outline alternative methods to study the physics of ULF wave occurrence. For example, examining what information about ULF waves are lost in each stage of model construction and investigating the ULF wave power occurrence in our model. This represents a strength of our statistical model: the ability to quantify changes in ULF wave power throughout the magnetosphere due to changes in solar wind parameters. Our primary suggested method of future analysis is therefore to test existing theories of ULF occurrence (by choosing appropriate solar wind input parameters) and to examine the expected ULF wave power throughout the magnetosphere. The logic behind this and some suggested questions can be found at in the final section of this chapter.

In Section 7.1 we approximate the statistical model using a multilinear regression. The applicability of this approximation and the ability to reproduce the underlying physics is tested. Instead of directly examining the resulting solar wind parameter

coefficients, the “effectiveness” of each solar wind parameter to describe changes in ULF wave power is studied in Section 7.2 using the separation proxy χ_S defined in Section 6.3.1. In Section 7.3 we briefly examine the mean square error between the statistical model and the original power values, to determine how well it approximates the original ULF wave power in each partition. We also outline how investigating the underlying normal approximation may be used to identify regions of physical interest. Finally, in Section 7.4 we outline how the power output of our statistical model can be used to investigate current theories of ULF wave generation and propagation and suggest several physical questions that can be approached first.

This chapter only contains physics questions directly evolving from our statistical model. Other future research ideas built on this work are covered in Chapter 8.

7.1 Multiple regression model

One of the original goals of this project was to consider the variation of ULF wave power with varying solar wind parameters in order to investigate the underlying physics. For this reason, one of the first extensions to the statistical model is a multilinear regression on the solar wind parameters. Although the dependence of ULF wave power on the solar wind parameters is unlikely to be truly linear, the approximation may still be good enough to identify physically interpreting variations of solar wind dependence by examining the variation in the coefficients. Furthermore, while the the statistical model in Chapter 6 is rigorously constructed, it is not particularly easy to use, distribute or analyse, in comparison to a multiple regression.

Here, we outline a multiple regression on the mean logpower values in the solar wind bins of each partition. Additionally, this will allow extrapolation to solar wind conditions from which the statistical model is currently unable to predict ULF wave power. In Section 5.3.2 we noted that the solar wind parameters are highly interdependent and that we should not assume PSD increases linearly with solar wind parameters. This multiple regression is constructed by assuming that once the behaviour change at $Bz = 0$ has been accounted for, the linear assumption is close enough to make this a reasonable approximation. We will discuss the applicability of this approach in Section 7.1.2. Testing for the quality of the fit is covered in Section 7.1.3 and Section 7.1.4, and an overview of how this may be used is given in Section 7.1.5.

7.1.1 Multiple regression overview

The aim of a multiple regression is to find the coefficient vector θ that most closely maps the input values \mathbf{x} (here, our binned solar wind properties) to the output values

\mathbf{y} , which are the mean logpower values μ for each bin. Therefore we are looking for coefficients θ_i to solve the following equation:

$$\theta_1 \overline{v_{sw}}(m) + \theta_2 \overline{\log_{10}(\text{var}(Np))}(m) + \theta_3 \overline{Bz}(m) + \theta_4 c(m) = \mu(m) \quad (7.1)$$

across bins $m = 1, 2, \dots, M$ in each partition, where M is the length of input \mathbf{x} . The maximum possible value of M is $10 \times 5 = 500$. However, most bins do not have enough observations to fit a normal distribution, so the multiple regression actually fits between 135 and 149 mean values. In Equation (7.1) the bar over the solar wind parameters indicates that they have all been normalised to the same 0-1 scale used in the statistical model. The coefficients are found by method of gradient descent; minimising the cost function until either it converges or we do too many iterations. The cost function is written as

$$J_C = \frac{1}{2M} (\mathbf{x}\theta - \mathbf{y})^2 \quad (7.2)$$

Hence J_C is equal to half the mean square error between our regression and the true values. The cost function associated with the multiple regression for each partition identifies whether the multiple regression is a good approximation of the underlying statistical model.

7.1.2 Assumptions used here

The two main assumptions underlying the multiple regression approximation are a linear dependence of logpower on the input variables, and independence between the variables. Clearly, Bz does not relate linearly to power due to the threshold at $Bz = 0$; we resolve this by constructing separate regressions for $Bz <, > 0$. By using $\log_{10}(\text{var}(Np))$ we have brought the $\text{var}(Np)$ contributions onto a (roughly) linear scale, alongside v_{sw} and Bz . The true nature for each solar wind property may need further investigation or refinement, however this “linear” assumption also ties in to our justification for the second multiple regression approximation: interdependence of parameters. Clearly, solar wind properties are not independent. However, if the relationship between parameters is linear then this will be swallowed into the final solution θ . This could be solved by deriving new input parameters from $v_{sw}, Bz, \text{var}(Np)$ which are orthogonal. However, the relationship between these is likely to vary with the region of the magnetosphere under study, so it is simpler to assume that this relationship is swallowed into the final θ .

The multiple regression model here only reproduces the mean values μ using the input parameters $v_{sw}, Bz, \text{var}(Np)$. As the variance values σ don't change significantly with v_{sw}, Bz or $\text{var}(Np)$ but instead appear to be drawn from a normal distribution

centred at $\sigma = 0.7$ (Figure 6-7) a reasonable approximation is to use 0.7 whenever a variance is necessary (e.g. if we choose to use the sampling method of prediction).

A common problem with multiple regressions is overfitting, or fitting to noise. By selecting only three physically motivated input parameters (which were all causally related to ULF wave power changes) and fitting to ~ 140 points, it is unlikely that overfitting is a problem. However, if the multiple regression model is used then significance testing will be necessary.

Smaller details that affect a multiple regression include choosing an appropriate starting solution $\tilde{\theta}$ and assuming that there is a single solution θ for each set of input parameters to which our regression uniquely converges. We find that this is true for all our partitions, which converge to the same solution regardless of starting value $\tilde{\theta}$.

7.1.3 Where the model approximates the statistical model

The cost function (Equation (7.2)) can be used to find and compare the mean square error from our regression fits to the standard deviation of all logpower values at a single frequency. The 99th percentile of J_C values is 0.0372, making one of the largest root mean square values between the regression approximation and the statistical model 0.27. Across all frequencies in 1-20 mHz, the average standard deviation of log-power values at a given frequency is 1.10. Therefore the ratio of the largest reasonable root mean square error to the standard deviation of logpower values at a single frequency is $0.25/1.10 = 0.23$. Hence even for our poorest regression fits, the error is within the variability.

We will briefly show the cost function results by station, magnetic local time, $Bz < 0$, $Bz > 0$ and by frequency to find any magnetospheric regions where multiple regressions are particularly good or poor approximations to the statistical model. This should be taken in conjunction with whether the statistical model is a good approximation in each of those regions (Section 7.4.2). Poor multiple regression approximations (high J_C) could be due to a poor choice of parameters (i.e. more parameters need), a poor underlying model or a nonlinear relationship between parameters. In Figure 7-1 we show the median and the upper and lower quartile of all cost functions at each station, split by MLT sector and by $Bz < 0$ (blue) and $Bz > 0$ (orange). The midnight sector is the most poorly approximated, although there are interesting variations by station and Bz : the multiple regression fits the statistical model better for southward IMF in the two outer stations, but better for a northward IMF in the two inner stations. It is unclear why this may be; perhaps this is an artefact due to the variation of the linear interdependence between partitions. For all stations, the $Bz < 0$ model fits the noon sector well. This does not fully correspond to the ability of the statistical model

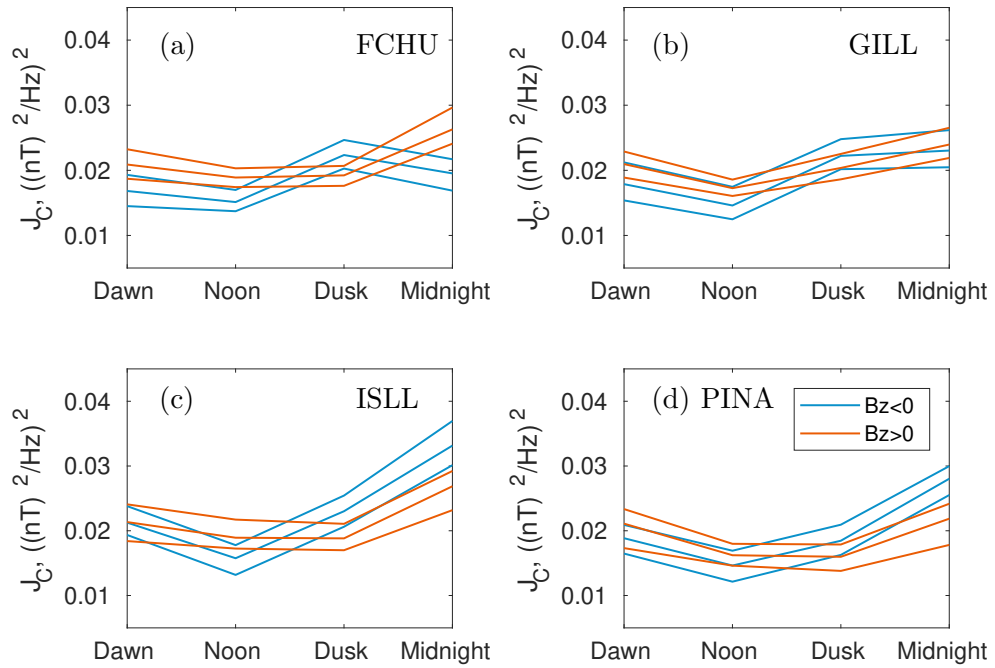


Figure 7-1: The cost function J_C is calculated for the multiple regression approximation of each partition. Here we show the median and upper and lower quartiles of J_C split by station and MLT sector, where orange indicates northward IMF $Bz > 0$ and blue shows southward IMF $Bz < 0$ (i.e. the quartiles are calculated over all frequencies for that station, MLT and $Bz < 0$ or $Bz > 0$). The multiple regression approximates the statistical model best in the noon sector and most poorly in midnight.

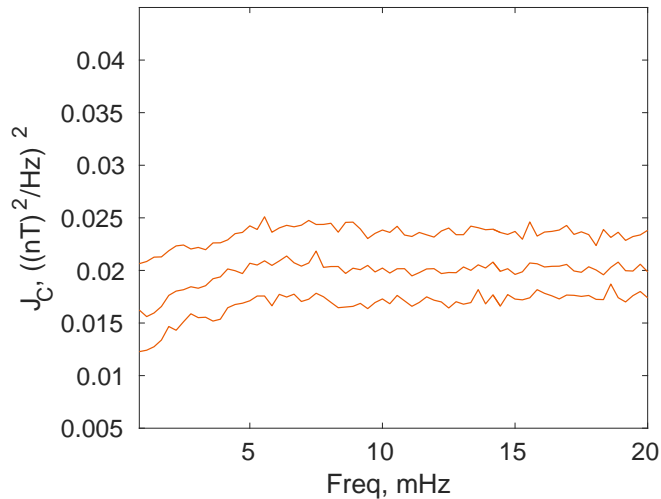


Figure 7-2: The cost function J_C is calculated for the multiple regression approximation of each partition. Here we show the median and upper and lower quartiles of J_C split by frequency (i.e. the quartiles are calculated over all stations, MLT sectors and $Bz < 0$ or $Bz > 0$).

to approximate power, shown in Figure 7-11 and discussed later. The mean square error (MSE) of the statistical model is low for noon for both $Bz < 0$ and $Bz > 0$, but a multiple regression far better approximates the statistical model for $Bz < 0$. In fact the cost functions vary far more between $Bz <, > 0$ than the mean square error of the statistical model does. For $Bz > 0$, the cost function is generally smallest in the dusk sector. There are many physical implications in Figure 7-1 that merit further study; it is likely they will require a detailed study into the nonlinear nature of the solar wind coupling - ULF wave power relationship to understand, and a comparison to the ability of the statistical model to reproduce the underlying power.

We can also consider the change in cost function with frequency; this is shown in Figure 7-2. The cost function increases with all partitions to around 6mHz, where it plateaus.

Understanding why the cost function changes this way with MLT, frequency, station and $Bz < 0$ and $Bz > 0$ requires further analysis. However, we note that it is encouraging that the cost function is smaller for the lowest frequencies, which are most important for radial transport in the outer radiation belt.

7.1.4 Forecasting skill

Another test determining the usefulness of the multiple regression is to look at the forecasting skill compared to the statistical model it approximates. Forecasting skill

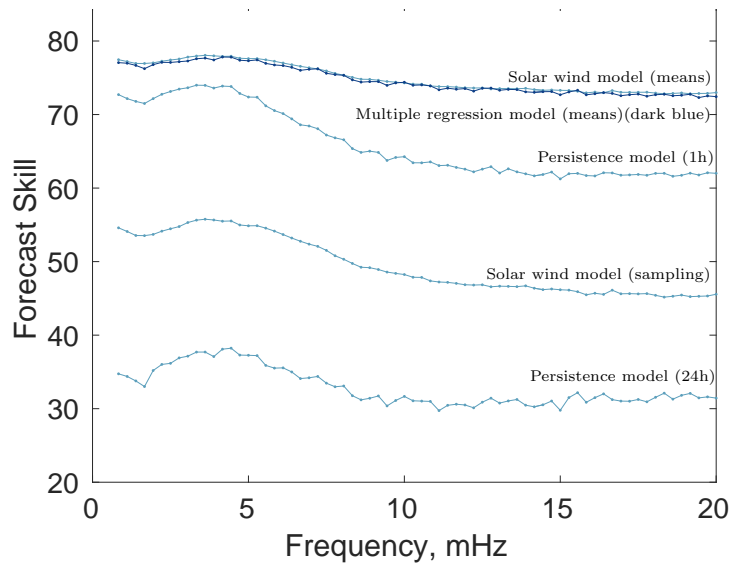


Figure 7-3: Forecasting skill at all frequencies for GILL, 1990-2005, where models are compared to a random reference model. Where any kind of sampling was used (i.e. random and solar wind model sampling), 500 runs were taken. The ranking of model types is consistent across all frequencies. The multiple regression approximation to the statistical solar wind model performs almost identically and can be extrapolated to values the statistical model was unable to predict.

was introduced in Section 6.3.2 using the mean square error of a time series to compare prediction methods. The forecasting skill for the multiple regression can be added to the results found for GILL, 1990-2005 in Figure 6-9. This is shown in Figure 7-3, where the multiple regression results are shown in dark blue. They are virtually indistinguishable from the forecast skill for the deterministic method, suggesting that this is a very good approximation of the statistical model.

An additional use for the multiple regression model is to extrapolate beyond the bounds of the solar wind statistical model, where there are not enough observations to fit a normal distribution. Although these extreme conditions will occur only rarely, it may be necessary for certain numerical methods to construct a complete time series. Such extrapolations may not be particularly good but will allow analysis that would otherwise be impossible. Of course, the forecasting skill is likely to decrease when extrapolating to these extreme values.

7.1.5 Analysis possibilities

The original goal of the multiple regression was the opportunity to easily examine the changing dependence on solar wind parameters by considering the coefficients. In

that case, a higher v_{sw} , Bz or $var(Np)$ coefficient would indicate that an increase in that parameter would result in a larger change in ULF wave power than a smaller coefficient. The constant coefficient would indicate “background” power, i.e. ULF wave power that is not included by this model. The background power could include persistence from previous hours, lagged drivers or internal mechanisms not included in our parameterisation. Unfortunately it is very difficult to study coefficients individually for two reasons. Firstly, having mapped each parameter to a 0-1 scale it is difficult to compare between coefficients of two different solar wind parameters. Secondly, as they are likely to still be interdependent, comparing a single type of coefficient between partitions is complicated. It is unclear a priori whether an analysis of the coefficients would be physically meaningful. As the separation proxy χ_S was designed to identify when each solar wind property is a “good” parameter (i.e. when ULF wave power varies significantly with variations of that parameter), we will use χ_S to investigate whether an analysis of the coefficients would be appropriate.

Whether or not the multiple regression can be used to examine the effect of individual coefficients, it appears to be a surprisingly good approximation of the statistical model. Therefore the multiple regression can be used as a “portable” version of the full statistical model, especially for predicting average ULF wave power for use in radial diffusion calculations. This is far more likely to be adopted by the space physics community and may be worth pursuing as long as there are no significant deviations in predicted ULF wave power. This would need to be in addition to the full model, which should remain easily available.

7.2 Separation proxy

In Section 6.3.1 we stated that the probability distribution of values in neighbouring bins in our parameterisation should be distinct to be a “good” parameterisation. We also defined the separation proxy χ_S which will be examined here across all partitions in the statistical model. Ideally, χ_S will identify where each solar wind parameter is an effective descriptor of ULF wave power and therefore help us identify the underlying solar wind coupling. We will show that it can also qualitatively identify “linearity” of the parameterisation. Hence while the cost function of a multiple regression (Section 7.1.3) will more quantitatively identify whether a multiple regression is a good approximation, χ_S can show us which parameters are responsible for good or poor fits and whether an analysis of the individual coefficients would be physically meaningful.

Partition	$\chi_S(v_{sw})$	$\chi_S(\log_{10}(\text{var}(Np)))$	$\chi_S(Bz)$
$Bz < 0$	0.5	0.28	0.37
$Bz > 0$	0.6	0.29	0.25

Table 7.1: Median $\chi_S(v_{sw})$, $\chi_S(\text{var}(Np))$ and $\chi_S(Bz)$ for GILL, 3.33 mHz, noon.

7.2.1 Interpreting distributions of χ_S in each partition

As χ_S is calculated between two neighbouring probability distributions, we use it to examine the “distinctness” between conditional log-power normal distributions along each parameter axis v_{sw} , $\text{var}(Np)$ and Bz in the statistical model. For example, to calculate all $\chi_S(v_{sw})$ for a given $[\text{var}(Np), Bz]$ we calculate χ_S between the distributions of log-power in the first and second speed bins, then the second and third, and so on. As we use 10 speed bins in each partition, for each $[\text{var}(Np), Bz]$ bin there are up to 9 values of χ_S . This is completed for every pair of $[\text{var}(Np), Bz]$. Therefore in total we could have up to $9 \times 10 \times 5 = 450$ values of $\chi_S(v_{sw})$, although in reality there are far fewer than this as many bins are empty. Similarly, we can calculate all $\chi_S(Bz)$ by iterating over all $[v_{sw}, \text{var}(Np)]$ bins, and $\chi_S(\text{var}(Np))$ by iterating over all $[v_{sw}, Bz]$ bins. For each partition, we then have a distribution of χ_S values for each parameter v_{sw} , $\text{var}(Np)$ and Bz . The example values from Section 6.3.1 are repeated here: for GILL, 3.33mHz, noon, the median values of χ_S for each solar wind parameter are shown in Table 7.1. For both $Bz < 0$ and $Bz > 0$, median χ_S is largest for speed. For $Bz < 0$ this is followed by Bz . This corresponds to the order of dominant parameters as expected after the work done on causal parameters. However, we can also examine the total distribution of χ_S values to infer more general properties of the parameterisation.

In general, larger values of χ_S indicate more distinct distributions and therefore a better parameterisation, as that parameter is then related more strongly to increases in ULF wave power. Therefore there are two particularly useful properties of each χ_S distribution in a partition. Firstly, the location of the peak tells us on average how effective that parameter is at quantifying change in ULF wave power. Secondly, the width of that peak tells us how consistent this distinctness is in the given partition. For example, a narrow peak would suggest that any two neighbouring distributions always have a similar amount of overlap, while a wider peak would suggest that the overlap between neighbouring distributions can vary more significantly. Width w is defined by the value w such that the interval $[\text{peak} - w, \text{peak} + w]$ contains half the distribution. A larger width in (for example) $\chi_S(v_{sw})$ could indicate that ULF wave power does not simply increase linearly with increases in v_{sw} - the amount of overlap may change either with the $[\text{var}(Np), Bz]$ bin chosen or the value of v_{sw} . In that case the relationship of v_{sw} to ULF wave power could be nonlinear (it could even include a threshold), or

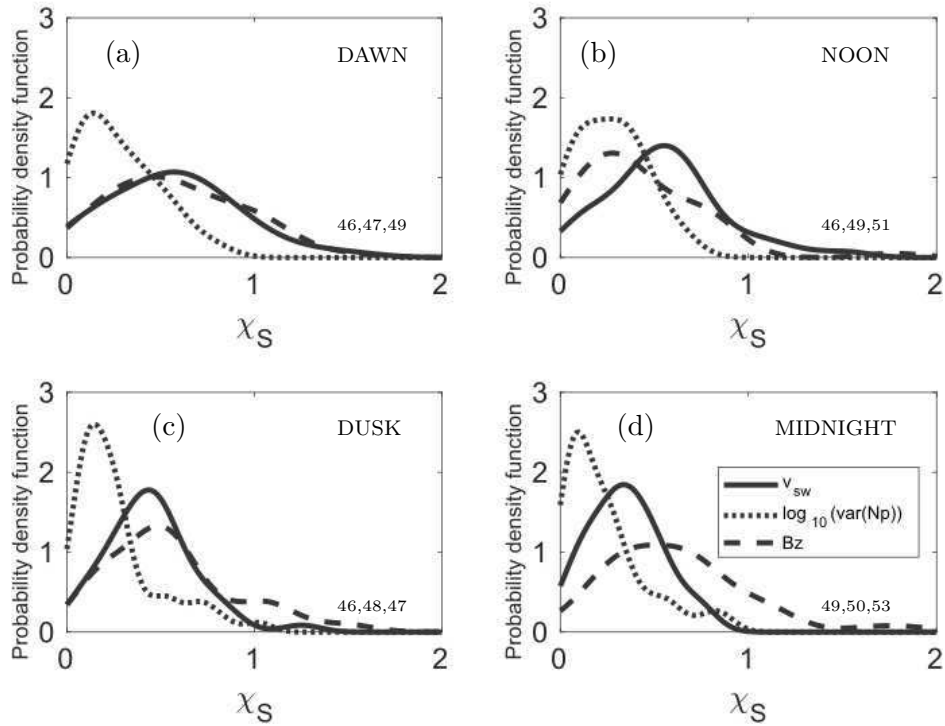


Figure 7-4: Distribution of separation proxy χ_S values for each parameter axis for each MLT sector in GILL, 3.33mHz, $Bz < 0$. The number of χ_S values used to create each probability distribution function are shown in each bottom right corner for v_{sw} , $\log_{10}(\text{var}(Np))$ and Bz respectively.

the v_{sw} contribution is not independent of $\text{var}(Np)$ and Bz . To summarise, a small w and hence narrow width, combined with a high peak value, would indicate that any two neighbouring distributions are relatively distinct, and that this distinctness does not vary much across all pairs of neighbouring distributions. Conversely, a large enough width, combined with a low peak value, would indicate that the parameter is not particularly efficient at describing variation in ULF wave power.

Some example χ_S distributions have been calculated and are shown in Figures 7-4 and 7-5. In Figure 7-4 we show the χ_S values between all neighbouring distributions along the three solar wind parameters v_{sw} , $\text{var}(Np)$ and Bz for GILL, 3.33 mHz, $Bz < 0$ for all four MLT sectors. In Figure 7-5 we show the same for $Bz > 0$. Ideally we would examine all the distributions and compare how they change with station, frequency, MLT sector and IMF direction to identify some of the underlying physics - for example, if a χ_S distribution were made of two combined distributions it may indicate the presence of two separate physical processes. However, as most of the distributions are composed of fewer than fifty points it is unclear how significant or reliable such

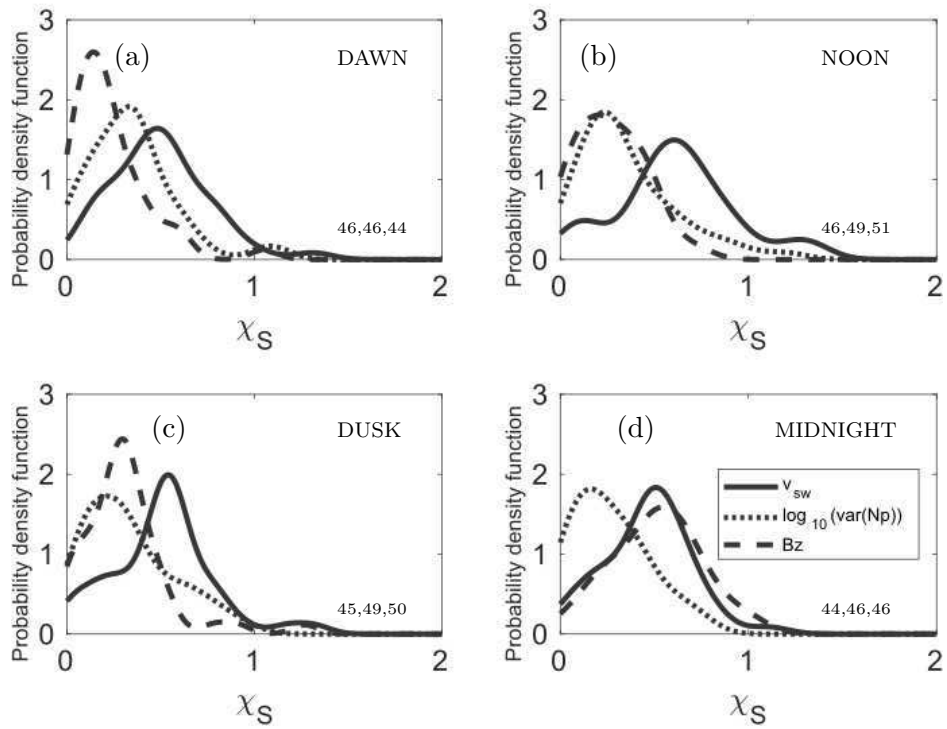


Figure 7-5: Distribution of separation proxy χ_S values for each parameter axis for each MLT sector in GILL, 3.33mHz, $Bz > 0$. The number of χ_S values used to create each probability distribution function are shown in each bottom right corner for v_{sw} , $\log_{10}(\text{var}(N_p))$ and Bz respectively.

an analysis would be. Instead we can reduce each distribution to two representative measures; we can see how the peak and width change on average over many partitions and identify whether there are partitions where our choice of parameters is particularly good or poor.

7.2.2 Analysis of separation proxy χ_S across many partitions

To examine the ability of our parameters to describe variance in ULF wave power across different regions of the magnetosphere, we use the peak location and the width w of each χ_S distribution in each partition (to recap, partitions are split by station latitude, frequency, MLT sector and $Bz \leq 0$, Table 6.1). Scatter plots of all of these values across many partitions show how much they vary. First, we examine the overall scatter plots in Figure 7-6. All χ_S distributions have been found for each parameter across all partitions. The peak and width for each $\chi_S(v_{sw})$, $\chi_S(\text{var}(Np))$ and $\chi_S(Bz)$ are shown in Figure 7-6 (a),(b) and (c) respectively. There appears to be a roughly linear relationship between the peak and width w of χ_S distributions along v_{sw} . This suggests that when v_{sw} describes more of the variation in ULF wave power, it does not do so as uniformly across the partition. This could be because the relationship between v_{sw} and power is nonlinear, either due to an onset threshold (e.g. at higher speeds $\sim 500 \text{ km s}^{-1}$) or a monochromatic nonlinear relationship such as a power law.

The scatter plot for $\chi_S(\text{var}(Np))$ is quite dense and this suggests that the effect of $\text{var}(Np)$ is most consistent across all partitions out of v_{sw} , $\text{var}(Np)$ and Bz , although it is also the smallest. For Bz , there is again a roughly linear relationship but with much more spread in w . While it looks like there is a steeper gradient between w and the peak for $\chi_S(Bz)$ than for $\chi_S(v_{sw})$ this could be an artefact of our bin choices (most of the Bz values are in the bins nearest $Bz = 0$). Some partitions have very high peak values of $\chi_S(Bz)$, indicating that Bz is particularly strongly correlated with ULF wave power in some partitions.

Changes in χ_S by $Bz < 0, Bz > 0$

In Figure 7-7 the scatter plot of all χ_S peaks and widths are shown for each parameter, separated by $Bz < 0$ and $Bz > 0$. The $\chi_S(v_{sw})$ distributions change only marginally between IMF directions; there are fewer partitions with high peak values for v_{sw} when $Bz > 0$, and a steeper gradient for $Bz < 0$. The fewer peak values for $Bz > 0$ is unexpected as Kelvin-Helmholtz waves are longer-lived and more common during northward IMF conditions [Kavosi and Raeder, 2015] and therefore expected to drive ULF waves more strongly, although on average there is usually more power observed when $Bz < 0$

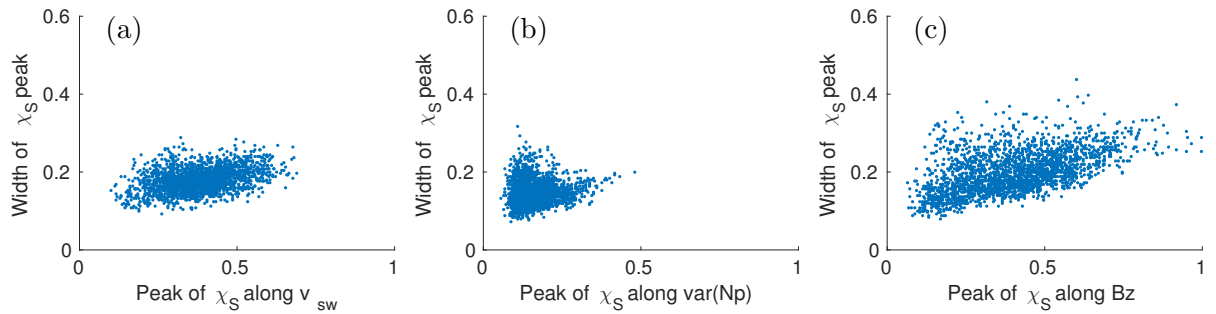


Figure 7-6: χ_S for (a) v_{sw} , (b) $var(Np)$ and (c) Bz distributions have been calculated across all partitions. They are shown here as scatter plots of the peak location of that distribution and the width w .

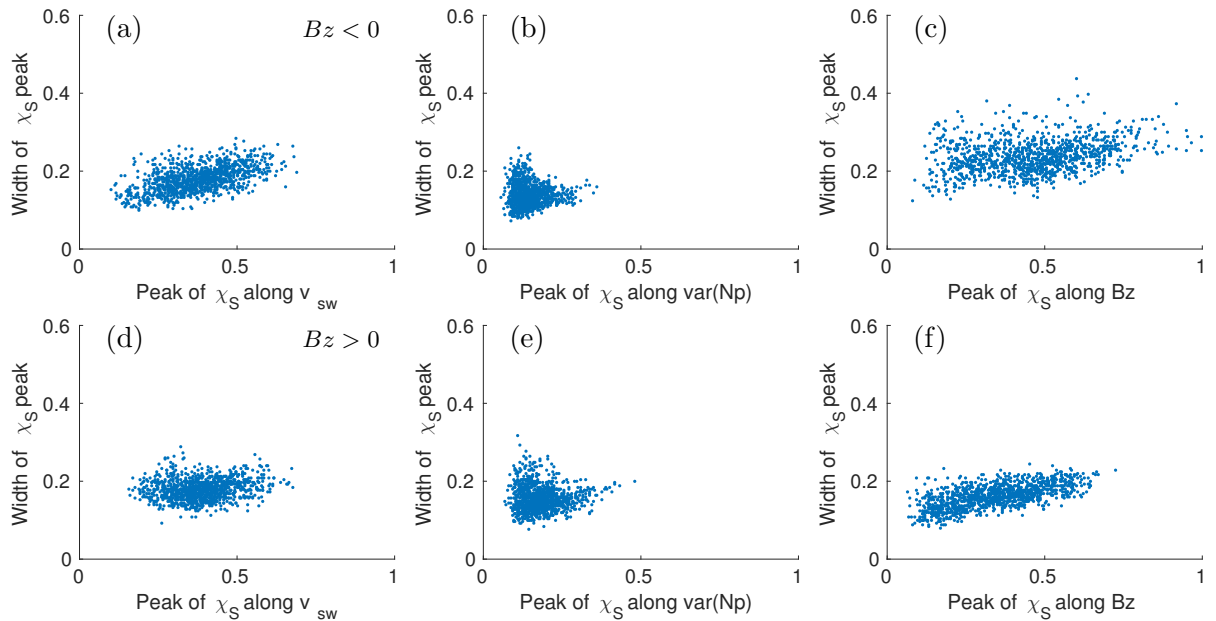


Figure 7-7: Scatter plots of the peak and width values of each χ_S distribution for each parameter and every partition, separated by whether the partition is $Bz < 0$ (a-c) or $Bz > 0$ (d-f).

(see Section 7.4.1). Instead these results suggest that v_{sw} can be a more effective driver for $Bz < 0$ than for $Bz > 0$, although the corresponding increase in width suggests that this increased effectiveness is nonlinear or varies across the partition. In fact this effect emphasises the difficulty of distinguishing driving mechanisms in statistical studies; v_{sw} and Bz both moderate the growth of the Kelvin-Helmholtz instability and the formation of FTEs, which interact. However, this increase in peak values for $\chi_S(v_{sw})$ could also be due the increased convection electric field vBz (a dawn-dusk electric field that arises from the motion of magnetic flux tubes tailward during reconnection through $\mathbf{E} = -\mathbf{v} \times \mathbf{B}$ [Baumjohann and Treumann, 1996; Kivelson and Russell, 1995]). vBz is a proxy for the strength of the Dungey cycle and indicates that more substorm activity and faster FTE formation may be in play. w is higher for $\chi_S(Bz)$ when $Bz < 0$, indicating that the Bz contribution to ULF wave power is still nonlinear after accounting for the $Bz = 0$ threshold. The change in peak and width for Bz suggest that in general Bz is a more consistent but less effective driver for $Bz > 0$. It appears likely that there will be some partitions where ULF wave power changes equally significantly with IMF northward or southward. These results justify retaining Bz as a parameter for $Bz > 0$, even though we could not distinguish this parameter in our study of causally correlated parameters. Overall, however, these results emphasise the difficulty in attributing power changes to any one parameter (because of their interdependence) or to any one mechanism (because of their interactions throughout the magnetosphere).

Changes in χ_S by station

In Figure 7-8 the scatter plot of all χ_S peaks and widths are shown for each parameter, separated by station (ordered from highest latitude to lowest). These scatter plots are similar between stations. For v_{sw} the linear relationship observed in Figure 7-6 still holds, although PINA seems to have fewer cases where the peak value is larger than 0.5. $\chi_S(\text{var}(Np))$ distributions change very little across stations, while $\chi_S(Bz)$ achieve far higher peak locations as stations decrease in latitude.

At first impression these results for $\chi_S(v_{sw})$ and $\chi_S(Bz)$ can be explained by existing theories for ULF generation mechanisms; v_{sw} may be less good for low latitude stations (ISLL, PINA) as magnetopause-deformation generated waves (e.g. by Kelvin-Helmholtz instability) will be less likely to penetrate to lower-latitude stations. Correspondingly, if Kelvin-Helmholtz deformations of the magnetopause do not penetrate to low latitude, then FTE driven perturbations are unlikely to either. In which case the increase in peak $\chi_S(Bz)$ for low latitude stations may suggest that substorms, rather than magnetopause FTEs, are the source of this ULF wave power correlation. However, Frey [2004] suggests that the median latitude corresponding to substorm onset

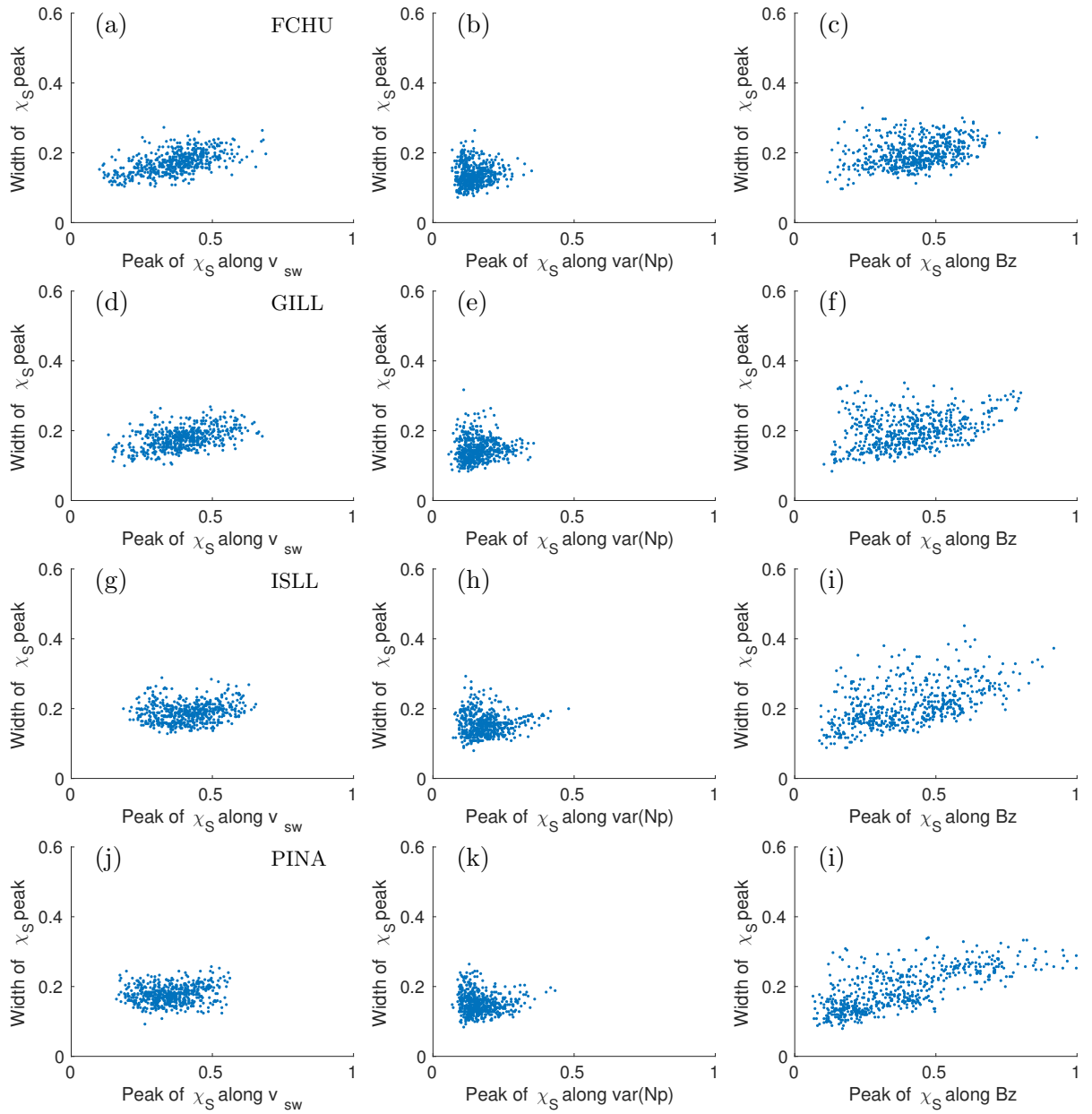


Figure 7-8: Scatter plots of the peak and width values of each χ_S distribution for each parameter and every partition, separated by station FCHU (a), GILL (b), ISLL (c) or PINA (d).

is closest to GILL, yet peak $\chi_S(Bz)$ increases with decreasing station latitude. Given this ambiguity and the interdependencies that make the multiple regression difficult to analyse, these interpretations remain speculative.

Changes in χ_S by MLT sector

In Figure 7-9 are shown the scatter plots of peaks and widths from χ_S distributions of each parameter, separated by MLT sector. There are notable differences across sectors for v_{sw} and Bz , but still little change for $var(Np)$ except perhaps a slightly more dense scatter at dusk. For v_{sw} the dawn and noon scatters have very similar peaks and widths, while dusk scatters are mostly in a single cluster with a fairly low peak and a common width. This is difficult to interpret as we would naïvely expect the flanks to be similar for both solar wind or substorm driver, as physics along the flanks of the magnetosphere will be very similar and substorm driving at midnight is likely to affect both the dawn and dusk sectors. This could be understood as an inability of the dusk sector to support ULF waves due to a higher variability of magnetospheric plasma density [Sheeley *et al.*, 2001], but if this were the case then we would expect Bz to show a similar trend. This is clearly not the case; indeed for $\chi_S(Bz)$ the dawn and dusk flanks are the most similar. For the midnight sector both high and low peak values of $\chi_S(Bz)$ can be found. This could be due to the different latitude of the four stations used; some will be connected directly to substorm drivers while others may be on open field lines.

Whilst the variation of power by MLT and our modelling of it is one of the underlying physical questions we would like to investigate, these results are very difficult to understand. It may be that the interdependencies between mechanisms change between MLT sectors more significantly than our parameterisation does, making it almost impossible to consider individual mechanisms.

Changes in χ_S by frequency

In Figure 7-10 we show the peak and width w for $\chi_S(v_{sw}, var(Np), Bz)$ for all partitions in three frequency bins. These are all very similar. There are marginally more high peak values for the lowest frequency bin, which may simply be due to fact that our model performs better at lower frequencies (Figure 7-11). Otherwise there are very few differences with frequency. This is surprising as we would expect a gradual change with frequency to different driving mechanisms.

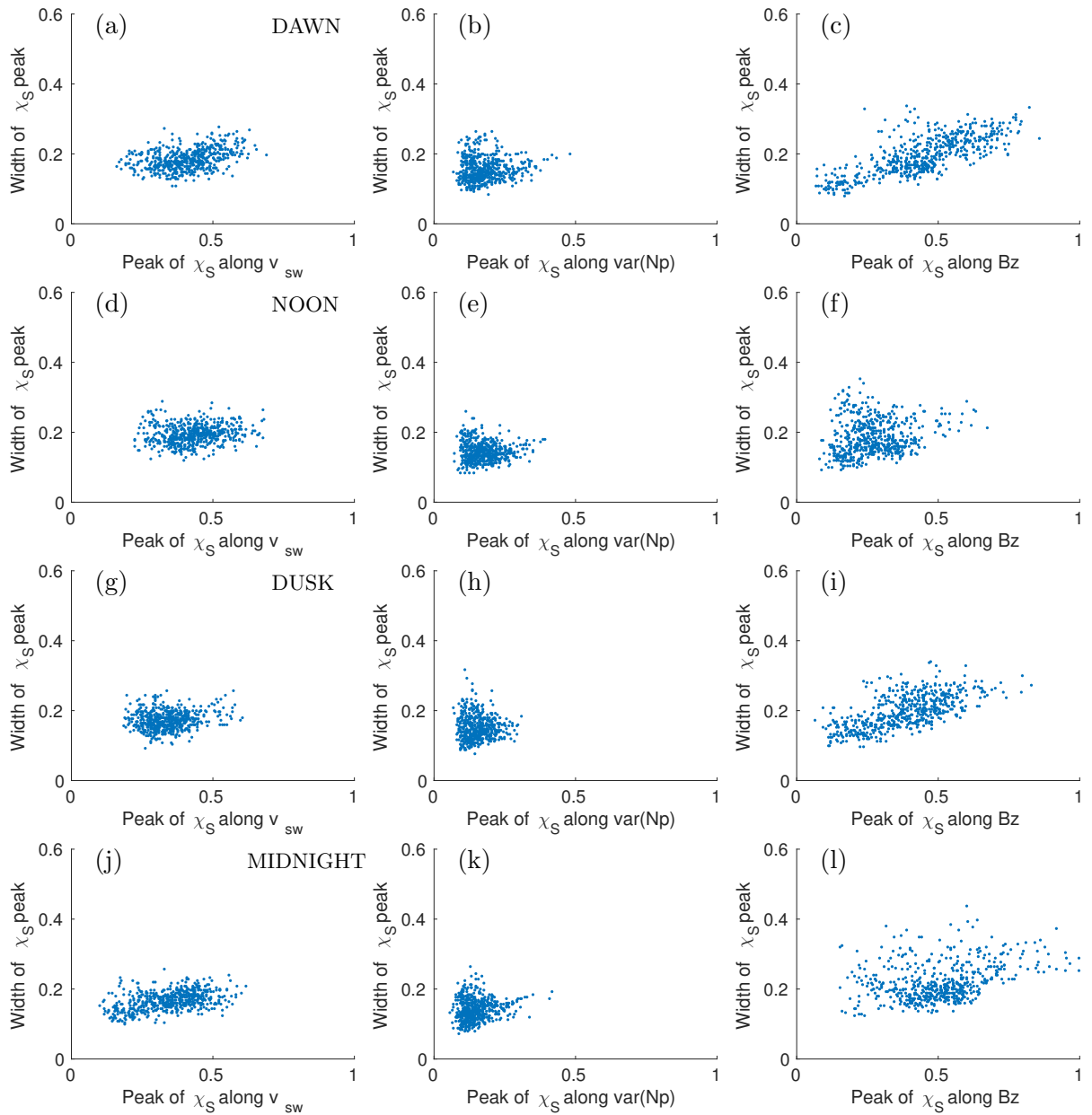


Figure 7-9: Scatter plots of the peak and width values of each χ_S distribution for each parameter and every partition, separated by whether the partition is in the dawn (3-9 MLT, (a-c)), noon (9-15 MLT, (d-f)), dusk (15-21 MLT, (g-i)) or midnight (21-3 MLT, (j-l)) sector.

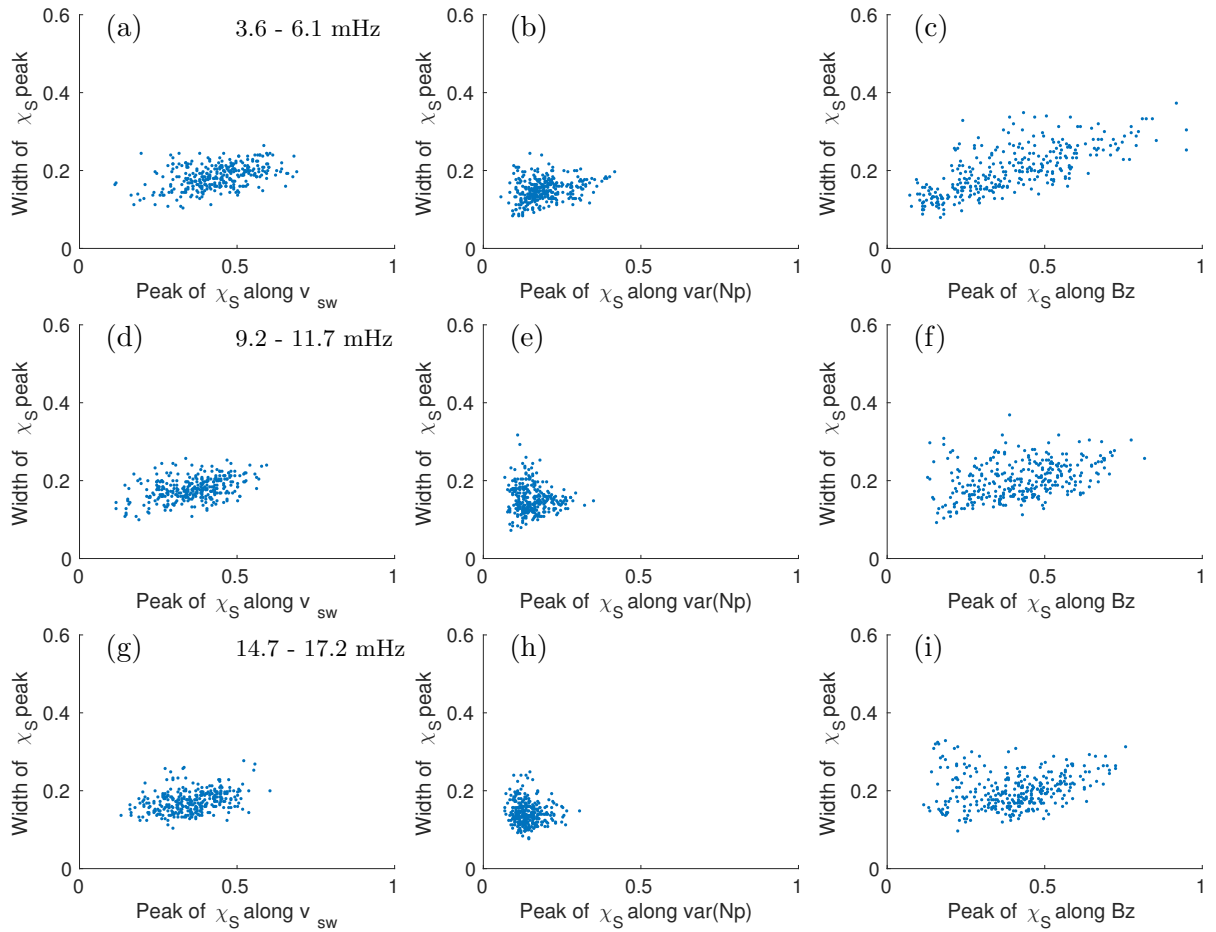


Figure 7-10: Scatter plots of the peak and width values of each χ_S distribution for each parameter and every partition, for three groups of frequency values 3.6-6.1 mHz (a-c), 9.2 - 11.7 mHz (d-f) and 14.7 -17.2 mHz (g-i).

Summary

This initial analysis demonstrates the complex dependence of ULF wave power on the different solar wind parameters identified in Chapter 5. In Chapter 5 we considered a single frequency and station, whereas here we have extended to four stations, 1-20 mHz and separated by MLT sector. There does not appear to be any systematic change in the “effectiveness” (peak value) and “consistency” (width w) of each parameter with station, MLT, frequency or $Bz < 0$ or $Bz > 0$. Instead, the peak and width values for $\chi_S(v_{sw}, Bz, var(Np))$ each appear to be drawn from a single distribution.

Our previous assessment (Chapter 5) that it is difficult and misleading to attempt to separate individual mechanisms or parameters appears to be accurate. For this reason, we cannot easily say whether the effectiveness of one parameter in a given partition would reduce the effectiveness of a multiple regression. Instead, the similarity of peak values and widths w across multiple partitions suggest that the parameters are reasonably consistently effective.

Another difficulty in interpreting χ_S is that fact that it is highly dependent on our choice of bins; the concentration of $\chi_S(var(Np))$ values indicates that our $var(Np)$ bins may not be suitable.

Without further study of these χ_S distributions, our main physical conclusions are firstly that we cannot dismiss the relationship between the KHI and FTEs when considering individual parameters, and secondly that we should consider substorms as well as FTEs to be characterised by Bz . Despite the different location of origin for these two processes (dayside magnetopause vs. midnight sector) it may be difficult to distinguish them without additional ground stations as they will increase in number together with increased strength of the Dungey cycle.

As for the individual parameters, it is clear that we should not use multiple regression coefficients to consider the effectiveness of driving parameters or processes. An underlying assumption of this χ_S approach was that the parameters are independent enough to consider their effectiveness separately. This does not appear to be true and therefore justifies the decision not to analyse the multiple regression coefficients, instead using the multiple regression as a “portable” model.

7.3 Information loss during model construction

A simple test of the statistical model uses the mean square error (MSE) of each partition to examine where the statistical model accurately approximates the underlying ULF wave power in the original data. In Section 6.3.2 the forecasting skill utilised the MSE to compare different methods of predicting ULF wave power in a time series.

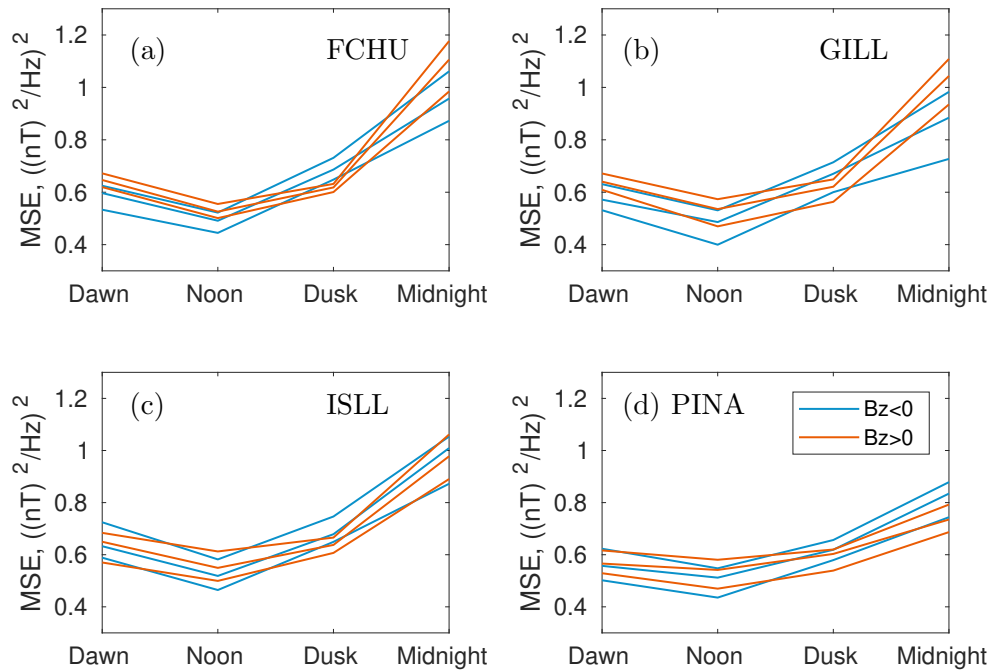


Figure 7-11: The median, upper and lower quartiles of mean square error between statistical model and original data values in each partition are shown, where quartiles are calculated over all frequency values for the corresponding station, MLT sector and $Bz > 0$ (orange) and $Bz < 0$ (blue).

Here, the MSE can be used to identify what regions of the magnetosphere the statistical model performs well in.

In Figure 7-11 the median and the upper and lower quartiles of the mean square error is shown at each station, split by MLT sector and by $Bz < 0$ (blue) and $Bz > 0$ (orange). For all stations, the highest mean square error (and hence the poorest approximation) is in the midnight sector. This is unsurprising as the solar wind parameters we have used will not necessarily represent substorm activity during each individual hour, yet substorms are important for ULF activity [McPherron, 2005; Murphy et al., 2011a; Rae et al., 2011]. Furthermore on the nightside the dipole approximation for our field lines fail; the magnetic field stretches out far into the tail and it is possible that the higher-latitude stations (FCHU and GILL) are in fact on open field lines. This could be why the MSE in midnight is ranked by station latitude. For all stations, the noon sector performs best. There are multiple possible reasons for this. It could be that the three solar wind properties are sufficient to describe generation processes here but not elsewhere. This may be because substorms are not adequately represented in midnight, nor in the neighbouring flank sectors. Alternatively, in the noon sector the Earth's magnetic field is least variable and most similar to a dipole, therefore the ground-based

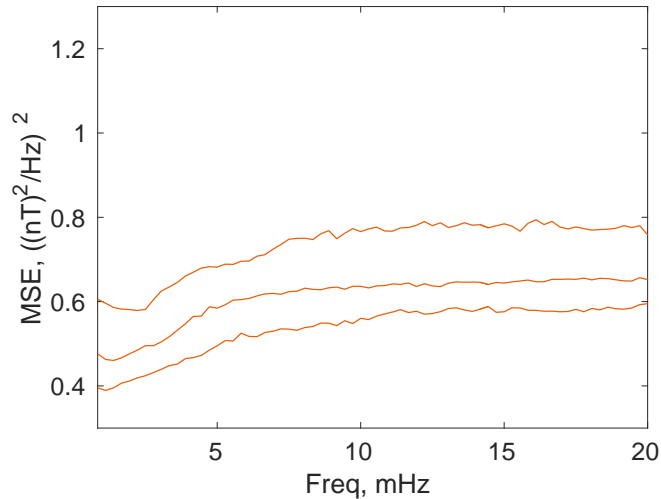


Figure 7-12: The median, upper and lower quartiles of mean square error between statistical model and original data values in each partition are shown, where quartiles are calculated over all station, MLT sector and $Bz > 0$ or $Bz < 0$ values at the corresponding frequency.

observations consistently correspond to a smaller region of space, resulting in smaller uncertainty as we average over a smaller spatial extent.

In Figure 7-12 we see the median, upper and lower quartiles of MSE for all partitions split by frequency. Our model is best at reproducing power in frequencies below 10 mHz and particularly in the lowest frequency waves. Recall that our parameters were chosen (and tested qualitatively for) a frequency range of 1-10 mHz. Higher frequencies may require more internal parameters as higher frequency waves are more strongly damped as they propagate through the magnetosphere. Alternatively, different solar wind parameters may be suitable, or internal drivers more significant.

Further study is necessary to examine the ability of the statistical model to approximate the underlying physics. In Chapter 6 the ability of the model to reproduce ULF wave power has been examined in general for the overall distribution and the production of ULF wave power time series. These tests are still averaged and can be broken down further by station, MLT sector, Bz and frequency, as can the MSE method presented here. Additionally, we can undertake a detailed investigation into the applicability of the normal distribution used to approximate the logpower in each solar wind bin. In Chapter 6 we concluded that this was a reasonable approximation but identifying any bins where this does not hold, and determining the reason behind this and behind the relatively uniform variance of $\sigma \sim 0.7$, could identify some interesting physics. In particular, if a bin were to contain two distributions it would indicate that two distinct ULF processes were active.

7.4 Testing ULF occurrence theories using the model

ULF wave generation and propagation processes can be analysed by examining the occurrence of wave power throughout the magnetosphere for given solar wind properties. Previous studies of these processes have included the effect of different solar wind conditions [Pahud *et al.*, 2009; Rae *et al.*, 2012] or included maps of ULF wave occurrence. However, using our statistical model the effect of variability in the solar wind parameters on the variability of ULF wave power can be quantified. Therefore each theory of generation or magnetospheric propagation can be tested using appropriate solar wind input conditions and examining the magnetospheric response.

This section begins with a brief review of mean power in each unparameterised partition, for reference with the rest of this chapter. In Section 7.4.2 we suggest physical questions about the magnetosphere that can be addressed with the statistical model (and will be, in future work).

7.4.1 Power in the original data

In this section we show the mean power in each partition of the original data set as a useful comparison for later sections. In Figure 7-13 the median and the upper and lower quartiles of the mean logpower is shown at each station, split by MLT sector and by $Bz < 0$ (blue) and $Bz > 0$ (orange). The quartiles are calculated over all corresponding frequency partitions. The ULF wave power spans several orders of magnitude and is higher at the higher latitude stations and for $Bz < 0$. The distribution of power is expected to vary by MLT sector, with more power in the midnight sector and a dawn-dusk asymmetry [Pahud *et al.*, 2009; Rae, 2017]. These MLT differences can be better studied using the solar-wind model as explained in Section 7.4.2.

Similarly, we show the median and the upper and lower quartile of mean power across partitions, split by frequency, in Figure 7-14 (a). As expected, the power drops off with frequency. The interquartile range does not particularly change. In Figure 7-14 this is shown with a logarithmic frequency scale to aid comparison to Rae *et al.* [2012]; here we have not split by station or MLT sector yet it still resembles a power law with a “bump” at the median and upper quartile, suggesting the presence of field line resonances smeared across the lower frequencies. This should be investigated in further detail by station, frequency and MLT sector.

7.4.2 Power in the statistical model

With measures such as the mean power or the upper quartile the statistical model can be used to consider many existing theories of ULF wave generation and propaga-

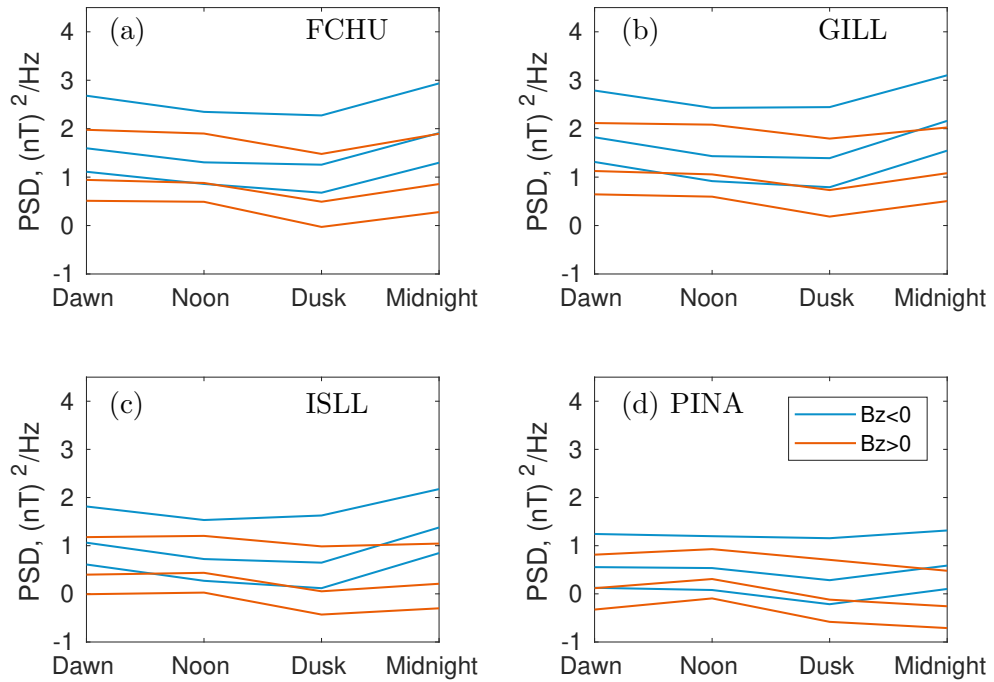


Figure 7-13: The median, upper and lower quartiles of mean power in each partition are shown, where quartiles are calculated over all frequency values for the corresponding station, MLT sector and $Bz > 0$ (orange) and $Bz < 0$ (blue).

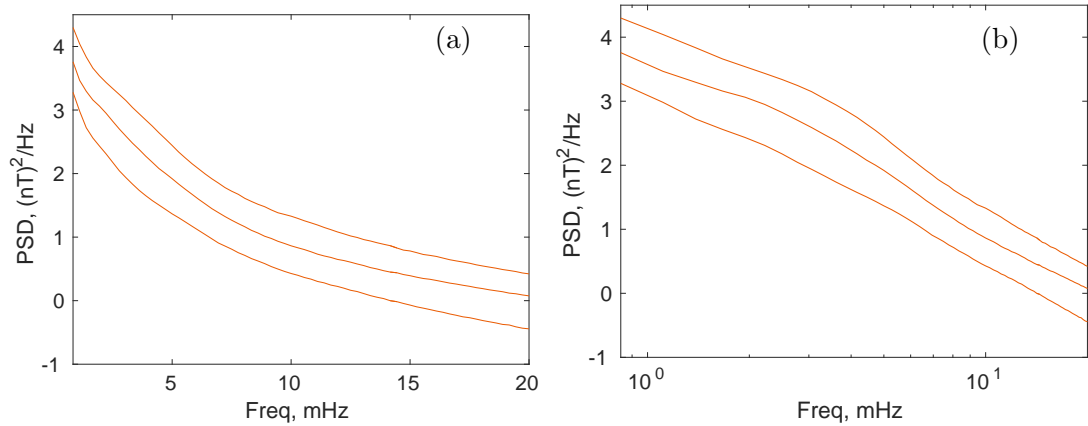


Figure 7-14: The median, upper and lower quartiles of mean power in each partition are shown, where quartiles are calculated over all station, MLT sector and $Bz > 0$ or $Bz < 0$ for each frequency. This is shown on a linear frequency scale (a) and a log-frequency scale (b).

tion. We suggest two complementary approaches to physics analysis using this model: identifying where a particular driving process is most effective, and examining existing theories of ULF wave generation and propagation. To do so properly, a comprehensive list of magnetospheric ULF phenomena needs to be compiled. For the processes already covered in this thesis, we can suggest a few questions to illustrate the versatility of the statistical model.

To identify where a driving process is most effective, we can find solar wind conditions known to be associated with each driving mechanism and investigate what station and MLT sectors they drive the most wave power in. For example, for Kelvin-Helmholtz conditions is there more power on the dawn or dusk flanks? (We would expect Kelvin-Helmholtz instabilities to be effective on both flanks yet there is often more power in the dawn sector associated with external drivers [Rae, 2017]). Similar analysis can be performed for other drivers such as FTEs and number density variations; where is the resultant power observed and is that where current theories expect it to be? Unlike many previous empirical studies, this can be quantified using methods outlined in this chapter. We can also quantify the variability in the ULF waves resulting from small variations in those input parameters. Given the difficulty in separating the effect of individual parameters and mechanisms earlier in this chapter, it is very possible that we still cannot study the mechanisms separately. That would still be an important result as it would inform the space physics community to consider the combined effect of driving processes - that they are too interdependent to consider individually.

Our other suggestion is to examine existing theories of generation and propagation more directly. For example, over all solar wind conditions, do we see the dawn/dusk asymmetry [Rae, 2017], where externally driven waves have a stronger amplitude in the dawn sector while internally driven waves dominate in the dusk sector? Where the solar wind parameters themselves are not of interest, choosing an interval of $v_{sw}, Bz, var(Np)$ to analyse represents a statistical study of ULF wave power when the magnetosphere is under similar driving conditions and/or under a similar configuration, as the nose of the magnetosphere and hence compression of Earth's dipole field is determined by v_{sw} and Bz [Shue *et al.*, 1998]. Thus the statistical model is of use for studying phenomena such as standing waves, which may be more detectable when accounting for the stand-off distance to the nose of the magnetosphere. For example, is there any evidence of cavity modes; standing waves between the plasmasphere or ionosphere and the magnetosphere [Kivelson *et al.*, 1984; Wright, 1994; Wright and Mann, 2013]? This could be addressed by finding sudden drop-offs of power at an inner station for a certain set of frequencies. This type of analysis is likely to be more effective once more stations have been added. We can also look for field-line resonances, and see how these change with different

magnetospheric configurations. With the highly averaged data presented so far, we have seen very little evidence of field line resonances. FLRs are a central component of many descriptions of magnetospheric ULF waves and therefore this should be investigated in individual partitions, to see if certain frequencies are particularly strongly driven under the correct conditions. For example in a given $v_{sw}, Bz, var(Np)$ bin (representing a single configuration of the magnetosphere under the same driving conditions) does one frequency stand out? These results should be compared to the cross-phase method *Waters et al.* [1991]; *Sandhu et al.* [2018], which identifies the eigenfrequency at a certain latitude and can be used to find the average fundamental frequency associated with a station and MLT sector. Where we are interested in standing waves, the upper quartile of ULF wave power may be of more interest than the mean as it will represent the higher powered (standing) waves.

In addition, using static solar wind conditions to study a single magnetospheric configuration, we can use the statistical model to investigate theories where ULF wave propagation is modulated by the solar wind properties. For example, when considering solar wind properties strongly associated with external drivers, is higher power observed at the highest-latitude stations on the dayside? In other words, are ULF waves damped as they propagate inwards and are waves of each frequency reflected at the L -shell we would expect them to be, due to density and hence Alfvén velocity variability [*Waters et al.*, 2000]? This is different to examining the cavity mode as we are looking for an attenuation of power with decreasing station latitude - perhaps with a sudden drop-off representing where the waves are reflected - instead of constant power across stations with a sharp drop-off. Whether or not we find either of these may indicate how important standing waves are on average.

In the section above (Section 7.4.1) we noted that ULF amplitude differs with MLT; *Pahud et al.* [2009] found significant differences by MLT sector and by fast compared to slow solar wind speeds for the same stations used in our study. In *Pahud et al.* [2009] the midnight sector was shown to have the most power for $v_{sw} < 500 \text{ km s}^{-1}$, with significantly increased power in dawn for $v_{sw} > 500 \text{ km s}^{-1}$. These phenomena should be investigated and compared to the results from our statistical model, which has better solar wind parameter resolution, although poorer MLT resolution.

Other interactions of generation and propagation processes to be studied with the statistical model include overreflection and Bz drivers. Overreflection entails an increased effectiveness of externally driven waves driving standing modes [*Mann et al.*, 1999], and is currently hypothesised to require a speed threshold of $\sim 500 \text{ km s}^{-1}$. Finally, given the ULF wave power observed in the midnight, dawn and dusk sectors, an investigation into substorms compared to FTEs as ULF drivers may be necessary, de-

spite our initial conclusion in Chapter 5 that as a dayside driver, Bz likely represented FTEs. The analysis of separation proxy χ_S suggests that substorm contributions are more important than previously considered in Chapter 5. However, it is as yet unclear how to complete such an investigation using our statistical model; both the statistical and multiple regression models do poorly in the midnight sector which may or may not be possible to resolve without additional parameters that describe substorm activity.

Some more open-ended questions may yield results interesting either for their physics or their insight into the uncertainty underlying the prediction of these waves. In areas where the underlying physical approximations are known to be particularly variable, is there more variability in the wave power? For example, analysis should focus on partitions corresponding to the plasmopause (where the underlying plasma density will be variable [Sheeley *et al.*, 2001; Moldwin, 2002]) or high-latitude stations in the midnight sector (which may be on open rather than closed field lines)?

These kinds of analysis follow on naturally from the model presented in this thesis and are examples of its strength as a statistical model compared to previous studies comparing ULF wave power and solar wind properties [Pahud *et al.*, 2009; Rae *et al.*, 2012]. REMOVED:In the remainder of this chapter we briefly outline how some remaining methods that may be used to investigate the underlying physics, by testing where models accurately reproduce the underlying physics and thereby identifying which physical approximations are appropriate in different regions of the magnetosphere.

7.5 Summary

The strength of the statistical model for investigating the underlying ULF wave physics lies in the ability to quantify changes in ULF wave power with changes in solar wind parameters. This enables us to investigate many existing theories of ULF generation and propagation quantitatively. Example physical questions are given in Section 7.4.2. The questions suggested in this chapter can be addressed with the statistical (or possibly the multiple regression) model; other future research directions are reviewed in Chapter 8.

The initial approach taken was to examine the individual effectiveness of the driving parameters. However, this appears not to be physically meaningful. This is an important result as both the driving parameters and the driving mechanisms themselves are highly interdependent. As a result it is highly likely that we cannot (and should not) distinguish the contribution of individual driving mechanisms. This remaining interdependence means that we cannot analyse the multiple regression coefficients as

initially intended and must instead substitute in full solar wind properties, examining the results power as suggested in Section 7.4. However, the multiple regression model performs surprisingly well at reproducing ULF wave power and is capable of extrapolating to solar wind conditions that the statistical model does not cover, suggesting that it is well suited to use as a “portable” version of the statistical model for future diffusion coefficient modelling.

CHAPTER 8

CONCLUSIONS

The goal of this work was to characterise magnetospheric ULF waves for use in radiation belt modelling. ULF wave-driven radial diffusion is currently poorly characterised in radiation belt diffusion models [*Horne et al.*, 2013]. To calculate radial diffusion coefficients, we require estimates of the power spectral density of ULF waves in the equatorial plane. One component of the equatorial electric field amplitudes at the equator can be estimated using ground-based PSD [*Ozeke et al.*, 2009], for use in simulations of the outer radiation belt [*Ozeke et al.*, 2014; *Li et al.*, 2016].

We have achieved our primary goal, creating a robust statistical model of ground-based ULF wave power driven by solar wind conditions. The model has been tested across four ground-based stations that span a range of latitudes which map to the outer radiation belt. The model effectively reproduces realistic ULF wave power distributions (when used probabilistically) and time series (when used deterministically, see Chapter 6). Throughout construction of this model the secondary goals have also been considered; the theoretical ULF generation mechanisms were reviewed and their importance discussed following the identification of ULF-effective solar wind parameters in Chapter 5. Requirements for improved radiation belt diffusion modelling determined our choices of radial and azimuthal resolution in the statistical model, and drove the decision to produce probabilistic output.

Review of results

In Chapter 5 we accounted for solar wind parameter interdependencies and nonlinear relationships to identify three solar wind properties that are causally correlated with near-instantaneous ULF wave power using fifteen years of ground-based magnetic field

measurements and the corresponding solar wind observations. The three resulting ULF-effective properties - solar wind speed v_{sw} , perturbations in number density δNp and southward interplanetary magnetic field, Bz - should all be considered as they contribute significantly to ULF wave power. Additionally, the behaviour change at $Bz = 0$ indicates that the simple nonlinear approach was necessary and that $Bz \leq 0$ should be addressed separately. We used these three parameters to guide a review of the solar wind driving mechanisms of ULF waves, suggesting that the Kelvin-Helmholtz instability, travelling flux tubes and density pulses are the dominant external drivers of magnetospheric ULF waves.

In Chapter 6 we described how these three solar wind parameters may be used to construct a statistical model of ULF wave power from 1-20 mHz. By investigating requirements of such a model for radiation belt diffusion modelling, we defined a “good” parameterisation, used the appropriate spatial resolution throughout the magnetosphere and chose to construct a probabilistic model. Testing on the four initial stations demonstrated that a deterministic time series outperforms hourly persistence, whilst total power over extended periods is best reproduced probabilistically. This statistical model was also compared to a similar geomagnetic activity (Kp) based model, suggesting that Kp represents an additional contribution to power. Kp would be an unsuitable parameter for our final model because of its temporal resolution but these results suggest that processes internal to the magnetosphere should be included. Additionally, time-lagged input may be necessary, rather than solely instantaneous measurements. However, these improvements are not immediately necessary as the model has performed surprisingly well in testing. Instead, the results demonstrate that the statistical model is ready to be implemented in existing diffusion models in order to improve accuracy of diffusion coefficients and to provide a direct link between solar wind driving and outer radiation belt variability.

Major implications

There are several results that merit special mention.

1. Firstly, the $Bz = 0$ threshold of ULF behaviour change identifies two situations containing very different physics. This warrants further study and suggests that statistical studies involving the effect of solar wind drivers on magnetospheric ULF waves (and therefore electron flux in the radiation belts) should not average between these two situations.
2. At multiple points throughout this thesis we have attempted to study the individual driving parameters or mechanisms. However, it is becoming increasingly

apparent that this kind of approach is unsuitable due to the complex interactions between mechanisms. Instead, future studies should consider their combined effects. This hypothesis will be confirmed when using the statistical model to test the underlying physics, as described in Chapter 7.

3. The construction of the statistical model has been shown to predict ground-based magnetic field power well enough that it can be included in existing radiation belt diffusion models, using existing mapping techniques to calculate diffusion coefficients [Ozeke *et al.*, 2009, 2012]. As it contains azimuthal variations in power, it satisfies one of the criteria for an improved radiation belt model [Horne *et al.*, 2013].
4. The construction of a probabilistic model represents an important step forward for radiation belt physics, to capture behaviour that is intrinsically variable and to identify model components that contain the most uncertainty. Furthermore, a probabilistic approach was shown to be necessary to reproduce the distribution of power over extended time periods. The ability to reproduce properties such as the total distribution is necessary for modelling techniques such as stochastic parameterisation [Watt *et al.*, 2017; Berner *et al.*, 2017].
5. Finally, the statistical model also has important implications for the testing current theories of ULF generation and propagation. Given specific solar wind conditions, the average occurrence of ULF waves throughout the magnetosphere can be quantified to test each hypothesis.

Limitations of the statistical model

The statistical model is based on only three near-instantaneous solar wind parameters and as such its performance is remarkably good (Chapter 6). However, the statistical model lacks internal driving mechanisms such as the drift-bounce resonance or substorms [McPherron, 2005; Yeoman *et al.*, 2016; Murphy *et al.*, 2011a; Rae *et al.*, 2011] and the persistence of ULF waves from previous hours. These, and processes driving ULF waves on timescales of longer than an hour, are only included on average and may account for some of the remaining variability in the statistical model. This is also true of some aspects of the internal configuration of the magnetosphere such as the plasma density. However, note that the compression of the magnetic field and the stand-off distance to the magnetopause is included implicitly as this is predominantly determined by the solar wind parameters v_{sw} and Bz used in our model [Shue *et al.*, 1998]. These limitations could be addressed by future improvements discussed below.

Other limitations would be more difficult to address, such as the lack of magnetosheath or post-L1 processing.

For use in radiation belt diffusion modelling, the major limitation is simply the work necessary to get this statistical model ready for use in existing models (see below).

Additionally, the new statistical model is only valid for the radial diffusion coefficient D_{LL}^E and similar analyses based on this work will need to be completed for D_{LL}^B (Section 3.4).

Future work

For the statistical model constructed in this project to be used directly in radiation belt diffusion models, some adaptations must be made. The first steps will be to package and publish the statistical model itself, or the multiple regression approximation. This must be done in such a way that is easy for potential users. More stations need to be added to include lower latitudes for complete coverage of the radiation belts. All ground-based power predictions must be mapped to the equatorial plane [following *Ozeke et al.*, 2009, 2012]. This mapping will need to be tested using in situ measurements. This is the minimum work necessary for the statistical model to be put into use in existing radiation belt diffusion models.

Comparison to a similar statistical Kp model and initial results of the physics analysis in Chapter 7 suggest that including substorms may improve the current statistical model. Other improvements to this model can be made by including time-lagged processes, the plasmopause location, persistence of ULF waves and any other internal sources. Additionally, the binning method could be improved to mitigate the effect of densely packed (and therefore low-resolution) Bz parameters. These improvements would mitigate two chief limitations of the model; the fact that we only use solar wind drivers, which are near-instantaneous.

To investigate the underlying physics, the statistical and multiple regression models can be used as suggested in Chapter 7. This primarily involves choosing solar wind properties and comparing the ULF wave power output, either by testing the occurrence of waves from driving conditions found in case studies (e.g. for magnetopause perturbations) or by choosing parameter intervals to represent a constant configuration of the magnetosphere (e.g. to study standing waves). These methods should be used to examine current theories such as Kelvin-Helmholtz instability driving on the flanks, FTEs and number density perturbations, dawn/dusk asymmetries, ULF penetration distance and standing waves such the cavity mode and field line resonances. Whilst these mechanisms have been clearly identified in case studies, these processes may or may not contribute significantly on average over our fifteen-year timescale. These inves-

tigations will constitute an advancement in our understanding of ULF wave occurrence as we can test and quantify the average effects of different solar wind conditions.

In Chapter 7 we also suggested that investigating where information was lost in each step of the model could identify where the underlying physical approximations failed. For example, in Chapter 6 our statistical model was based on the approximation that the underlying logpower distribution is normal in each bin. This could provide some insightful physics; it may be indicative of a multiplicative process and there may be a limit to the variance, which may be dependent on the length of the time window chosen. If there are regions of the magnetosphere where this approximation does not hold it may identify areas of particularly interesting physics. More generally, areas where the statistical model fails indicate regions where we have not appropriately considered how ULF waves are generated or processed by the magnetosphere and therefore need to reconsider the underlying physics.

Other future research into the physics behind ULF waves highlighted by this work include a study of ULF persistence; investigating the relationship of power between successive hours and whether this is significant compared to variation by MLT or due to solar wind drivers. Additionally, in Figure 5-1 (b) the intensity map of ULF wave power observed at single frequency for each solar wind speed has a very clear cut upper limit. This upper limit of power is not due to the instrumentation and changes with station and frequency, suggesting an upper limit to the power that can be supported by oscillations of the Earth's magnetic field. This may require a deep understanding of the coupling of ULF waves to the ionosphere to explain.

Finally, future research can also be undertaken to improve our method of calculating the effect of the ULF waves on radiation belt electrons. Existing mappings to the equatorial electric field include multiple physical approximations (for example a dipole magnetic field, ionospheric constants) and should be addressed probabilistically in order to construct a fully probabilistic model. The theoretical formalism behind our method of calculating radial diffusion coefficients is necessarily idealised and some key assumptions should be investigated (Section 6.4). Furthermore, the impact of radial diffusion needs to be more fully understood; the resulting energisation of electrons is typically addressed only in idealised resonant situations [*Elkington et al.*, 1999; *Degeling et al.*, 2007; *Elkington*, 2013; *Roederer and Zhang*, 2014].

Overall, the statistical model constructed here represents not only the first step towards a probabilistic model of radial diffusion but also a simple tool for analysing ULF behaviour in a novel way throughout the magnetosphere.

APPENDIX A

FAST-MODE COMPRESSIONAL WAVES CORRESPONDING TO OBSERVED DENSITY PERTURBATIONS δN_p

In Section 5.7.3 we used the properties of fast-mode compressional waves to identify the source of solar wind pressure perturbations. Here we confirm that the relationship between the amplitude of number density and velocity perturbations would be detectable using our solar wind observations. We derive this relationship and justify the extent to which it is valid.

Here, we consider the possibility that ULF-effective δN_p are a result of MHD waves originating at the Sun. While Alfvén waves may reach the Earth, they are not associated with density perturbations so we do not consider them here. Both slow and fast mode compressional waves are damped in high β plasmas and therefore may not reach the Earth, but slow mode waves are far more strongly damped [Barnes, 1966]. Therefore we only use fast mode waves in this analysis. We cannot and do not study entropy waves (i.e. density structures bound to the moving plasma) with this method.

In Section 4.2.3 we summed the power in N_p across frequencies 1.7-6.7 mHz to find δN_p . Here we can use the power at 2.5 mHz, $\mathcal{P}_{N_p}(2.5\text{mHz})$. The square root of this is then the amplitude of number density perturbations in that hour at 2.5 mHz, N_{p1} . Using the median mass density perturbation amplitude at 2.5 mHz, $n_1 = m_p N_{p1}$, and “average” (median) solar wind plasma values for unperturbed mass density $n_0 = m_p N_{p0}$, unperturbed magnetic field \mathbf{B}_0 , Alfvén velocity v_A and sound speed v_S , we can estimate the magnitudes for the corresponding velocity perturbations \mathbf{v}_1 of an “average” compressional wave. If these perturbations are of the same order as mean hourly values then they are detectable from the background, and so we should be able to identify whether they are correlated with power at all. If the perturbations are small

compared to the background we will not be able to identify whether or not they have a contribution.

We use two different co-ordinate systems: the GSE frame in which we have our OMNI data observations and the wave-centred frame with basis $\hat{\mathbf{a}}, \hat{\mathbf{b}}, \hat{\mathbf{c}}$. In this basis we define the $\hat{\mathbf{c}}$ -direction to be along the magnetic field, the $\hat{\mathbf{a}}$ -direction to be the direction of propagation perpendicular to \mathbf{B}_0 and $\hat{\mathbf{b}}$ to complete the set. \mathbf{k} is the direction of propagation of the wave, so that

$$\begin{aligned}\hat{\mathbf{a}} &= \frac{\mathbf{a}}{|\mathbf{a}|}, & \mathbf{a} &= \mathbf{k} - (\mathbf{k} \cdot \hat{\mathbf{c}})\hat{\mathbf{c}} \\ \hat{\mathbf{b}} &= \hat{\mathbf{c}} \times \hat{\mathbf{a}} \\ \hat{\mathbf{c}} &= \frac{\mathbf{B}_0}{|\mathbf{B}_0|}.\end{aligned}\tag{A.1}$$

Then in this basis \mathbf{k} can be written

$$\mathbf{k} = k[\sin \theta \quad 0 \quad \cos \theta],\tag{A.2}$$

where θ is the angle of propagation from the magnetic field and can also be found in the dispersion relation [Walker, 2005]

$$\left(\frac{\omega}{k}\right)^2 = v_{ph}^2 = \frac{1}{2} \left[v_A^2 + c_S^2 \pm [(v_A^2 + c_S^2)^2 - 4v_A^2 c_S^2 \cos^2 \theta]^{\frac{1}{2}} \right],\tag{A.3}$$

where $+$ describes the fast mode and $-$ the slow mode. We only use the fast mode as discussed above, which gives us an upper bound on the amplitude of velocity perturbations.

We can work out relationships with the total magnitude of perturbations n_1 and $|\mathbf{v}_1|$ in the wave-centred frame which can then be applied to any orthonormal co-ordinate system, removing the necessity of calculating the direction of propagation. We consider the effect of the bulk streaming of the solar wind plasma later.

Using the following linearised MHD equation

$$n_1 = \frac{n_0}{\omega} \mathbf{k} \cdot \mathbf{v}_1,\tag{A.4}$$

we see that there can be velocity perturbations in directions $\hat{\mathbf{a}}$ and/or $\hat{\mathbf{c}}$,

$$\frac{n_1}{n_0} v_{ph} = \hat{\mathbf{k}} \cdot \mathbf{v}_1 = \hat{k}_a v_{1a} + \hat{k}_c v_{1c}.\tag{A.5}$$

We can use this to put a limit on the magnitude of velocity perturbations by writing

it as

$$\mathbf{v}_1 = [v_{1a} \quad 0 \quad v_{1c}] = v_1 [\sin \theta_v \quad 0 \quad \cos \theta_v], \quad (\text{A.6})$$

describing all possible solutions in this basis using a new parameter θ_v . Then

$$\left| \frac{n_1}{n_0} v_{ph} \right| = \sqrt{|\mathbf{v}_1|^2 + 2v^2 \sin \theta \cos \theta \sin \theta_v \cos \theta_v} = |\mathbf{v}_1| \sqrt{1 + 2 \sin \theta \cos \theta \sin \theta_v \cos \theta_v}, \quad (\text{A.7})$$

and so we know the amplitude of velocity perturbations is within the range

$$\frac{1}{\sqrt{3}} \left| \frac{n_1}{n_0} v_{ph} \right| \leq |\mathbf{v}_1| \leq \left| \frac{n_1}{n_0} v_{ph} \right|, \quad (\text{A.8})$$

which is independent of basis. This range will change with angle of propagation θ as v_{ph} is dependent on θ . The total range in which velocity perturbations lie for all θ and the plasma values used are shown in Table A.1. We find that the maximum and

n_0	5.2 cm ⁻³
n_1	3.7 cm ⁻³
v_A	52.0 km s ⁻¹
v_s	55.8 km s ⁻¹
$v_{ph_{min}}$	55.8 km s ⁻¹
$v_{ph_{max}}$	76.3 km s ⁻¹

Table A.1: Table of median values used to calculate the resultant size of velocity perturbations we expect from fast mode compressional waves.

minimum total speed perturbations using Equation (A.8) are $v_{min} \sim 44.8$ km s⁻¹ and $v_{max} \sim 106.2$ km s⁻¹. This shows that for an ‘‘average’’ wave the speed perturbations are of an order that is distinguishable from background solar wind values.

We have not yet included the effect of the bulk flow of the solar wind plasma. The velocity along the Sun-Earth line means that for a velocity oscillation along x , corresponding velocity perturbations in the y and z components will appear to be of different frequencies. However, *Walker* [2002] uses the approximation that a fast mode wave will be propagating close to the Sun-Earth line by the time it reaches us. In this case, as velocity perturbations are along the magnetic field and axis of propagation, the component of compressional wave velocity perturbations away from the bulk flow (the shifted y and z components) should be relatively small. We do not need to identify every instance of a compressional wave to study their relationship to magnetospheric ULF wave power. We do not expect any velocity perturbations to represent a negative contribution to ULF power and so even a relatively small proportion with a positive contribution would manifest by indicating that δv has some

relationship with the resultant ULF power in Figure 5-9, which we do not see.

To summarise, the amplitude range of velocity perturbations corresponding to ULF-effective δN_p are resolved by our data. Therefore as long as there are enough waves with these characteristics, if compressional waves are the solar wind source of ULF-effective δN_p we would expect to see apparent increases of ULF power with the correlated δv . As we do not, the δN_p that are ULF-effective cannot come from coherent solar wind compressional waves, as concluded in Section 5.7.

BIBLIOGRAPHY

- Agapitov, O., K. H. Glassmeier, F. Plaschke, H. U. Auster, D. Constantinescu, V. Angelopoulos, W. Magnes, R. Nakamura, C. W. Carlson, S. Frey, and J. P. McFadden (2009), Surface waves and field line resonances: A THEMIS case study, *Journal of Geophysical Research: Space Physics*, *114*(12), 1–10, doi:10.1029/2008JA013553.
- Ali, A. F., D. M. Malaspina, S. R. Elkington, A. N. Jaynes, A. A. Chan, J. Wygant, and C. A. Kletzing (2016), Electric and magnetic radial diffusion coefficients using the Van Allen probes data, *Journal of Geophysical Research: Space Physics*, *121*(10), 9586–9607, doi:10.1002/2016JA023002.
- Alperovich, L. S., and E. N. Fedorov (2007), *Hydromagnetic Waves in the Magnetosphere and Ionosphere*, Springer.
- Archer, M. O., T. S. Horbury, J. P. Eastwood, J. M. Weygand, and T. K. Yeoman (2013), Magnetospheric response to magnetosheath pressure pulses: A low-pass filter effect, *Journal of Geophysical Research: Space Physics*, *118*(9), 5454–5466, doi:10.1002/jgra.50519.
- Baker, D. N., R. D. Belian, P. R. Higbie, R. W. Klebesadel, and J. B. Blake (1987), Deep dielectric charging effects due to high-energy electrons in earth's outer magnetosphere, *Journal of Electrostatics*, *20*(1), 3–19, doi:10.1016/0304-3886(87)90082-9.
- Baker, G. J., E. F. Donovan, and B. J. Jackel (2003), A comprehensive survey of auroral latitude Pc5 pulsation characteristics, *Journal of Geophysical Research: Space Physics*, *108*(A10), 1–14, doi:10.1029/2002JA009801.
- Barnes, A. (1966), Collisionless Damping of Hydromagnetic Waves, *Physics of Fluids*, *9*(8), 1483, doi:10.1063/1.1761882.

-
- Baumjohann, W., and R. A. Treumann (1996), *Basic Space Plasma Physics*, 1 ed., 329 pp., Imperial College Press, London.
- Bentley, S. N. (2019), A probabilistic, empirical model of magnetospheric ultra-low frequency wave power., doi:10.17864/1947.190, University of Reading Research Data Archive. (dataset).
- Bentley, S. N., C. E. J. Watt, M. J. Owens, and I. J. Rae (2018), ULF Wave Activity in the Magnetosphere: Resolving Solar Wind Interdependencies to Identify Driving Mechanisms, *Journal of Geophysical Research: Space Physics*, 123(4), 2745–2771, doi:10.1002/2017JA024740.
- Bentley, S. N., C. E. J. Watt, I. J. Rae, M. J. Owens, K. Murphy, M. Lockwood, and J. K. Sandhu (2019), Capturing uncertainty in magnetospheric ultra-low frequency wave models, *Space Weather (in press)*, doi:10.1029/2018SW002102.
- Berner, J., U. Achatz, L. Batté, L. Bengtsson, A. De La Cámara, H. M. Christensen, M. Colangeli, D. R. Coleman, D. Crommelin, S. I. Dolaptchiev, C. L. Franzke, P. Friederichs, P. Imkeller, H. Järvinen, S. Juricke, V. Kitsios, F. Lott, V. Lucarini, S. Mahajajaajan, T. N. Palmer, C. Penland, M. Sakradzija, J. S. Von Storch, A. Weisheimer, M. Weniger, P. D. Williams, and J. I. Yano (2017), Stochastic parameterization toward a new view of weather and climate models, *Bulletin of the American Meteorological Society*, 98(3), 565–587, doi:10.1175/BAMS-D-15-00268.1.
- Berube, D., J. Sanny, R. Taus, and A. Garoutte (2014), Dayside distribution of Pc5 wave power in the quiet magnetosphere and its response to the solar wind, *Planetary and Space Science*, 97, 1–8, doi:10.1016/j.pss.2014.04.012.
- Birn, J., J. F. Drake, M. A. Shay, B. N. Rogers, R. E. Denton, M. Hesse, M. Kuznetsova, Z. W. Ma, A. Bhattacharjee, A. Otto, and P. L. Pritchett (2001), Geospace Environmental Modeling (GEM) Magnetic Reconnection Challenge, *Journal of Geophysical Research: Space Physics*, 106(A3), 3715–3719, doi:10.1029/1999JA900449.
- Bittencourt, J. A. (2004), *Fundamentals of Plasma Physics*, 3rd ed., Springer New York, New York, NY, doi:10.1007/978-1-4757-4030-1.
- Borovsky, J. E., and K. Yakymenko (2017), Substorm occurrence rates, substorm recurrence times, and solar wind structure, *Journal of Geophysical Research: Space Physics*, 122(3), 2973–2998, doi:10.1002/2016JA023625.
- Bothmer, V., and I. A. Daglis (2007), *Space Weather- Physics and Effects*, Springer Berlin Heidelberg, Berlin, Heidelberg, doi:10.1007/978-3-540-34578-7.
-

- Brautigam, D. H., and J. M. Albert (2000), Radial diffusion analysis of outer radiation belt electrons during the October 9, 1990, magnetic storm, *Journal of Geophysical Research: Space Physics*, *105*(A1), 291–309, doi:10.1029/1999JA900344.
- Brautigam, D. H., G. P. Ginet, J. M. Albert, J. R. Wygant, D. E. Rowland, A. Ling, and J. Bass (2005), CRRES electric field power spectra and radial diffusion coefficients, *Journal of Geophysical Research: Space Physics*, *110*(A2), 1–15, doi:10.1029/2004JA010612.
- Cabinet Office (2017), National Risk Register of Civil Emergencies.
- Cao, M., R. L. McPherron, and C. T. Russell (1994), Statistical study of ULF wave occurrence in the dayside magnetosphere, *Journal of Geophysical Research*, *99*(A5), 8731, doi:10.1029/93JA02905.
- Cary, J. R., and A. J. Brizard (2009), Hamiltonian theory of guiding-center motion, *Reviews of Modern Physics*, *81*(2), 693–738, doi:10.1103/RevModPhys.81.693.
- Cayton, T. E., R. D. Belian, S. P. Gary, T. A. Fritz, and D. N. Baker (1989), Energetic electron components at geosynchronous orbit, *Geophysical Research Letters*, *16*(2), 147–150, doi:10.1029/GL016i002p00147.
- Chan, A. A. (1998), Noncanonical Hamiltonian methods for particle motion in magnetospheric hydromagnetic waves, *Journal of Geophysical Research: Space Physics*, *103*(A9), 20,501–20,513, doi:10.1029/98JA01742.
- Chen, and Hasegawa (1974a), A theory of long-lived magnetic pulsations 2. Impulse excitation of surface eigenmode, *Journal of Geophysical Research*, *79*(7), 1033, doi:10.1029/JA079i007p01033.
- Chen, F. F. (2016), *Introduction to Plasma Physics and Controlled Fusion*, third ed., Springer International Publishing, Cham, Heidelberg, doi:10.1007/978-3-319-22309-4.
- Chen, L., and A. Hasegawa (1974b), A theory of long-period magnetic pulsations: 1. Steady state excitation of field line resonance, *Journal of Geophysical Research*, *79*(7), 1024–1032, doi:10.1029/JA079i007p01024.
- Chi, P. J., D. H. Lee, and C. T. Russell (2006), Tamao travel time of sudden impulses and its relationship to ionospheric convection vortices, *Journal of Geophysical Research: Space Physics*, *111*(8), 1–10, doi:10.1029/2005JA011578.

-
- Claudepierre, S. G., I. R. Mann, K. Takahashi, J. F. Fennell, M. K. Hudson, J. B. Blake, J. L. Roeder, J. H. Clemmons, H. E. Spence, G. D. Reeves, D. N. Baker, H. O. Funsten, R. H. W. Friedel, M. G. Henderson, C. A. Kletzing, W. S. Kurth, R. J. Macdowall, C. W. Smith, and J. R. Wygant (2013), Van Allen Probes observation of localized drift resonance between poloidal mode ultra-low frequency waves and 60 keV electrons, *Geophysical Research Letters*, *40*(17), 4491–4497, doi:10.1002/grl.50901.
- Cohen, J. (1988), *Statistical Power Analysis for the Behavioral Sciences*, 2nd ed ed., 567 pp., Erlbaum, Hillsdale, N.J.
- Cowley, S. W. H. (1982), The causes of convection in the Earth’s magnetosphere: A review of developments during the IMS, *Reviews of Geophysics*, *20*(3), 531, doi: 10.1029/RG020i003p00531.
- Cowley, S. W. H., and M. Lockwood (1992), Excitation and decay of solar wind-driven flows in the magnetosphere-ionosphere system, *Annales Geophysicae*, *10*, 103–115.
- Davis, T. N., and M. Sugiura (1966), Auroral electrojet activity index AE and its universal time variations, *Journal of Geophysical Research*, *71*(3), 785–801, doi:10.1029/JZ071i003p00785.
- Degeling, A., R. Rankin, K. Kabin, R. Marchand, and I. Mann (2007), The effect of ULF compressional modes and field line resonances on relativistic electron dynamics, *Planetary and Space Science*, *55*(6), 731–742, doi:10.1016/j.pss.2006.04.039.
- Degeling, A. W., L. G. Ozeke, R. Rankin, I. R. Mann, and K. Kabin (2008), Drift resonant generation of peaked relativistic electron distributions by Pc 5 ULF waves, *Journal of Geophysical Research: Space Physics*, *113*(2), 1–10, doi: 10.1029/2007JA012411.
- Dungey, J. W. (1961), Interplanetary Magnetic Field and the Auroral Zones, *Physical Review Letters*, *6*(2), 47–48, doi:10.1103/PhysRevLett.6.47.
- Elkington, S. R. (2013), A Review of ULF Interactions with Radiation Belt Electrons, *Magnetospheric ULF Waves: Synthesis and New Directions*, *169*, 177–193, doi:10.1029/169GM12.
- Elkington, S. R., M. K. Hudson, and A. A. Chan (1999), Acceleration of relativistic electrons via drift-resonant interaction with toroidal-mode Pc-5 ULF oscillations, *Geophysical Research Letters*, *26*(21), 3273–3276, doi:10.1029/1999GL003659.

- Elkington, S. R., M. K. Hudson, and A. A. Chan (2003), Resonant acceleration and diffusion of outer zone electrons in an asymmetric geomagnetic field, *Journal of Geophysical Research: Space Physics*, *108*(A3), 1–15, doi:10.1029/2001JA009202.
- Engebretson, M., K.-H. Glassmeier, M. Stellmacher, W. J. Hughes, and H. Lühr (1998), The dependence of high-latitude PcS wave power on solar wind velocity and on the phase of high-speed solar wind streams, *Journal of Geophysical Research: Space Physics*, *103*(A11), 26,271–26,283, doi:10.1029/97JA03143.
- Fälthammar, C.-G. (1965), Effects of Time-Dependent Electric Fields on Geomagnetically Trapped Radiation, *J. Geophys. Res.*, *70*(11), 2503–2516, doi:10.1029/JZ070i011p02503.
- Falthammar, C.-G. (1968), Radial Diffusion by Violation of the Third Adiabatic Invariant, in *Earth's Particles and Fields, Proceedings of the NATO Advanced Study Institute, July 31-August 11, 1967*, edited by B. McCormac, pp. 157–169, Reinhold Book Corporation, Chicago, Illinois.
- Farrugia, C. J., R. C. Elphic, D. J. Southwood, and S. W. H. Cowley (1987), Field and flow perturbations outside the reconnected field line region in flux transfer events: Theory, *Planetary and Space Science*, *35*(2), 227–240, doi:10.1016/0032-0633(87)90091-2.
- Farrugia, C. J., F. T. Gratton, L. Bender, H. K. Biernat, N. V. Erkaev, J. M. Quinn, R. B. Torbert, and V. Dennisenko (1998), Charts of joint Kelvin-Helmholtz and Rayleigh-Taylor instabilities at the dayside magnetopause for strongly northward interplanetary magnetic field, *Journal of Geophysical Research*, *103*(A4), 6703, doi:10.1029/97JA03248.
- Fei, Y., A. A. Chan, S. R. Elkington, and M. J. Wiltberger (2006), Radial diffusion and MHD particle simulations of relativistic electron transport by ULF waves in the September 1998 storm, *Journal of Geophysical Research*, *111*(A12), A12,209, doi:10.1029/2005JA011211.
- Fok, M.-C., N. Y. Buzulukova, S.-H. Chen, A. Glocer, T. Nagai, P. Valek, and J. D. Perez (2014), The Comprehensive Inner Magnetosphere-Ionosphere Model, *Journal of Geophysical Research: Space Physics*, *119*(9), 7522–7540, doi:10.1002/2014JA020239.
- Frederickson, A. (1996), Upsets related to spacecraft charging, *IEEE Transactions on Nuclear Science*, *43*(2), 426–441, doi:10.1109/23.490891.

-
- Freeman, M. P., and S. K. Morley (2004), A minimal substorm model that explains the observed statistical distribution of times between substorms, *Geophysical Research Letters*, *31*(12), 2–5, doi:10.1029/2004GL019989.
- Frey, H. U. (2004), Substorm onset observations by IMAGE-FUV, *Journal of Geophysical Research*, *109*(A10), A10,304, doi:10.1029/2004JA010607.
- Geiss, J., G. Gloeckler, and R. von Steiger (1995), Origin of the Solar Wind from Cosition Data, *Space Science Reviews*, *72*, 49–60, doi:10.1007/BF00768753.
- Gillis, E. J., R. Rijnbeek, R. Kling, T. W. Speiser, and T. A. Fritz (1987), Do flux transfer events cause long-period micropulsations in the dayside magnetosphere?, *Journal of Geophysical Research*, *92*(A6), 5820, doi:10.1029/JA092iA06p05820.
- Gjerloev, J. W. (2012), The SuperMAG data processing technique, *Journal of Geophysical Research: Space Physics*, *117*(9), 1–19, doi:10.1029/2012JA017683.
- Glassmeier, K. H., M. Lester, W. A. C. Mier-Jedrzejowicz, C. A. Green, G. Rostoker, D. Orr, U. Wedeken, H. Junginger, and E. Amata (1984), Pc5 pulsations and their possible source mechanisms: a case study, *Journal of Geophysics - Zeitschrift fuer Geophysik*, *55*, 109–119.
- Glauert, S. A., R. B. Horne, and N. P. Meredith (2014), Three-dimensional electron radiation belt simulations using the BAS Radiation Belt Model with new diffusion models for chorus, plasmaspheric hiss, and lightning-generated whistlers, *Journal of Geophysical Research: Space Physics*, *119*(1), 268–289, doi:10.1002/2013JA019281.
- Goldstein, H., C. Poole, J. Safko, and S. R. Addison (2002), *Classical Mechanics*, 3rd ed., 3rd ed., Addison-Wesley.
- Gratton, F. T., C. J. Farrugia, and S. W. H. Cowley (1996), Is the magnetopause Rayleigh-Taylor unstable sometimes?, *Journal of Geophysical Research: Space Physics*, *101*(A3), 4929–4937, doi:10.1029/95JA03064.
- Gurnett, D. A., and A. Bhattacharjee (2005), *Introduction to Plasma Physics: With Space and Laboratory Applications*, Cambridge University Press, Cambridge, doi:10.1017/CBO9780511809125.
- Haerendel, G. (1968), Diffusion Theory of Trapped Particles and the Observed Proton Distribution, in *Earth's Particles and Fields, Proceedings of the NATO Advanced Study Institute, July 31-August 11, 1967*, edited by B. McCormac, Reinhold Book Corporation, Chicago, Illinois.

- Hapgood, M. A. (1992), Space physics coordinate transformations: a user guide, *Planetary and Space Science*, *40*(5), 711–717, doi:10.1016/0032-0633(92)90012-D.
- Hartering, M. D., D. L. Turner, F. Plaschke, V. Angelopoulos, and H. Singer (2013), The role of transient ion foreshock phenomena in driving Pc5 ULF wave activity, *Journal of Geophysical Research: Space Physics*, *118*(1), 299–312, doi:10.1029/2012JA018349.
- Horne, R. B., S. A. Glauert, N. P. Meredith, D. Boscher, V. Maget, D. Heynderickx, and D. Pitchford (2013), Space weather impacts on satellites and forecasting the Earth’s electron radiation belts with SPACECAST, *Space Weather*, *11*(4), 169–186, doi:10.1002/swe.20023.
- Huba, J. D. (2016), NRL Plasma Formulary, *Naval Research Laboratory*.
- Hughes, W. (1974), The effect of the atmosphere and ionosphere on long period magnetospheric micropulsations, *Planetary and Space Science*, *22*(8), 1157–1172, doi:10.1016/0032-0633(74)90001-4.
- Hughes, W. J. (1983), Hydromagnetic waves in the magnetosphere, in *Solar-Terrestrial Physics: Principles and Theoretical Foundations Based Upon the Proceedings of the Theory Institute Held at Boston College, August 9-26, 1982*, vol. 104, edited by R. L. Carovillano and J. M. Forbes, pp. 453–477, Springer Netherlands.
- Hughes, W. J., and D. J. Southwood (1976), The screening of micropulsation signals by the atmosphere and ionosphere, *Journal of Geophysical Research*, *81*(19), 3234–3240, doi:10.1029/JA081i019p03234.
- Hundhausen, a. J., S. J. Bame, J. R. Asbridge, and S. J. Sydoriak (1970), Solar wind proton properties: Vela 3 observations from July 1965 to June 1967, *Journal of Geophysical Research*, *75*, 4643, doi:10.1029/JA075i025p04643.
- Hwang, K. J., and D. G. Sibeck (2016), Role of Low-Frequency Boundary Waves in the Dynamics of the Dayside Magnetopause and the Inner Magnetosphere, in *Low-Frequency Waves in Space Plasmas*, edited by A. Keiling, D.-H. Lee, and V. Nakariakov, pp. 213–239, John Wiley & Sons, Inc, doi:10.1002/9781119055006.ch13.
- Jacobs, J. A., Y. Kato, S. Matsushita, and V. A. Troitskaya (1964), Classification of Geomagnetic Micropulsations, *Geophysical Journal of the Royal Astronomical Society*, *8*(3), 341–342, doi:10.1029/JZ069i001p00180.

-
- Jian, L., C. T. Russell, J. G. Luhmann, and R. M. Skoug (2006), Properties of stream interactions at one AU during 1995 - 2004, *Solar Physics*, 239(1-2), 337–392, doi:10.1007/s11207-006-0132-3.
- Johnson, N. L., S. Kotz, and N. Balakrishnan (1995), *Continuous Univariate Distributions, Vol. 2*, second ed., John Wiley & Sons, Inc, Hoboken, NJ.
- Jursa, A. (Ed.) (1985), *Handbook of Geophysics and the Space Environment*, Air Force Geophysics Laboratory.
- Kavosi, S., and J. Raeder (2015), Ubiquity of Kelvin–Helmholtz waves at Earth’s magnetopause, *Nature Communications*, 6(May), 7019, doi:10.1038/ncomms8019.
- Keiling, A., D.-H. Lee, and V. Nakariakov (Eds.) (2016), *Low-Frequency Waves in Space Plasmas*, Geophysical Monograph Series, John Wiley & Sons, Inc, Hoboken, NJ, doi:10.1002/9781119055006.
- Kellerman, A. C., and Y. Y. Shprits (2012), On the influence of solar wind conditions on the outer-electron radiation belt, *Journal of Geophysical Research: Space Physics*, 117(5), 1–14, doi:10.1029/2011JA017253.
- Kepko, L., and H. E. Spence (2003), Observations of discrete, global magnetospheric oscillations directly driven by solar wind density variations, *Journal of Geophysical Research: Space Physics*, 108(A6), 1–13, doi:10.1029/2002JA009676.
- Kepko, L., H. E. Spence, and H. J. Singer (2002), ULF waves in the solar wind as direct drivers of magnetospheric pulsations, *Geophysical Research Letters*, 29(8), 39–1–39–4, doi:10.1029/2001GL014405.
- Kim, K. H., C. A. Cattell, D. H. Lee, K. Takahashi, K. Yumoto, K. Shiokawa, F. S. Mozer, and M. Andre (2002), Magnetospheric responses to sudden and quasiperiodic solar wind variations, *Journal of Geophysical Research: Space Physics*, 107(A11), 1–12, doi:10.1029/2002JA009342.
- King, J. H., and N. E. Papitashvili (2005), Solar wind spatial scales in and comparisons of hourly Wind and ACE plasma and magnetic field data, *Journal of Geophysical Research: Space Physics*, 110(A2), 1–9, doi:10.1029/2004JA010649.
- Kivelson, M. G., and C. T. Russell (Eds.) (1995), *Introduction to Space Physics*, Cambridge University Press.

- Kivelson, M. G., and D. J. Southwood (1986), Coupling of global magnetospheric MHD eigenmodes to field line resonances, *Journal of Geophysical Research*, *91*(A4), 4345, doi:10.1029/JA091iA04p04345.
- Kivelson, M. G., J. Etcheto, and J. G. Trotignon (1984), Global compressional oscillations of the terrestrial magnetosphere: The evidence and a model, *Journal of Geophysical Research: Space Physics*, *89*(A11), 9851–9856, doi:10.1029/JA089iA11p09851.
- Komar, C. M., and P. A. Cassak (2016), The local dayside reconnection rate for oblique interplanetary magnetic fields, *Journal of Geophysical Research A: Space Physics*, *121*(6), 5105–5120, doi:10.1002/2016JA022530.
- Kuo, H., C. T. Russell, and G. Le (1995), Statistical studies of flux transfer events, *Journal of Geophysical Research: Space Physics*, *100*(A3), 3513–3519, doi:10.1029/94JA02498.
- Lai, S. T. (2011), *Fundamentals of Spacecraft Charging*, 272 pp., Princeton University Press, Princeton.
- Lanzerotti, L. J., and C. G. Morgan (1973), ULF geomagnetic power near $L = 4$: 2. Temporal variation of the radial diffusion coefficient for relativistic electrons, *Journal of Geophysical Research*, *78*(22), 4600–4610, doi:10.1029/JA078i022p04600.
- Lejosne, S., D. Boscher, V. Maget, and G. Rolland (2012), Bounce-averaged approach to radial diffusion modeling: From a new derivation of the instantaneous rate of change of the third adiabatic invariant to the characterization of the radial diffusion process, *Journal of Geophysical Research: Space Physics*, *117*(8), 1–10, doi:10.1029/2012JA018011.
- Lejosne, S., D. Boscher, V. Maget, and G. Rolland (2013), Deriving electromagnetic radial diffusion coefficients of radiation belt equatorial particles for different levels of magnetic activity based on magnetic field measurements at geostationary orbit, *Journal of Geophysical Research: Space Physics*, *118*(6), 3147–3156, doi:10.1002/jgra.50361.
- Li, W., Q. Ma, R. M. Thorne, J. Bortnik, X.-J. Zhang, J. Li, D. N. Baker, G. D. Reeves, H. E. Spence, C. A. Kletzing, W. S. Kurth, G. B. Hospodarsky, J. B. Blake, J. F. Fennell, S. G. Kanekal, V. Angelopoulos, J. C. Green, and J. Goldstein (2016), Radiation belt electron acceleration during the 17 March 2015 geomagnetic storm: Observations and simulations, *Journal of Geophysical Research: Space Physics*, *121*(6), 5520–5536, doi:10.1002/2016JA022400.

-
- Littlejohn, R. G. (1983), Variational principles of guiding centre motion, *Journal of Plasma Physics*, *29*(01), 111, doi:10.1017/S002237780000060X.
- Liu, J., V. Angelopoulos, D. Sibeck, T. Phan, Z. Y. Pu, J. McFadden, K. H. Glassmeier, and H. U. Auster (2008), THEMIS observations of the dayside traveling compression region and flows surrounding flux transfer events, *Geophysical Research Letters*, *35*(17), 1–6, doi:10.1029/2008GL033673.
- Liu, W., T. E. Sarris, X. Li, R. Ergun, V. Angelopoulos, J. Bonnell, and K. H. Glassmeier (2010), Solar wind influence on Pc4 and Pc5 ULF wave activity in the inner magnetosphere, *Journal of Geophysical Research: Space Physics*, *115*(12), 1–11, doi:10.1029/2010JA015299.
- Liu, W., W. Tu, X. Li, T. Sarris, Y. Khotyaintsev, H. Fu, H. Zhang, and Q. Shi (2016), On the calculation of electric diffusion coefficient of radiation belt electrons with in situ electric field measurements by THEMIS, *Geophysical Research Letters*, *43*(3), 1023–1030, doi:10.1002/2015GL067398.
- Lockwood, M. (1991), Flux transfer events at the dayside magnetopause: Transient reconnection or magnetosheath dynamic pressure pulses?, *Journal of Geophysical Research*, *96*(A4), 5497, doi:10.1029/90JA02389.
- Lockwood, M. (2013), Reconstruction and Prediction of Variations in the Open Solar Magnetic Flux and Interplanetary Conditions, *Living Reviews in Solar Physics*, *10*, doi:10.12942/lrsp-2013-4.
- Lockwood, M., M. J. Owens, L. A. Barnard, S. Bentley, C. J. Scott, and C. E. Watt (2016), On the origins and timescales of geoeffective IMF, *Space Weather*, *14*(6), 406–432, doi:10.1002/2016SW001375.
- Mann, I. R., and A. N. Wright (1999), Diagnosing the excitation mechanisms of Pc5 magnetospheric flank waveguide modes and FLRs, *Geophysical Research Letters*, *26*(16), 2609–2612, doi:10.1029/1999GL900573.
- Mann, I. R., A. N. Wright, K. J. Mills, and V. M. Nakariakov (1999), Excitation of magnetospheric waveguide modes by magnetosheath flows, *Journal of Geophysical Research*, *104*, 333–353, doi:10.1029/1998JA900026.
- Mann, I. R., D. K. Milling, I. J. Rae, L. G. Ozeke, A. Kale, Z. C. Kale, K. R. Murphy, A. Parent, M. Usanova, D. M. Pahud, E. A. Lee, V. Amalraj, D. D. Wallis, V. Angelopoulos, K. H. Glassmeier, C. T. Russell, H. U. Auster, and H. J. Singer (2008),
-

-
- The upgraded CARISMA magnetometer array in the THEMIS era, *Space Science Reviews*, *141*, 413–451, doi:10.1007/s11214-008-9457-6.
- Mann, I. R., K. R. Murphy, L. G. Ozeke, I. J. Rae, D. K. Milling, and A. Kale (2012), The role of ultralow frequency waves in radiation belt dynamics, *Geophysical Monograph Series*, *199*, 69–91, doi:10.1029/2012GM001349.
- Mann, I. R., E. A. Lee, S. G. Claudepierre, J. F. Fennell, A. Degeling, I. J. Rae, D. N. Baker, G. D. Reeves, H. E. Spence, L. G. Ozeke, R. Rankin, D. K. Milling, A. Kale, R. H. W. Friedel, and F. Honary (2013), Discovery of the action of a geophysical synchrotron in the Earth’s Van Allen radiation belts, *Nature Communications*, *4*, 1–6, doi:10.1038/ncomms3795.
- Mathie, R. A., and I. R. Mann (2000), A correlation between extended intervals of ULF wave power and storm-time geosynchronous relativistic electron flux enhancements, *Geophysical Research Letters*, *27*(20), 3261–3264, doi:10.1029/2000GL003822.
- Mathie, R. a., and I. R. Mann (2001), On the solar wind control of Pc5 ULF pulsation power at mid-latitudes: Implications for MeV electron acceleration in the outer radiation belt, *Journal of Geophysical Research*, *106*(A12), 796,29,729–29,783, doi:10.1029/2001JA000002.
- McIlwain, C. E. (1961), Coordinates for mapping the distribution of magnetically trapped particles, *Journal of Geophysical Research*, *66*(11), 3681–3691, doi:10.1029/JZ066i011p03681.
- McIlwain, C. E. (1966), Magnetic coordinates, *Space Science Reviews*, *5*(5), 585–598, doi:10.1007/BF00167327.
- McPherron, R. L. (2005), Magnetic pulsations: Their sources and relation to solar wind and geomagnetic activity, *Surveys in Geophysics*, *26*(5), 545–592, doi:10.1007/s10712-005-1758-7.
- Menk, F. W. (2011), Magnetospheric ulf waves: A review, in *The Dynamic Magnetosphere*, edited by W. Liu and M. Fujimoto, pp. 223–256, Springer Netherlands, doi:10.1007/978-94-007-0501-2.
- Meredith, N. P., R. B. Horne, and R. R. Anderson (2001), Substorm dependence of chorus amplitudes: Implications for the acceleration of electrons to relativistic energies, *Journal of Geophysical Research: Space Physics*, *106*(A7), 13,165–13,178, doi:10.1029/2000JA900156.
-

-
- Mishin, V. V. (1993), Accelerated Motions of the Magnetopause as a Trigger of the Kelvin-Helmholtz Instability, *Journal of Geophysical Research*, *98*(A12), 21,365–21,371, doi:10.1029/93JA00417.
- Moldwin, M. B. (2002), A new model of the location of the plasmopause: CRRES results, *Journal of Geophysical Research*, *107*(A11), 1339, doi:10.1029/2001JA009211.
- Murphy, K. R., I. J. Rae, I. R. Mann, and D. K. Milling (2011a), On the nature of ULF wave power during nightside auroral activations and substorms: 1. Spatial distribution, *Journal of Geophysical Research: Space Physics*, *116*(A5), doi:10.1029/2010JA015757.
- Murphy, K. R., I. R. Mann, I. J. Rae, and D. K. Milling (2011b), Dependence of ground-based pc5 ulf wave power on f10.7 solar radio flux and solar cycle phase, *Journal of Atmospheric and Solar-Terrestrial Physics*, *73*(11), 1500 – 1510, doi:https://doi.org/10.1016/j.jastp.2011.02.018, influence of Solar Activity on Interplanetary and Geophysical Phenomena.
- Murphy, K. R., I. R. Mann, and D. G. Sibeck (2015), On the dependence of storm time ULF wave power on magnetopause location: Impacts for ULF wave radial diffusion, *Geophysical Research Letters*, *42*(22), 9676–9684, doi:10.1002/2015GL066592.
- Murphy, K. R., I. R. Mann, I. J. Rae, D. G. Sibeck, and C. E. J. Watt (2016), Accurately characterizing the importance of wave-particle interactions in radiation belt dynamics: The pitfalls of statistical wave representations, *Journal of Geophysical Research: Space Physics*, *121*(8), 7895–7899, doi:10.1002/2016JA022618.
- Murphy, K. R., A. R. Inglis, D. G. Sibeck, I. J. Rae, C. E. J. Watt, M. Silveira, F. Plaschke, S. G. Claudepierre, and R. Nakamura (2018), Determining the mode, frequency, and azimuthal wave number of ULF waves during a HSS and moderate geomagnetic storm, *Journal of Geophysical Research: Space Physics*, doi:10.1029/2017JA024877.
- Nakagawa, T., A. Nishida, and T. Saito (1989), Planar magnetic structures in the solar wind, *Journal of Geophysical Research*, *94*(A9), 11,761, doi:10.1029/JA094iA09p11761.
- National Semiconductor Corporation (1980), Power Spectra Estimation, *National Semiconductor Corporation Application Note 255*.
- Navarro, A. B. (2012), Gyrokinetic Large Eddy Simulations, Ph.D. thesis, Université Libre de Bruxelles.
-

-
- Newbury, J. A., C. T. Russell, J. L. Phillips, and S. P. Gary (1998), Electron temperature in the ambient solar wind: Typical properties and a lower bound at 1 AU, *Journal of Geophysical Research*, *103*(A5), 9553, doi:10.1029/98JA00067.
- Newell, P. T., and J. W. Gjerloev (2011), Evaluation of SuperMAG auroral electrojet indices as indicators of substorms and auroral power, *Journal of Geophysical Research: Space Physics*, *116*(12), 1–12, doi:10.1029/2011JA016779.
- Northrop, T. G. (1963), Adiabatic charged-particle motion, *Reviews of Geophysics*, *1*(3), 283, doi:10.1029/RG001i003p00283.
- Obayashi, T., and J. A. Jacobs (1958), Geomagnetic Pulsations and the Earth's Outer Atmosphere, *Geophysical Journal of the Royal Astronomical Society*, *1*(1), 53–63, doi:10.1111/j.1365-246X.1958.tb00034.x.
- Oberparleiter, M. (2015), Interaction between the neoclassical equilibrium and microturbulence in gyrokinetic simulations, Ph.D. thesis, Universitat Ulm.
- Otto, A., L. C. Lee, and Z. W. Ma (1995), Magnetic field and plasma properties associated with pressure pulses and magnetic reconnection at the dayside magnetopause, *Journal of Geophysical Research*, *100*(A8), 14,895, doi:10.1029/95JA00417.
- Owens, M., and P. Cargill (2004), Non-radial solar wind flows induced by the motion of interplanetary coronal mass ejections, *Annales Geophysicae*, *22*(12), 4397–4406, doi:10.5194/angeo-22-4397-2004.
- Owens, M. J., and R. J. Forsyth (2013), The Heliospheric Magnetic Field, *Living Reviews in Solar Physics*, *10*, doi:10.12942/lrsp-2013-5.
- Owens, M. J., P. J. Cargill, C. Pagel, G. L. Siscoe, and N. U. Crooker (2005), Characteristic magnetic field and speed properties of interplanetary coronal mass ejections and their sheath regions, *Journal of Geophysical Research: Space Physics*, *110*(A1), 1–9, doi:10.1029/2004JA010814.
- Owens, M. J., R. Challen, J. Methven, E. Henley, and D. R. Jackson (2013), A 27 day persistence model of near-Earth solar wind conditions: A long lead-time forecast and a benchmark for dynamical models, *Space Weather*, *11*(5), 225–236, doi:10.1002/swe.20040.
- Owens, M. J., P. Riley, and T. S. Horbury (2017), Probabilistic Solar Wind and Geomagnetic Forecasting Using an Analogue Ensemble or “Similar Day” Approach, *Solar Physics*, *292*(5), 1–16, doi:10.1007/s11207-017-1090-7.
-

-
- Ozeke, L. G., I. R. Mann, and I. J. Rae (2009), Mapping guided Alfvén wave magnetic field amplitudes observed on the ground to equatorial electric field amplitudes in space, *Journal of Geophysical Research: Space Physics*, *114*(A1), n/a–n/a, doi:10.1029/2008JA013041.
- Ozeke, L. G., I. R. Mann, K. R. Murphy, I. J. Rae, D. K. Milling, S. R. Elkington, A. A. Chan, and H. J. Singer (2012), ULF wave derived radiation belt radial diffusion coefficients, *Journal of Geophysical Research: Space Physics*, *117*(4), 1–16, doi:10.1029/2011JA017463.
- Ozeke, L. G., I. R. Mann, K. R. Murphy, I. Jonathan Rae, and D. K. Milling (2014), Analytic expressions for ULF wave radiation belt radial diffusion coefficients, *Journal of Geophysical Research: Space Physics*, *119*(3), 1587–1605, doi:10.1002/2013JA019204.
- Pahud, D. M., I. J. Rae, I. R. Mann, K. R. Murphy, and V. Amalraj (2009), Ground-based Pc5 ULF wave power: Solar wind speed and MLT dependence, *Journal of Atmospheric and Solar-Terrestrial Physics*, *71*(10-11), 1082–1092, doi:10.1016/j.jastp.2008.12.004.
- Paschmann, G., G. Haerendel, I. Papamastorakis, N. Sckopke, S. J. Bame, J. T. Gosling, and C. T. Russell (1982), Plasma and Magnetic Field Characteristics of Magnetic Flux Transfer Events, *J. Geophys. Res.*, *87*(1), 2159–2168, doi:10.1029/JA087iA04p02159.
- Percival, D. B., and A. T. Walden (1993), *Spectral analysis for physical applications: multitaper and conventional univariate techniques*, Cambridge University Press, Cambridge.
- Pizzo, V. (1978), A three-dimensional model of corotating streams in the solar wind, 1. Theoretical foundations, *Journal of Geophysical Research*, *83*(A12), 5563, doi:10.1029/JA083iA12p05563.
- Plunkett, S. P., and S. T. Wu (2000), Coronal mass ejections (CMEs) and their geoeffectiveness, *IEEE Transactions on Plasma Science*, *28*(6), 1807–1817, doi:10.1109/27.902210.
- Pokhotelov, D., I. J. Rae, K. R. Murphy, and I. Mann (2015), The influence of solar wind variability on magnetospheric ULF wave power, *Annales Geophysicae*, doi:10.5194/angeocom-33-697-2015.
-

-
- Pokhotelov, D., I. J. Rae, K. R. Murphy, and I. R. Mann (2016), Effects of ULF wave power on relativistic radiation belt electrons: 8–9 October 2012 geomagnetic storm, *Journal of Geophysical Research: Space Physics*, *121*(12), 11,766–11,779, doi:10.1002/2016JA023130.
- Prandoni, P., and M. Vetterli (2008), *Signal Processing for Communications*, first ed., EPFL Press, Lausanne, Switzerland.
- Priest, E. R. (2014), *Magnetohydrodynamics of the Sun*, 576 pp., Cambridge University Press.
- Radoski, H. R. (1966), Magnetic toroidal resonances and vibrating field lines, *Journal of Geophysical Research*, *71*(7), 1891, doi:10.1029/JZ071i007p01891.
- Rae, I. J. (2017), *Dawn-Dusk Asymmetries in Ultra-Low-Frequency Waves*, chap. 14, pp. 187–198, American Geophysical Union (AGU), doi:10.1002/9781119216346.ch14.
- Rae, I. J., E. F. Donovan, I. R. Mann, F. R. Fenrich, C. E. Watt, D. K. Milling, M. Lester, B. Lavraud, J. A. Wild, H. J. Singer, H. Rème, and A. Balogh (2005), Evolution and characteristics of global Pc5 ULF waves during a high solar wind speed interval, *Journal of Geophysical Research: Space Physics*, *110*(A12), 1–16, doi:10.1029/2005JA011007.
- Rae, I. J., K. R. Murphy, C. E. J. Watt, and I. R. Mann (2011), On the nature of ULF wave power during nightside auroral activations and substorms: 2. Temporal evolution, *Journal of Geophysical Research: Space Physics*, *116*(A5), doi:10.1029/2010JA015762.
- Rae, I. J., I. R. Mann, K. R. Murphy, L. G. Ozeke, D. K. Milling, A. A. Chan, S. R. Elkington, and F. Honary (2012), Ground-based magnetometer determination of in situ Pc4-5 ULF electric field wave spectra as a function of solar wind speed, *Journal of Geophysical Research: Space Physics*, *117*(A4), n/a–n/a, doi:10.1029/2011JA017335.
- Reeves, G. D., S. K. Morley, R. H. W. Friedel, M. G. Henderson, T. E. Cayton, G. Cunningham, J. B. Blake, R. A. Christensen, and D. Thomsen (2011), On the relationship between relativistic electron flux and solar wind velocity: Paulikas and Blake revisited, *Journal of Geophysical Research: Space Physics*, *116*(2), 1–14, doi:10.1029/2010JA015735.
- Richardson, J. D., and K. I. Paularena (1998), The orientation of plasma structure in the solar wind, *Geophysical Research Letters*, *25*(12), 2097–2100, doi:10.1029/98GL01520.
-

-
- Roederer, J. G., and H. Zhang (2014), *Dynamics of Magnetically Trapped Particles*, vol. 403, 2 ed., Springer-Verlag Berlin Heidelberg, doi:10.1007/978-3-642-41530-2.
- Rostoker, G., J. C. Samson, F. Creutzberg, T. J. Hughes, D. R. McDiarmid, A. G. McNamara, A. V. Jones, D. D. Wallis, and L. L. Cogger (1995), Canopus - A ground-based instrument array for remote sensing the high latitude ionosphere during the ISTP/GGS program, *Space Science Reviews*, 71(1-4), 743–760, doi:10.1007/BF00751349.
- Russell, C. T., and R. C. Elphic (1978), Initial ISEE magnetometer results: magnetopause observations, *Space Science Reviews*, 22(6), 681–715, doi:10.1007/BF00212619.
- Russell, C. T., and R. C. Elphic (1979), ISEE observations of flux transfer events at the dayside magnetopause, *Geophysical Research Letters*, 6(1), 33–36, doi:10.1029/GL006i001p00033.
- Russell, C. T., G. Le, and H. Kuo (1996), The occurrence rate of flux transfer events, *Advances in Space Research*, 18(8), 197–205, doi:10.1016/0273-1177(95)00965-5.
- Saito, T. (1969), Geomagnetic pulsations, *Space Science Reviews*, 10(3), 319–412, doi:10.1007/BF00203620.
- Samson, J. C., J. A. Jacobs, and G. Rostoker (1971), Latitude-dependent characteristics of long-period geomagnetic micropulsations, *Journal of Geophysical Research*, 76(16), 3675–3683, doi:10.1029/JA076i016p03675.
- Sandhu, J. K., T. K. Yeoman, M. K. James, I. J. Rae, and R. C. Fear (2018), Variations of High-Latitude Geomagnetic Pulsation Frequencies: A Comparison of Time-of-Flight Estimates and IMAGE Magnetometer Observations, *Journal of Geophysical Research: Space Physics*, 123(1), 567–586, doi:10.1002/2017JA024434.
- Sarris, T. E., and X. Li (2017), Geomagnetic activity and local time dependence of the distribution of ultra low-frequency wave power in azimuthal wavenumbers, m, *Annales Geophysicae*, 35(3), 629–638, doi:10.5194/angeo-35-629-2017.
- Schulz, M., and A. Eviatar (1969), Diffusion of equatorial particles in the outer radiation zone, *Journal of Geophysical Research*, 74(9), 2182–2192, doi:10.1029/JA074i009p02182.
- Schulz, M., and L. J. Lanzerotti (1974), *Particle Diffusion in the Radiation Belts, Physics and Chemistry in Space*, vol. 7, Springer Berlin Heidelberg, Berlin, Heidelberg, doi:10.1007/978-3-642-65675-0.
-

-
- Schwartz, S. J., G. Paschmann, N. Sckopke, T. M. Bauer, M. Dunlop, A. N. Fazakerley, and M. F. Thomsen (2000), Conditions for the formation of hot flow anomalies at Earth's bow shock, *Journal of Geophysical Research: Space Physics*, *105*(A6), 12,639–12,650, doi:10.1029/1999JA000320.
- Sciffer, M. D. (2002), Propagation of ULF waves through the ionosphere: Analytic solutions for oblique magnetic fields, *Journal of Geophysical Research*, *107*(A10), 1297, doi:10.1029/2001JA000184.
- Sheeley, B. W., M. B. Moldwin, H. K. Rassoul, and R. R. Anderson (2001), An empirical plasmasphere and trough density model: CRRES observations, *Journal of Geophysical Research: Space Physics*, *106*(A11), 25,631–25,641, doi:10.1029/2000JA000286.
- Shprits, Y. Y., A. C. Kellerman, A. Y. Drozdov, H. E. Spence, G. D. Reeves, and D. N. Baker (2015), Combined convective and diffusive simulations: VERB-4D comparison with 17 March 2013 Van Allen Probes observations, *Geophysical Research Letters*, *42*(22), 9600–9608, doi:10.1002/2015GL065230.
- Shue, J.-H., P. Song, C. T. Russell, J. T. Steinberg, J. K. Chao, G. Zastenker, O. L. Vaisberg, S. Kokubun, H. J. Singer, T. R. Detman, and H. Kawano (1998), Magnetopause location under extreme solar wind conditions, *Journal of Geophysical Research*, *103*(A8), 17,691, doi:10.1029/98JA01103.
- Sibeck, D. G. (1990), A model for the transient magnetospheric response to sudden solar wind dynamic pressure variations, *Journal of Geophysical Research*, *95*(A4), 3755–3771, doi:10.1029/JA095iA04p03755.
- Simms, L. E., V. A. Pilipenko, and M. J. Engebretson (2010), Determining the key drivers of magnetospheric Pc5 wave power, *Journal of Geophysical Research: Space Physics*, *115*(10), 1–16, doi:10.1029/2009JA015025.
- Song, P. Le, G. Russell, C. T. (1994), Observational differences between flux transfer events and surface waves at the magnetopause, *Journal of Geophysical Research*, *99*, 2309–2320, doi:10.1029/93JA02852.
- Southwood, D. (1974), Some features of field line resonances in the magnetosphere, *Planetary and Space Science*, *22*(3), 483–491, doi:10.1016/0032-0633(74)90078-6.
- Southwood, D. J., and M. G. Kivelson (1990), The magnetohydrodynamic response of the magnetospheric cavity to changes in solar wind pressure, *Journal of Geophysical Research*, *95*(A3), 2301, doi:10.1029/JA095iA03p02301.
-

-
- Spasojevic, M., Y. Y. Shprits, and K. Orlova (2015), Global empirical models of plasmaspheric hiss using Van Allen Probes, *Journal of Geophysical Research A: Space Physics*, *120*(12), 10,370–10,383, doi:10.1002/2015JA021803.
- Stix, T. (1997), *Waves in Plasmas*, 2nd ed., American Institute of Physics.
- Stoica, P., and R. Moses (2005), *Spectral analysis of signals*, Prentice Hall, Inc, Upper Saddle River.
- Su, Z., F. Xiao, H. Zheng, and S. Wang (2010), STEERB: A three-dimensional code for storm-time evolution of electron radiation belt, *Journal of Geophysical Research: Space Physics*, *115*(A9), n/a–n/a, doi:10.1029/2009JA015210.
- Subbotin, D., Y. Shprits, and B. Ni (2010), Three-dimensional VERB radiation belt simulations including mixed diffusion, *Journal of Geophysical Research: Space Physics*, *115*(A3), n/a–n/a, doi:10.1029/2009JA015070.
- Takahashi, K. (2016), ULF Waves in the Inner Magnetosphere, in *Low-Frequency Waves in Space Plasmas*, edited by A. Keiling, D.-H. Lee, and V. Nakariakov, pp. 51–63, John Wiley & Sons, Inc, doi:10.1002/9781119055006.ch4.
- Takahashi, K., and A. Y. Ukhorskiy (2007), Solar wind control of Pc5 pulsation power at geosynchronous orbit, *Journal of Geophysical Research: Space Physics*, *112*(11), 1–16, doi:10.1029/2007JA012483.
- Takahashi, K., and A. Y. Ukhorskiy (2008), Timing analysis of the relationship between solar wind parameters and geosynchronous Pc5 amplitude, *Journal of Geophysical Research: Space Physics*, *113*(12), 1–13, doi:10.1029/2008JA013327.
- Takahashi, K., K. Yumoto, S. G. Claudepierre, E. R. Sanchez, O. A. Troshichev, and A. S. Janzhura (2012), Dependence of the amplitude of Pc5-band magnetic field variations on the solar wind and solar activity, *Journal of Geophysical Research: Space Physics*, *117*(4), 1–18, doi:10.1029/2011JA017120.
- Tanskanen, E. I. (2009), A comprehensive high-throughput analysis of substorms observed by IMAGE magnetometer network: Years 1993–2003 examined, *Journal of Geophysical Research: Space Physics*, *114*(5), 1–11, doi:10.1029/2008JA013682.
- Thomsen, M. F. (2004), Why Kp is such a good measure of magnetospheric convection, *Space Weather*, *2*(11), n/a–n/a, doi:10.1029/2004SW000089.
- Thomson, D. J. (1982), Spectrum Estimation and Harmonic Analysis, *Proceedings of the IEEE*, *70*(9), 1055–1096, doi:10.1109/PROC.1982.12433.
-

-
- Thorne, K. S., and R. D. Blandford (2017), *Modern Classical Physics*, Princeton University Press, Princeton.
- Toffoletto, F., S. Sazykin, R. Spiro, and R. Wolf (2003), Inner Magnetospheric Modeling with the Rice Convection Model, *Space Science Reviews*, 107(1/2), 175–196, doi:10.1023/A:1025532008047.
- Treumann, R. A., and W. Baumjohann (1997), *Advanced Space Plasma Physics*, Imperial College Press, London.
- Walker, A. D. (1981), The Kelvin-Helmholtz instability in the low-latitude boundary layer, *Planetary and Space Science*, 29(10), 1119–1133, doi:10.1016/0032-0633(81)90011-8.
- Walker, A. D. M. (2002), Excitation of field line resonances by MHD waves originating in the solar wind, *Journal of Geophysical Research: Space Physics*, 107(A12), 1–14, doi:10.1029/2001JA009188.
- Walker, A. D. M. (2005), *Magnetohydrodynamic Waves in Geospace*, IOP Publishing, London.
- Wang, C. P., R. Thorne, T. Z. Liu, M. D. Hartinger, T. Nagai, V. Angelopoulos, J. R. Wygant, A. Breneman, C. Kletzing, G. D. Reeves, S. G. Claudepierre, and H. E. Spence (2017), A multispacecraft event study of Pc5 ultralow-frequency waves in the magnetosphere and their external drivers, *Journal of Geophysical Research: Space Physics*, 122(5), 5132–5147, doi:10.1002/2016JA023610.
- Wang, Y. L., R. C. Elphic, B. Lavraud, M. G. G. T. Taylor, J. Birn, C. T. Russell, J. Raeder, H. Kawano, and X. X. Zhang (2006), Dependence of flux transfer events on solar wind conditions from 3 years of Cluster observations, *Journal of Geophysical Research: Space Physics*, 111(4), 1–13, doi:10.1029/2005JA011342.
- Waters, C. L., F. W. Menk, and B. J. Fraser (1991), The resonance structure of low latitude Pc3 geomagnetic pulsations, *Geophysical Research Letters*, 18(12), 2293–2296, doi:10.1029/91GL02550.
- Waters, C. L., B. G. Harrold, F. W. Menk, J. C. Samson, and B. J. Fraser (2000), Field line resonances and waveguide modes at low latitudes: 2. A model, *Journal of Geophysical Research: Space Physics*, 105(A4), 7763–7774, doi:10.1029/1999JA900267.
- Watt, C. E., I. J. Rae, K. R. Murphy, C. Anekallu, S. N. Bentley, and C. Forsyth (2017), The parameterization of wave-particle interactions in the Outer Radiation
-

-
- Belt, *Journal of Geophysical Research: Space Physics*, *122*(9), 9545–9551, doi:10.1002/2017JA024339.
- Weimer, D. R., D. M. Ober, N. C. Maynard, W. J. Burke, M. R. Collier, D. J. McComas, N. F. Ness, and C. W. Smith (2002), Variable time delays in the propagation of the interplanetary magnetic field, *J. Geophys. Res.*, *107*(1), doi:10.1029/2001ja009102.
- Wilcox, J. M. (1968), The interplanetary magnetic field. Solar origin and terrestrial effects, *Space Science Reviews*, *8*(2), 258–328, doi:10.1007/BF00227565.
- Wing, S., J. R. Johnson, E. Camporeale, and G. D. Reeves (2016), Information theoretical approach to discovering solar wind drivers of the outer radiation belt, *Journal of Geophysical Research: Space Physics*, *121*(10), 9378–9399, doi:10.1002/2016JA022711.
- Wolfe, A. (1980), Dependence of mid-latitude hydromagnetic energy spectra on solar wind speed and interplanetary magnetic field direction, *Journal of Geophysical Research*, *85*(A11), 5977, doi:10.1029/JA085iA11p05977.
- Wright, A. N. (1994), Dispersion and wave coupling in inhomogeneous MHD waveguides, *Journal of Geophysical Research*, *99*(A1), 159, doi:10.1029/93JA02206.
- Wright, A. N., and I. R. Mann (2013), *Global MHD Eigenmodes of the Outer Magnetosphere*, pp. 51–72, American Geophysical Union (AGU), doi:10.1029/169GM06.
- Wright, A. N., and G. J. Rickard (1995), ULF pulsations driven by magnetopause motions: Azimuthal phase characteristics, *Journal of Geophysical Research*, *100*(A12), 23,703, doi:10.1029/95JA01765.
- Yeoman, T. K., and D. M. Wright (2001), ULF waves with drift resonance and drift-bounce resonance energy sources as observed in artificially-induced HF radar backscatter, *Annales Geophysicae*, *19*(2), 159–170, doi:10.5194/angeo-19-159-2001.
- Yeoman, T. K., M. K. James, D. Y. Klimushkin, and P. N. Mager (2016), Energetic Particle-Driven ULF Waves in the Ionosphere, in *Low-Frequency Waves in Space Plasmas*, edited by A. Keiling, D.-H. Lee, and V. Nakariakov, pp. 1–14, John Wiley & Sons, Inc, doi:10.1002/9781119055006.ch1.
- Zong, Q. G., X. Z. Zhou, X. Li, P. Song, S. Y. Fu, D. N. Baker, Z. Y. Pu, T. A. Fritz, P. Daly, A. Balogh, and H. Réme (2007), Ultralow frequency modulation of energetic particles in the dayside magnetosphere, *Geophysical Research Letters*, *34*(12), 1–5, doi:10.1029/2007GL029915.
-